SEISMIC BEHAVIOR OF STEEL FIBER-REINFORCED CONCRETE COUPLING BEAMS WITHOUT DIAGONAL BARS

by

Ángel L. Pérez Irizarry

A dissertation submitted in partial fulfillment of
the requirements for the degree of

Doctor of Philosophy

(Civil Engineering)

at the

UNIVERSITY OF WISCONSIN–MADISON

2020

Date of final oral examination: February 6, 2020

The dissertation is approved by the following members of the Final Oral Committee:
Gustavo J. Parra-Montesinos, C.K. Wang Professor, Civil & Envr. Engineering
José A. Pincheira, Associate Professor, Civil & Envr. Engineering
Brock D. Hedegaard, Asst. Professor, Civil & Envr. Engineering (UM-Duluth)
Roderic S. Lakes, Wisconsin Distinguished Professor, Engineering Physics

To my parents, Alma E. Irizarry and Ángel L. Pérez, for their love, support, and encouragement throughout this journey. And to the loving memory of my grandfather, Juan A. Irizarry Ramos.

ACKNOWLEDGMENTS

The writer would like to acknowledge the financial support provided by the Charles Pankow Foundation, main sponsor of this research project, as well as that provided by Bekaert Corporation, ACI Concrete Research Council, and the American Society of Concrete Contractors. ArcelorMittal is also acknowledged for their donation of fibers used in some of the coupling beam specimens and Erico Corp. for their assistance with the procurement of materials for the construction of the test setup.

Special thanks are due my mentors Prof. Gustavo Parra-Montesinos, Prof. José Pincheira, Prof. Brock Hedegaard, and Prof. Roderic Lakes for their guidance, support, and teachings throughout my time in graduate school. Also thanks are due to the staff of the Wisconsin Structures and Materials Testing Laboratory, namely Bill Lang and Jacob Zeuske, for their advice and guidance in the laboratory, as well as for their help in the instrumentation and testing of the specimens.

The writer extends its gratitude to the fellow students who were involved during the various stages of the project for their much valued and needed help; in particular, Jonathan Stensberg, Alexander Restlaff, Andrew Rexrode, Daniela Rincón-Morassutti, and Peter Weatherer. Furthermore, the writer is especially grateful for the encouragement and many thought-provoking conversations with Mohamed Al-Tameemi and Dr. Le Pham. To conclude, the completion of this dissertation would not have been possible without the support and encouragement of my family and friends; thank you for being there for me through highs and lows and contributing to my professional and personal growth.

To all of you and many more not mentioned, Thank you!

— Ángel L. Pérez Irizarry (2020)

CONTENTS

Contents iii

List of Tables viii

List of Figures x

Abstract xxii

Chapter **1:** Introduction 1
- 1.1 Background and Motivation 1
- 1.2 Research Objectives 3

Chapter **2:** Literature Review 5
- 2.1 Fiber-Reinforced Concrete 5
  - 2.1.1 Tensile Behavior and Classification of FRC 8
  - 2.1.2 Compressive Behavior of FRC 10
  - 2.1.3 Shear Behavior of FRC Flexural Members 12
- 2.2 Coupling Beams 13
  - 2.2.1 Reinforced Concrete Coupling Beams 14
  - 2.2.2 Steel and Hybrid Coupling Beams 19
  - 2.2.3 Current Design Provisions for Reinforced Concrete Coupling Beams 19
  - 2.2.4 High-Performance Fiber-Reinforced Concrete Coupling Beams 22

Chapter **3:** Experimental Program 26
- 3.1 Overview 26
- 3.2 Coupling Beam Test Specimens 27
  - 3.2.1 Coupling Beam Reinforcement Design 28
- 3.3 Steel Fiber-Reinforced Concretes Investigated 34
- 3.4 Mixing of SFRC and Coupling Beam Construction 36

3.5 Test Setup, Displacement History and Instrumentation 41
3.6 Characterization of Steel Fiber-Reinforced Concrete Mechanical Properties 48
3.6.1 Four-Point Flexural Tests 48
3.6.2 Direct Tension Tests 49
3.6.3 Compression Cylinder Tests 50
3.7 Material Test Results 52
3.7.1 Four-Point Flexural Tests 52
3.7.2 Direct Tensile Tests 59
3.7.3 Compressive Tests 60
3.7.4 Steel Reinforcement Tensile Tests 64

Chapter **4:** Behavior of SFRC Test Coupling Beams 67
4.1 Overall Coupling Beam Behavior 67
4.1.1 Coupling Beam Specimen CB1 69
4.1.2 Coupling Beam Specimen CB2 72
4.1.3 Coupling Beam Specimen CB3 74
4.1.4 Coupling Beam Specimen CB4 76
4.1.5 Coupling Beam Specimen CB5 79
4.1.6 Coupling Beam Specimen CB6 82
4.1.7 Coupling Beam Specimen CB7 84
4.1.8 Coupling Beam Specimen CB8 87
4.2 SFRC Performance Criteria and Classification 90
4.3 Reinforcement Strains 93
4.3.1 Transverse Reinforcement 94
4.3.2 Confinement Reinforcement 99
4.3.3 Longitudinal and Dowel Reinforcement 101
4.4 Curvature Distribution 110
4.5 Behavior of Beam-to-Wall Connections 112
4.6 Flexural Behavior of SFRC Coupling Beams 117
4.6.1 Moment-Curvature Response 117

4.6.1.1 Concrete Compressive Stress-Strain Model 117
4.6.1.2 Steel Reinforcement Stress-Strain Model 119
4.6.1.3 SFRC Tensile Stress-Strain Model 121
4.6.1.4 Flexural Strength 123
4.6.1.5 Experimental Moment Curvature Response 126
4.6.2 Flexural Rigidity for Use in Linear Elastic Analysis 132
4.6.3 SFRC Compressive Strain Limits 134
4.6.4 Spread of Plasticity and Plastic Hinge Rotation Capacity . . 149
4.6.4.1 Plastic Hinge Rotation 150
4.7 Shear Behavior of SFRC Coupling Beams 153
4.7.1 Shear Response Outside Plastic Hinges 153
4.7.1.1 Shear Strains and SFRC Shear Strength Contribution 153
4.7.1.2 Effective Shear Stiffness 158
4.7.2 Shear Behavior of Plastic Hinges 161
4.7.2.1 Onset of Shear Sliding 166
4.7.3 Shear Friction Analysis 170
4.8 Axial Force and Elongations 177
4.9 Drift Component Analysis 181
4.10 Energy Dissipation 186

Chapter **5:** Design and Modeling Recommendations 191
5.1 SFRC Tensile and Flexural Response Evaluation 191
5.1.1 Relationship Between Tensile Post-Cracking Strength and Fiber Reinforcing Parameters 191
5.1.1.1 Post-Cracking Tensile Strength Versus Fiber Volume Fraction 191
5.1.1.2 Peak Post-Cracking Strength Versus Fiber Tensile Strength and Aspect Ratio 195
5.1.1.3 Calculated Peak Post-Cracking Strength Ratios . . . 196
5.2 SFRC Tensile Versus Flexural Response 198
5.3 Design of SFRC Coupling Beams 204

5.3.1 Dowel Reinforcement Cut-off 204
5.3.2 Plastic Sectional Analysis 205
5.3.2.1 Development of Tensile Stress Block 207
5.3.2.2 Validation of Proposed Sectional Analysis 211
5.4 Modeling Shear-Drift Response Envelopes 213
5.4.1 SFRC Coupling Beam Strength 214
5.4.2 Reinforcement Bond-Slip Response 214
5.4.2.1 Bond-Slip Model 214
5.4.2.2 Calculated Bond Strengths 216
5.4.2.3 Calculated Versus Experimental Bar Slip and Interface Rotations 221
5.4.3 Flexural Response 224
5.4.3.1 Elastic Beam Element with Shear Deformations . . 225
5.4.3.2 Effective Flexural Rigidity of SFRC Coupling Beams 225
5.4.3.3 Plastic Hinge Model - Inelastic Flexure 228
5.4.4 Shear-Sliding Displacements 230
5.4.5 Rotational Spring And Drift Calculations 235
5.4.6 Modeled vs. Experimental Backbone Curves 238

Chapter **6:** Summary And Conclusions 244
6.1 Study Summary 244
6.1.1 Summary of Coupling Beam Tests 246
6.1.2 Summary of Analytical Work 246
6.2 Conclusions and Recommendations 247
6.3 Recommendations for Future Work 252

References 254

Appendices 268

A: Optotrak Certus Data Processing 269
A.1 Drift Calculation with Support Rotations 269

A.2 Four-Point Flexural Tests 270
A.3 Direct Tensile Tests 272
A.4 Calculation of Coupling Beam Shear Distortions 275
A.5 Calculation of Coupling Beam Curvatures 278
A.5.1 Curvatures Calculated With Outer Markers 278
A.5.2 Curvatures and Rotations Calculated Using Linear Fits . . . 279

B: SFRC Flexural and Tensile Response Plots 282
B.1 SFRC Notched Beams 282
B.2 SFRC Un-Notched Beams 290
B.3 SFRC Tension Specimens 299

C: Specimen Test Dates 304

LIST OF TABLES

3.1 SFRC Mixtures Investigated. 35
3.2 SFRC Design Mixture Proportions. 36
3.3 Slumps of SFRCs Used in Coupling Beam Specimens. 39
3.4 Notched Beam Average Response Summary. 54
3.5 Equivalent Flexural Stress-Deflection Behavior Summary for Un-notched Beams. 56
3.6 Summary of Un-notched Beam Test Results Based on Crack Widths. . . 58
3.7 Summary of Tensile Test Results Summary. 59
3.8 Average Compressive Response Parameters. 62
3.9 Measured Steel Reinforcement Properties. 66

4.1 Summary of Coupling Beam Peak Responses. 68
4.2 SFRC Mixtures Classification. 92
4.3 Shear Strength Resisted by Transverse Reinforcement and the SFRC. . . 96
4.4 Calculated Shear Stress Contributions and Recommended Limits. . . . 98
4.5 Theoretical Yield Curvatures. 112
4.6 SFRC Tensile Response Model Parameters. 123
4.7 Calculated Peak Shear Demands using M–ϕ Analysis. 125
4.8 SFRC Limiting Compressive Strain in Plastic Hinge Regions. 148
4.9 Average Contribution of Deformation Mechanisms to Drift Demand. . 184
4.10 Lateral Drift Contributions for 1.0% Drift Cycle. 185
4.11 Lateral Drift Contributions for 3.0% Drift Cycle. 185
4.12 Lateral Drift Contributions for 5.0% Drift Cycle. 186
4.13 Normalized Dissipated Energy for RC and SFRC Coupling Beams. . . . 190

5.1 SFRC Average Tensile Responses. 192
5.2 Stresses and Strains for Modeling the Average Response of Each SFRC Class. 209
5.3 Tensile Stress Block Parameters at Peak Flexural Strength. 211

5.4 Calculated Shear Demands for SFRC Coupling Beams. 212
5.5 Calculated and Experimental Reinforcement-Slip Rotations at Peak Strength. 224
5.6 Effective Flexural Rigidity of SFRC Coupling Beams. 227
5.7 Calculated Response Summary. 238

C.1 Tensile and Compressive Test Dates. 304
C.2 Bending Test Dates. 305

LIST OF FIGURES

1.1 Coupled Walls and Coupling Beam Actions. 2

2.1 Examples of Fibers used to Reinforce Concretes (scale: inches). . . . 6
2.2 Classification of FRCCs, from Naaman and Reinhardt (2006). 7
2.3 Typical Responses of Fiber Reinforced Cement Composites (FRCCs) From Naaman (2007a). a) Strain-Softening FRCCs, b) Strain-Hardening FRCCs. 10
2.4 Effect of Fibers on Compressive Behavior of Concrete. From Fanella and Naaman (1985). 11
2.5 Diagonally-reinforced Coupling Beam Geometry and Internal Actions (Paulay and Binney, 1974). 16
2.6 Coupling Beam Reinforcement Layouts Investigated by Tassios et al. (1996) and Tegos and Penelis (1988), adapted from Setkit (2012). . . 18
2.7 Confinement Requirements for Diagonally-Reinforced Coupling Beams (from ACI 318-19). a) Confinement of Diagonals; b) Full-Section Confinement. 21
2.8 Coupling Beam Under Construction (Courtesy of R. Lequesne). . . . 21
2.9 Damage Comparison of HPFRC and RC Coupling Beams (Photos courtesy of R. Lequesne). 24

3.1 Reinforcement Detailing of Coupling Beam CB1. 30
3.2 Reinforcement Detailing of Coupling Beams CB2 and CB3. 31
3.3 Reinforcement Detailing of Coupling Beams CB4 and CB5. 31
3.4 Reinforcement Detailing of Coupling Beam CB6. 31
3.5 Reinforcement Detailing of Coupling Beams CB7 and CB8. 32
3.6 Reinforcement for the End Blocks Simulating Wall Boundary Regions. 33
3.7 Steel Fiber Reinforcement. 35
3.8 Mixing SFRC and Coupling Beam Specimen Ready for Casting. . . . 37
3.9 Precast SFRC Coupling Beam Being Inserted Into End Blocks. 39

3.10 Casting of End Blocks. 40
3.11 Finished Coupling Beam Specimen. 40
3.12 Coupling Beam Test Setup. 42
3.13 Intended Coupling Beam Test Displacement Histories. a) Specimen CB1; b) Specimens CB2-CB8. 43
3.14 Optotrak™ Marker Layout For Coupling Beams with $l_n/h = 3.0$. . . . 44
3.15 Optotrak™ Marker Layout For Coupling Beams with $l_n/h = 2.0$. . . . 45
3.16 Strain Gauge Installation (Top) and Strain Gauges with Finished Coating (Bottom). 46
3.17 Strain Gauge Location and ID (Specimen CB1). 46
3.18 Strain Gauge Location and ID (Specimens CB2-CB5). 47
3.19 Strain Gauge Location and ID (Specimens CB6-CB8). 47
3.20 Flexural Test Setup and Optical Sensor Layout. a) Notched Beams; b) Un-Notched Beams. 49
3.21 Tension Specimen and Marker Layout. 50
3.22 Marker Layout for Cylinder Compression Tests. 51
3.23 Normalized Equivalent Flexural Stress Versus Deflection Response of SFRC Notched Beams. 53
3.24 Normalized Equivalent Flexural Stress Versus Crack Opening Response of SFRC Notched Beams. 54
3.25 Normalized Equivalent Flexural Stress Versus Deflection Response of SFRC Un-notched Beams. 55
3.26 Normalized Equivalent Flexural Stress Versus Crack Width of SFRC Un-notched Beams. 57
3.27 Average Tensile Response of the SFRCs Investigated. 60
3.28 Estimation of the Post-Peak Compressive Response of SFRC Cylinders. 61
3.29 Normalized Average Compressive Stress Versus Strain Response of SFRCs Investigated. 63
3.30 Optotrak™ Marker Layout for the Tensile Testing of Reinforcing Bars. 64
3.31 Sample Reinforcement Tensile Stress-Strain Responses. a) #3 Bars; b) #4 Bars. 65

3.32 Sample Reinforcement Tensile Stress-Strain Responses. a) #5 Bars; b) #6 Bars. 65

4.1 Shear Failure of Specimen CB1. 69
4.2 Hysteresis Response of Specimen CB1. 70
4.3 Damage Progression in Specimen CB1. a) 1.0% Drift; b) 2.0% Drift; c) 3.0% Drift. 71
4.4 Hysteresis Response of Specimen CB2. 72
4.5 Damage Progression in Specimen CB2. a) 2.0% Drift; b) 4.0% Drift; c) $\approx$-5.5% Drift. 73
4.6 Hysteresis Response of Specimen CB3. 74
4.7 Damage Progression in Specimen CB3. a) -2.0% Drift; b) -4.0% Drift; c) -5.6% Drift. 75
4.8 Hysteresis Response of Specimen CB4. 76
4.9 Damage Progression in Specimen CB4. a) 2.0% Drift; b) 4.1% Drift; c) 6.0% Drift. 78
4.10 Ends of Specimen CB4. a) 6.0% Drift; b) -6.5% Drift; c) After Removal of Spalled Concrete. 78
4.11 Hysteresis Response of Specimen CB5 (P = Axial Force). 80
4.12 Damage Progression in Specimen CB5. a) 2.0% Drift; b) 4.0% Drift; c) 6.2% Drift. 81
4.13 Damage after test - Specimen CB5. a) Through-Depth Cracks at Top and Bottom Plastic Hinges; b) Fractured Flexural Reinforcement (Top Plastic Hinge); c) Fractured Flexural Reinforcement (Bottom Plastic Hinge). 82
4.14 Hysteresis Response of Specimen CB6 (P = Axial Force). 83
4.15 Damage Progression in Specimen CB6. a) 2.1% Drift; b) 4.1% Drift; c) 6.0% Drift. 84
4.16 Hysteresis Response for Specimen CB7. 85
4.17 Damage Progression in Specimen CB7. a) -2.2% Drift; b) 5.0% Drift; c) Sliding Shear Failure at -5.7% Drift. 86

4.18 Hysteresis Response for Specimen CB8 (P = Axial Force). 88
4.19 Ends of Coupling Beam CB8. a) Top and Bottom Beam-to-Wall Interfaces (-2.1% drift); b) Damage at Top and Bottom Ends (5.1% Drift). 89
4.20 Damage Progression in Specimen CB8. a) -2.1% Drift; b) 4.2% Drift; c) 8.2% Drift. 89
4.21 Recommended Coupling Beam Shear Stress-Drift Limits for the Proposed SFRC Classes (Pérez-Irizarry and Parra-Montesinos, 2017). . . 91
4.22 Stresses Calculated from Measured Strains - Strain Gauge F2 in Specimen CB6. 93
4.23 Strain Envelopes for Transverse Reinforcement Outside Plastic Hinges (Coupling Beams with $l_n/h = 3.0$). Left: Specimen CB2; Right: Specimen CB4. 95
4.24 Strain Envelopes for Transverse Reinforcement Outside Plastic Hinges (Coupling Beams with $l_n/h = 2.0$). Left: Specimen CB6; Right: Specimen CB8. 95
4.25 Shear Stress Carried by the SFRC ($v_c = v_u - v_s$) with v_s Calculated using $(f_s)_{M-P}$. 98
4.26 Plastic Hinge Confinement Reinforcement Strain Envelopes for Coupling Beams with $l_n/h = 3.0$. Left: Specimen CB2; Right: Specimen CB4. 100
4.27 Plastic Hinge Confinement Reinforcement Strain Envelopes for Coupling Beams with $l_n/h = 2.0$. Left: Specimen CB6; Right: Specimen CB8. 100
4.28 Strain Response of Main Flexural Reinforcement-Specimen CB2. a) Beam-Wall Interface; b) $h/2$ from Support. 102
4.29 Strain Response of Main Flexural Reinforcement-Specimen CB4. a) Beam-Wall Interface; b) $h/2$ from Support. 102
4.30 Strain Response of Main Flexural Reinforcement-Specimen CB6. a) Beam-Wall Interface; b) $h/5$ from Support. 103
4.31 Strain Response of Main Flexural Reinforcement-Specimen CB8. a) Beam-Wall Interface; b) $h/5$ from Support. 103

4.32 Longitudinal Reinforcement Strains at 1.0% Drift (Specimens CB2–CB5). a) Positive Drifts; b) Negative Drifts. 104
4.33 Longitudinal Reinforcement Strains at 3.0% Drift (Specimens CB2–CB5). a) Positive Drifts; b) Negative Drifts. 105
4.34 Longitudinal Reinforcement Strains at 5.0% Drift (Specimens CB2–CB5). a) Positive Drifts; b) Negative Drifts. 106
4.35 Longitudinal Reinforcement Strains at 1.0% Drift (Specimens CB6–CB8). a) Positive Drifts; b) Negative Drifts. 107
4.36 Longitudinal Reinforcement Strains at 3.0% Drift (Specimens CB6–CB8). a) Positive Drifts; b) Negative Drifts. 108
4.37 Longitudinal Reinforcement Strains at 5.0% Drift (Specimens CB6–CB8). a) Positive Drifts; b) Negative Drifts. 109
4.38 Sample Curvature Profiles - Specimen CB5. a) Positive Drifts; b) Negative Drifts. 110
4.39 Sample Curvature Profiles - Specimen CB6. a) Positive Drifts; b) Negative Drifts. 111
4.40 Moment Versus Rotation Response at Beam-to-Wall Connections. a) Specimen CB2; b) Specimen CB3. 113
4.41 Moment Versus Rotation Response at Beam-to-Wall Connections. a) Specimen CB4; b) Specimen CB5. 113
4.42 Moment-Rotation Response at Beam-to-Wall Connections for Specimen CB6. 114
4.43 Moment-Rotation Response at Beam-to-Wall Connections. a) Specimen CB7; b) Specimen CB8. 115
4.44 Interface Rotation versus Average Cycle Drift. 116
4.45 Compressive Stress-Strain Response Model. 118
4.46 Stress-Strain Model and Experimental Responses for Steel Reinforcement (Specimen CB4). 120
4.47 SFRC Tensile Stress Versus Strain Model (Specimen CB4). 122
4.48 SFRC Coupling Beam Critical Sections. 124
4.49 Experimental Moment Versus Curvature Responses - Specimen CB2. 127

4.50 Experimental Moment Versus Curvature Responses - Specimen CB3. 127
4.51 Experimental Moment Versus Curvature Responses - Specimen CB4. 128
4.52 Experimental Moment Versus Curvature Responses - Specimen CB5. 128
4.53 Experimental Moment Versus Curvature Responses - Specimen CB6. 130
4.54 Experimental Moment Versus Curvature Responses - Specimen CB7. 130
4.55 Experimental Moment Versus Curvature Responses - Specimen CB8. 131
4.56 Effective Flexural Rigidity for Equivalent Linear Elastic Analysis. . . 133
4.57 Sample Strain Profile and Linear Fit - Top Plastic Hinge of Specimen CB2. 135
4.58 Strain Profile and Linear Fit - Top Plastic Hinge of Specimen CB4. . . 137
4.59 Pearson's Correlation Coefficients for Strain Profile Linear Fits (f = frequency; n = sample size). 137
4.60 Calculated Curvatures - Specimen CB4. a) Top Hinge (Strip 2); b) Bottom Hinge (Strip 11). 138
4.61 Opening and Closing of Flexural Cracks during Reversed Cyclic Displacements. 139
4.62 Tangents used to Calculate Upper-Bound Compressive Strain in Specimen CB5. a) Bottom Hinge; b) Top Hinge. 140
4.63 Determination of Lower- and Upper-Bound Compressive Strains. a) Points Corresponding to Zero Compressive Strain on a M–θ Cycle; b) Calculated Strains at Beam Edges. 141
4.64 Calculated Compressive Strains - Specimen CB2. a) Upper-bound Estimate; b) Lower-bound Estimate. 142
4.65 Calculated Compressive Strains - Specimen CB3. a) Upper-bound Estimate; b) Lower-bound Estimate. 142
4.66 Calculated Compressive Strains - Specimen CB4. a) Upper-bound Estimate; b) Lower-bound Estimate. 143
4.67 Calculated Compressive Strains - Specimen CB5. a) Upper-bound Estimate; b) Lower-bound Estimate. 143
4.68 Calculated Lower-Bound Compressive Strains - Specimen CB6. 144

4.69 Calculated Lower-Bound Compressive Strains. a) Specimen CB7; b) Specimen CB8. 145
4.70 Average Concrete Compressive Strain versus Drift. a) Specimen CB5 Upper- and Lower-Bound Strains; and b) Specimen CB8 Interface Lower-Bound Strains. 146
4.71 Evidence of Crushing - Specimen CB5. 147
4.72 Shear Versus Rotation Response - Specimen CB3. 151
4.73 Shear Versus Rotation Response - Specimen CB4. 151
4.74 Shear Versus Rotation Response - Specimen CB7. 152
4.75 Shear Versus Rotation Response - Specimen CB8. 152
4.76 Shear Strain Distribution - Specimen CB1. 154
4.77 Shear Strain Distribution - Specimen CB8. 154
4.78 Average Shear Strains Outside Plastic Hinges (γ_{avg} in rad). 155
4.79 Coupling Beam Shear Stress Contributions - Specimens CB1 through CB4 ($\sqrt{f'_c}$ in psi units). 156
4.80 Coupling Beam Shear Stress Contributions - Specimens CB5 through CB8 ($\sqrt{f'_c}$ in psi units). 157
4.81 Mid-span region Shear Response Comparison - Specimens CB1, CB4 and CB8. 159
4.82 Effective Secant Shear Stiffness. a) Effective-to-Uncracked Shear Moduli Ratio; b) Effective Shear Modulus as Fraction of the Young's Modulus of Concrete. 160
4.83 Plastic Hinge Shear Response. a) Specimen CB2; b) Specimen CB3. . 162
4.84 Plastic Hinge Shear Response - Specimen CB7. 163
4.85 Plastic Hinge Shear Response - Specimen CB8. 163
4.86 Plastic Hinge Shear Strain-Rotation Responses. a) Specimens with $l_n/h = 3.0$; b)Specimens with $l_n/h = 2.0$. 165
4.87 Plastic Hinge Shear Strain-Rotation Average Responses. a) Specimens with $l_n/h = 3.0$; b)Specimens with $l_n/h = 2.0$. 165
4.88 Definition of Changes in Shear Strain for Two Consecutive Hysteresis Cycles. 167

4.89 Shear-Rotation Change Ratio Versus Shear Stress in SFRC Plastic Hinges - Specimens with $l_n/h = 3.0$. a) Dowel Cut-Off Section; b) Beam-Wall Interfaces. 168
4.90 Shear-Rotation Change Ratio Versus Shear Stress in SFRC Plastic Hinges - Specimens with $l_n/h = 2.0$. a) Dowel Cut-Off Section; b) Beam-Wall Interfaces. 168
4.91 Specimen CB2 - Shear Friction-Sliding Response. Solid and hollow markers correspond to positive and negative drifts, respectively. . . . 172
4.92 Specimen CB3 - Shear Friction-Sliding Response. Solid and hollow markers correspond to positive and negative drifts, respectively. . . . 172
4.93 Specimen CB4 - Shear Friction-Sliding Response. Solid and hollow markers correspond to positive and negative drifts, respectively. . . . 173
4.94 Specimen CB5 - Shear Friction-Sliding Response. Solid and hollow markers correspond to positive and negative drifts, respectively. . . . 173
4.95 Specimen CB6 - Shear Friction-Sliding Response. Solid and hollow markers correspond to positive and negative drifts, respectively. . . . 175
4.96 Specimen CB7 - Shear Friction-Sliding Response. Solid and hollow markers correspond to positive and negative drifts, respectively. . . . 176
4.97 Specimen CB8 - Shear Friction-Sliding Response. Solid and hollow markers correspond to positive and negative drifts, respectively. . . . 176
4.98 Average Axial Strain Versus Drift Envelopes for Specimens CB2 through CB8. 178
4.99 Coupling Beam Axial Force versus Longitudinal Strains. 179
4.100 Coupling Beam Axial Force versus Longitudinal Strains. 180
4.101 Relative Contributions to Drift. a) Specimen CB1; b) Specimen CB2. . 182
4.102 Relative Contributions to Drift. a) Specimen CB3; b) Specimen CB4. . 183
4.103 Relative Contributions to Drift. a) Specimen CB5; b) Specimen CB6. . 183
4.104 Relative Contributions to Drift. a) Specimen CB7; b) Specimen CB8. . 184
4.105 Energy Dissipated per Drift Cycle. 187
4.106 Normalized Dissipated Energy. a) Coupling Beam and Equivalent Elasto-Plastic Hysteresis Loops; b) Normalized Energy per Drift Cycle. 188

5.1 Influence of Fiber Volume Fraction on SFRC Peak Post-Cracking Tensile Strength. 194
5.2 Relation Between $(R_{pc})_{1.5\%}$ and Fiber Aspect Ratio and Tensile Strength. 196
5.3 Experimental and Calculated Tensile Strength Ratios. 197
5.4 Stress Distributions for SFRC Bending Analysis; a) "Real" Stresses; b) Assumed Stresses at Peak Post-Cracking Strength; c) Assumed Stresses at Residual Strength ($\delta = \frac{L}{150}$). 199
5.5 Comparison of Calculated and Experimental Flexural and Tensile Stresses; a) Flexural Stress from Tensile Response; b) Tensile Stress from Flexural Response. 201
5.6 Assumed Tensile Response for Calculation of Flexural Strength of ASTM C1609 Beams at a Midspan Deflection of $\frac{L}{150}$. 203
5.7 Coupling Beam Moment Capacity/Demand Diagram. 205
5.8 Assumed Strain Distribution and Internal Forces. 207
5.9 Measured and Modeled SFRC Average Tensile Responses. 209
5.10 SFRC Stress Distributions and Corresponding Stress Blocks. 210
5.11 Calculated and Experimental Coupling Beam Shear Demands. 212
5.12 Reinforcement Bond-Slip Model. a) Embedded Bar in Tension; b) Assumed Bond Stresses; c) Bar Stresses; d) Bar Strains; and e) Bar-Slip Rotation. 216
5.13 Stresses/Forces Acting on Differential Bar Length. 216
5.14 Location of Strain Gauges Used for Bond Stress Calculations in Specimens with Span-to-Depth Ratio of 3.0. 217
5.15 Calculated Bond Stress Response.
a) Specimen CB3; b) Specimen CB4; and c) Specimen CB5. 218
5.16 Bond Stress Response During 3.0% Drift Cycle of Specimen CB3. a) Bond Stress versus Strain; b) Calculated Bar Stresses. 219
5.17 Increased Role of Slip in Coupling Beams with $l_n/h = 2.0$. a) Applied Drift Versus Measured Strains within the Support; and b) Rotations Due to Bond-Slip Versus Drift. 220

5.18 Proposed Variation of Uniform Bond Strength τ_i for SFRC Coupling Beams. 221
5.19 Experimental and Modeled Reinforcement Slip Responses. a) Specimen CB2; b) Specimen CB3; c) Specimen CB4; and d) Specimen CB5. 222
5.20 Calculated and Measured Slip Rotations at Peak Strength. 223
5.21 Plastic Hinge Flexural Rigidity. a) Specimen CB4; b) Specimen CB6. . 227
5.22 Assumed Curvature Distribution. 229
5.23 Proposed Plastic Hinge Length for SFRC Coupling Beams. 230
5.24 Relationship Between Drift Due To Sliding Displacements and Drift Due To Bar Slip Plus Elastic and Plastic Flexural Deformations (θ_{S+F}). a) Coupling Beams with $l_n/h \geqslant 3.0$; and b) Coupling Beams with $l_n/h = 2.0$. 231
5.25 Shear-Sliding Empirical Model for SFRC Coupling Beams. a) Variation of Model Slope; and b) Proposed Slip plus Flexure Drift Contribution Limit. 232
5.26 Average Sliding Displacement versus Normalized Frictional Strength (μ_{Eff}) at a 20% Strength Decay. 234
5.27 Lumped Plasticity Model for SFRC Coupling Beams. 235
5.28 Inelastic Rotational Spring Response. 235
5.29 Shear Force Versus Drift Backbone Model. 237
5.30 Calculated SFRC Coupling Beam Backbone Responses ($l_n/h = 3.0$). . 239
5.31 Calculated SFRC Coupling Beam Backbone Responses ($l_n/h = 2.0$ and 2.25). 240
5.32 Calculated Backbone Responses for SFRC Coupling Beams tested by Setkit (2012). a) $l_n/h = 3.3$; and b) $l_n/h = 2.75$. 241
5.33 Comparison of Calculated and Measured Response. a) Shear Strength; and b) Lateral Drift. 243

A.1 Coupling Beam Chord Rotation with Support Rotation. 269
A.2 Crack Opening Calculation Schematic (Notched Beams). 270
A.3 Crack Opening Calculation Schematic (Un-notched Beams). 271

A.4 Vectors To Calculate Crack Opening for Direct Tension Specimens. . . 273
A.5 Centroid Coordinates on Plane XZ for Plane Above Notch. 274
A.6 Marker Strips for Coupling Beams with $l_n/h = 3.0$. 275
A.7 Marker Strips for Coupling Beams with $l_n/h = 2.0$. 276
A.8 Shear Distortion of Individual Element. 277
A.9 Curvature Calculation Variables For a Given Strip. 278
A.10 Optical Markers Near the Coupling Beam Ends. 279
A.11 Curvatures Calculated Using Different Methods for Strip 11 of Specimen CB5. a) Entire Test; b) Last Few Cycles. 281

B.1 Stress-Deflection Response (Notched Beams from Specimen CB1). . . 282
B.2 Stress-Deflection Response (Notched Beams from Specimen CB2). . . 283
B.3 Stress-Deflection Response (Notched Beams from Specimen CB3). . . 283
B.4 Stress-Deflection Response (Notched Beams from Specimen CB4). . . 284
B.5 Stress-Deflection Response (Notched Beams from Specimen CB5). . . 284
B.6 Stress-Deflection Response (Notched Beams from Specimen CB6). . . 285
B.7 Stress-Deflection Response (Notched Beams from Specimen CB7). . . 285
B.8 Stress-Deflection Response (Notched Beams from Specimen CB8). . . 286
B.9 Stress-Crack Width Response (Notched Beams from Specimen CB1). 286
B.10 Stress-Crack Width Response (Notched Beams from Specimen CB2). 287
B.11 Stress-Crack Width Response (Notched Beams from Specimen CB3). 287
B.12 Stress-Crack Width Response (Notched Beams from Specimen CB4). 288
B.13 Stress-Crack Width Response (Notched Beams from Specimen CB5). 288
B.14 Stress-Crack Width Response (Notched Beams from Specimen CB6). 289
B.15 Stress-Crack Width Response (Notched Beams from Specimen CB7). 289
B.16 Stress-Crack Width Response (Notched Beams from Specimen CB8). 290
B.17 Stress-Deflection Response (Un-notched Beams from Specimen CB1). 291
B.18 Stress-Deflection Response (Un-notched Beams from Specimen CB2). 291
B.19 Stress-Deflection Response (Un-notched Beams from Specimen CB3). 292
B.20 Stress-Deflection Response (Un-notched Beams from Specimen CB4). 292
B.21 Stress-Deflection Response (Un-notched Beams from Specimen CB5). 293

B.22 Stress-Deflection Response (Un-notched Beams from Specimen CB6). 293
B.23 Stress-Deflection Response (Un-notched Beams from Specimen CB7). 294
B.24 Stress-Deflection Response (Un-notched Beams from Specimen CB8). 294
B.25 Flexural Response (Un-notched Beams from Specimen CB1). 295
B.26 Flexural Response (Un-notched Beams from Specimen CB2). 296
B.27 Flexural Response (Un-notched Beams from Specimen CB3). 296
B.28 Flexural Response (Un-notched Beams from Specimen CB4). 297
B.29 Flexural Response (Un-notched Beams from Specimen CB5). 297
B.30 Flexural Response (Un-notched Beams from Specimen CB6). 298
B.31 Flexural Response (Un-notched Beams from Specimen CB7). 298
B.32 Flexural Response (Un-notched Beams from Specimen CB8). 299
B.33 Tensile Response (Tension Specimens Beams from Specimen CB1). . 300
B.34 Tensile Response (Tension Specimens Beams from Specimen CB2). . 300
B.35 Tensile Response (Tension Specimens Beams from Specimen CB3). . 301
B.36 Tensile Response (Tension Specimens Beams from Specimen CB4). . 301
B.37 Tensile Response (Tension Specimens Beams from Specimen CB5). . 302
B.38 Tensile Response (Tension Specimens Beams from Specimen CB6). . 302
B.39 Tensile Response (Tension Specimens Beams from Specimen CB7). . 303
B.40 Tensile Response (Tension Specimens Beams from Specimen CB8). . 303

ABSTRACT

Medium- to high-rise buildings in regions of high seismicity in the USA often rely on coupled wall systems for lateral load resistance. The strength, stiffness, as well as deformation and energy dissipation capacities of coupling beams greatly influence the response of coupled wall systems. However, the high shear stresses and deformation demands coupling beams are expected to sustain during strong ground motions require the use of complex reinforcement detailing that includes large amounts of transverse and diagonal reinforcement, which makes them difficult and time-consuming to construct. Previous studies have shown that the use of a tensile strain-hardening, steel fiber-reinforced concrete (SFRC) reinforced with high-strength (330 ksi) hooked fibers at a 1.5% volume fraction allowed significant reductions of transverse reinforcement and the elimination of diagonal bars in coupling beams with span-to-depth ratios of 2.2 or greater. Despite the substantial reinforcement reduction and observed adequate coupling beam behavior, the use of SFRCs for coupling beam design has been limited in practice, in part due to experimental data on the behavior of SFRC coupling beams without diagonal bars being limited to a single fiber type and dosage.

In this study, the behavior of SFRC coupling beams without diagonal bars, constructed with various SFRCs, was experimentally investigated. To this end, eight large-scale precast SFRC coupling beams without diagonal bars were tested under large displacement reversals. The main experimental variables considered were coupling beam span-to-depth ratio (3.0 and 2.0) and peak shear stress (7 to $12\sqrt{f'_c}$), fiber type, and fiber dosage. Three different hooked steel fibers and fiber volume fractions (1.0, 1.25, and 1.50%) were considered in this study for a total of six different SFRCs.

Test results showed that coupling beams without diagonal bars can achieve drift capacities exceeding 5% while subjected to peak shear stresses between 6 and $10\sqrt{f'_c}$. Based on results from this and previous investigations, performance criteria for SFRCs based on ASTM C1609-12 test results were proposed. The proposed

SFRC performance criteria were tied to coupling beam span-to-depth ratio and peak shear stress demand to achieve a target coupling beam drift capacity of 6%. Additionally, design recommendations that include reinforcement detailing, calculation of flexural and shear strength, and a lumped plasticity model for simulating the shear versus drift envelope response of SFRC coupling beams were proposed. The proposed model accounts for inelastic flexural rotations, concentrated rotations due to reinforcement slip, and shear sliding. The simple model showed good agreement with experimental results from this and other studies.

1 INTRODUCTION

1.1 Background and Motivation

Coupled wall systems are frequently used as the primary lateral load resisting system of medium- to high-rise buildings in regions of high seismicity due to their lateral stiffness, strength, and ability to dissipate energy (Barney et al., 1980; Harries et al., 2000; Naish et al., 2013a; and Parra-Montesinos et al., 2014). Commonly, coupled walls are part of elevator cores where consecutive openings along the building height result in deep beams connecting two or more adjacent wall piers, as shown in Figure 1.1. The ability of coupled walls to provide lateral stiffness and strength during strong ground motions greatly relies on the behavior of coupling beams, which allow coupling action—force couple resulting from shear transfer between structural walls and coupling beams. Furthermore, coupling beams, if properly designed, represent a significant source of energy dissipation during strong ground motions. Therefore, coupling beam shear strength, stiffness, and energy dissipating capacity are paramount for the adequate performance of coupled walls during strong ground motions.

Modern construction practices typically lead to coupling beams with span-to-depth ratios (l_n/h) between 2 and 4 (Harries et al., 2000; and Naish et al., 2009). Seismic design provisions in ACI 318-19 (ACI Committee 318, 2019) allow coupling beams with intermediate span-to-depth ratios (i.e., $2 \leqslant l_n/h \leqslant 4$) to be designed either with two intersecting groups of diagonal reinforcement cages or as beams of special moment resisting frames. In practice, coupling beams with diagonal bars, designed to resist the entire calculated shear demand, are still the predominant choice among designers for coupling beams with intermediate span-to-depth ratios due to their proven seismic performance and higher allowed peak average shear stress ($10\sqrt{f'_c}$, psi). However, diagonally-reinforced coupling beams require intricate reinforcement detailing that include large amounts of diagonal and transverse reinforcement, making them difficult and time-consuming to construct.

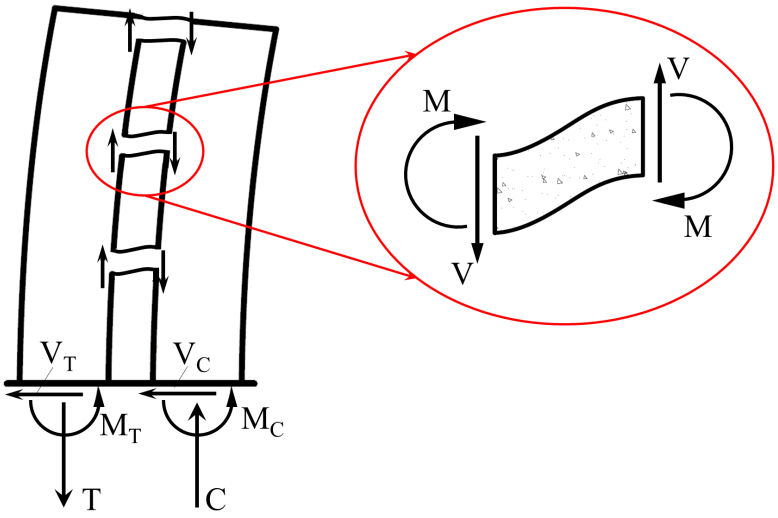

Figure 1.1: Coupled Walls and Coupling Beam Actions.

Given the difficulties associated with the construction of coupling beams with diagonal bars, many researchers have looked for alternative designs to simplify their construction (Tegos and Penelis, 1988; Tassios et al., 1996; Harries et al., 2000; and Canbolat et al., 2005). Research efforts over the past decade have resulted in significant simplifications in the detailing of coupling beams through the use of fiber-reinforced concrete. In particular, the experimental results of the work by Lequesne (2011) and Setkit (2012) demonstrated that steel fiber-reinforced concrete (SFRC) coupling beams may exhibit adequate strength, stiffness, and deformation capacity under load reversals, paving the way for their implementation in several buildings on the west coast of the USA. For example, The Martin and the Lincoln Square expansion, both in the State of Washington and designed by Cary Kopczynski & Company, feature SFRC coupling beams (Kopczynski and Whiteley, 2016). Cost analysis of reinforced concrete and SFRC coupling beams have shown that the substantial reduction in reinforcement achieved by using SFRC results in material cost savings on the order of 20 to 30% for highly stressed coupling beams and even more in slender beams if diagonal bars are eliminated (Kopczynski and

Whiteley, 2016). Moreover, the elimination of diagonal bars in coupling beams could reduce construction time by one day per floor. It should be mentioned, however, that sufficient data are only available on the behavior of SFRC coupling beams constructed with Bekaert RC 80/30 BP steel fibers (330 ksi tensile strength, 1.2 in. long, and 0.015 in. in diameter) at a 1.5% volume fraction, which has been shown to exhibit tensile strain-hardening behavior (Liao et al., 2006; Tameemi and Lequesne, 2015; and Pérez-Irizarry and Parra-Montesinos, 2017). Applications of SFRC in the field have thus been limited to this fiber type at a 1.5% volume fraction.

The observed potential of SFRC to significantly simplify the reinforcement detailing and construction of coupling beams and associated cost savings has increased the interest of practicing engineers on the use of SFRCs as a design alternative for coupling beams of intermediate span-to-depth ratios. However, for a broader implementation of SFRC coupling beams, engineers must be able to select from a variety of fibers and dosages. For this purpose, coupling beam span-to-depth ratio, strength, and deformation capacity must be tied to a minimum SFRC material performance, based on standardized tests. Therefore, it is essential to study and understand the behavior of SFRC coupling beams without diagonal bars constructed with various types of SFRCs (i.e., different types of fibers and dosages) and to relate the mechanical properties of SFRCs to coupling beam response, before design provisions can be included in building codes such as ACI-318. The research objectives discussed in the following section aim to address this need.

1.2 Research Objectives

The research study reported herein focused primarily on coupling beams with span-to-depth ratios between 2.0 and 3.0, which cover most current applications in the United States. The research was aimed at providing new information for a better understanding of the behavior of SFRC coupling beams constructed with various types of SFRCs and no diagonal bars, establishing minimum SFRC performance criteria based on coupling beam required strength and drift capacity, and developing design and modeling recommendations for SFRC coupling beams.

Specifically, the main objectives of this study were:

I- Evaluate the strength, deformation, and energy dissipation capacity of coupling beams without diagonal bars and constructed with various SFRCs.

II- Investigate the feasibility of using tensile strain-softening SFRCs for coupling beams without diagonals bars.

III- Characterize the tensile, flexural, and compressive response of various SFRCs to develop performance-based classification criteria for their use in coupling beams.

IV- Provide modeling and design recommendations for SFRC coupling beams without diagonal bars.

To accomplish these objectives, eight large-scale, precast SFRC coupling beam specimens were tested under large displacement reversals and a series of material tests were performed on companion SFRC specimens. The experimental variables considered were coupling beam span-to-depth ratio, fiber type and dosage, and peak shear stress demand. To provide modeling and design recommendations, the analytical phase of the study focused on: 1) developing an empirical model that relates fiber volume fraction, strength, and aspect ratio to SFRC peak post-cracking strength; 2) strain analysis of the SFRC coupling beam plastic hinges to estimate in-place compressive strain limits for SFRCs and corresponding plastic hinge rotation capacity; and 3) analyzing the plastic hinge shear-sliding and reinforcement-slip, flexural, and shear responses of SFRC coupling beams to develop a lumped plasticity model for the estimation of the moment (or shear) versus drift response of SFRC coupling beams without diagonal bars.

2 LITERATURE REVIEW

2.1 Fiber-Reinforced Concrete

The addition of fibers to concrete to improve its mechanical properties is not a new concept. In fact, the idea of fiber reinforced concrete (FRC) can be traced back to the late 19^{th} century and the patent granted to A. Berard in California, as well as a French patent in 1918 to H. Alfsen; however, it was not until after the 1960s that major developments in fiber-reinforced concrete, including structural applications, took place (Naaman, 1985). Many different types of fibers are used to reinforce concrete. The most common fiber materials are probably steel and polypropylene fibers, and these fibers are available in different shapes (e.g., straight, crimped, twisted or hook-ended steel fibers and plain, twisted or fibrillated polypropylene fibers). Typically, fibers used to reinforce concrete are short and discontinuous, and are mixed in to achieve an even but random distribution. Some examples of fibers used to reinforce concrete are shown in Figure 2.1.

Inclusion of fibers in the concrete matrix leads to improvements of the tensile, flexural, compressive, and shear behavior of the resulting composite (Shah and Rangan, 1970, 1971; Johnston, 1974; Wafa and Ashour, 1992; Mirsayah and Banthia, 2002; and Thomas and Ramaswamy, 2007). However, the most significant improvement, by far, is the increased energy absorption capacity or toughness of the composite (Shah and Rangan, 1970; Johnston, 1974; and Naaman, 1985). The discussion presented herein will focus on the use of steel fibers to reinforce concrete and some of the major benefits of using steel fiber reinforced concrete (SFRC) in structural elements.

Figure 2.1: Examples of Fibers used to Reinforce Concretes (scale: inches).

The performance of an FRC is significantly influenced by the reinforcing index, $RI = \frac{V_f l_f}{d_f}$, where V_f is the fiber volume fraction and $\frac{l_f}{d_f}$ is the fiber length-to-diameter ratio (Johnston, 1974; Johnston and Coleman, 1974; and Fanella and Naaman, 1985). Furthermore, the fiber-matrix bond is typically the weakest link and governs most of the mechanical properties of the FRC (Naaman, 1999). The fiber-matrix bond is composed of chemical adhesion, friction, mechanical anchorage, and fiber-to-fiber interlock. A detailed description of the fiber-matrix bond is beyond the scope of this study and the interested reader is referred to Naaman (1999) and Weiler et al. (1999). Moreover, traditional fiber composite models, such as the composite strength model by Cox (1952), are not applicable to FRCs, as these are limited to linear elastic behavior and cannot account for the post-cracking response of FRCs (see Naaman et al., 1974). A discussion of the post-cracking tensile response of FRCs is provided in the following section.

Due to the developments in concrete, fiber technologies, and the better understanding of FRC mechanics, there have been an increased number of FRCs developed, as well as increased possible applications for FRCs. Typically, FRCs are classified based on their tensile and flexural response, which can substan-

tially differ depending on the materials that constitute it. Naaman and Reinhardt (2006) proposed a classification scheme for fiber-reinforced cement composites (FRCCs) based on the post-cracking response under either bending or direct tension. Deflection-hardening composites exhibit a hardening response under bending accompanied, in general, by multiple cracking. However, a deflection-hardening composite does not necessarily exhibit a hardening response under direct tension (i.e., strain-hardening response). Figure 2.2 summarizes the FRC classification proposed by Naaman and Reinhardt (2006), where HPFRCC refers to high-performance fiber-reinfroced cement composites, DFRCC to deflection-hardening FRCC, and $(V_{f_{crit}})_{tension}$ & $(V_{f_{crit}})_{bending}$ are the minimum fiber volume fractions needed to achieve a hardening response in tension and bending, respectively. For a detailed discussion on strain-hardening and deflection-hardening FRCC mechanics, refer to Naaman (2003) and Naaman and Reinhardt (2006).

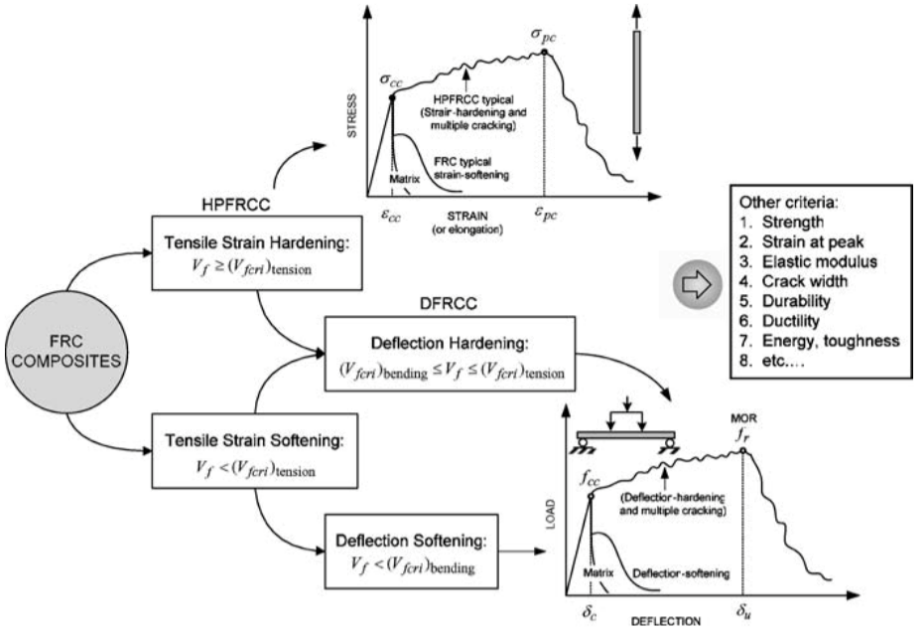

Figure 2.2: Classification of FRCCs, from Naaman and Reinhardt (2006).

2.1.1 Tensile Behavior and Classification of FRC

The addition of fibers to cement-based matrices greatly enhances the composite's energy dissipating capacity, ductility and resistance to crack growth (Shah and Rangan, 1971; Johnston and Coleman, 1974; and Gopalaratnam and Shah, 1987b). However, the effect on the cracking strength of the composite is negligible, except in composites with very high fiber volume fractions; e.g., volume fraction greater than approximately 10% (Shah, 1992). Failure of FRCs is often caused by a fiber-matrix bond failure (Naaman and Shah, 1976). Typically, the tensile behavior is characterized by a linear elastic response up to first cracking of the matrix, followed by fiber pullout as deformation is further increased. Gopalaratnam and Shah (1987a) provided a discussion of the several failure mechanisms of FRCs and some of the aspects regarding modeling of their tensile behavior. Following first cracking of the composite, tensile behavior of SFRCs is characterized by either a sudden, total strength loss due to fiber fracture, a softening behavior due to fiber pullout, or strain-hardening with multiple cracking, followed by fiber pullout (Gopalaratnam and Shah, 1987a). Clearly, fiber pullout plays major role in the overall composite response. Consequently, several researchers have studied the pullout mechanism of various fibers to understand and enhance the fiber-matrix bond behavior, fiber efficiency, and the overall performance of the composite (e.g., Naaman and Shah, 1976; Li, 1993; Naaman, 1999; and Weiler et al., 1999). Given their improved mechanical properties, the following discussion focuses on FRCCs whose response is controlled by fiber pullout rather than fiber fracture.

The tensile response of FRCCs can be classified as either strain-softening or strain-hardening. Strain-softening FRCCs exhibit a linear elastic region up to first cracking, followed by a softening behavior due to fiber pullout at the crack location. Strain-hardening FRCCs also behave linearly elastic up to first cracking. However, deformation beyond first crack leads to increased strength accompanied by multiple cracking up to the peak post-cracking strength. Reaching the tensile capacity at one of the cracks leads to damage localization and a softening behavior similar to that of strain-softening FRCCs. A comparison of the responses of strain-softening

and strain-hardening FRCCs is shown in Figure 2.3, taken from Naaman (2007b) and first published in Naaman (2003).

Several strain-hardening FRCCs have been developed in the past decades, e.g., slurry infiltrated fiber concrete (SIFCON; Lankard, 1984), slurry infiltrated mat concrete (SIMCON; Krstulovic-Opara and Malak, 1997), engineered cementitious composites (ECC; Li, 1993), and more recently, self-consolidating high-performance fiber reinforced concretes (SCHPFRC; Liao et al., 2006). Because of their enhanced deformation capacity and toughness, these strain-hardening materials have been commonly referred to as high performance fiber-reinforced concretes (HPFRCs) or, more generally, high performance fiber-reinforced cement composites (HPFRCCs). Further discussion on the characterization of HPFRCCs and the conditions required for strain-hardening behavior can be found in Naaman and Reinhardt (1995). Included in their discussion are the development of several expressions for the critical fiber volume fraction (i.e., minimum fiber volume fraction required to achieve strain-hardening behavior) and the evaluation of FRCCs based on their toughness indices and fracture energy. Beyond a minimum fiber volume fraction, the use of fibers with slip-hardening bond characteristics is believed to be the most effective way of developing strain-hardening HPFRCCs (Naaman, 1999).

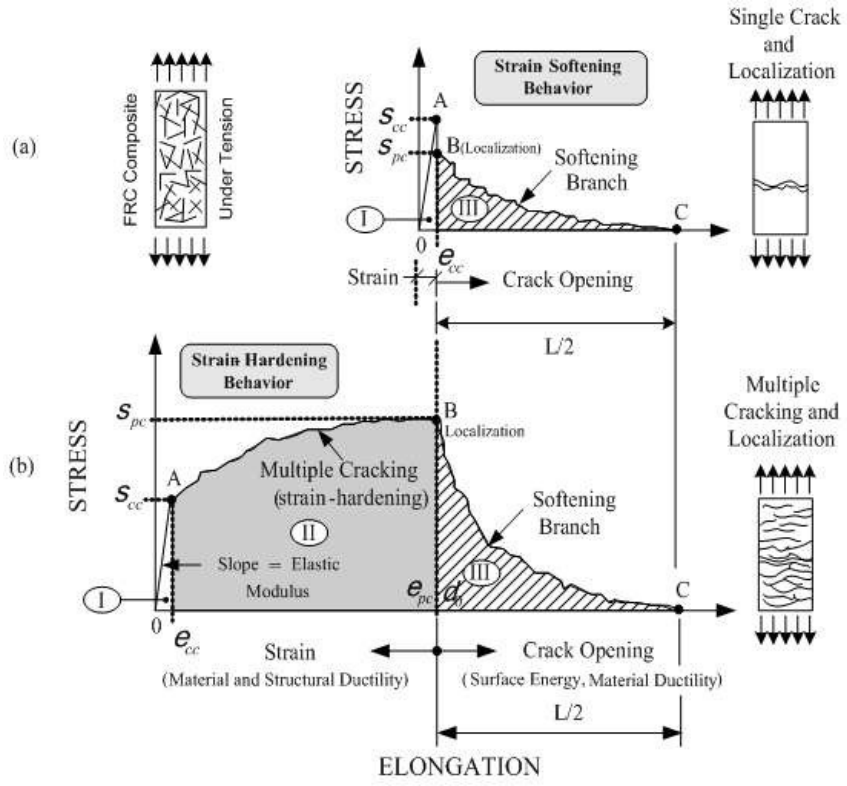

Figure 2.3: Typical Responses of Fiber Reinforced Cement Composites (FRCCs) From Naaman (2007a). a) Strain-Softening FRCCs, b) Strain-Hardening FRCCs.

2.1.2 Compressive Behavior of FRC

Onset of concrete failure under uniaxial compression is due typically to the propagation and opening of splitting cracks formed along the compression axis, initially due to Poisson's effect. The propagation and opening of these cracks leads to concrete dilation and strength decay. It is well know that confining the concrete can substantially enhance the concrete compression deformation capacity and strength (Richart et al., 1928; Roy and Sozen, 1964; Kent and Park, 1971; Wight and Sozen, 1975; and Ahmad and Shah, 1982). Typically, closely spaced closed transverse reinforcement (e.g., hoops or spirals) is provided in concrete members for confinement. However, inclusion of fibers in concrete leads to similar benefits by effectively de-

laying the propagation of cracks and thus, enhancing the post-peak behavior of the concrete (Shah and Rangan, 1970; Fanella and Naaman, 1985; Balaguru and Shah, 1992; and Thomas and Ramaswamy, 2007). The level of confinement provided by the inclusion of fibers is dependent on the fiber type, geometry and volume fraction, as evidenced by the results presented in Johnston (1974), Fanella and Naaman (1985), Otter and Naaman (1988), Wafa and Ashour (1992), and Ezeldin and Balaguru (1992). The effect of increasing fiber volume fraction and aspect ratio on the compressive behavior of SFRC is shown in Figure 2.4-a and Figure 2.4-b, respectively. Further information on the compressive behavior of FRC can be found in Mansur et al. (1999), Nataraja et al. (1999), Foltz et al. (2008), and Sirijaroonchai et al. (2010). There is significant evidence that FRCs have superior compressive behavior compared to their unreinforced counterparts. Perhaps the most important characteristic, with regards to their implementation in earthquake-resistant structures, is the improved deformation capacity exhibited by FRCs.

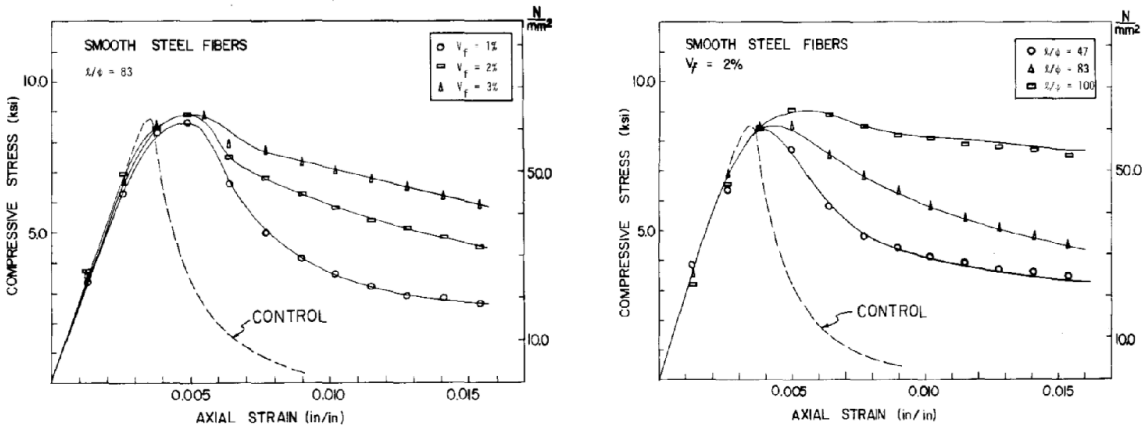

a) Effect of Fiber Volume Fraction b) Effect of Fiber Aspect Ratio

Figure 2.4: Effect of Fibers on Compressive Behavior of Concrete. From Fanella and Naaman (1985).

2.1.3 Shear Behavior of FRC Flexural Members

Fibers contribute to shear resistance of concrete flexural members primarily by transferring tensile stresses across diagonal cracks and controlling crack width, which leads to increased aggregate interlock along diagonal cracks. Early studies on FRC beams without transverse reinforcement showed that the inclusion of fibers in concrete significantly increases the shear strength of the member and that fibers can effectively be used as shear reinforcement (e.g., Batson et al., 1972; Swamy and Bahia, 1985; and Narayanan and Darwish, 1987). Furthermore, fibers can in many cases provide the necessary shear strength to change the beam failure mode from a brittle shear failure to a ductile flexural failure.

A summary of early studies comprising over 400 FRC beams without stirrups and a discussion of the results of several large-scale beam specimens subjected to uniform shear was provided by Adebar et al. (1997). More recently, a database of over 200 SFRC beam tests analyzed by Parra-Montesinos (2006) led to the inclusion of deformed steel fibers as minimum shear reinforcement in the ACI 318-08 building code (ACI Committee 318, 2008) for certain design scenarios. Further evidence in support of the use of fibers as minimum shear reinforcement was provided by Dinh et al. (2010) and Susetyo et al. (2011). Moreover, analytical models for calculating the shear strength of SFRC beams without stirrups have been proposed by Khuntia et al. (1999), Choi et al. (2007), and more recently, by Dinh et al. (2011). These models were shown to reasonably estimate the shear strength of previously tested SFRC beams.

Parra-Montesinos and Chompreda (2006) studied the behavior of FRC flexural members under reversed cyclic displacements. Their tests showed that members constructed with tensile strain-hardening FRCs and no transverse reinforcement can exhibit a stable flexural response and were more deformation tolerant than similar reinforced concrete members. The improved tensile strength and deformation capacity of strain-hardening FRCs enhanced the shear resisting mechanisms of the test beams and thus, it led to a delay in shear strength decay.

In summary, it is generally recognized that fibers enhance the shear strength

of flexural members. Furthermore, fibers can delay the deterioration of shear resisting mechanisms in flexural members subjected to large displacement reversals. Therefore, FRCs, particularly those with strain-hardening behavior (HPFRCs), are attractive for use in shear critical regions of reinforced concrete structures (Parra-Montesinos, 2005).

2.2 Coupling Beams

Coupling beams are an essential component of coupled wall systems. Their stiffness, deformation capacity, and strength greatly influence the overall performance of coupled walls. The coupling effect provided by the beams in coupled walls is responsible of resisting a large portion of the total overturning moment (typically, between 30-50% of the total overturning moment capacity of the system) by means of shear forces transferred into the walls, thus increasing the overall stiffness and strength of the system. Therefore, the improved stiffness of coupled walls makes them an attractive design alternative for medium- to high-rise buildings located in regions of high seismicity. However, the deformation demands to which coupling beams are subjected to during strong ground motions require them to possess significant deformation and energy dissipating capacity while subjected to numerous inelastic displacement reversals.

During the 1964 Alaskan earthquake, many coupling beams suffered brittle failures. These failures led to numerous research efforts aimed at understanding the behavior of coupling beams during strong earthquakes and developing alternative designs that would improve their seismic performance. Current design provisions for reinforced concrete coupling beams are largely based on the work by Paulay (1970, 1971),Paulay and Binney (1974), and Paulay and Santhakumar (1976). As will be discussed in the following sections, reinforced concrete coupling beams are not the only alternative that has been investigated. Steel and/or hybrid steel-concrete coupling beams, and more recently FRC coupling beams, have been studied and implemented in the field.

2.2.1 Reinforced Concrete Coupling Beams

Prior to the 1970s, coupling beams were generally designed as conventional beams with a reinforcement detailing that consisted of primary and distributed (skin reinforcement) longitudinal bars, and transverse reinforcement. However, observations after the 1964 Alaska earthquake and research conducted in subsequent years indicated that conventionally reinforced coupling beams did not provide the desired seismic performance due to their susceptibility to diagonal tension failures. Paulay (1971) emphasized that preventing a diagonal tension failure in coupling beams by providing transverse reinforcement to carry the whole shear corresponding to flexural yielding was essential for developing their ultimate strength and improving their deformation capacity. Despite the improved performance achieved by increasing the amount of transverse reinforcement, the deformation capacity of conventionally reinforced coupling beams may be limited by sliding shear failures, especially if subjected to high shear stress reversals (evidence of sliding in flexural members under large shear reversals and the benefits of closer stirrup spacing were also reported by Brown and Jirsa, 1971). Furthermore, Paulay and Binney (1974) showed that conventionally reinforced coupling beams possessed inadequate ductility for the expected demands on earthquake-resistant coupled walls. In conclusion, it is recognized that conventionally reinforced coupling beams are not adequate due to their susceptibility to sliding shear failures and limited deformation capacity.

The work of researchers in Argentina (Luisoni et al., 1970) and New Zealand (Paulay and Binney, 1974; Paulay and Santhakumar, 1976) marked an important point in the development of a new coupling beam design after the 1964 Alaska earthquake and greatly influenced modern coupling beam design practice. Paulay and Binney (1974) proposed a design that relies on a steel reinforcement truss to carry the entire shear demand to avoid sliding shear failures. Their proposed design and shear resisting mechanism are simply summarized in Figure 2.5, adapted from

Paulay and Binney (1974). The shear strength of such a beam is calculated as,

$$V_n = 2A_s f_y \sin \alpha \tag{2.1}$$

where A_s is the area of steel in one of the diagonal reinforcement groups, f_y is the yield strength of the diagonal reinforcing steel, and α is the angle of inclination of the diagonals with respect to the beam longitudinal axis. This expression for the shear strength of diagonally-reinforced coupling beams was first included in the ACI 318-99 code (ACI Committee 318, 1999) and is now equation 18.10.7.4 in ACI 318-19 (ACI Committee 318, 2019). The results of the first large-scale tests of diagonally-reinforced coupling beams (Paulay and Binney, 1974) demonstrated their superior performance over conventionally-reinforced coupling beams to resist earthquake induced deformation demands. Diagonally-reinforced coupling beams exhibit stable hysteresis with wide loops resembling that of steel members, large deformation capacity, and adequate strength retention. However, it was observed that to ensure a stable response and prevent premature instability of the compression diagonals, confinement reinforcement was needed in the form of closed transverse steel over the length of the diagonal steel groups. Paulay and Santhakumar (1976) published further evidence of the improved performance of diagonally-reinforced coupling beams, based on tests of coupled walls constructed with either conventionally-reinforced coupling beams or diagonally-reinforced coupling beams. Details of their tests can be found in Santhakumar (1974).

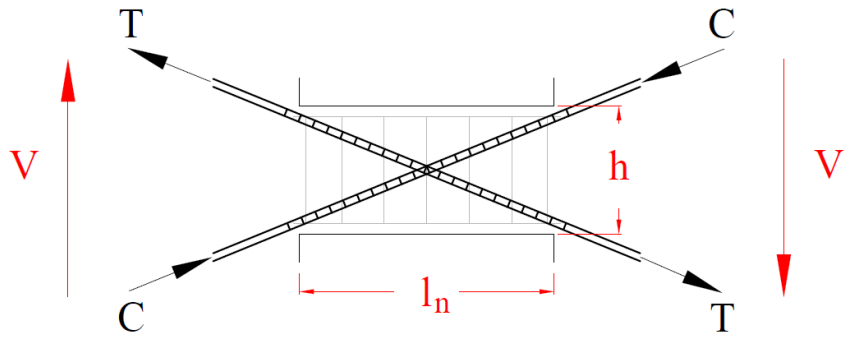

Figure 2.5: Diagonally-reinforced Coupling Beam Geometry and Internal Actions (Paulay and Binney, 1974).

The Portland Cement Association (PCA) conducted an extensive study on the behavior of coupling beams subjected to load reversals. Eight coupling beam specimens were tested to study the influence of span-to-depth ratio, reinforcement configuration, and size of the confined core on the hysteresis behavior of coupling beams. Span-to-depth ratios were 2.5 and 5.0, and the reinforcement configurations included conventional reinforcement, full-length diagonal reinforcement as recommended by Paulay and Binney (1974), and diagonal reinforcement at the hinging regions based on recommendations given by Bertero and Popov (1975). Maximum shear stresses ranged from 7 to $11\sqrt{f'_c}$ (psi) for coupling beams with span-to-depth ratios of 2.5, whereas coupling beams with span-to-depth ratios of 5.0 were subjected to peak shear stresses ranging from 3.5 to $5.3\sqrt{f'_c}$ (psi). Further details of the coupling beam tests performed by PCA can be found in Shiu et al. (1978) and Barney et al. (1980).

The findings from the experiments by Barney et al. (1980) influenced current coupling beam design provisions, particularly the adoption of the $10\sqrt{f'_c}$ (psi) limit on the maximum nominal shear stress for diagonally-reinforced coupling beams (first included in AC 318-99). Furthermore, the results of this study showed that diagonally-reinforced coupling beams exhibit superior performance compared to

the other designs evaluated. The improvements in behavior of diagonally-reinforced coupling beams were more significant for short-span coupling beams. For longer spans (i.e., span-to-depth ratios of 5 or greater), the improvements were deemed insufficient to warrant diagonal reinforcement.

Others researchers have studied diagonal reinforcement as well as other alternatives for the design of coupling beams. Tegos and Penelis (1988) studied the seismic behavior of short columns and coupling beams reinforced with inclined rhombic reinforcement. They tested 24 specimens with span-to-depth ratios between 2 and 5, of which 18 specimens featured a rhombic truss reinforcement, 3 specimens included diagonal reinforcement, and the remaining 3 specimens were conventionally reinforced. Contrary to the other research programs discussed so far, these series of experiments included the effects of axial loads on the behavior of the specimens. Tassios et al. (1996), on the other hand, reported on the testing of short-span coupling beams ($l_n/h < 2$) to study the effects of reinforcement layout on their hysteresis response. Figure 2.6a,b,d-f show schematics of the reinforcement layouts studied by Tassios et al. (1996) and Figure 2.6a-c show those studied by Tegos and Penelis (1988). The results of these experiments further confirmed the superiority of diagonal reinforcement to resist inelastic displacement reversals over all other reinforcement layouts tested, as well as the unsatisfactory behavior of conventionally-reinforced short members. The superior performance of diagonally-reinforced coupling beams, as well as the improvements in behavior through the use of "bent up" bars (see Figure 2.6d) over conventionally-reinforced coupling beams, were more evident for span-to-depth ratio of approximately 1.0 and diminished with increased span-to-depth ratios. Further experiments on short coupling beams ($l_n/h < 1.5$) with rhombic reinforcement were conducted by Galano and Vignoli (2000). Their results favored the use of rhombic reinforcement over diagonal reinforcement for the design of earthquake-resistant short coupling beams. However, the deformation capacity of the diagonally-reinforced coupling beams they tested was limited by premature instability of the diagonals struts.

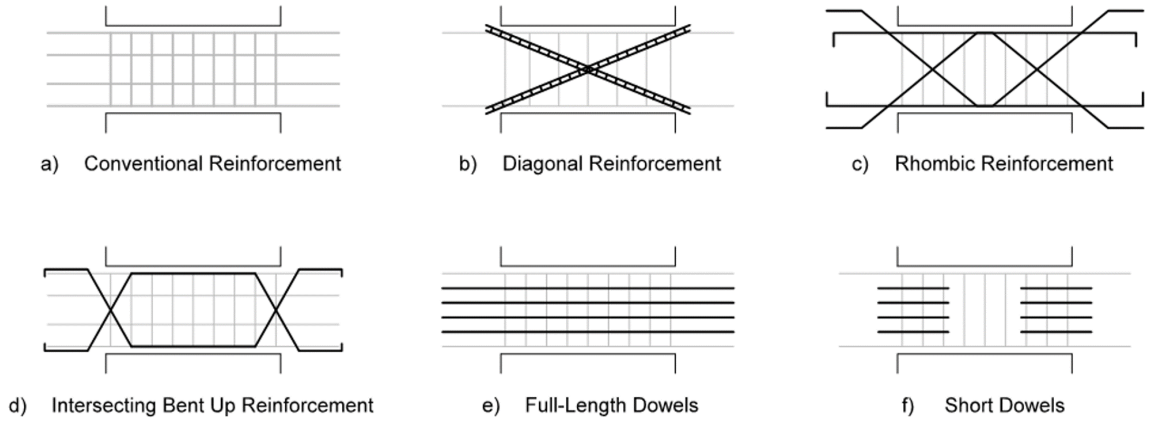

Figure 2.6: Coupling Beam Reinforcement Layouts Investigated by Tassios et al. (1996) and Tegos and Penelis (1988), adapted from Setkit (2012).

Recently, Naish et al. (2009, 2013a,b) published results from the tests of eight approximately half-scale coupling beam specimens with different geometries, reinforcement configuration (diagonally- or conventionally-reinforced), and with or without floor slabs. The beams had span-to-depth ratios of either 2.4 or 3.3. Among the beam specimens with diagonal reinforcement two different confinement reinforcement alternatives were studied, confining hoops over the length of the diagonals and full cross-section confinement. Their results showed that coupling beams detailed with diagonal reinforcement and full section confinement exhibited equal or improved performance in terms of ductility and strength compared to those of coupling beams with confined diagonals.

Diagonally-reinforced concrete coupling beams are the preferred and predominant design alternative in modern building construction given their proven seismic performance. However, the main hurdle with diagonally-reinforced coupling beams is that given their relatively short spans (typically $2h \leqslant l_n < 4h$) combined with high shear stresses often exceeding $6\sqrt{f'_c}$ (psi), diagonally-reinforced coupling beams require intricate reinforcement layouts that continue to be challenging for designers and contractors alike.

2.2.2 Steel and Hybrid Coupling Beams

Several researchers, e.g., Harries et al. (1997, 2000, 2005), Harries and Shahrooz (2005), Park and Yun (2005), and Motter et al. (2014), have studied different alternatives for the design of coupling beams, primarily because of the difficulties associated with heavily congested concrete coupling beams, as well as restrictions on maximum floor clearances. Where concrete coupling beams become unpractical, steel coupling beams or concrete-encased steel coupling beams (i.e., hybrid coupling beams) can become a viable design alternative (Harries and Shahrooz, 2005; Park and Yun, 2005).

Steel sections have proven to provide superior energy dissipation and overall performance than diagonally- and conventionally-reinforced concrete coupling beams (Harries et al., 1997, 2005). The advantages are more evident for shear-critical steel coupling beams, which exhibit excellent energy dissipation characteristics due to the development of a stable shear yielding mechanism (Hjelmstad and Popov, 1983). However, steel coupling beams require long embedment lengths into the adjoining structural walls that often interfere with the wall boundary element reinforcement. Although the connections can be challenging, steel and hybrid coupling beams have been successfully implemented in practice. According to Harries and Shahrooz (2005), the first coupled wall structure with steel coupling beams was built in the mid 1960's in Wellington, New Zealand. Despite the excellent performance of steel coupling beams, they have not been widely implemented in the USA. This is likely due to the complexity of the beam-wall connections and the increased coordination required between steel and concrete labors.

2.2.3 Current Design Provisions for Reinforced Concrete Coupling Beams

Modern design guidelines for reinforced concrete coupling beams are largely based on findings from research work conducted in the late 1960's and early 1970's. ACI 318-19, Building Code Requirements for Structural Concrete (ACI Committee 318, 2019), include provisions for the design and detailing of coupling beams based

on the coupling beam aspect ratio (l_n/h) and the shear stress demand. Moreover, the nominal shear strength of diagonally-reinforced RC coupling beams (V_n) is limited to $10\sqrt{f'_c}A_{cw}$, where A_{cw} is the cross-sectional area of the coupling beam and f'_c is the concrete compressive strength in psi. This limit is supported by the results presented in Barney et al. (1980). Section 18.10.7 of ACI 318-19 provides the following design requirements for earthquake-resistant coupling beams:

- Coupling beams with $l_n/h \geqslant 4$ must be designed as beams of special moment resisting frames per ACI 318-19 Section 18.6.
- Coupling beams with $l_n/h < 2$ and with V_u exceeding $4\sqrt{f'_c}A_{cw}$ must be reinforced with two intersecting groups of diagonal reinforcement symmetrical about mid-span and satisfying the confinement requirements of Section 18.10.7.4 for plastic hinge regions of columns. The confinement requirements allow engineers to either confine each individual group of diagonal reinforcement or the entire coupling beam.
- Coupling beams with $2 \leqslant l_n/h < 4$ can be designed either as beams of special moment resisting frames or diagonally-reinforced coupling beams.

Despite the flexibility of the ACI Code on the design of coupling beams with intermediate aspect ratios ($2 \leqslant l_n/h < 4$), diagonally-reinforced coupling beams are still the preferred design alternative for these beams due to their improved performance over conventionally-reinforced coupling beams and the higher allowable shear stress demand. However, the detailing requirements for diagonally-reinforced coupling beams lead to intricate reinforcement detailing, often including large amounts of diagonal and transverse reinforcement that are difficult and time consuming to construct. Figure 2.7, from ACI 318-19, shows the confinement requirements for diagonally-reinforced coupling beams, while Figure 2.8 shows a diagonally-reinforced coupling beam under construction. Considering the challenges associated with diagonally-reinforced coupling beams and the numerous efforts undertaken to develop alternate designs for earthquake-resistant coupling beams, it is evident that a new, simpler design is needed.

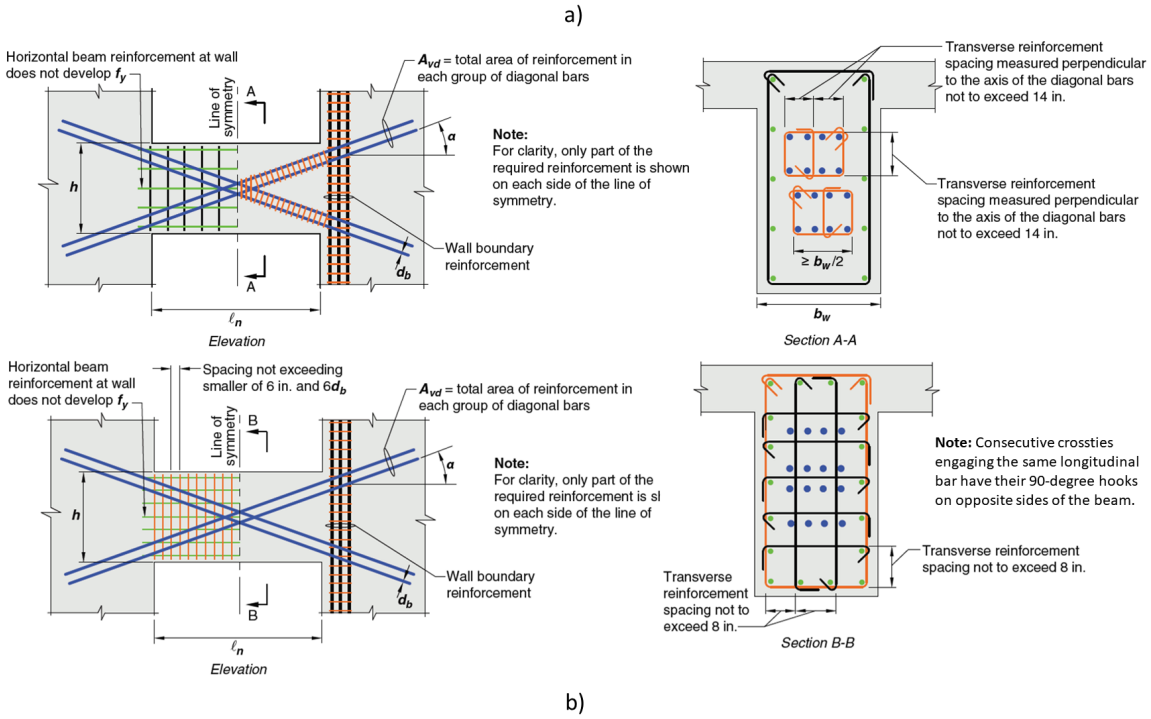

Figure 2.7: Confinement Requirements for Diagonally-Reinforced Coupling Beams (from ACI 318-19). a) Confinement of Diagonals; b) Full-Section Confinement.

Figure 2.8: Coupling Beam Under Construction (Courtesy of R. Lequesne).

2.2.4 High-Performance Fiber-Reinforced Concrete Coupling Beams

The use of tensile strain-hardening or high-performance fiber-reinforced concrete (HPFRC) in coupling beams has gained significant attention over the past decade due to the possible simplifications in the design and construction of reinforced concrete coupling beams and coupled wall systems. The improved post-cracking strength and deformability of these FRCs allow reductions in coupling beam reinforcement on the order of 40 to 60% and overall cost savings of approximately 30% without compromising the seismic performance of the structure (Lequesne et al., 2011). Several investigations on the seismic performance of coupling beams constructed with strain-hardening FRCs (e.g., Canbolat et al., 2005; Lequesne, 2011; Setkit, 2012) have led to the implementation of FRC coupling beams in high-rise building construction.

The first experimental study to consider the use of HPFRCs as means to reduce the reinforcement requirements for diagonally-reinforced coupling beams was the work of Canbolat et al. (2005). Canbolat tested four approximately $\frac{3}{4}$-scale precast coupling beam specimens with a span-to-depth ratio of 1.0 under reversed cyclic displacements. The main variables considered in the research program were the type of cementitious material, fiber type and reinforcement detailing. The first specimen was a control RC coupling beam with diagonal reinforcement designed in accordance with ACI318-99 (ACI Committee 318, 1999), similar to current ACI-code provisions (ACI Committee 318, 2019). The three other specimens were constructed using one of two HPFRC materials and a different reinforcement detailing for each specimen. The results of these experiments confirmed the potential of fiber reinforcement for use in earthquake-resistant coupling beams and demonstrated the improved performance as well as simplifications possible by incorporating HPFRC in the design of coupling beams.

Following the success of the tests by Canbolat et al. (2005), Lequesne (2011) conducted further experiments on HPFRC coupling beams and coupled walls. Three precast HPFRC coupling beam specimens with aspect ratio (i.e. span-to-

depth ratio) of 1.75 and a simplified diagonal reinforcement detailing were tested. The main objectives of these component tests were: 1) confirm the effectiveness of HPFRC on confining the diagonal reinforcement; 2) quantify the shear strength contribution of HPFRC; 3) evaluate the stiffness, energy dissipation and drift (i.e., beam chord rotation) capacity of HPFRC coupling beams with relatively low aspect ratio; and 4) compare different alternatives of connecting precast coupling beams to structural walls without interfering with the boundary reinforcement.

The second phase of this study focused on studying the behavior of coupled wall systems with precast HPFRC coupling beams. Two approximately $\frac{1}{3}$-scale 4-story coupled walls were built and tested under simulated earthquake loads. In both, component and coupled wall tests the HPFRC used contained 1.2 in. long, 0.015 in. diameter, hooked steel fibers with a nominal tensile strength of 330 ksi. These fibers were RC 80/30 BP manufactured by Bekaert corporation and were used at a 1.5% volume fraction (further details on these and other fibers are provided in Chapter 3 and Figure 3.7). A detailed discussion of these tests can be found in Lequesne et al. (2009, 2010); Lequesne (2011); and Lequesne et al. (2013, 2016).

Some of the important conclusions and observations from this work were: 1) coupling beam behavior was highly dominated by flexure and their strength was controlled by flexural hinging; 2) although HPFRC provides adequate confinement and stability to the diagonal bars, special column-type confinement is needed over the plastic hinge regions to ensure a stable hysteresis behavior; 3) the shear contribution of HPFRC could be conservatively assumed to be $5\sqrt{f'_c}$ (psi); 4) the plastic hinge length can be approximated as h/2 from the face of the wall at each end of the HPFRC beams, where h is the beam depth; 5) the energy dissipation capacity of HPFRC was found to be comparable to that exhibited by well-detailed diagonally-reinforced coupling beams with similar aspect ratio; 6) it was observed that HPFRC coupling beams are much more deformation tolerant than RC coupling beams; and 7) coupling beams experienced tensile axial strains between 0.5 and 1.7% at beam drifts exceeding 2%. This was found to be consistent with the axial strains developed in the coupling beam component tests. Figure 2.9 shows the damage sustained by the four coupling beams in Specimen CW2 from Lequesne

(2011), after termination of the test (coupled-wall system drifts of approximately 2.5 and 3.5% in the positive and negative direction, respectively; these coupled wall drifts corresponded to coupling beam drifts of 7.0 to 9.0%). The 2^{nd} story beam was an RC coupling beam, whereas all other were HPFRC beams.

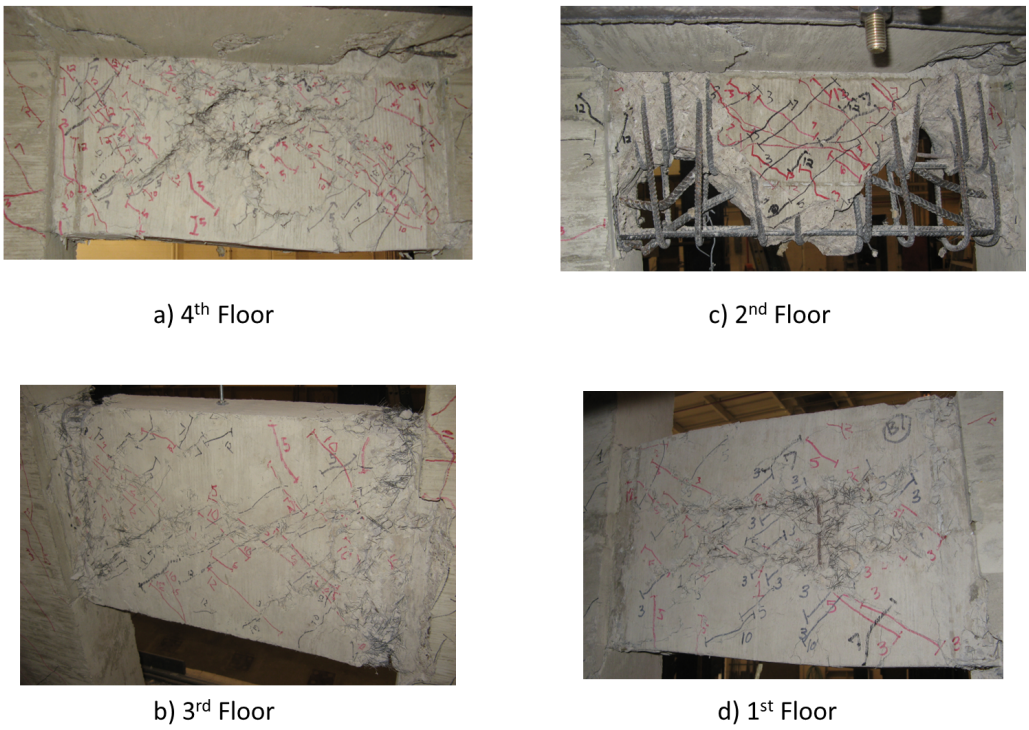

Figure 2.9: Damage Comparison of HPFRC and RC Coupling Beams (Photos courtesy of R. Lequesne).

The observed potential of HPFRC to contribute to shear strength, confinement and reductions in reinforcement in coupling beams with aspect ratios less than 2.0 was encouraging and led to further tests on relatively slender coupling beams ($l_n/h \approx 3$). It was expected that the use of HPFRC would allow greater simplifications in reinforcement without compromising the seismic performance of coupling beams. Setkit (2012) conducted a study to evaluate the performance of slender HPFRC coupling beams, evaluate the possibility of further simplifications and/or

the elimination of diagonal reinforcement, and develop a new design for slender earthquake-resistant HPFRC coupling beams. In his study, six coupling beam specimens with aspect ratios of either 2.75 or 3.3 were tested under displacement reversals. The main experimental variables were beam aspect ratio, reinforcement detailing, and concrete type (i.e. regular concrete or HPFRC). Furthermore, the same HPRFC evaluated in Lequesne's research was used.

Some of the most important conclusions and observations from Setkit's study were: 1) coupling beams constructed with RC 80/30 BP fibers at a 1.5% volume fraction and no diagonal reinforcement, subjected to peak shear stress reversals in the range of 8.7 to $10.7\sqrt{f'_c}$ (psi), exhibited a stable hysteresis behavior with drift capacities of 6.8% and 5.8% for aspect ratios of 3.3 and 2.75, respectively; 2) it was estimated that the total contribution of the diagonal reinforcement, when included, to the shear strength of the beams was below 15% of the total shear strength; and 3) HPFRC coupling beams exhibited normalized energy dissipation capacities comparable to well-detailed diagonally-reinforced coupling beams of similar aspect ratios, despite the elimination of diagonal reinforcement. Further discussion of Setkit's work and HPFRC coupling beams without diagonal reinforcement can be found in Lequesne et al. (2011), and Parra-Montesinos et al. (2010, 2014, 2017a,b).

Parra-Montesinos et al. (2014) showed that the successful elimination of diagonal reinforcement in coupling beams with span-to-depth ratios greater than 2.2 is possible with the use of HPFRCs. However, the design of HPFRC coupling beams proposed thus far have only considered a single HPFRC reinforced with RC 80/30 BP fibers at a 1.5% volume fraction, thus limiting its widespread implementation in practice. For designers to adopt the use of HPFRC or steel fiber-reinforced concretes (SFRCs) in the design of coupling beams, a design approach that accounts for the different performance of SFRCs, through the use of a performance-based classification criteria for SFRCs is needed. The work discussed in the following chapters builds upon the work of Lequesne (2011) and Setkit (2012) and expands the scope to various types of SFRCs, including strain-softening SFRCs.

3 EXPERIMENTAL PROGRAM

3.1 Overview

Past experimental research (Parra-Montesinos et al., 2014; Setkit, 2012) showed that the use of tensile strain-hardening fiber-reinforced concrete in coupling beams with span-to-depth ratio (l_n/h) of 2.2 or greater allowed the elimination of diagonal reinforcement while ensuring adequate shear strength and drift (beam chord rotation) capacity. However, only a single strain-hardening FRC was investigated, which featured 1.18-in. long, 0.015-in. diameter hooked steel fibers with a tensile strength of 330-ksi at a 1.5% fiber volume fraction (V_f). Elimination of the diagonal reinforcement translates into significant reductions in construction time, which is highly appealing for the construction industry. However, due to the limited experimental data on the behavior of SFRC coupling beams the use of SFRC for coupling beam design has been quite limited. Therefore, to achieve a widespread use of SFRC in the design of coupling beams, there is a need to: 1) evaluate the possibility of using lower fiber dosages and/or other fiber types; 2) to evaluate the strength, ductility, and failure mechanisms of SFRC coupling beams without diagonal reinforcement; and 3) develop a framework or methodology to evaluate the adequacy of a given SFRC for the design of coupling beams based on the expected coupling beam drift and shear stress demands.

The experimental phase of this study, discussed in this chapter, focused on 1) evaluating the performance of SFRC coupling beams without diagonal reinforcement constructed with various SFRCs (fiber types and dosages) subjected to large displacement reversals; 2) characterizing the compressive, tensile, and flexural behavior of the various SFRCs investigated; and 3) establishing a link between the mechanical properties of SFRCs and the structural performance of the SFRC coupling beams.

3.2 Coupling Beam Test Specimens

To evaluate the seismic performance of coupling beams constructed with different SFRCs, and the adequacy of the different SFRCs for use in coupling beams, eight large-scale SFRC coupling beams were tested under reversed cyclic displacements. Each coupling beam specimen consisted of a precast, rectangular coupling beam connected to two rectangular blocks that simulated the wall boundary regions in a coupled wall system. The main variables investigated were: 1) coupling beam span-to-depth ratio; 2) peak shear stress demand; and 3) type of fiber reinforced concrete (i.e., fiber type and dosage).

Although it is possible to use cast-in-place SFRC coupling beams (Parra-Montesinos et al., 2014, 2017a,b; Kopczynski and Whiteley, 2016), precast coupling beams can simplify the construction process, allowing the placement of the steel and casting of the walls up to the bottom surface of the coupling beams. Moreover, precast construction can also offer superior quality control during construction of each coupling beam. To have better control of the experimental SFRC mixtures used to cast the coupling beam specimens, precast construction was preferred over cast-in-place construction. Furthermore, precast connections are more critical than those in cast-in-place construction and thus, the results of this study are applicable to cast-in-place SFRC coupling beams.

Five of the coupling beam specimens had a span-to-depth ratio (aspect ratio or l_n/h) of 3.0 and the other three had an aspect ratio of 2.0. Coupling beams constructed with the SFRCs expected to show the best performance were designed for shear stress demands of approximately 8 to $10\sqrt{f'_c}$ (where f'_c is the concrete compressive strength in psi), whereas coupling beams constructed with lower performing SFRCs were designed for lower shear stresses of approximately 6 to $8\sqrt{f'_c}$ (psi). Furthermore, SFRCs expected to perform best were used in the coupling beams with $l_n/h = 2.0$ given the increased role of shear in these beams compared to those with $l_n/h = 3.0$.

3.2.1 Coupling Beam Reinforcement Design

The coupling beam specimens investigated in this experimental work had a span-to-depth ratio (l_n/h) of either 2.0 or 3.0. As discussed in Section 2.2.3, ACI 318-19 provides two alternatives for the design of coupling beams with span-to-depth ratio between 2.0 and 4.0. Coupling beams with $2.0 \leqslant l_n/h < 4.0$ ratio can be designed either as beams of special moment resisting frames per Section 18.6 of ACI 318-19 or as diagonally-reinforced coupling beams following ACI 318-19 Section 18.10.7.2. The coupling beam specimens of this experimental work were not designed following either of the two alternatives. Instead a design following the work of Setkit (2012) was used.

Given the enhanced ductility, shear strength and confinement provided by SFRCs, as well as results from previous investigations (Parra-Montesinos et al., 2014; Setkit, 2012), a simplified reinforcement detailing without diagonal reinforcement was used in all coupling beam specimens. The SFRC coupling beams were designed to encourage the development of plastic hinges at both ends of the member and thus, their design shear force was dictated by the plastic flexural strength of the beams. From equilibrium considerations the expected shear demand (V_{target}) is related to the plastic flexural strength (M_p) of the beams as $V_{target} = (2M_p)/l_n$, where l_n is the clear span length of the coupling beams. The design started with the selection of V_{target}. Then, based on V_{target}, the longitudinal reinforcement was selected such that M_p closely corresponded to the pre-selected shear demand. Finally, the transverse reinforcement of the coupling beams was detailed to provide enough shear capacity such that a flexural failure would precedeca shear failure.

Coupling beam shear strength was assumed to be the result of contributions from the SFRC, referred to herein as V_c, and the transverse steel, V_s (truss mechanism). Results from previous research on coupling beams constructed using a tensile strain-hardening SFRC suggest a shear stress (v_c) of $5\sqrt{f'_c}$ (psi) as an upper limit for the FRC contribution to the overall shear capacity of the coupling beams (Lequesne, 2011). The coupling beams tested in this study, except for one case, were designed so that the shear "demand" on the SFRC would not exceed this limit.

For each specimen, two different transverse steel designs were provided, one for the plastic hinge regions, and the other for the region outside of the plastic hinges. For design purposes, and based on previous work (Lequesne, 2011; Lequesne et al., 2013), the plastic hinge regions were assumed to extend half the overall beam depth from each end. The spacing (s) of the transverse reinforcement outside the plastic hinge regions, selected to consist of single #3 hoops, was calculated per Equation 3.1,

$$s \leqslant \frac{A_v f_{yt}\, d}{V_{target} - V_c} \tag{3.1}$$

where A_v is the area of one transverse steel hoop ($0.22\ in^2$), f_{yt} is the nominal yield strength of the transverse steel (60 ksi), and d is the effective depth of the coupling beam. Figure 3.1 through Figure 3.5 show the reinforcement detailing and geometry of each of the coupling beam specimens.

The transverse reinforcement in the plastic hinge regions was detailed following, as practicably as possible, the provisions for columns of special moment resisting frames of Chapter 18 of ACI 318-14, particularly the provisions shown in Table 18.7.5.4. The column-type transverse reinforcement was expected to provide adequate confinement to the plastic hinge regions, preserving the core integrity through large inelastic rotation reversals and high shear stress demands. The provisions of Table 18.7.5.4 resulted in a 1.8 in. spacing for double hoops made of #4 bars. Such a small spacing is not practical and thus, the #4 hoops were spaced at 2.5 in. on center. This spacing satisfied the confinement provisions only in the direction parallel to the width of the coupling beams. The detailing, however, was deemed appropriate considering that the fiber reinforcement would also contribute to the confinement of the concrete core.

As previously mentioned, the longitudinal reinforcement was selected such that the expected flexural capacity of the coupling beam would closely corresponded to the pre-selected V_{target}. Because no fibers would cross the cold joint at the beam-to-wall interface, U-shaped dowels were provided to strengthen this section, controling inelastic deformations at the interface and thus, preventing a premature

sliding shear failure. Therefore, two critical sections were considered for flexure, the beam-to-wall interface and the section adjacent to the termination of the dowel reinforcement. The moment capacity was taken as the maximum moment obtained from moment-curvature (M–ϕ) analyses assuming an axial force equal to V_{target}, Hognestad's model for concrete compression (discussed in Section 4.6.1.1), a steel stress-strain model similar to that discussed in Mander, 1983 (see Section 4.6.1.2), and a tri-linear model for the tensile response of SFRCs, as recommended by Setkit (2012). Previous experiments showed that the axial forces developed in similar coupling beam specimens ranged from 60-90% of the total applied shear (Setkit, 2012). Therefore, the magnitude of the axial forces was conservatively assumed to be equal to the target shear demand. The intention was to avoid underestimating the flexural capacity of the coupling beams and consequently the shear demand.

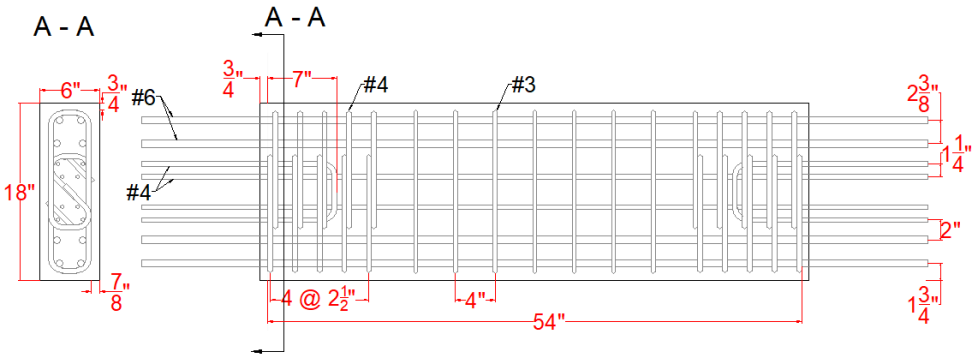

Figure 3.1: Reinforcement Detailing of Coupling Beam CB1.

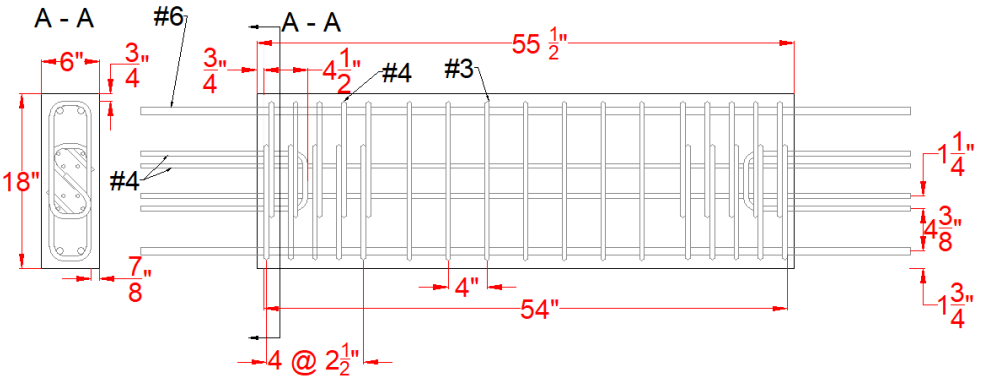

Figure 3.2: Reinforcement Detailing of Coupling Beams CB2 and CB3.

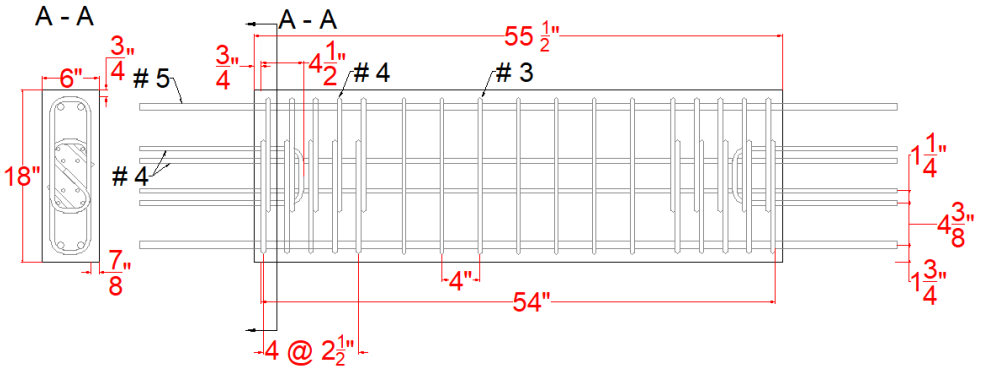

Figure 3.3: Reinforcement Detailing of Coupling Beams CB4 and CB5.

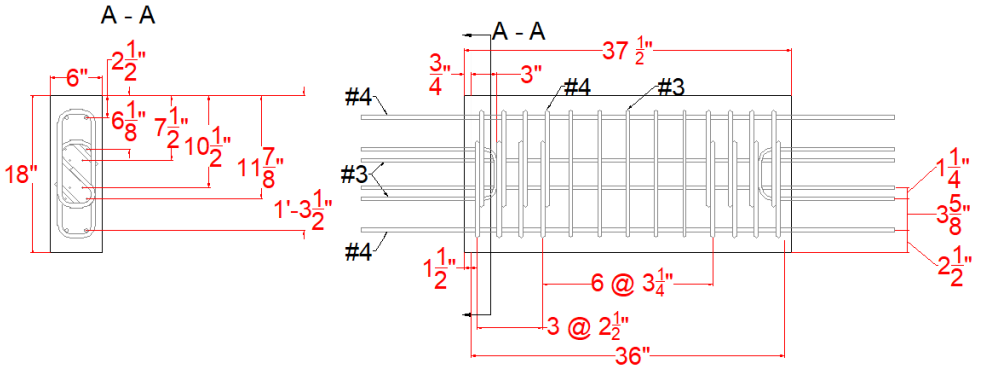

Figure 3.4: Reinforcement Detailing of Coupling Beam CB6.

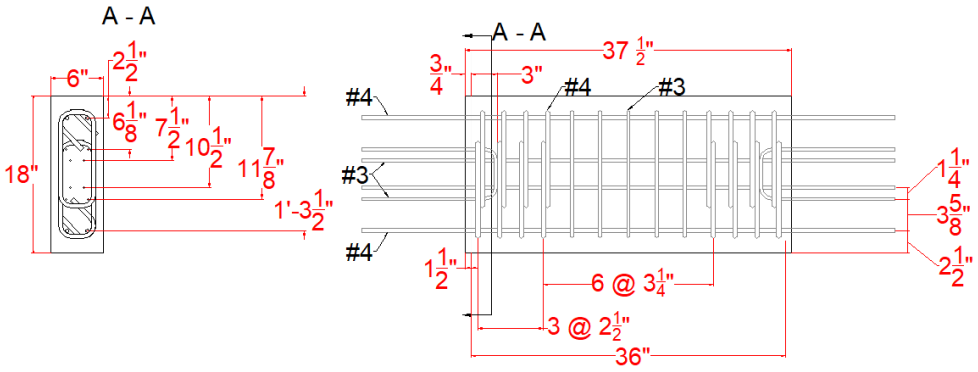

Figure 3.5: Reinforcement Detailing of Coupling Beams CB7 and CB8.

As mentioned above, each coupling beam specimen was connected to two large blocks meant to simulate the boundary regions of the walls being coupled. These end blocks were designed for the forces associated with a coupling beam shear of 150 kips, which is significantly larger than the maximum expected shear in any of the test coupling beams. Figure 3.6 shows the reinforcement detailing and a typical cross section of both end blocks. PVC pipes, used to insert through bolts for connection to the strong floor and other test setup fixtures, are omitted from the drawings for clarity. All the steel reinforcement used in this project was A615 Gr.60, and was cut and bent to specifications by a local supplier.

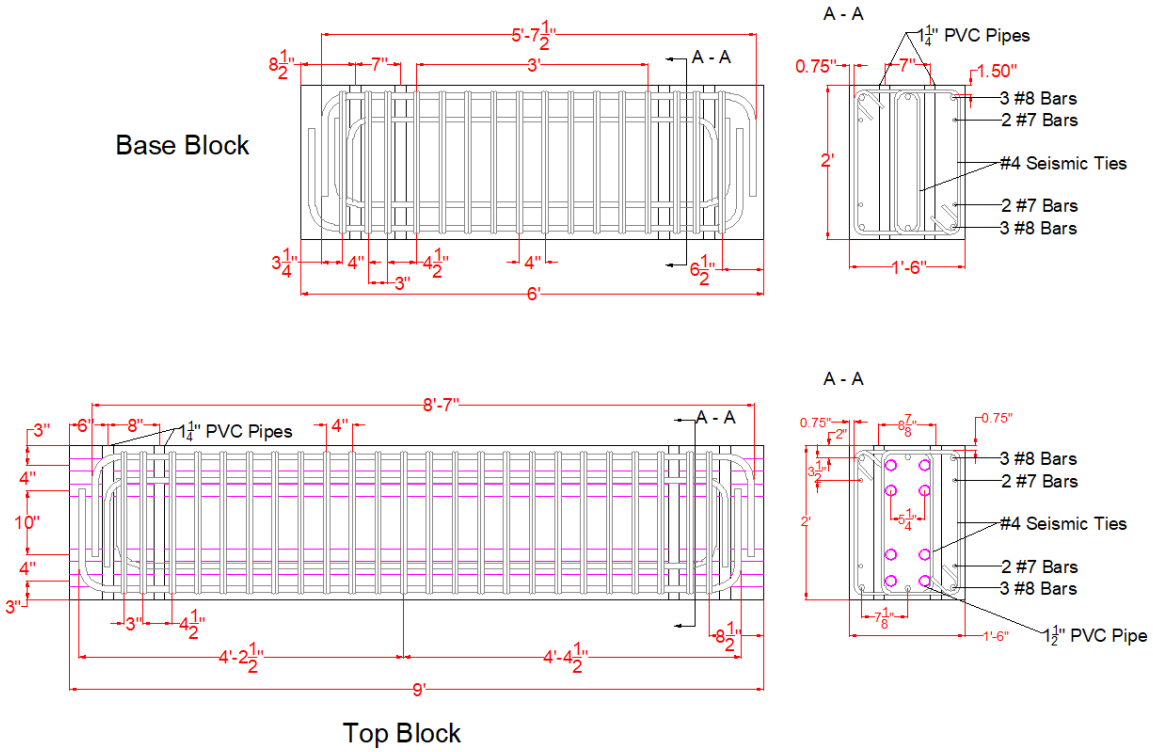

Figure 3.6: Reinforcement for the End Blocks Simulating Wall Boundary Regions.

3.3 Steel Fiber-Reinforced Concretes Investigated

Along with the casting of each coupling beam specimen, several material samples were cast from the same concrete batches to evaluate their flexural, tensile and compressive response. Fiber type and dosage were selected depending on the coupling beam span-to-depth ratio and expected peak shear stress. On average, the SFRCs considered in this experimental work had a compressive strength of approximately 9000 psi (material testing and responses are discussed in Section 3.6).

For the experimental SFRC mixtures, three different hooked steel fibers were evaluated, HE 55/35, RC 55/30 BG and RC 80/30 BP fibers, with a nominal tensile strength of 275 ksi, 195 ksi and 330 ksi, respectively. The geometry and properties of these fibers are shown in Figure 3.7. In addition, three different volume fractions were considered for a total of six different SFRCs mixtures, as shown in Table 3.1. In general, the tensile and flexural strength of SFRCs are primarily dependent on the strength, volume fraction, and length-to-diameter ratio of the fibers. An increase in these parameters generally results in a better performing composite in terms of tensile and flexural strength, as well as post-cracking behavior.

All the investigated fibers came in bundles glued by a water-soluble binder that dissolves during the mixing process to allow for a random fiber distribution in the fresh concrete. The HE 55/35 fibers were manufactured by ArcelorMittal and both RC 55/30 BG and RC 80/30 BP fibers were manufactured by Bekaert Corporation. Note that each manufacturer employs a distinct fiber designation (e.g. RC 80/30 BP) that provides information about the fiber geometry[1].

[1] The first number represents the length-to-diameter ratio or the fiber diameter in hundredths of mm for fibers manufactured by Bekaert and ArcelorMittal, respectively. The second number corresponds to the fiber length in mm.

Table 3.1: SFRC Mixtures Investigated.

Fiber Type	V_f	Coupling Beam Specimen
HE 55/35	1.25%	CB1 and CB2
HE 55/35	1.5%	CB6
RC 55/30 BG	1.0%	CB4
RC 55/30 BG	1.25%	CB3
RC 80/30 BP	1.0%	CB5
RC 80/30 BP	1.5%	CB7 and CB8

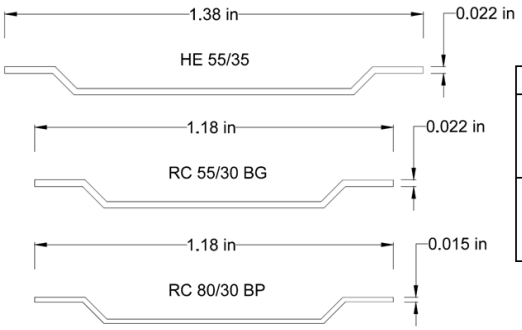

a)

Steel Fiber Properties				
Fiber Name	Fiber Length (in/mm)	Fiber Diameter (in/mm)	l_f/d_f	Tensile Strength (ksi/MPa)
HE 55/35	1.38/35	.022/.55	64	275/1900
RC 55/30 BG	1.18/30	.022/.55	55	195/1350
RC 80/30 BP	1.18/30	.015/.38	79	330/2300

b)

Figure 3.7: Steel Fiber Reinforcement.

3.4 Mixing of SFRC and Coupling Beam Construction

All SFRCs used in the coupling beam specimens and material test samples were mixed and batched in the Wisconsin Structures and Materials Testing Laboratory (WSMTL). The SFRCs studied in this project followed similar proportions to one of the strain-hardening SFRC mixtures previously investigated for coupling beam applications and used in Setkit (2012). However, no viscosity modifying agents or super plasticizers were used for the mixtures investigated in this study. The main constituents of the SFRC mixtures were Type I Portland cement, $\frac{3}{8}$ in. maximum size crushed limestone, and Torpedo sand. Torpedo Sand is the local name for washed gravel sand typically graded from mesh #200 to $\frac{3}{16}$ in. Table 3.2 presents the design mixture proportions for the investigated SFRCs.

Table 3.2: SFRC Design Mixture Proportions.

Material	Batch Weight lbs per $3.5ft^3$	Proportions by Weight
Portland Cement	131.3	1.2
Class C Fly Ash	32.8	0.3
Torpedo Sand	188.8	1.7
Coarse Aggregate	108.5	1.0
Water	63.7	0.6

Three SFRC batches of approximately 3.5 ft^3 each were mixed for each coupling beam specimen. Half of each coupling beam plus several material samples were cast with each of the first two batches of SFRC, while the third batch was used to finish casting the remainder material test samples. The concrete mixer, along with several materials sample forms and a coupling beam specimen ready for casting, can be seen in Figure 3.8. The SFRC was mixed using the following procedure:

1. Fly ash, cement and sand were added into the concrete mixer and mixed until all three materials were mixed thoroughly and uniformly (approximately 4 minutes).

2. Between 50 to 70% of the water was gradually added and mixed until a fairly workable mortar was achieved.

3. Coarse aggregate was then added and mixed thoroughly for approximately 3 minutes. Additional water was added as needed until the concrete consistency was deemed acceptable.

4. Fibers were added and mixed for approximately 3 minutes. The mixer was then stopped for 2-3 minutes to allow the glue binding the fibers to dissolve. The concrete was mixed again for an additional 2-3 minutes to disperse the fibers throughout the fresh concrete.

Figure 3.8: Mixing SFRC and Coupling Beam Specimen Ready for Casting.

None of the aggregates were oven dried before mixing and their moisture content varied considerably. Therefore, adjustments due to moisture content of the aggregates were not possible. Because of this, often the amount of water required by design was not entirely used. The decision of how much water to use was made by inspecting the fresh concrete until the workability of the mixture was deemed acceptable. Approximately 85-95% of the required water was typically used. The average slump of each SFRC used to cast the coupling beam specimens is given in Table 3.3.

Each coupling beam specimen was cast and covered with plastic until it was demolded a day or two after casting, remaining thereafter uncovered in the laboratory until testing. To complete a specimen, the precast coupling beam was inserted into the end blocks forms, which had all the reinforcement already in place. Figure 3.9 shows a coupling beam being inserted into the end block forms in preparation for casting of the end blocks. Each coupling beam was embedded into the end blocks approximately $\frac{3}{4}$ in. (i.e., depth of concrete clear cover in end blocks). Once the beam was inserted into the forms, it was squared and leveled as best as possible and finally secured for casting the end blocks. The end blocks were cast using ready-mix concrete with a specified compressive strength of 5,000 psi and a maximum aggregate size of $\frac{3}{8}$ in., ordered from a local supplier. A set of end blocks being cast can be seen in Figure 3.10 and a finished coupling beam specimen is shown in Figure 3.11.

Table 3.3: Slumps of SFRCs Used in Coupling Beam Specimens.

Coupling Beam Specimen	Fiber Type	V_f	Slump (in.)
CB1	HE 55/35	1.25%	9.1
CB2	HE 55/35	1.25%	7.8
CB3	RC 55/30 BG	1.25%	7.2
CB4	RC 55/30 BG	1.0%	7.0
CB5	RC 80/30 BP	1.0%	6.9
CB6	HE 55/35	1.5%	4.6
CB7	RC 80/30 BP	1.5%	5.8
CB8	RC 80/30 BP	1.5%	5.4

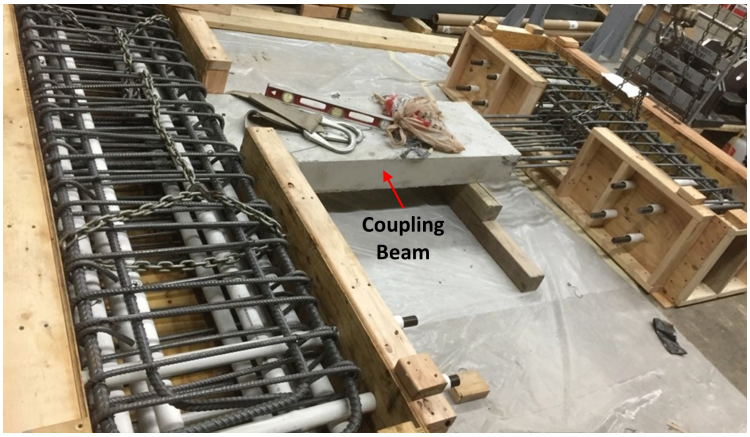

Figure 3.9: Precast SFRC Coupling Beam Being Inserted Into End Blocks.

Figure 3.10: Casting of End Blocks.

Figure 3.11: Finished Coupling Beam Specimen.

3.5 Test Setup, Displacement History and Instrumentation

A schematic of the test setup and a photograph of the actual setup are shown in Figure 3.12. The coupling beams were rotated 90° from their typical horizontal orientation for testing convenience. Two vertical steel arms were used to keep both end blocks parallel during testing and were each instrumented with a 100-kip capacity load cell. These load cells allowed monitoring the axial load developed in the coupling beams as the beams elongated during testing.

The coupling beam specimens were subjected to a quasi-static history of increasing displacement reversals. The displacements were applied using a horizontal 200-kip hydraulic actuator connected at one end to a concrete reaction block and at the other end to a stiff steel arm, in turn connected to the top block of the specimen, as shown in Figure 3.12. Lateral or coupling beam drift in the context of this study refers to the coupling beam chord rotation, calculated as the relative lateral displacement between the end blocks divided by the beam clear span length, l_n (an adjustment due to relative rotation between the end-blocks was made; see Appendix A.1). The intended applied drift histories are shown in Figure 3.13. After the test of Specimen CB1, the displacement history (Figure 3.13-a) was considered excessive and thus, the remainder coupling beams were tested following the displacement history shown in Figure 3.13-b. Only one cycle was applied to each drift level, except for the cycles to drift levels below 1.0%, which were applied twice (see Figure 3.13). Positive and negative drifts corresponded to the actuator pulling and pushing on the coupling beams, respectively.

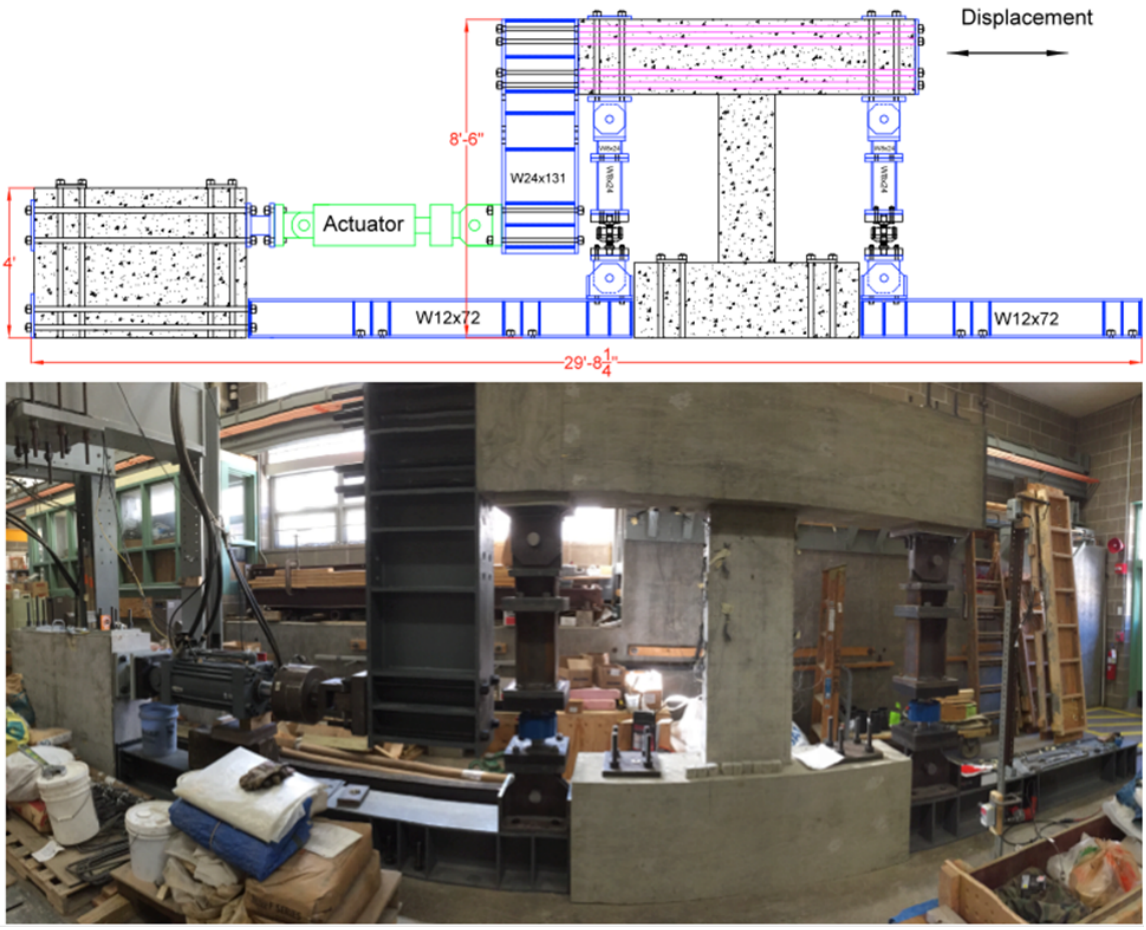

Figure 3.12: Coupling Beam Test Setup.

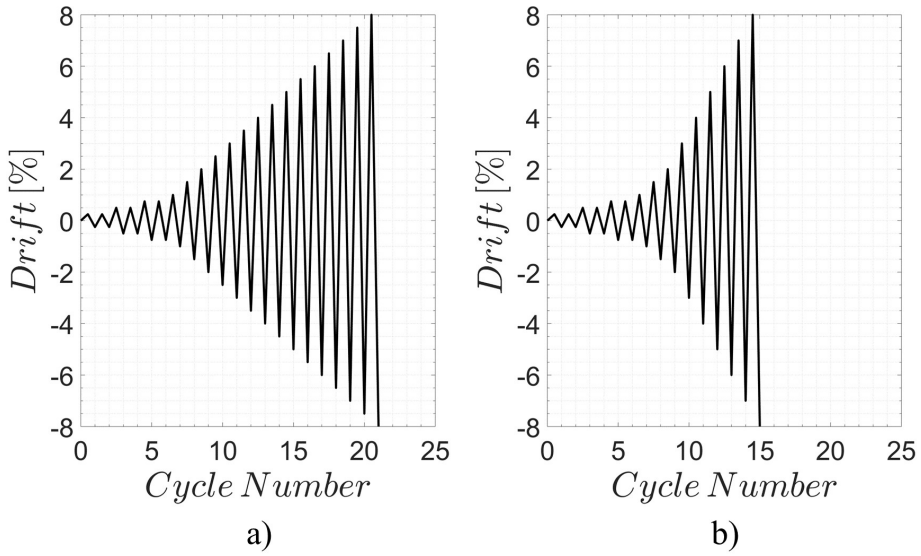

Figure 3.13: Intended Coupling Beam Test Displacement Histories. a) Specimen CB1; b) Specimens CB2-CB8.

A dense network of sensors was employed to monitor displacements, forces and deformations applied to or experienced by the coupling beam specimens. Displacements and forces applied by the hydraulic actuator were monitored through an LVDT and load cell attached to the actuator. Two horizontal string potentiometers, attached to the top and bottom end blocks, were used during the test as feedback to control the applied relative horizontal displacement. Relative block displacements, as well as deformations experienced by the coupling beams, were also monitored with an array of Optotrak™ markers. The Optotrak Certus HD™ system is an infrared-based system (NDI Measurement Sciences, 2014) that monitors the position of markers attached to the specimen surface during testing with a precision ranging from 0.004 to 0.01 in. The marker grid used for the coupling beams with l_n/h of 3.0 and 2.0 are presented in Figures 3.14 and 3.15, respectively.

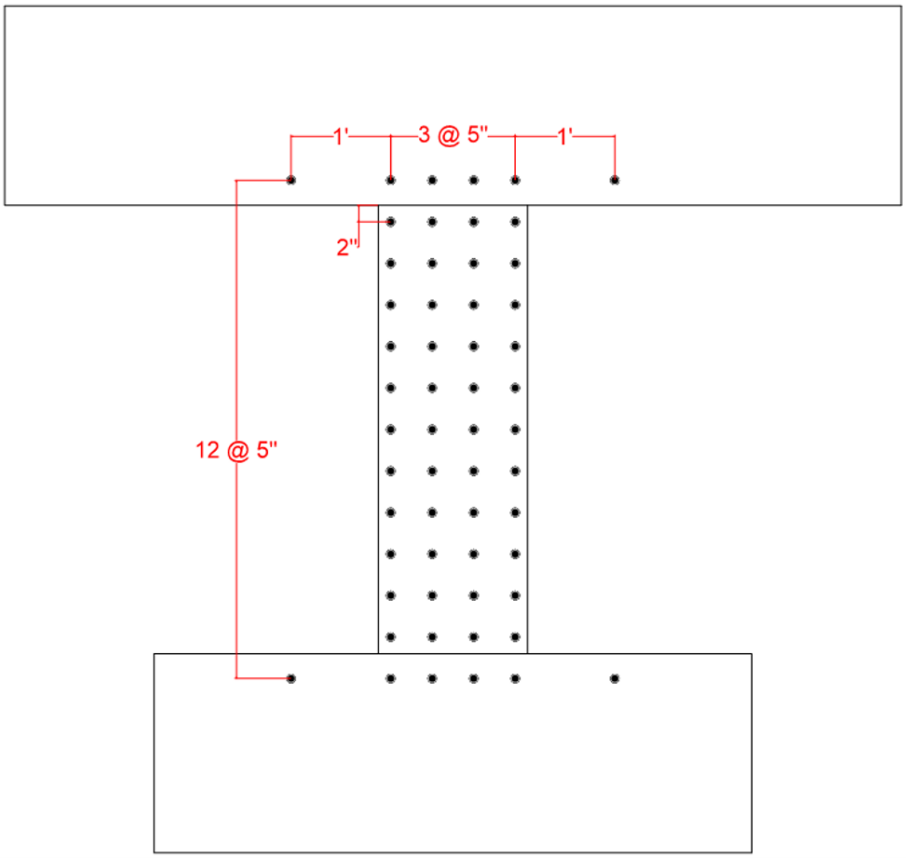

Figure 3.14: Optotrak™ Marker Layout For Coupling Beams with $l_n/h = 3.0$.

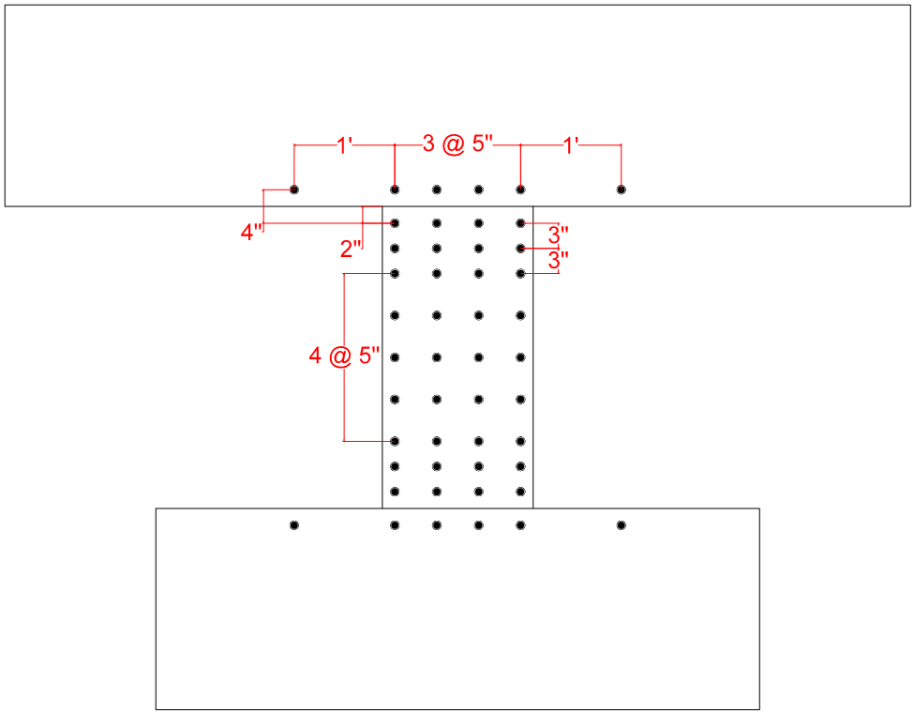

Figure 3.15: Optotrak™ Marker Layout For Coupling Beams with $l_n/h = 2.0$.

Strain gauges were installed on the longitudinal, transverse and dowel reinforcement to monitor strains in the reinforcement at various locations. Figure 3.16 shows strain gauges being installed and coated strain gauges prior to pouring of concrete. The location of the strain gauges in the longitudinal bars was selected such that yielding of the flexural reinforcement could be identified at the beam-wall interface and at approximately $h/2$ and $h/4$ for coupling beams with l_n/h of 3.0 and 2.0, respectively. Strains in the transverse reinforcement inside and outside of the plastic hinges were also measured. The location of the strain gauges installed on the reinforcement of the coupling beam specimens is shown in Figure 3.17 through Figure 3.19. Strain gauges on longitudinal, transverse and dowel reinforcement are labeled as F (flexural), S (shear), and D (dowel), respectively.

Figure 3.16: Strain Gauge Installation (Top) and Strain Gauges with Finished Coating (Bottom).

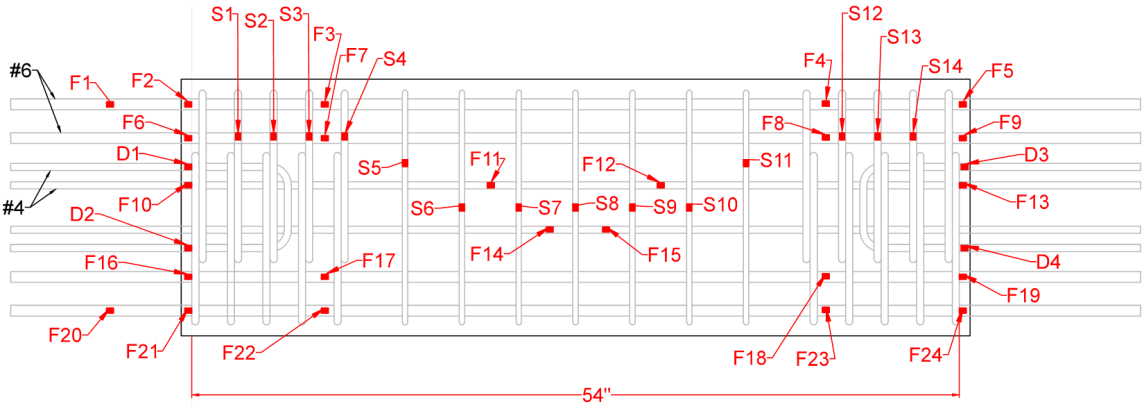

Figure 3.17: Strain Gauge Location and ID (Specimen CB1).

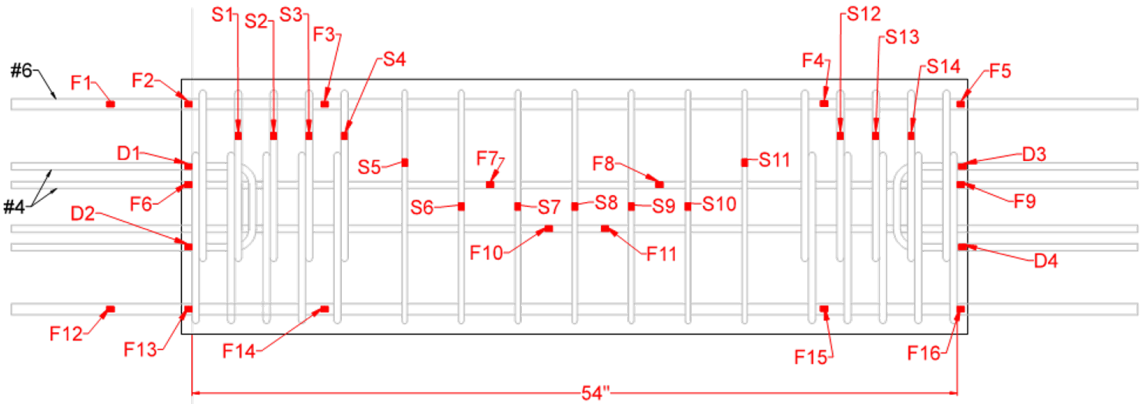

Figure 3.18: Strain Gauge Location and ID (Specimens CB2-CB5).

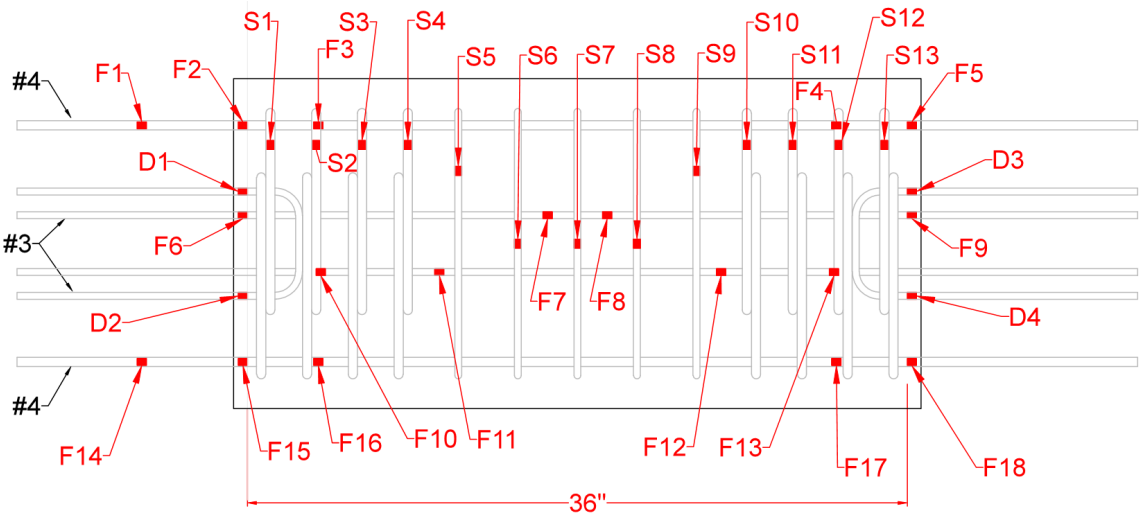

Figure 3.19: Strain Gauge Location and ID (Specimens CB6-CB8).

3.6 Characterization of Steel Fiber-Reinforced Concrete Mechanical Properties

Understanding the mechanical properties of SFRC is necessary to effectively use them in structural members. Moreover, the post-peak behavior of the SFRCs plays an important role in the behavior of members undergoing significant plastic deformations (e.g. coupling beams). Therefore, to characterize the mechanical properties of the SFRC mixtures evaluated, a series of tests were conducted with concrete samples obtained from the same batches of concrete used to cast each of the eight SFRC coupling beam specimens. The following sections describe the specimens, test setup, and instrumentation utilized to evaluate the flexural, tensile, and compressive response of each SFRC investigated in this study.

3.6.1 Four-Point Flexural Tests

To study the flexural response of the six SFRC mixtures considered in this study, four-point bending tests similar to that specified in ASTM C1609 (2012) were conducted. Two series of tests using either notched or un-notched 6 by 6 by 20 in. specimens were conducted. Note that ASTM 1609 applies to unnotched beams. A hydraulic loading frame was used for all the flexural tests. The tests were displacement controlled at a rate of 0.005 in./min., based on the actuator head movement. In addition, infrared optical sensors from the Optotrak Certus HD™ system were glued to the concrete specimens to measure the position in space of each marker. The coordinate data of each marker were used in the calculation of deformations in each specimen, such as deflections, rotations, and crack opening. The test setup and marker layout used for the notched and un-notched test series are shown in Figure 3.20-a and Figure 3.20-b, respectively. For the notched beam specimens, a notch 1.5 in. deep and approximately 1/8 in. wide was saw cut at mid-span. Details on the Optotrak™ data analysis are provided in Appendix A.2.

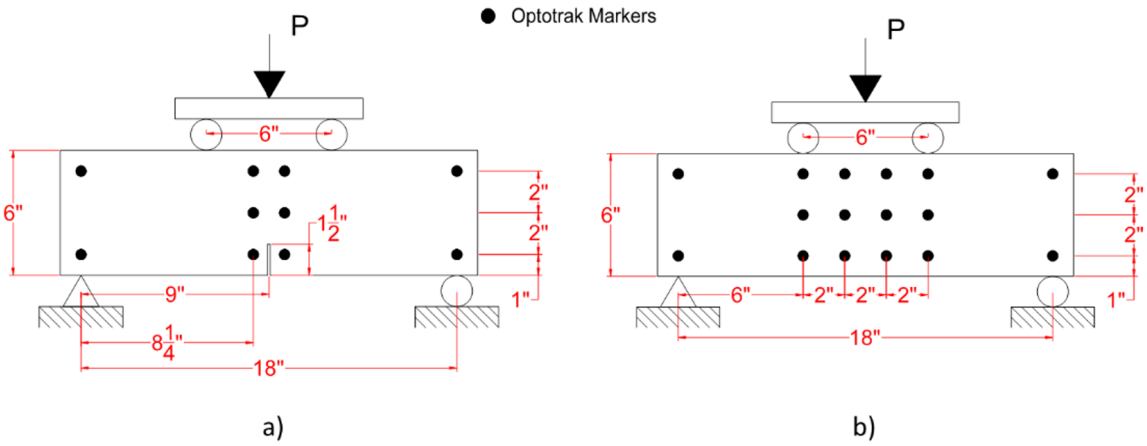

Figure 3.20: Flexural Test Setup and Optical Sensor Layout. a) Notched Beams; b) Un-Notched Beams.

3.6.2 Direct Tension Tests

Specimens tested to study the behavior of the various SFRCs under direct tension consisted of 6 by 6 by 14 in. concrete prisms with a #5 steel reinforcement bar along their longitudinal axis. The reinforcement bar was discontinuous at mid-length of the specimen, where a 3/4 in. deep notch was saw-cut around the specimen to force the failure to occur at this location. The bar ends were clamped into a hydraulic load frame and then tested under displacement control at a displacement rate of 0.002 in./min. until the specimen cracked. After cracking, the displacement rate was increased to 0.02 in./min. and kept constant for the remainder of the test. Optotrak™ markers were used to track the crack opening throughout the tests. A tension specimen and the optical marker layout are shown in Figure 3.21. A discussion of the data processing for the tension specimens is provided in Appendix A.3.

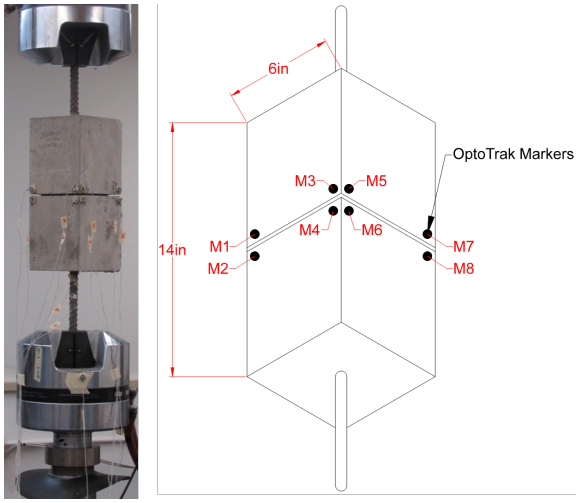

Figure 3.21: Tension Specimen and Marker Layout.

3.6.3 Compression Cylinder Tests

To determine the compressive strength and behavior of the various SFRCs considered in this study, a minimum of four standard 6 by 12 in. cylinders were prepared and then cured in a moisture room for at least 27 days. Two different compression tests were conducted using a 400-kip compression frame. To determine the compressive strength of the SFRC of each coupling beam specimen, cylinders were tested in accordance with ASTM C39 (2016) the same day the coupling beam specimens were tested. However, to measure the stress-strain response of the SFRC cylinders, most of the cylinders were tested under displacement control at a displacement rate of 0.01 in./min. For these tests, a grid of Optotrak™ markers was used to monitor axial strains. The marker layout consisted of three columns of sensors located at 90° arcs. Figure 3.22 shows the marker layout used for the cylinder compression tests. The markers located on the sides of the cylinders (based on the camera point of view and shown in Figure 3.22) were glued on small aluminum angles that had previously been epoxied to the cylinder sides to allow the Optotrak™ camera to detect these markers. All the cylinders tested were capped with a sulfur-based compound.

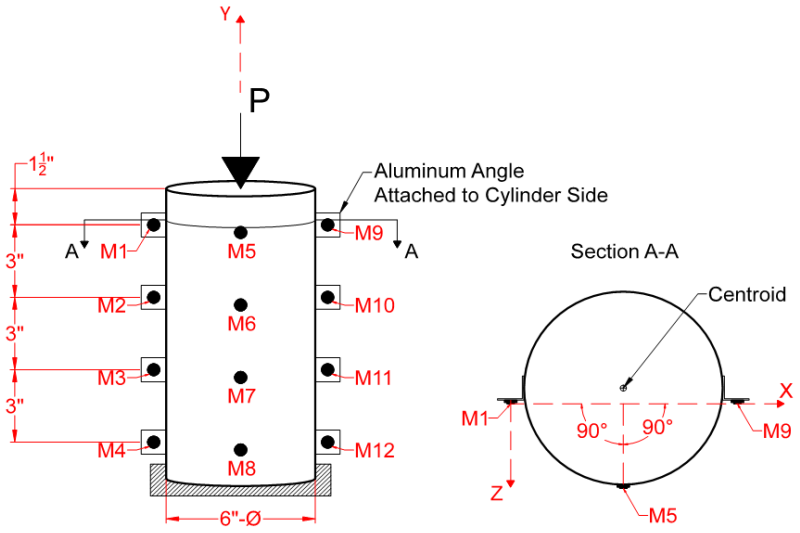

Figure 3.22: Marker Layout for Cylinder Compression Tests.

The axial strains for each cylinder were calculated for all three columns of markers using the top and bottom markers (i.e., markers 1 and 4, 5 and 8 and 9 and 12). The resulting strains were also compared to the strains calculated at each third of the cylinder (e.g., between markers 1 and 2, 2 and 3 and 3 and 4) to ensure that the strains considered were representative of the overall compressive behavior of the cylinder. Finally, the strains near the centroid of the cylinder were calculated by averaging vertical coordinate (Y) of markers 1 and 9 and markers 4 and 12, and calculating the strain using the difference of these average Y coordinates. An effort was made to glue the angles along a line passing through the cylinder centroid, but no accurate measurements of the actual position of the side markers with respect to the centroid was possible. Thus, it was assumed that the strains calculated from the average coordinates of markers 1 and 9 and markers 4 and 12 were a reasonable approximation of the axial strains at the centroid of the cylinder.

3.7 Material Test Results

The previous section described the different mechanical tests conducted to study the flexural, tensile, and compressive behavior of the various SFRCs considered in this study. In the following sections, the results of each series of tests are presented. In addition to the tests conducted on SFRC samples, the tensile responses of the reinforcing steel of each SFRC coupling beam are presented. Testing dates and age of each SFRC specimen are provided in Appendix C.

3.7.1 Four-Point Flexural Tests

Stress versus deformation responses were calculated for each concrete sample tested (see Appendix B). The average stress for a given deformation level (e.g. crack opening or deflection) was then calculated to generate average responses for each type of SFRC. The flexural responses were calculated in terms of equivalent flexural stress (f) versus either mid-span deflection or crack opening. The stress f was calculated as $PL/(bh^2)$, where P is the total applied load, L is the span length, and b and h are the beam width and depth, respectively. For ease of comparison, the flexural responses were normalized by the maximum flexural stress at first cracking (f_{cr}) of the corresponding SFRC. As expected, the post-cracking behavior of each sample exhibited significant variability with respect to the calculated average responses (roughly between 15-30%). This variability was mainly attributed to the random distribution of fibers in the concrete matrix and their distribution throughout the samples.

Average normalized notched beam responses for all SFRCs are presented in Figure 3.23 and Figure 3.24, where $\delta_{mid-span}$ is the deflection of the beam at mid-span and w_{cr} is the crack width or crack opening. Each curve is the average of at least three samples; see Appendix B.1 for the flexural responses of all the notched beams tested. In general, the flexural behavior of SFRC notched beams was characterized by a linear elastic portion, a slight strength drop right after first cracking, a nonlinear hardening region, and a nearly linear descending or softening branch. Some of the SFRCs with a volume fraction of 1.5%, however, did not exhibit

a strength drop after first cracking. On average, all the SFRCs considered in this study exhibited significant deflection hardening response in the notched beam tests. Two measures of ductility were used to further evaluate the behavior of the SFRCs, 1) peak strength ductility (μ_{pc}), calculated as the ratio of the mid-span deflection at peak strength (δ_{pc}) to the deflection at first cracking (δ_{cr}); and 2) the ductility corresponding to $f = f_{cr}$ during the softening branch ($\mu_{f_{cr}}$), calculated as the ratio of the deflection once the stress dropped to f_{cr} ($\delta_{f_{cr}}$), to δ_{cr}. The peak post-cracking strength, (f_{pc}), among other parameters used to describe the flexural response of the SFRC notched beams, are presented in Table 3.4.

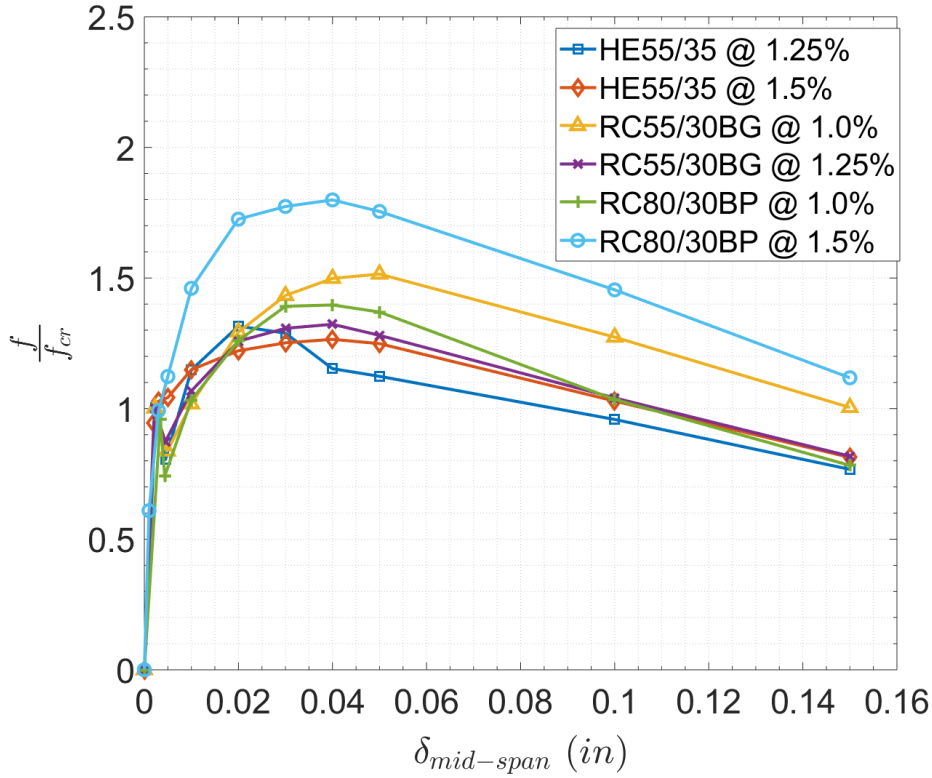

Figure 3.23: Normalized Equivalent Flexural Stress Versus Deflection Response of SFRC Notched Beams.

Table 3.4: Notched Beam Average Response Summary.

Fiber Type	V_f	f_{cr} (psi)	f_{pc} (psi)	$\frac{f_{pc}}{f_{cr}}$	δ_{cr} (in.)	δ_{pc} (in.)	$\delta_{f_{cr}}$ (in.)	$\mu_{pc} = \frac{\delta_{pc}}{\delta_{cr}}$	$\mu_{f_{cr}} = \frac{\delta_{f_{cr}}}{\delta_{cr}}$
HE 55/35	1.25%	730	960	1.31	0.0025	0.020	0.087	8.0	35
HE 55/35	1.5%	780	980	1.27	0.0030	0.040	0.107	13	36
RC 55/30 BG	1.0%	650	990	1.51	0.0022	0.050	0.150	23	68
RC 55/30 BG	1.25%	700	930	1.32	0.0022	0.040	0.109	18	50
RC 80/30 BP	1.0%	760	1060	1.40	0.0034	0.040	0.107	12	31
RC 80/30 BP	1.5%	800	1440	1.80	0.0030	0.040	0.168*	13	56

*Linearly extrapolated assuming the descending branch slope was constant beyond a deflection of 0.15in.

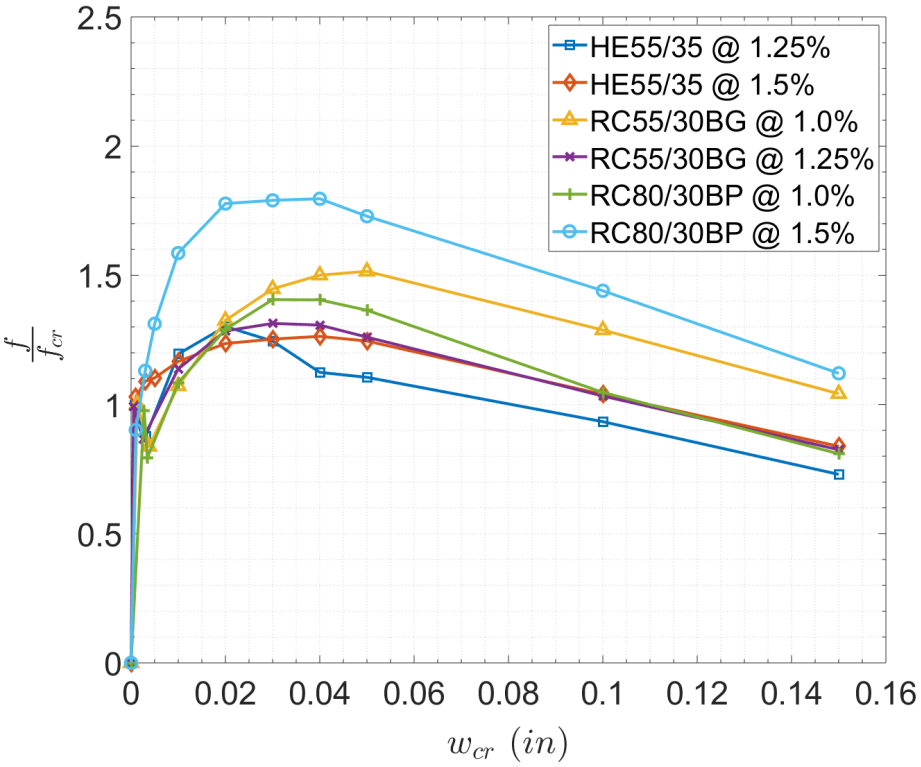

Figure 3.24: Normalized Equivalent Flexural Stress Versus Crack Opening Response of SFRC Notched Beams.

The flexural responses of all the un-notched beams tested are provided in Appendix B.2. The responses were also determined in terms of equivalent flexural stress versus mid-span deflection and versus crack opening. The average normalized un-notched beam responses of all SFRCs are presented in Figure 3.25. Each curve is the average of at least four beam samples.

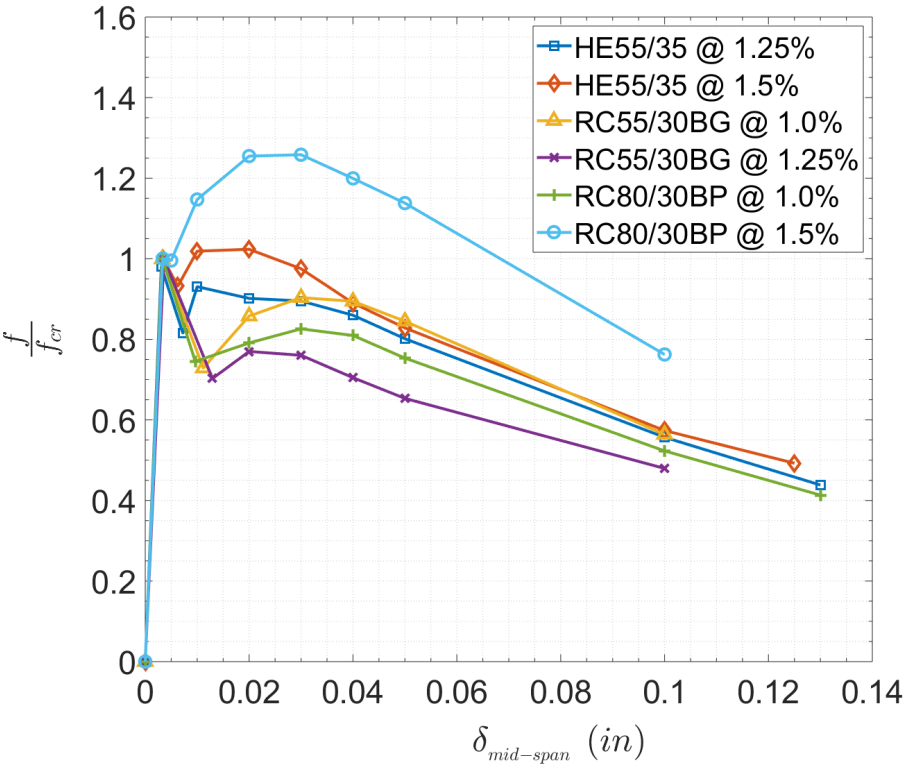

Figure 3.25: Normalized Equivalent Flexural Stress Versus Deflection Response of SFRC Un-notched Beams.

After the sudden strength drop following first cracking, SFRCs with a fiber volume fraction V_f of 1.25% and 1.0% exhibited strength recovery of approximately 80% of the first cracking strength. No deflection hardening was observed in these SFRCs. On the other hand, both SFRCs with a volume fraction of 1.5% exhibited deflection hardening behavior. Results from these tests are summarized in Table

3.5.The reported ductility (μ_{75}) was calculated as the ratio of the mid-span deflection corresponding to a strength equal to $0.75 f_{cr}$ (δ_{75}) and the deflection at first cracking (δ_{cr}). To further characterize the post-cracking behavior of the SFRCs, the mid-span deflections corresponding to the peak post-cracking strength (δ_{pc}) and to the post-cracking strength $f = 0.5 f_{cr}$ (δ_{50}) were also determined and are presented in Table 3.5. Also included in Table 3.5 is the ratio of the equivalent flexural stress at a mid-span deflection equal to $\frac{1}{150}$ of the span length, (f_{150}) to the peak post-cracking stress.

Table 3.5: Equivalent Flexural Stress-Deflection Behavior Summary for Un-notched Beams.

Fiber Type	V_f	f_{cr} (psi)	f_{pc} (psi)	$\frac{f_{pc}}{f_{cr}}$	$\frac{f_{150}}{f_{pc}}$	δ_{cr} (in.)	δ_{pc} (in.)	δ_{75} (in.)	δ_{50} (in.)	μ_{75}
HE 55/35	1.25%	890	825	0.93	0.44	0.0032	0.010	0.050	0.114	16
HE 55/35	1.5%	1100	1140	1.04	0.49	0.0034	0.020	0.065	0.122	19
RC 55/30 BG	1.0%	940	850	0.90	0.60	0.0033	0.030	0.070	0.111*	21
RC 55/30 BG	1.25%	1020	790	0.77	0.54	0.0036	0.020	0.030	0.094	8.3
RC 80/30 BP	1.0%	940	775	0.82	0.54	0.0033	0.030	0.050	0.106	15
RC 80/30 BP	1.5%	930	1170	1.26	0.49	0.0034	0.030	0.100	0.135*	29

*Linearly extrapolated assuming the descending branch slope was constant beyond a deflection of 0.15in.

The behavior of the SFRC with RC 55/30 BG fibers at a 1.0% volume fraction was slightly better than that of the SFRC with the same fiber at a 1.25% volume fraction, which was unexpected and counter-intuitive. The quantity of fibers in each beam specimen for these two SFRCs was counted and as expected, the SFRC samples reinforced at a 1.25% volume fraction had more fibers across the failure surface than the samples reinforced at a 1.0% ($\approx$ 13% more).

Recognizing that the concrete will not necessarily crack exactly at mid-span, crack opening at the bottom of the beam (see Appendix A.2 for calculation) was used to further study the flexural response of the SFRCs in the un-notched beam tests. The flexural response of the SFRC in terms of crack opening is a better probe of

the composite behavior in flexure. The average response of each of the investigated SFRCs is shown in Figure 3.26.

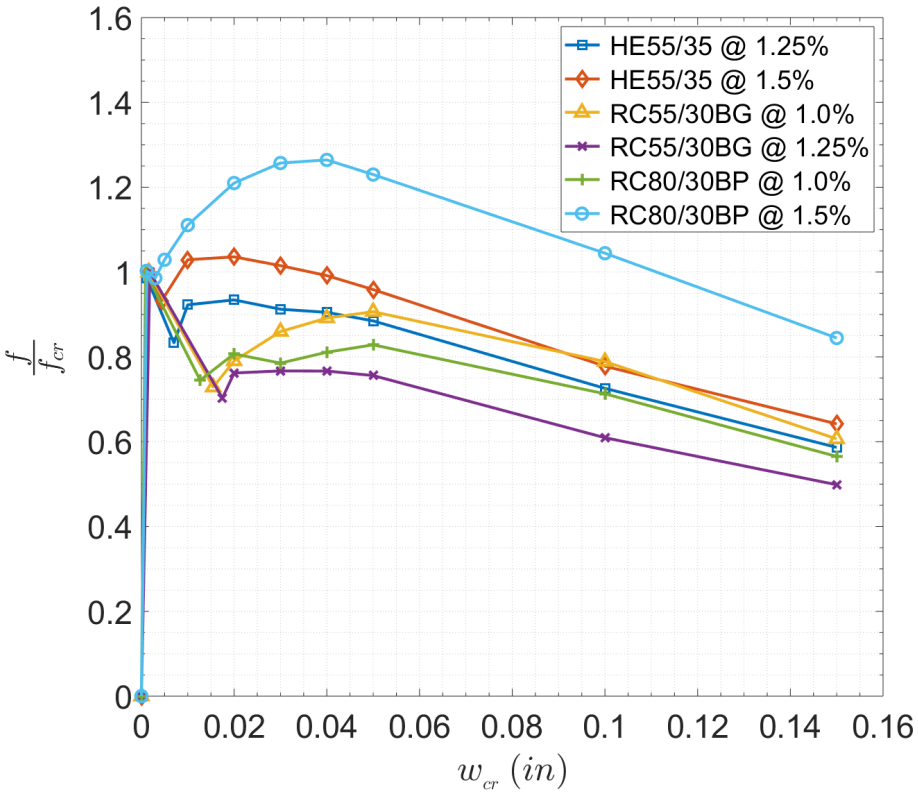

Figure 3.26: Normalized Equivalent Flexural Stress Versus Crack Width of SFRC Un-notched Beams.

Table 3.6 provides a summary of the main parameters used to describe the flexural behavior of the un-notched SFRC beams, where w_{pc}, w_{75}, and w_{50} are the crack widths corresponding to f_{pc}, $f = 0.75 f_{cr}$, and $f = 0.5 f_{cr}$, respectively.

Table 3.6: Summary of Un-notched Beam Test Results Based on Crack Widths.

Fiber Type	V_f	f_{cr} (psi)	f_{pc} (psi)	$\frac{f_{pc}}{f_{cr}}$	w_{pc} (in)	w_{75} (in)	w_{50} (in)
HE 55/35	1.25%	890	825	0.93	0.040	0.072	0.181*
HE 55/35	1.5%	1100	1140	1.04	0.020	0.110	0.202
RC 55/30 BG	1.0%	940	850	0.90	0.050	0.111	0.179
RC 55/30 BG	1.25%	1020	790	0.77	0.030	0.052	0.149
RC 80/30 BP	1.0%	940	775	0.82	0.050	0.084	0.174*
RC 80/30 BP	1.5%	930	1170	1.26	0.040	0.174*	0.236*

*Linearly extrapolated assuming the descending branch slope was constant beyond a crack opening of 0.15 in.

Comparing the behavior of the notched and un-notched SFRC beams, the following observations can be made:

- The un-notched bending tests showed that only the SFRCs with $V_f = 1.5\%$ exhibited deflection hardening behavior, whereas all the SFRCs exhibited deflection hardening in the notched beam tests.

- The flexural behavior of the SFRC with RC 80/30 BP fibers at a volume fraction of 1.5% outperformed all other SFRCs in both notched and un-notched beam tests.

- Excluding the SFRC containing RC 80/30 BP fibers at a 1.5% volume fraction, SFRCs containing HE 55/35 fibers exhibited a slightly better behavior in the un-notched beam tests than the rest of the SFRCs. However, these SFRCs were slightly outperformed at large deflections/crack widths in notched beam tests by the SFRC with RC 55/30 BG fibers at a 1.0% volume fraction. The reason for this apparent change in performance is unclear.

- In general, most of the SFRCs (excluding the SFRC reinforced with RC 80/30 BP fibers at a 1.5% volume fraction) exhibited a similar flexural behavior on each type of bending test. That is, only the SFRC reinforced with RC 80/30

BP fibers at a 1.5% volume fraction exhibited a markedly superior flexural response.

3.7.2 Direct Tensile Tests

The tensile behavior of the SFRCs considered in this study was characterized by a linear elastic region up to first cracking, at which point there was a sudden drop in strength followed by a hardening region, and ending with a softening branch. The amount of tensile hardening or softening can be proportionally described using the ratio of peak post-cracking stress (f_{pc}) to first cracking stress (f_{cr}). The SFRCs with volume fractions of 1.0% and 1.25% were able to achieve a peak post-cracking strength of at least $f_{cr}/2$, while only the specimens with RC 80/30 BP fibers at a 1.5% volume fraction exhibited a hardening response (i.e., $\frac{f_{pc}}{f_{cr}} > 1.0$). The responses of each tension sample are provided in Appendix B.3 and the average results of the SFRC tensile tests are summarized in Table 3.7, where f_{05} and f_{10} are the residual strengths at crack openings of 0.05in. and 0.10in., respectively.

Table 3.7: Summary of Tensile Test Results Summary.

Fiber Type	V_f	Coupling Beam Specimen	f_{cr} (psi)	f_{pc} (psi)	f_{05} (psi)	f_{10} (psi)	$\frac{f_{pc}}{f_{cr}}$	w_{pc} (in.)
HE 55/35	1.25%	CB1	460	205	205	150	0.44	0.029
HE 55/35	1.25%	CB2	510	300	270	220	0.59	0.030
RC 55/30 BG	1.25%	CB3	500	250	215	160	0.50	0.024
RC 55/30 BG	1.0%	CB4	550	280	235	170	0.51	0.026
RC 80/30 BP	1.0%	CB5	555	310	305	235	0.55	0.028
HE 55/35	1.5%	CB6	505	370	330	250	0.74	0.019
RC 80/30 BP	1.5%	CB7	590	645	550	350	1.09	0.023
RC 80/30 BP	1.5%	CB8	520	510	425	270	0.98	0.017

For comparison purposes, the average tensile response of all the SFRCs were normalized by $\sqrt{f'_c}$ (measured f'_c), as shown in Figure 3.27. The first cracking strength of the SFRCs ranged from 5.2–5.8$\sqrt{f'_c}$ (psi), with an average of 5.6$\sqrt{f'_c}$

(psi). Only the specimens with RC 80/30 BP fibers at a 1.5% volume fraction exhibited hardening behavior, as mentioned earlier. Note that the behavior of both SFRCs with RC 55/30 BG fibers was almost identical, which could be due to the fact that, on average, the specimens from these two SFRCs had a similar number of fibers crossing the crack surface. The fibers crossing the crack surface of the other SFRCs were not counted.

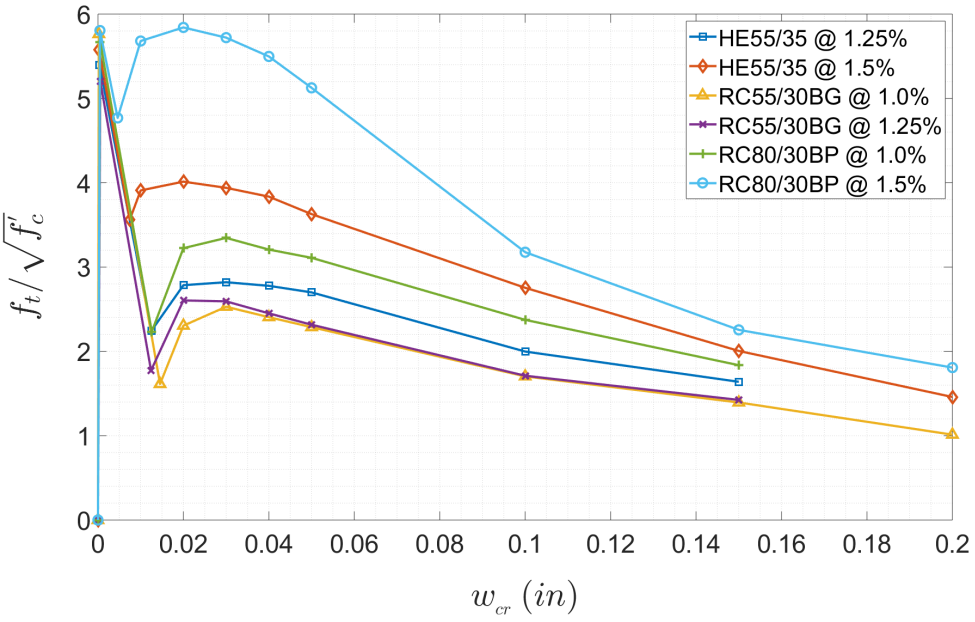

Figure 3.27: Average Tensile Response of the SFRCs Investigated.

3.7.3 Compressive Tests

The use of the Optotrak™ system allowed the measurement of deformations up to peak strength. However, in most cases, the amount of damage and cracking after reaching the peak strength caused the optical markers to fall off the cylinders, preventing accurate measurement of post peak deformations. Because of this, a hybrid response was used to describe the compressive behavior of the SFRCs. The hybrid responses were generated using the deformations calculated based on the Optotrak™ data up to peak strength, while the post peak responses were based on

the displacement data obtained from the test frame. To obtain a continuous and compatible stress-strain curve, the strains calculated from the test frame displacement data were adjusted to ensure that the strain at peak strength matched that calculated with the Optotrak™ data. Figure 3.28 illustrates how the hybrid curves were generated.

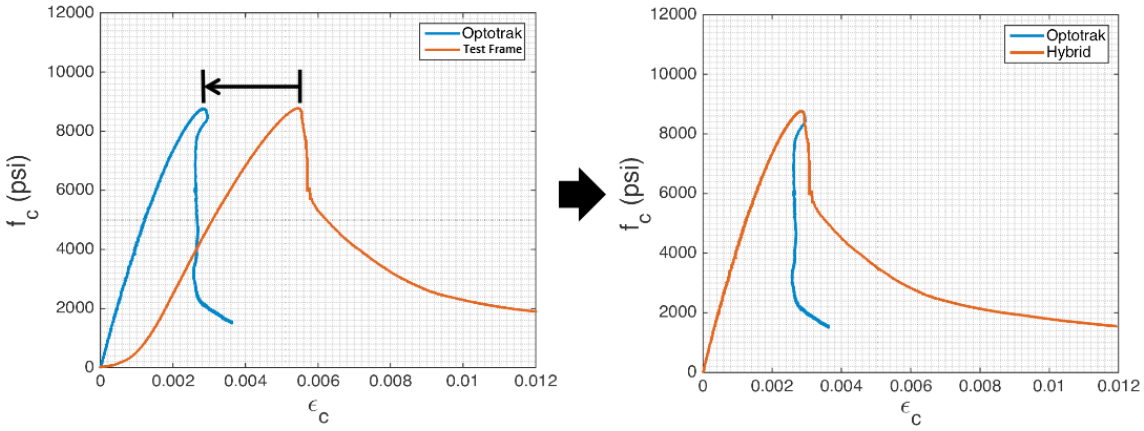

Figure 3.28: Estimation of the Post-Peak Compressive Response of SFRC Cylinders.

The stress-strain curves obtained for each cylinder were averaged to generate average response curves for each of the SFRCs. The main parameters used to describe the responses, i.e., compressive strength (f'_c), strain at peak strength (ϵ_0), and strain at a 50% strength loss (ϵ_{50}), are summarized in Table 3.8. The elastic modulus (E_c) was defined as the secant modulus of elasticity at a stress equal to $0.5f'_c$. Also reported is the slope of the descending branch of the response normalized by f'_c (Z). The slope Z was defined as the negative of the slope of a linear segment connecting the point of peak strength to the point at which the strength decreased by 50%, divided by f'_c, as shown below.

$$Z = \frac{0.5}{\epsilon_{50} - \epsilon_0} \tag{3.2}$$

Table 3.8: Average Compressive Response Parameters.

Fiber Type	V_f	Coupling Beam Specimen	f'_c (psi)	ϵ_0	ϵ_{50}	E_c (ksi)	Z
HE 55/35	1.25%	CB1	7790	0.0024	0.0042	4700	280
HE 55/35	1.25%	CB2	8690	0.0024	0.0034	5090	500
RC 55/30 BG	1.25%	CB3	8490	0.0027	0.0038	4370	455
RC 55/30 BG	1.0%	CB4	9180	0.0029	0.0039	4440	500
RC 80/30 BP	1.0%	CB5	9790	0.0029	0.0041	4240	420
HE 55/35	1.5%	CB6	8860	0.0026	0.0050	5250	210
RC 80/30 BP	1.5%	CB7	10,800	0.0029	0.0071	4820	120
RC 80/30 BP	1.5%	CB8	8510	0.0024	0.0056	4460	155

The average compressive responses of each SFRC are presented in Figure 3.29. For comparison purposes the curves shown in Figure 3.29 were normalized by their respective compressive strengths. For each type of fiber, an increase in the strain at peak strength was observed with an increase in f'_c, also, an increase in fiber volume fraction led to a larger ϵ_{50}. As expected, SFRCs with V_f =1.5% exhibited the most ductile compressive response. However, V_f had a negligible effect on the peak compressive strength and ϵ_0; the fibers are most effective in improving the ductility of the compressive response and thus, minimal influence on the response up to peak strength was expected.

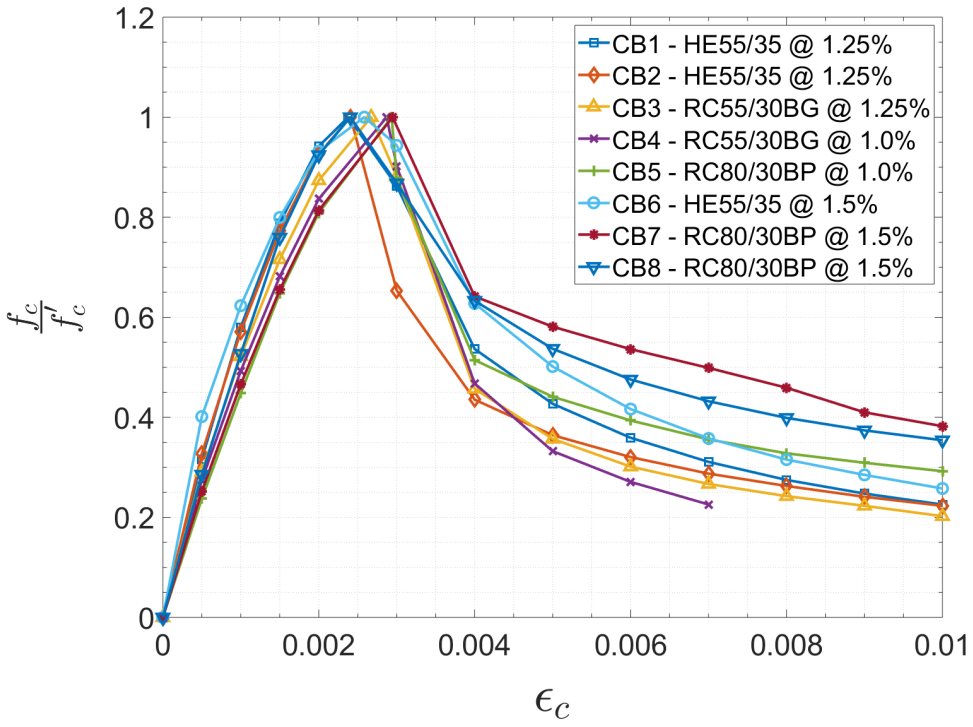

Figure 3.29: Normalized Average Compressive Stress Versus Strain Response of SFRCs Investigated.

3.7.4 Steel Reinforcement Tensile Tests

All the reinforcing bars used in this study were ASTM A615 (2016) Gr. 60 reinforcing bars. Test coupons were ordered with each set of coupling beam reinforcement to measure their actual mechanical properties. Samples from all the steel reinforcement used in the coupling beam specimens were tested in accordance with ASTM A370 (2014). Testing was load controlled at the minimum stress rate allowed of 10,000 psi/min. and the Optotrak™ system was used to monitor strains. Figure 3.30 shows the location of the markers used to monitor the deformations of the steel reinforcing bars. The strains were calculated over the central 8in. gauge length; however, whenever the coupon fractured outside the 8in. gauge length, the strains were calculated with the markers that resulted in elastic modulus in best agreement with the well-known value, $E_s = 29,000$ksi.

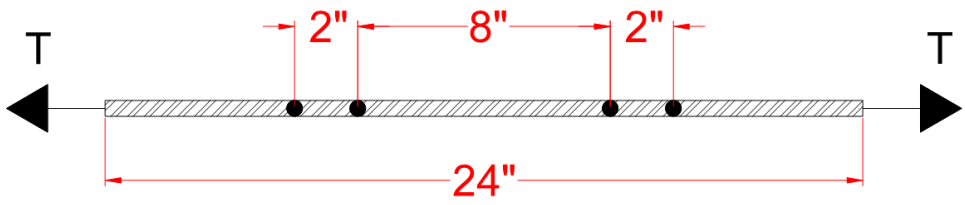

Figure 3.30: Optotrak™ Marker Layout for the Tensile Testing of Reinforcing Bars.

Sample measured stress versu strain responses of reinforcing bar coupons are shown in Figure 3.31 and Figure 3.32. Note that some of the reinforcement exhibited a clear yield plateau, while others did not. The reported yield strengths (f_y) were calculated as either the average strength in the yield plateau or using the 0.2% offset method whenever a yield plateau was not clearly defined. A summary of the mechanical properties of the reinforcement, i.e., yield strength, tensile strength (f_u), elastic modulus (E_s), strain at peak strength (ϵ_u), and strain at initiation of strain hardening (ϵ_{sh}), is provided in Table 3.9.

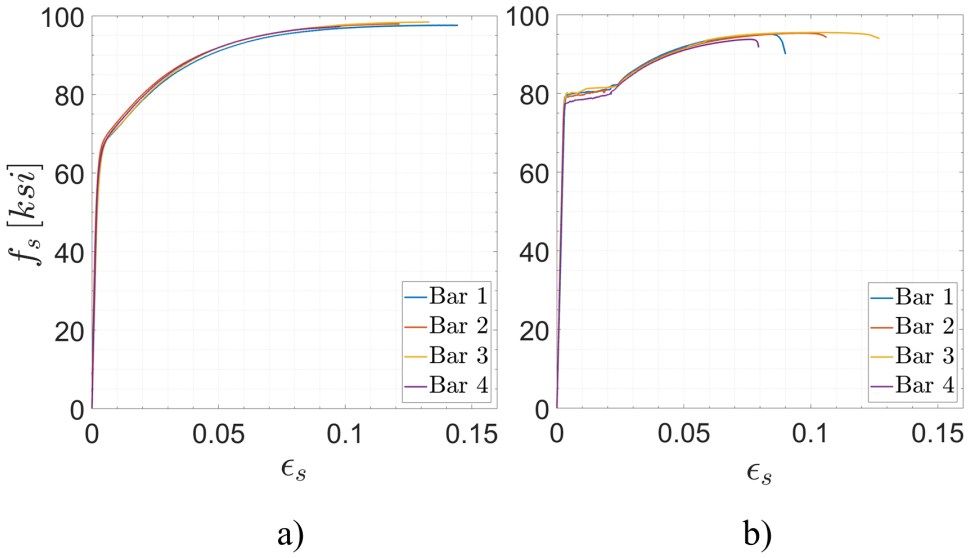

Figure 3.31: Sample Reinforcement Tensile Stress-Strain Responses. a) #3 Bars; b) #4 Bars.

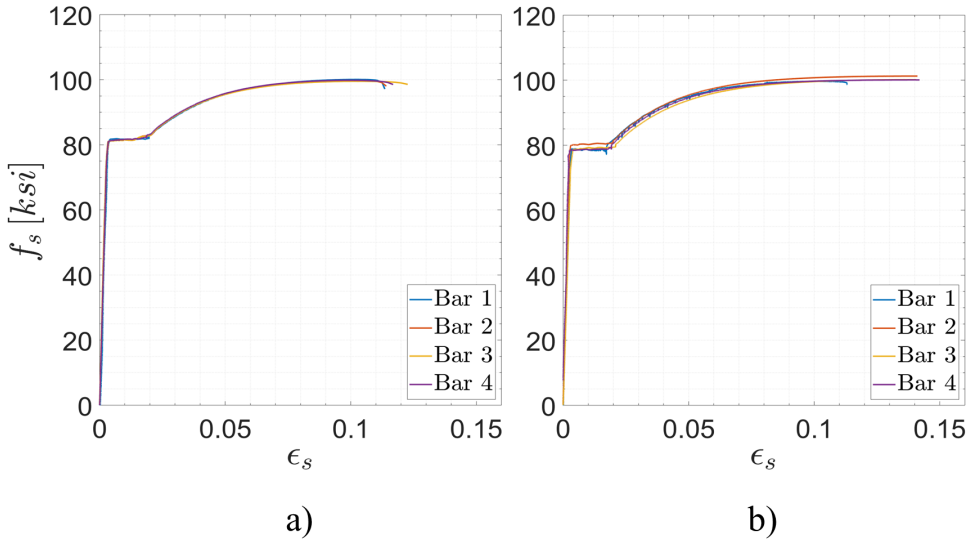

Figure 3.32: Sample Reinforcement Tensile Stress-Strain Responses. a) #5 Bars; b) #6 Bars.

Table 3.9: Measured Steel Reinforcement Properties.

Coupling Beam Specimen	Bar Size	f_y (ksi)	f_u (ksi)	E_s (ksi)	ϵ_u	ϵ_{sh}
CB1	#3	67	98	29200	0.13	**
	#4	67	102	29200	0.10	**
	#6	79	100	28900	0.14	0.020
CB2	#3	69	99	29100	0.12	**
	#4	84	99	29000	0.11	0.022
	#6	79	99	29000	0.14	0.020
CB3	#3	69	99	29100	0.12	**
	#4	84	99	29100	0.11	0.022
	#6	79	99	29000	0.14	0.020
CB4	#3	72	103	29200	0.13	**
	#4	80	95	29200	0.10	0.023
	#5	83	101	28900	0.10	0.019
CB5	#3	68	100	29000	0.10	0.016
	#4	84	101	28900	0.11	0.021
	#5	82	100	29100	0.12	0.020
CB6	#3	68	95	29100	0.13	**
	#4	74	103	28900	*	**
CB7	#3	69	99	29200	*	**
	#4	87	104	28900	0.10	0.022
CB8	#3	69	98	29100	0.16	**
	#4	70	104	29000	*	**

* Optotrak™ markers came off during testing.

** No clear yield plateau was exhibited.

4 BEHAVIOR OF SFRC TEST COUPLING BEAMS

4.1 Overall Coupling Beam Behavior

Coupling beam Specimens CB2 through CB8 exhibited a stable hysteresis response under large displacement reversals and achieved drift capacities of at least 5.0% while subjected to peak average shear stress demands (v_{max}) in the range of approximately 7 to $10\sqrt{f'_c}$ (psi). Coupling beam drift capacity, i.e., beam chord rotation capacity, was defined as the maximum drift sustained by the coupling beam prior to a 20% strength decay for each loading direction.

In general, early cracking in the coupling beams consisted of flexural cracks near the beam ends and small diagonal cracks throughout the mid-span region. As lateral displacements were further increased, diagonal cracks in the mid-span region of the beams remained narrow, while flexural cracks at the beam ends widened as reinforcement yielded near the beam ends. During large drifts cycles (typically 4.0% and greater), significant damage could be observed at the beam ends. This damage was characterized by concrete crushing and spalling, and the coalescing of flexural cracks corresponding to both loading directions. The coalescence of flexural cracks and severely damaged concrete led to the formation of through-depth cracks near the beam ends. Ultimately, significant shear sliding developed along the through-depth cracks, resulting in a substantial loss of lateral stiffness, strength.

In contrast, Specimen CB1 suffered a premature shear failure. The amount of longitudinal reinforcement in Specimen CB1 was greater than that provided in all other specimens, which translated into a higher shear stress demands of approximately $12.2\sqrt{f'_c}$ (psi) and a significantly lower deformation capacity of approximately 3.3% drift.

Coupling beam Specimens CB1 through CB5 and CB6 through CB8 had span-to-depth ratios of 3.0 and 2.0, respectively. Table 4.1 presents a summary of the coupling beam peak responses, including peak shear stress demand (v_{max}), peak axial load (P_{max}), and maximum drift prior to a strength decay of 20% and 30% based on the peak shear strength corresponding to each loading direction (positive and negative loading directions corresponded to the actuator pulling and pushing on the specimens, respectively). Also included in Table 4.1 is the concrete cylinder compressive strength at the day of each test (f'_c). The behavior and damage observed during the test of each coupling beam specimen is discussed in the following sections.

Table 4.1: Summary of Coupling Beam Peak Responses.

Specimen	f'_c (psi)	V_{max} (kips)	v_{max} (psi)	$v_{max}/\sqrt{f'_c}$	P_{max} (kips)	$P_{max}/(A_g f'_c)$	Drift Capacity			
							20% Strength Loss		30% Strength Loss	
							Positive	Negative	Positive	Negative
CB1	7930	117	1080	12.2	89.0	10.4%	3.3%	3.5%	3.3%	3.5%
CB2	8840	100	930	9.8	144	15.0%	5.3%	5.6%	5.6%	7.5%
CB3	8630	94.6	880	9.5	116	12.5%	5.3%	8.3%	5.3%	8.3%
CB4	9260	75.0	690	7.2	98.6	9.9%	5.1%	6.5%	6.0%	6.5%
CB5	9750	82.9	770	7.8/6.6**	91.1	8.6%	6.2%*	6.3%*	7.1%*	6.3%*
CB6	7950	78.2	720	8.1/7.3**	73.6	8.6%	5.1%*	6.2%*	6.0%*	6.2%*
CB7	9330	106	970	10.1	125	12.4%	5.0%	5.5%	5.0%	5.5%
CB8	8490	81.9	760	8.2	89.9	9.8%	6.2%	6.2%	8.4%	7.3%

* Drift capacity calculated based on peak shear stress after adjustment of axial force

** Peak shear stress after adjustment of axial force

4.1.1 Coupling Beam Specimen CB1

Coupling Beam CB1, reinforced with HE 55/35 fibers at a volume fraction of 1.25%, was subjected to a peak shear stress of 12.2 $\sqrt{f'_c}$ (psi). The calculated shear contribution of the transverse reinforcement in the mid-span region of the beam was 6.2$\sqrt{f'_c}$ (psi), assuming a longitudinal projection of a diagonal crack equal to the distance from the extreme compressive fiber to the extreme layer of tension longitudinal reinforcement and using the measured yield strength of the steel reinforcement (67 ksi, see Section 3.7.4). The shear stress demand on the SFRC therefore exceeded the maximum shear strength contribution of 5$\sqrt{f'_c}$ (psi) recommended by Lequesne (2011). The large shear demand in Specimen CB1 resulted in a rapid degradation of shear resisting mechanisms and, ultimately, in a premature shear failure, as shown in Figure 4.1.

Figure 4.1: Shear Failure of Specimen CB1.

The shear stress versus drift response for Specimen CB1 is presented in Figure 4.2. The applied shear stress (v) was calculated based on the gross cross-sectional area (A_g) and normalized by $\sqrt{f'_c}$ (psi). Drifts were adjusted to account for relative rotations between the top and bottom blocks using Equation A.1 in Appendix A.

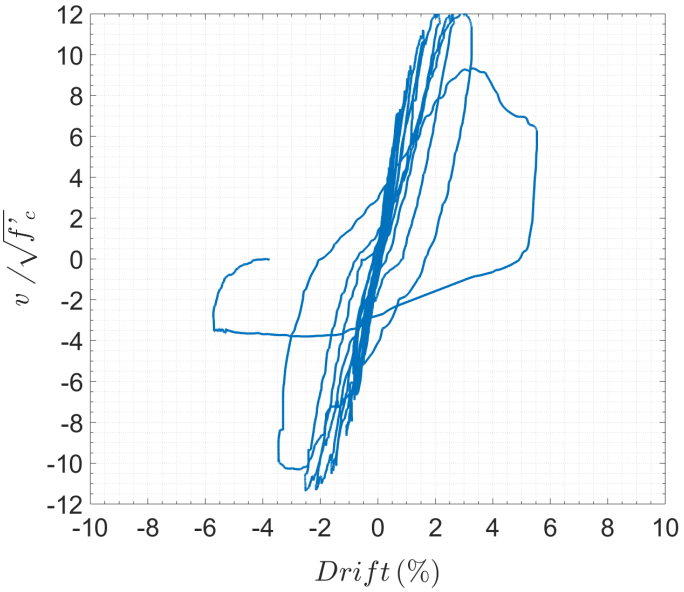

Figure 4.2: Hysteresis Response of Specimen CB1.

Cracking on Specimen CB1 started mainly as diagonal cracking throughout the mid-span region, along with some flexural cracks near the beam ends. As the applied lateral displacement increased, extensive diagonal cracking developed throughout the beam length. However, these cracks remained narrow ($\leqslant$ 0.02 in.) with minimal damage around the beam ends and beam-to-wall interface during displacement cycles of up to 3.0% drift. Figure 4.3 shows the crack pattern observed at 1.0%, 2.0% and 3.0% drift. As the beam was displaced to 4.0% drift, the coupling beam suffered a sudden strength loss caused by the shear failure of the mid-span region of the beam. This failure was characterized by severe beam dilation, widening of diagonal cracks, and the development of a splitting crack along the main longitudinal reinforcement near the top end of the beam (right end on Figure 4.1).

The maximum axial force developed in the beam, caused by beam elongation due to concrete cracking and the accumulation of plastic strains in the longitudinal reinforcement as the beam underwent displacement cycles, was 89.0 kips. This axial force corresponded to an average axial compressive stress of approximately

$0.10f'_c$, based on the beam gross cross-sectional area (A_g), and to 76% of the peak applied shear (V_{max}). Prior to failure, Specimen CB1 achieved a maximum axial elongation of 0.10 in., which corresponded to an average longitudinal tensile strain of approximately 0.2%.

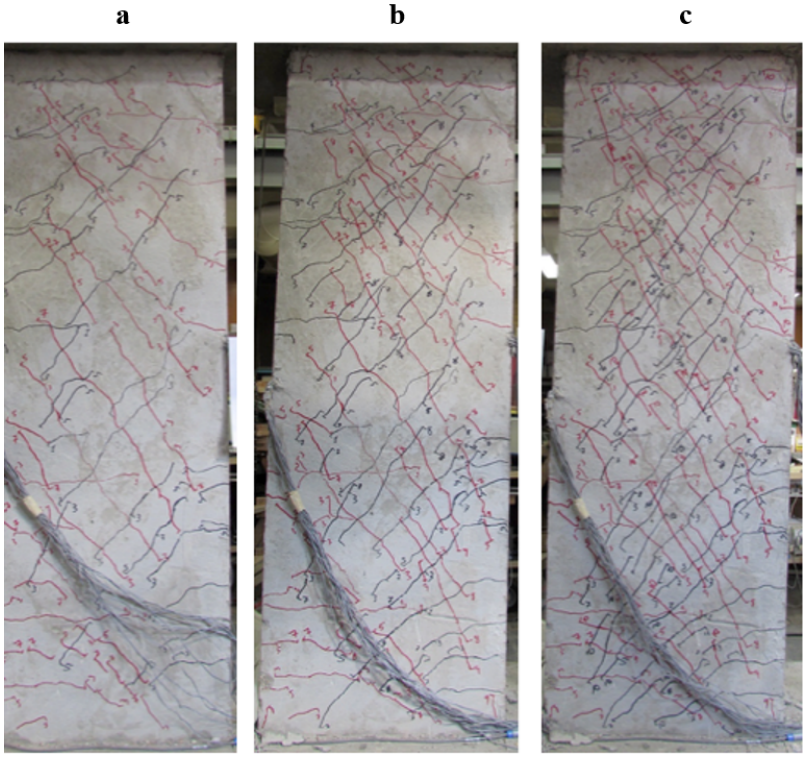

Figure 4.3: Damage Progression in Specimen CB1. a) 1.0% Drift; b) 2.0% Drift; c) 3.0% Drift.

4.1.2 Coupling Beam Specimen CB2

Coupling Beam CB2 was also reinforced with HE 55/35 fibers at a volume fraction of 1.25%. This beam exhibited relatively wide hysteresis loops throughout displacement cycles up to approximately 5.0% drift (Figure 4.4), which is indicative of a stable, flexurally-dominated response with good energy dissipation. This specimen was subjected to a peak shear stress close to the maximum limit allowed in ACI 318-19 of $10\sqrt{f'_c}$ (psi); however, the peak drift in the positive direction was limited by the test setup.

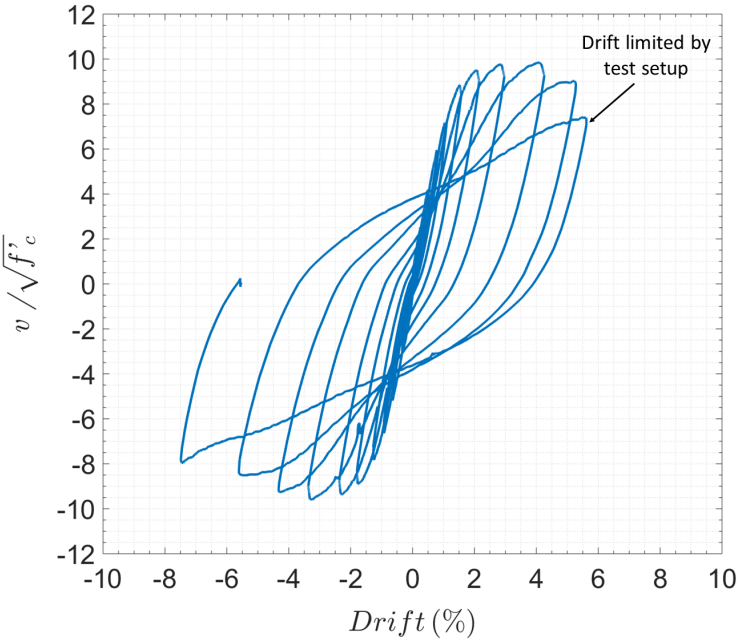

Figure 4.4: Hysteresis Response of Specimen CB2.

Specimen CB2 developed the highest axial load (144 kips) among the coupling beam specimens tested, which corresponded to an average compressive stress of $0.15f'_c$ based on A_g and approximately $1.4V_{max}$. The peak elongation was approximately 0.28 in., corresponding to an average axial strain of approximately 0.5%. The beam achieved a peak shear strength of $9.8\sqrt{f'_c}$ at approximately 2.8% drift in

the positive loading direction. The peak shear force in subsequent drift cycles up to 5.0% drift (inclusive) was greater than 90% of V_{max}.

Flexural cracks in Specimen CB2 were observed at the ends of the beam during small displacements cycles ($<$ 1.0% drift). Despite the presence of diagonal cracks in the mid-span region of the beam, flexural cracks were predominant. Cracking continued to spread throughout the beam up to approximately 2.0% drift, after which only a few new cracks formed. As the displacement demands were further increased, cracking and damage concentrated at the beam ends, primarily near the section where the U-shaped dowels were terminated. During drifts cycles greater than approximately 4.0%, significant damage concentrated at the beam ends. Once flexural cracks corresponding to the two loading directions coalesced to form a through-depth crack, shear sliding displacements became evident (during 4.0% and 5.0% drift cycles). The condition of Specimen CB2 at approximately 2.0%, 4.0% and 5.5% drift is shown in Figure 4.5.

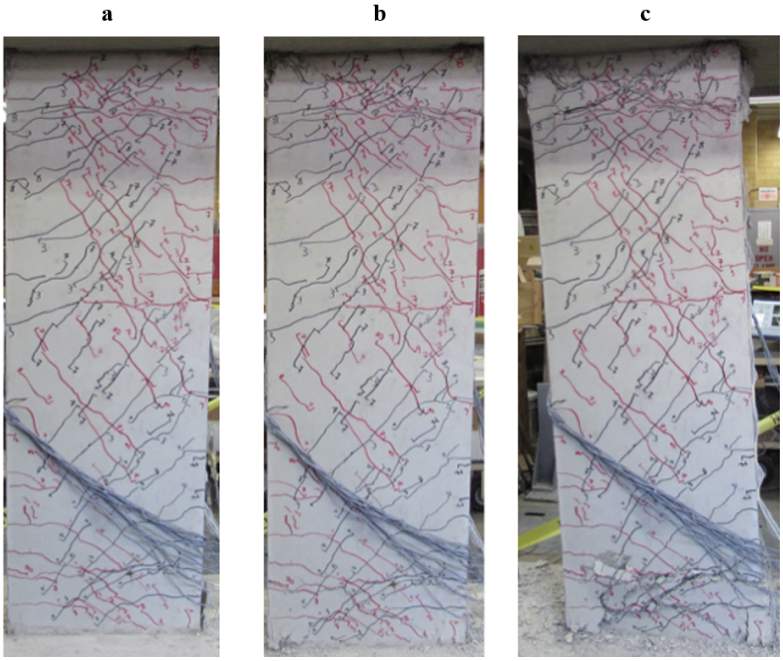

Figure 4.5: Damage Progression in Specimen CB2. a) 2.0% Drift; b) 4.0% Drift; c) $\approx$-5.5% Drift.

4.1.3 Coupling Beam Specimen CB3

The behavior of Specimen CB3 was very similar to that of Specimen CB2. However, Specimen CB3 was reinforced with RC 55/30 BG fibers (instead of HE 55/35 fibers) at a volume fraction of 1.25%. The beam underwent drifts of approximately 5.3% and 5.6% in the positive and negative loading directions, respectively, while maintaining at least 80% of its peak shear strength ($9.5\sqrt{f'_c}$, psi). Moreover, the peak shear demand occurred at approximately 4.0% drift. Overall, Specimen CB3 exhibited a stable hysteresis, characterized by relatively wide loops, as shown in Figure 4.6. The specimen developed a maximum axial compressive force of 116 kips, which corresponded to a stress of approximately $0.12\,f'_c$ based on A_g.

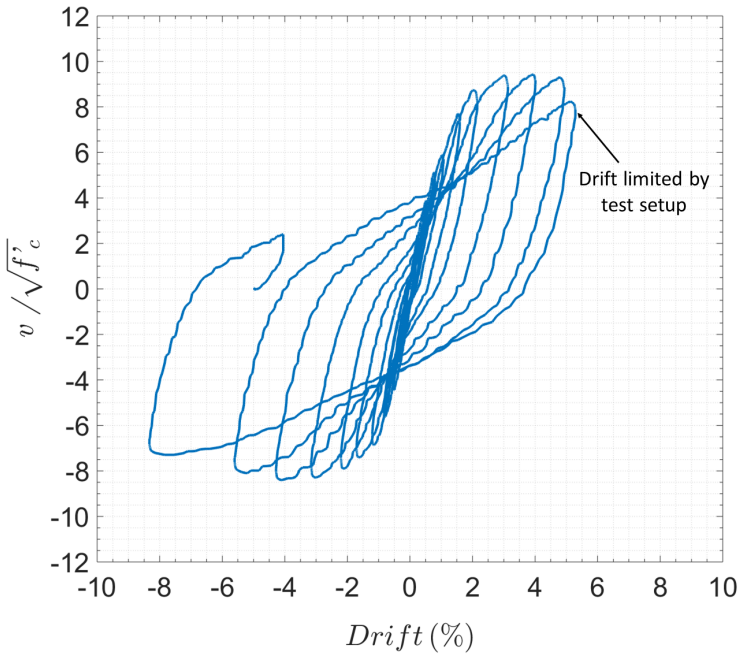

Figure 4.6: Hysteresis Response of Specimen CB3.

The initial displacement cycles (up to 1.0% drift) were characterized by the formation of flexural cracks near the beam ends and some diagonal cracks throughout the mid-span region. Flexural and shear cracks continued to form throughout the beam up to approximately 2.0% drift. As the applied displacement increased, the cracks near the ends grew wider and at 4.0% drift, considerable damage had accumulated near the beam ends. Figure 4.7 shows the damage sustained by Specimen CB3 at approximately 2.0%, 4.0% and 5.6% drift. As can be seen in Figure 4.7c, towards the end of the test, wide through-depth flexural cracks had formed, allowing significant shear sliding displacements and ultimately leading to failure.

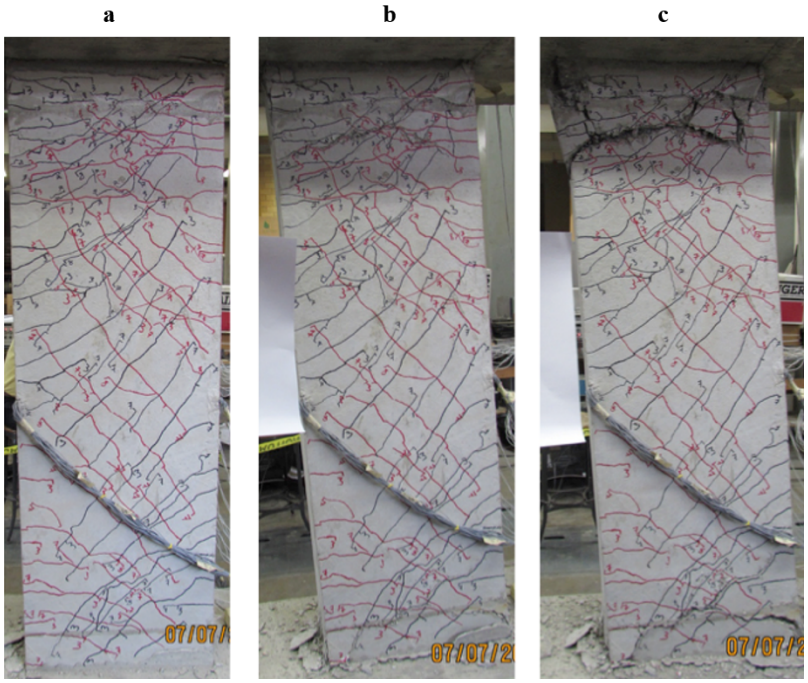

Figure 4.7: Damage Progression in Specimen CB3. a) -2.0% Drift; b) -4.0% Drift; c) -5.6% Drift.

4.1.4 Coupling Beam Specimen CB4

Specimen CB4 was the first beam constructed using an SFRC with a volume fraction of 1.0% (RC 55/30 BG fibers were used). Due to the expected lower performance of this SFRC, Specimen CB4 was designed for a lower shear stress demand (6-8$\sqrt{f'_c}$, psi) compared to Specimens CB2 and CB3 (8-10$\sqrt{f'_c}$, psi). The peak shear stress demand was 7.2$\sqrt{f'_c}$ (psi), which was achieved at approximately 3.2% drift in the positive direction (see hysteresis in Figure 4.8). Despite some strength decay during subsequent drift cycles, Specimen CB4 sustained at least 80% of its peak strength up to 5.1% and 5.2% drift in the positive and negative loading directions, respectively. Specimen CB4 elongated a maximum of approximately 0.27 in. This elongation corresponded to an average axial strain of approximately 0.5% and resulted in a peak axial compression of 99 kips (1.32 V_{max}), which corresponded to an average axial compressive stress of approximately 0.10 f'_c based on the beam gross cross-sectional area.

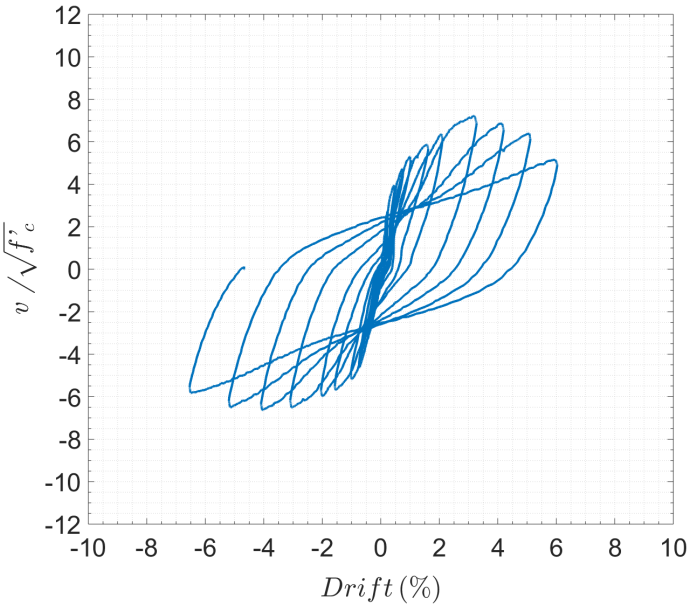

Figure 4.8: Hysteresis Response of Specimen CB4.

Flexural cracks formed near the beam ends during the early displacement cycles and cracking continued to spread throughout the beam, similarly to what was observed in previous specimens. However, cracking was not as dense as the cracking pattern exhibited by previous specimens with steel fibers at a 1.25% volume fraction. A large flexural crack (0.1 in. wide) was noted at approximately 1.5% drift near the top end of the beam. This crack continued to widen as the applied displacement was further increased, achieving a width of approximately $\frac{5}{16}$ in. as the beam was displaced to 3.0% drift. The cracking pattern observed, as well as the damage at later stages of the test, are shown in Figure 4.9. During the last cycles, extensive damage accumulated at both beam ends, as shown in Figure 4.10a and b, mostly localized along a single through-depth crack at each end.

After the test, the loosened and damaged concrete within the plastic hinges was removed to observe the extent of damage sustained. Figure 4.10c shows the significant amount of concrete that could be removed, which extended into the confined core. Note, however, that Specimen CB4 was subjected to large shear stress demands through cycles up to approximately 6.0% drift. Despite the high demands and the use of RC 55/30 BG fibers at a volume fraction of 1.0%, Specimen CB4 exhibited stable hysteresis up to at least 5.0% drift.

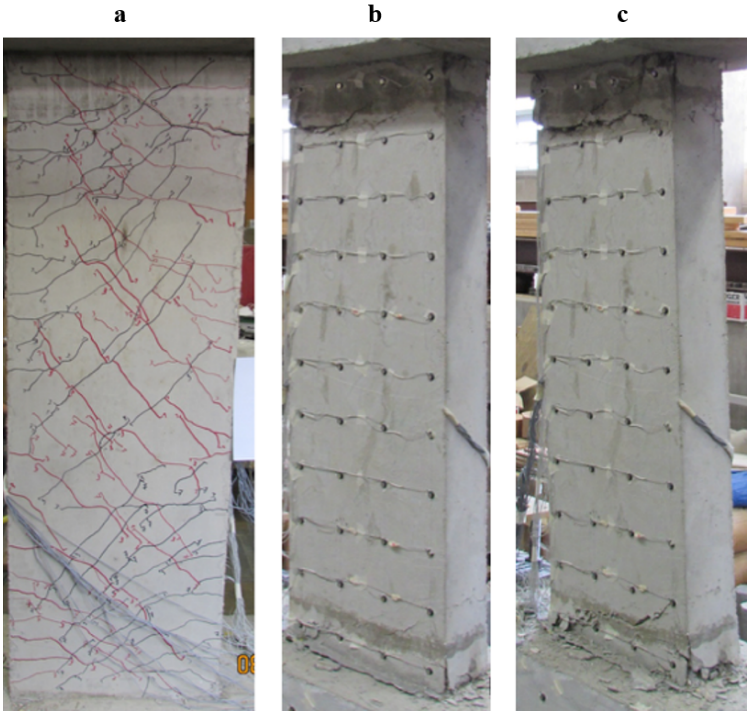

Figure 4.9: Damage Progression in Specimen CB4. a) 2.0% Drift; b) 4.1% Drift; c) 6.0% Drift.

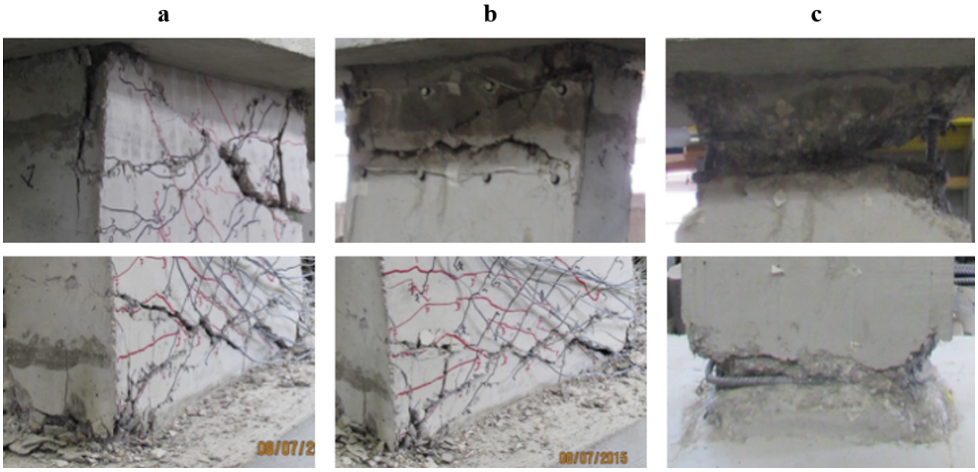

Figure 4.10: Ends of Specimen CB4. a) 6.0% Drift; b) -6.5% Drift; c) After Removal of Spalled Concrete.

4.1.5 Coupling Beam Specimen CB5

Specimen CB5 was the second specimen constructed using an SFRC with fibers at a 1.0% volume fraction. The fibers used were RC 80/30 BP fibers with a specified tensile strength of 330 ksi. The behavior of Specimen CB5 was characterized by a stable hysteresis response with a displacement capacity exceeding 6.0% drift, as shown in Figure 4.11.

A peak strength of $7.8\sqrt{f'_c}$ was achieved at a drift of approximately 3.1% in the positive displacement direction. At this point the axial force developed was 91 kips, which corresponded to a compressive stress of approximately $0.09\,f'_c$ based on the beam gross cross-sectional area. At this stage, the bolts connecting the steel links providing the axial restraint were loosened to avoid the development of larger axial compression and consequently, larger flexural strength and corresponding shear stress demands. The intent was to avoid significantly exceeding the target shear demand of $8\sqrt{f'_c}$ (psi). A similar peak axial compression was developed in later cycles as the beam continued to elongate (approximately 88 kips or $1.06v_{max}$) and the maximum elongation was approximately 0.38 in. (average axial strain of approximately 0.7%).

After the axial restraint was adjusted, the highest shear stress achieved was $6.6\sqrt{f'_c}$ (psi) at approximately 5.1% drift. The decrease in shear stress was due to the reduction in axial force and not to damage sustained by the specimen. Specimen CB5 exhibited drift capacities of approximately 6.2% and 6.3% in the positive and negative direction, respectively. These drift capacities were taken as the maximum drift achieved before a 20% strength loss relative to the peak strength after adjustment of the axial restraint.

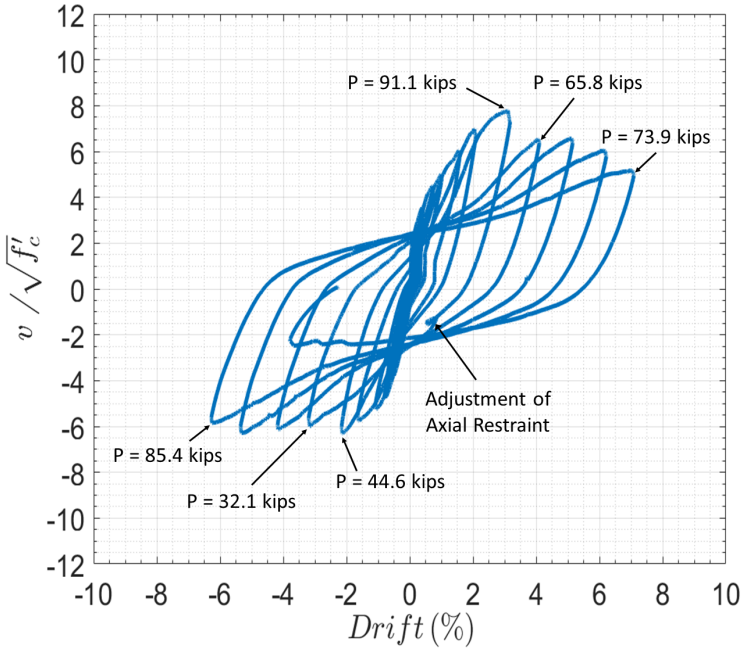

Figure 4.11: Hysteresis Response of Specimen CB5 (P = Axial Force).

During the early displacement cycles, flexural cracks formed near the beam ends and diagonal cracks formed throughout the mid-span region. New cracks continued to form throughout the beam up to drifts of approximately 2.0% (Figure 4.12a). In general, the cracking pattern was very similar to that of Specimen CB4. However, the crack widths remained much smaller ($\leqslant$ 0.08 in.) in Specimen CB5 up to drifts of approximately 3.0% in the positive direction. The use of RC 80/30 BP fibers thus led to better crack width control compared with the RC 55/30 BG fibers. Appreciable widening of flexural cracks began during drifts cycles exceeding 2.0%. During the 4.0% drift cycle, flexural cracks corresponding to both loading directions coalesced, forming a through-depth crack near the bottom support (Figure 4.12b). As the applied lateral displacements were further increased, damage continued to concentrate near the beam ends, leading to the formation of a through-depth crack at the top end of the beam, as shown in Figure 4.12c. A close-up of the through-depth cracks is provided in Figure 4.13a.

Failure of Specimen CB5 was due to the fracture of several main longitudinal reinforcing bars as the beam was displaced to a drift of approximately 7.0%. After termination of the test, the crushed concrete around the plastic hinges was removed to expose the fractured bars (marked red in Figures 4.13b and c).

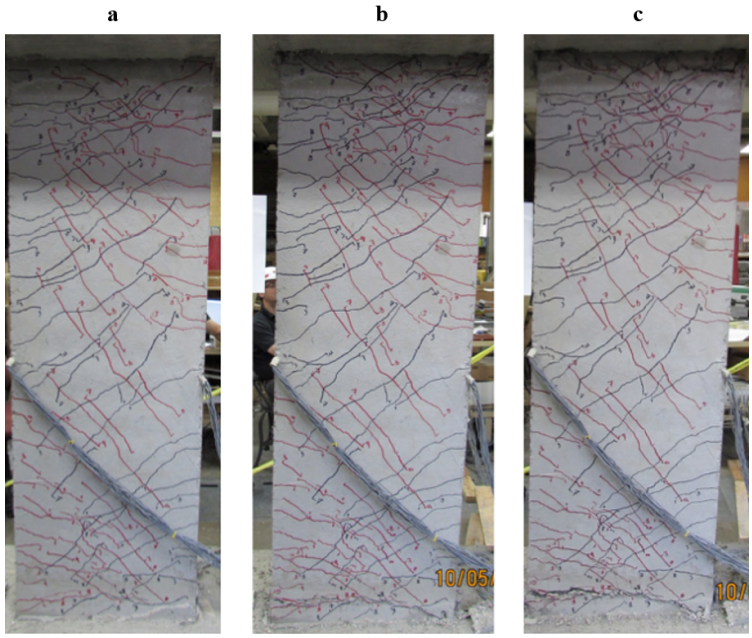

Figure 4.12: Damage Progression in Specimen CB5. a) 2.0% Drift; b) 4.0% Drift; c) 6.2% Drift.

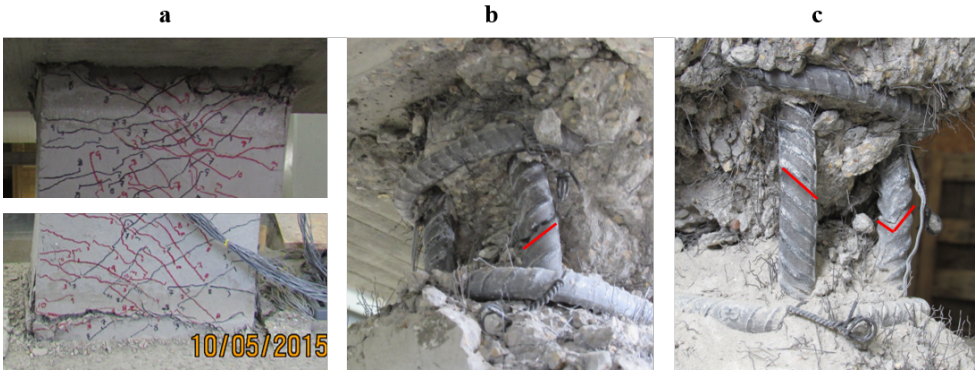

Figure 4.13: Damage after test - Specimen CB5. a) Through-Depth Cracks at Top and Bottom Plastic Hinges; b) Fractured Flexural Reinforcement (Top Plastic Hinge); c) Fractured Flexural Reinforcement (Bottom Plastic Hinge).

4.1.6 Coupling Beam Specimen CB6

Specimen CB6 was the first coupling beam tested with a span-to-depth ratio of 2.0. Given the increased role played by shear in deep members, Specimen CB6 was reinforced with a higher fiber volume fraction (1.5%) than any of the preceding specimens (i.e., Specimens CB1 trough CB5). The fibers used in Specimen CB6 were HE 55/35 fibers, having the second highest tensile strength and fiber aspect ratio among the investigated fibers.

Specimen CB6 exhibited a stable hysteresis with minor pinching and a large deformation capacity of approximately 5.1 and 6.2% drift in the positive and negative loading directions, respectively. This drift capacity was calculated based on the peak shear after adjustment of axial restraint [$7.3\sqrt{f'_c}$ (psi)]. The shear versus drift response of Specimen CB6 is shown in Figure 4.14. It should be mentioned that Specimen CB6 exhibited a slower development of axial load compared to the other specimens, which is attributed to a looser connection of the steel links and thus, reduced axial restraint. After the beam developed a shear stress exceeding $8\sqrt{f'_c}$ (psi) at a drift of approximately 3.6% in the negative direction, the links providing axial restraint were loosened. The peak axial load developed up to this point was 73.6 kips, corresponding to an average compressive stress of approximately 0.09

f'_c based on A_g. After the adjustment of the steel links, the maximum shear stress sustained by the beam was $7.3\sqrt{f'_c}$ (psi) at a drift of approximately 4.0%. Furthermore, the maximum axial force devolved after the links were loosened was 70 kips ($0.9V_{max}$) and the maximum elongation of the beam throughout the test was 0.33 in. (average axial strain of approximately 0.9%).

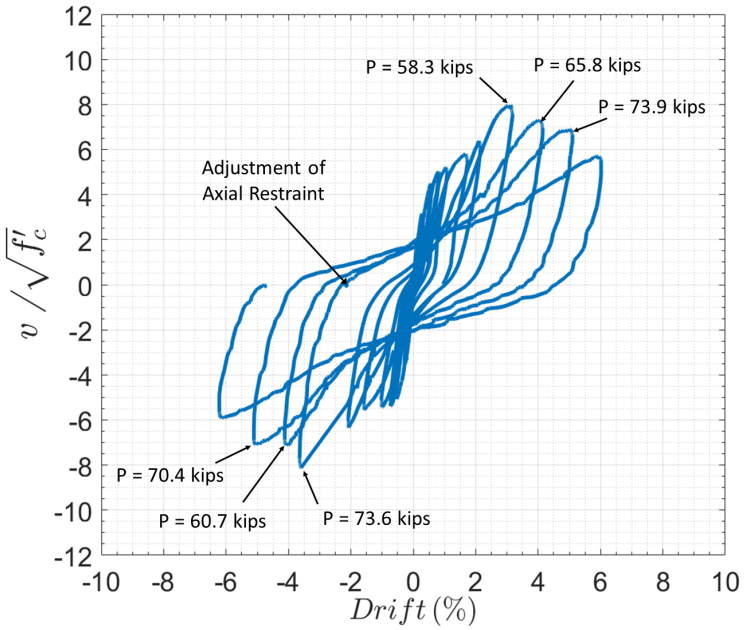

Figure 4.14: Hysteresis Response of Specimen CB6 (P = Axial Force).

During the initial displacement cycles several flexural cracks formed near the ends of the beam and some diagonal shear cracks near the mid-span region, as shown in Figure 4.15. Cracking was not as dense as in the specimens with span-to-depth ratio of 3.0. As the displacement demand was increased beyond 2.0% drift, cracking concentrated at the ends of the beam and significantly more damage occurred at the beam-to-wall interfaces compared to the more slender specimens. By the time a drift of approximately 4.0% was achieved, a large flexural crack had formed near the top end of the beam and the flexural cracks near the bottom support were starting to coalesce into a through-depth crack (see Figure 4.15b). As the

applied displacements were further increased, deformations continued to localize at the ends, leading to significant widening of the cracks and enabling shear sliding displacements.

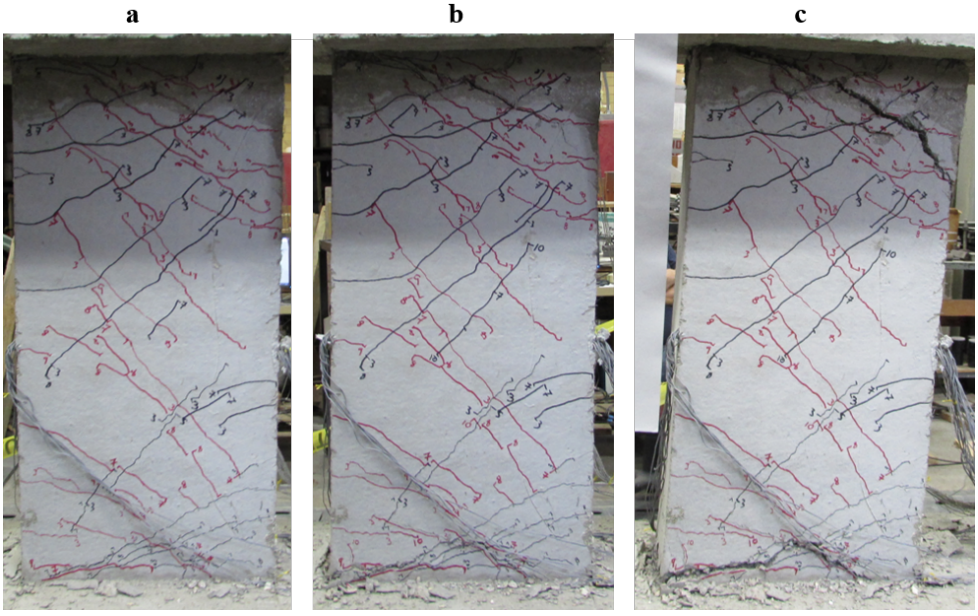

Figure 4.15: Damage Progression in Specimen CB6. a) 2.1% Drift; b) 4.1% Drift; c) 6.0% Drift.

4.1.7 Coupling Beam Specimen CB7

Similarly to Specimen CB6, an SFRC with a 1.5% fiber volume fraction was used in Specimen CB7. However, RC 80/30 BP fibers were used instead of HE55/35 fibers. Despite the large shear stress demand $(10.1\sqrt{f'_c}$, psi), Specimen CB7 had a stable hysteresis up to about 4.0% drift, as shown in Figure 4.16. Specimen CB7 developed the second highest axial load among the tested coupling beams (125 kips), which corresponded to an average compressive stress of approximately $0.12\,f'_c$ based on A_g; see Table 4.1. This beam underwent a maximum elongation of approximately 0.31 in., which corresponded to an average axial strain of approximately 0.9%.

The presence of the large axial compression substantially increased the beam

flexural strength, resulting in shear stress demands higher than intended. The beam suffered rapid strength loss as the displacements were increased beyond 4.0% drift (drift corresponding to the peak shear demand of $10.1\sqrt{f'_c}$, psi). This rapid loss of strength for drifts exceeding 4.0% can be observed in the hysteresis response shown in Figure 4.16. The combination of high shear stresses and displacement reversals led to significant sliding at the beam-wall interfaces, concentration of damage near the dowel cut-off sections, and a sliding shear failure at the dowel cut-off section during the cycle following the 5.0% drift cycle. Despite the high shear demands, Specimen CB7 achieved drifts of approximately 5.0% and 5.5% in the positive and negative direction, respectively, while retaining at least 80% of its peak strength in each direction.

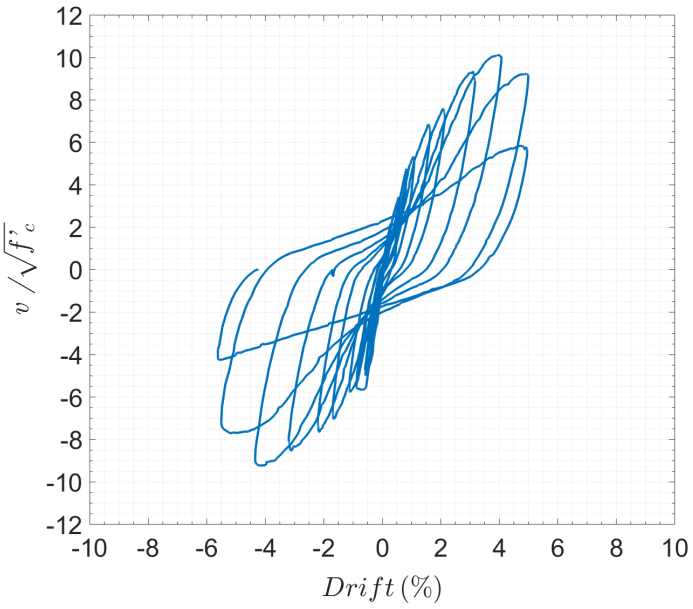

Figure 4.16: Hysteresis Response for Specimen CB7.

In terms of cracking progress, several flexural cracks formed near the ends of Specimen CB7 during the initial displacement cycles. The formation of diagonal cracks throughout the mid-span region of the beam was more pronounced than what was observed for Specimen CB6. Cracking continued to spread throughout

the beam up to approximately 2.0% drift. At this point, the deformations began localizing near the beam ends and at the bottom beam-to-wall interface. Moreover, a 0.04 in. wide flexural crack near the top end of the beam became noticeable. As the displacement demand was increased to approximately 5.0% drift, the flexural crack that formed near the top propagated (see Figure 4.17b) and several flexural cracks coalesced near the bottom end to form horizontal through-depth cracks. Shear sliding became significant as the beam was displaced to -5.6% drift. At this stage the beam had already lost more than 20% of its peak strength.

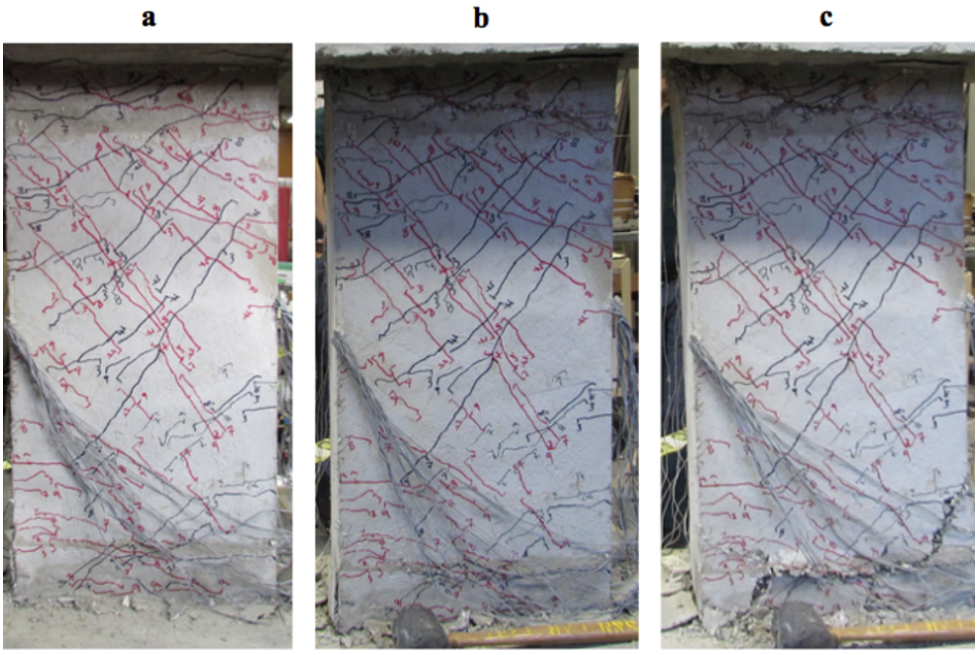

Figure 4.17: Damage Progression in Specimen CB7. a) -2.2% Drift; b) 5.0% Drift; c) Sliding Shear Failure at -5.7% Drift.

4.1.8 Coupling Beam Specimen CB8

Specimen CB8 was nominally identical to Specimen CB7. However, axial restraint was adjusted such as to limit the maximum shear stress to $8\sqrt{f'_c}$ (psi). Specimen CB8 exhibited a stable hysteresis with drift capacity exceeding 6% while being subjected to a peak shear stress of $8.2\sqrt{f'_c}$ (psi), as shown in Figure 4.18. The beam reached its peak strength at a drift of approximately 5.1%. Note that unlike the rest of the specimens, Specimen CB8 was loaded towards the negative displacement direction first. Upon reaching a 1.5% drift in the positive direction, the beam developed a peak shear stress of $7.2\sqrt{f'_c}$ (psi). To keep the shear stresses close to the target shear demand ($8\sqrt{f'_c}$, psi), the bolts connecting the steel links providing axial restraint were loosened prior to applying the 2.0% drift cycle. The adjustment led to a shear reduction during the following drift cycle. The peak axial compression developed in the beam was 89.9 kips ($1.1V_{max}$), which corresponded to an average compressive stress of approximately $0.10f'_c$ based on A_g. The beam elongated a maximum of approximately 0.27 in. (i.e., an average axial strain of approximately 0.8%). Specimen CB8 exhibited a large deformation capacity (approximately 6.2% drift) while maintaining approximately 90% of its peak strength. Moreover, Specimen CB8 sustained a shear stress of at least $6\sqrt{f'_c}$ (psi) while displaced to approximately 7.0% and 8.0% drift in the negative and positive loading directions, respectively.

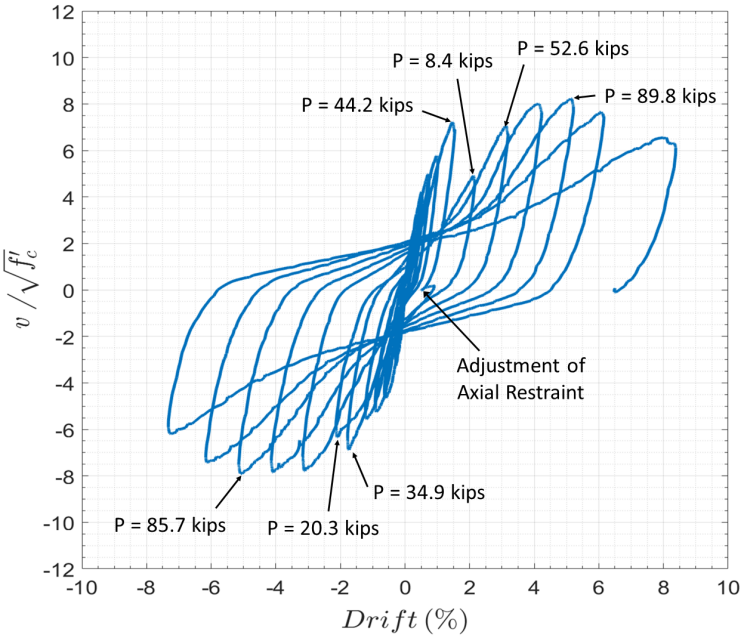

Figure 4.18: Hysteresis Response for Specimen CB8 (P = Axial Force).

Multiple flexural and diagonal cracks formed during the initial cycles of the test. Cracking mostly continued to spread throughout the beam up to a drift of approximately 2.0%. After this, the damage began localizing at the beam ends. At a drift of approximately -2.0%, considerable rotations occurred at both beam-to-wall interfaces, as shown in Figure 4.19a. As the displacements were further increased, the cracks near the ends widened, achieving widths of up to 3/16 in. at a drift of approximately 4.2%. Figure 4.19b shows the accumulated damage at the beam ends at approximately 5.1% drift. The damage progression in Specimen CB8 is shown in Figure 4.20.

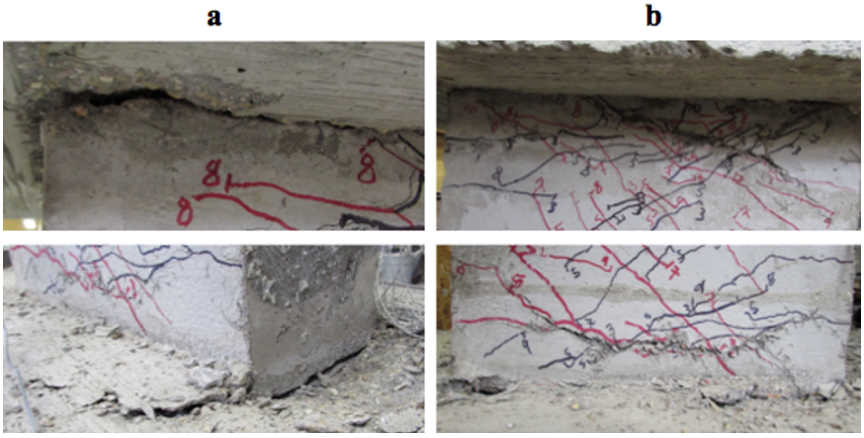

Figure 4.19: Ends of Coupling Beam CB8. a) Top and Bottom Beam-to-Wall Interfaces (-2.1% drift); b) Damage at Top and Bottom Ends (5.1% Drift).

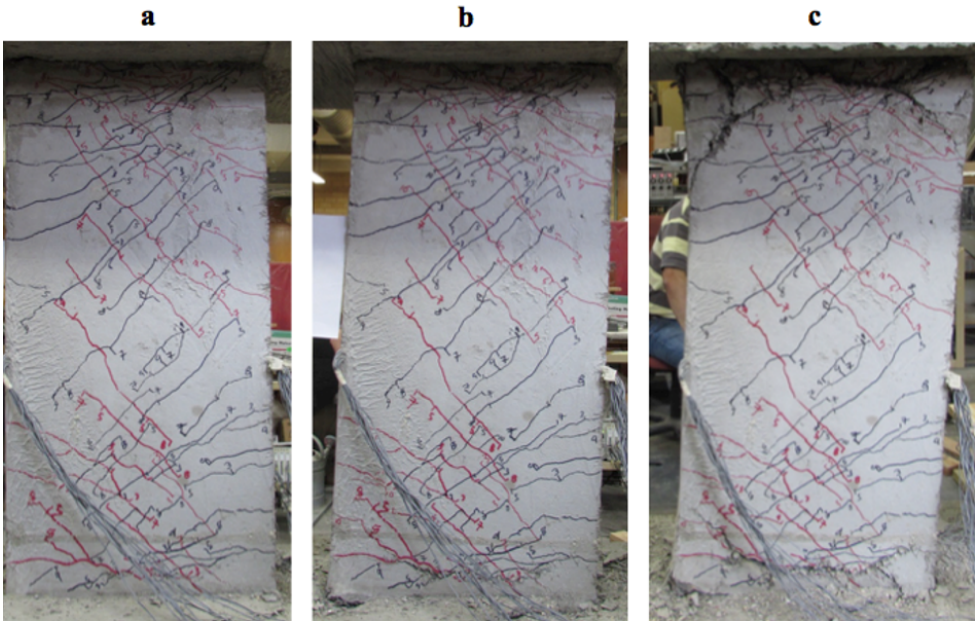

Figure 4.20: Damage Progression in Specimen CB8. a) -2.1% Drift; b) 4.2% Drift; c) 8.2% Drift.

4.2 SFRC Performance Criteria and Classification

Designers desiring to use SFRCs for coupling beam design must be able to relate the material behavior to the coupling beam shear strength and drift capacity. For this purpose, a performance-based classification system for SFRCs was proposed by Parra-Montesinos in Pérez-Irizarry and Parra-Montesinos (2017). The proposed classification was based on the results of four-point bending tests of un-notched beams discussed in Section 3.7.1 and related to coupling beam shear strength, aspect-ratio and deformation capacity. The SFRC classification was based on the tests reported herein and three other tests reported in Parra-Montesinos et al. (2014).

The proposed classification system consists of three SFRC classes (i.e., Class I, Class II and Class III SFRCs), based on the first cracking strength (f_{cr}), peak post-cracking strength (f_{pc}) and residual strength at a deflection of $\frac{L}{150}$ (f_{150}) obtained through ASTM C1609 tests. Steel fiber-reinforced concretes may be classified as Class I, Class II, and Class III following the performance criteria proposed in Pérez-Irizarry and Parra-Montesinos (2017) as follows:

Class I:
- Peak post-cracking strength greater than or equal to 1.2 times the first cracking strength and greater than or equal to $12\sqrt{f'_c}$ (psi).
- Residual strength $f_{150} \geqslant 0.4\, f_{pc}$.

Class II:
- Peak post-cracking strength greater than or equal to the first cracking strength and greater than or equal to $9\sqrt{f'_c}$ (psi).
- Residual strength $f_{150} \geqslant 0.4\, f_{pc}$.

Class III:
- Peak post-cracking strength greater than or equal to 0.8 times the first cracking strength and greater than or equal to $7.5\sqrt{f'_c}$ (psi).
- Residual strength $f_{150} \geqslant 0.4\, f_{pc}$.

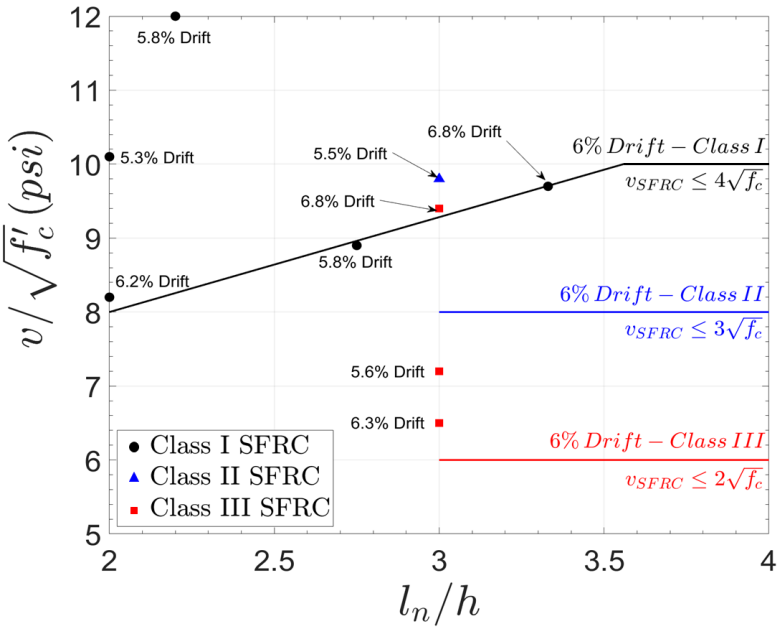

Figure 4.21: Recommended Coupling Beam Shear Stress-Drift Limits for the Proposed SFRC Classes (Pérez-Irizarry and Parra-Montesinos, 2017).

Figure 4.21, adapted from Pérez-Irizarry and Parra-Montesinos (2017), illustrates graphically the SFRC Classes and corresponding coupling beam design limits. Note that Specimen CB1 was not included in the analysis due to its shear failure, while Specimen CB6 was cast with a material not satisfying the requirements for a Class I SFRC, which is required for designing coupling beams with aspect-ratio of 2.0. Class I SFRC is meant to represent a tensile strain-hardening SFRC, while Class II and III are strain-softening SFRCs with lower flexural performance (i.e., lower f_{pc} and f_{150}). Table 4.2 shows the SFRC mixtures considered in this study and their classification based on the proposed system.

Table 4.2: SFRC Mixtures Classification.

Fiber Type	V_f	SFRC Class	Coupling Beam
HE 55/35	1.25%	Class II*	CB1 and CB2
HE 55/35	1.5%	Class II	CB6
RC 55/30 BG	1.0%	Class III	CB4
RC 55/30 BG	1.25%	Class III**	CB3
RC 80/30 BP	1.0%	Class III	CB5
RC 80/30 BP	1.5%	Class I	CB7 and CB8

* Did not satisfy the requirement $f_{pc} \geqslant f_{cr}$ ($f_{pc} = 0.95 f_{cr}$)
** Did not satisfy the requirement $f_{pc} \geqslant 0.8 f_{cr}$ ($f_{pc} = 0.77 f_{cr}$)

The four-point flexural test results of SFRC samples containing HE 55/35 fibers at a 1.25% volume fraction indicate that this material achieved a peak post-cracking strength of approximately 95% of f_{cr} and a residual strength f_{150} greater than 40% of its peak post-cracking strength. Therefore, it was deemed acceptable to classify this material as Class II SFRC. Similarly, the SFRC containing RC 55/30 BG fibers at a 1.25% achieved a peak post-cracking strength of approximately 77% of f_{cr} and a residual strength f_{150} greater than 40% of its peak post-cracking strength. Thus, it was classified as a Class III SFRC. As discussed previously in Section 3.7.1, the SFRC containing 1.0% of RC 55/30 BG fibers exhibited a better flexural performance than the SFRC containing the same fibers at a 1.25% volume fraction; therefore, further tests of SFRCs containing RC 55/30 BG fibers are recommended to clarify the observed unexpected behavior and validate their classification.

4.3 Reinforcement Strains

Reinforcement strains were measured using strain gauges installed on both longitudinal and transverse reinforcement at various locations along the beam length. The location and strain gauge IDs (e.g., F2, S2, D2) for all the specimens are shown in Figure 3.17 through Figure 3.19. To estimate the stresses developed in the reinforcement as the beams underwent displacement reversals, a cyclic stress-strain constitutive model is needed. Various models have been proposed in the literature to describe the cyclic stress-strain response of reinforcing bars, e.g., Dodd and Restrepo-Posada (1995), and Menegotto and Pinto (1973). In this study, the stresses in the reinforcing steel were calculated using a modified Menegotto-Pinto model as presented in Sakai and Mahin (2004). The model was implemented and calibrated to fit the monotonic stress-strain response experimentally obtained for the reinforcing bars used in this study (see Section 3.7.4). A sample stress-strain curve for a longitudinal reinforcement bar is presented in Figure 4.22, where the dashed line represents the "backbone" curve for the stress-strain model and the solid curve is the response calculated using the model.

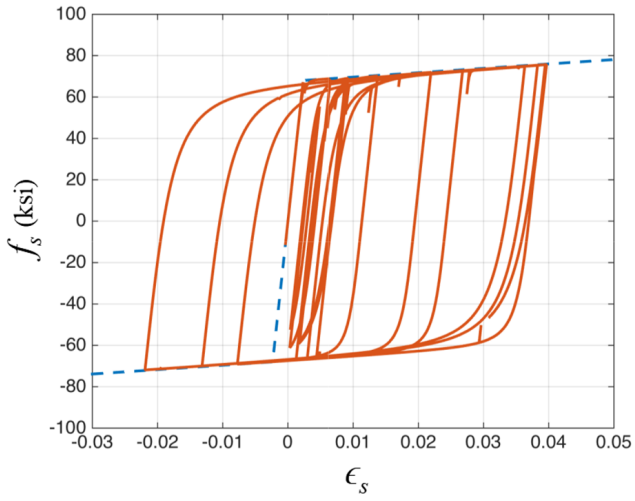

Figure 4.22: Stresses Calculated from Measured Strains - Strain Gauge F2 in Specimen CB6.

4.3.1 Transverse Reinforcement

The transverse reinforcement of all the coupling beam specimens outside the plastic hinge regions (beyond h/2 from each end) consisted of single #3 hoops at a spacing of either 4 in. or 3.25 in. for coupling beams with $l_n/h = 3.0$ and 2.0, respectively. Strain measurements obtained from the strain gauges indicate that the transverse reinforcement did not sustain very large strains. In general, the strains in the transverse reinforcement of coupling beam specimens with $l_n/h = 3.0$ remained in the elastic range until drift ratios of 1.5 to 2.0%, the deformation after which some of the hoops yielded (see Figure 4.23). The exception to this was specimen CB1, whose transverse reinforcement reached strains 5 to 8 times their yield strain at drifts exceeding approximately 3.0% (just prior to failure). In contrast, the transverse reinforcement of the specimens with $l_n/h = 2.0$ (Specimens CB6 to CB8) remained elastic throughout the tests with strains below 80% of the bar yield strain (ϵ_y).

The tests results suggest that the enhanced post-cracking tensile behavior of the SFRCs with $V_f = 1.5\%$ led to a better control of crack widths, thus reducing the strains on the transverse reinforcement. Furthermore, The relatively small strains measured in the transverse steel are in good agreement with the minor damage observed outside the plastic hinges of all the coupling beam specimens, except for Specimen CB1. Normalized strain versus drift responses for sample specimens with $l_n/h = 3.0$ and 2.0 are presented in Figure 4.23 and Figure 4.24, respectively.

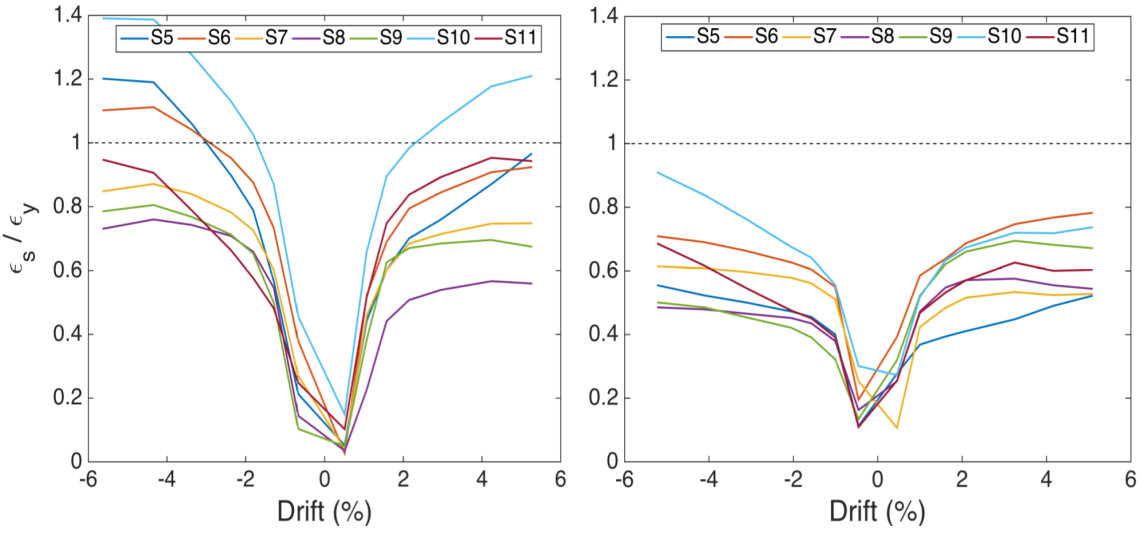

Figure 4.23: Strain Envelopes for Transverse Reinforcement Outside Plastic Hinges (Coupling Beams with $l_n/h = 3.0$). Left: Specimen CB2; Right: Specimen CB4.

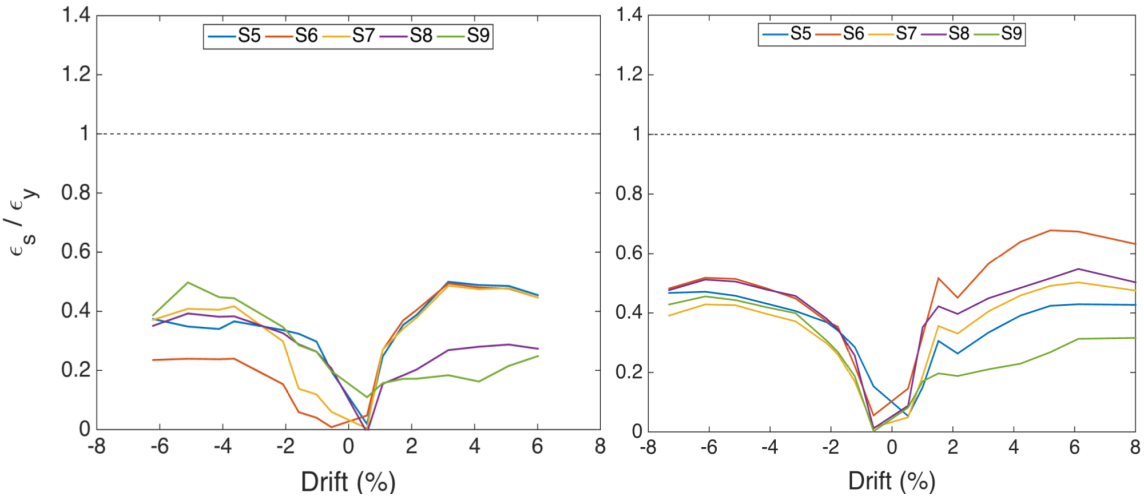

Figure 4.24: Strain Envelopes for Transverse Reinforcement Outside Plastic Hinges (Coupling Beams with $l_n/h = 2.0$). Left: Specimen CB6; Right: Specimen CB8.

The shear strength contribution of the hoops (V_s) was estimated using two different approaches. The first approach considered all the hoops achieving a stress equal to the measured yield strength, $(f_y)_{measured}$, while the second approach considered the stresses as calculated with the cyclic stress-strain model, $(f_s)_{M-P}$, based on the strain gauge data. To estimate the shear strength contribution, a truss analogy was assumed with a longitudinal projection of the diagonal crack equal to d. The distance d was taken as 16.25 and 15.5 in. for coupling beams with $l_n/h = 3.0$ and 2.0, respectively (approximately 90% and 85% of the overall member depth). Based on the calculated shear force in the transverse reinforcement, the average SFRC shear demand, V_c, was estimated for each coupling beam specimen as the difference between the peak applied shear and V_s calculated using the two approaches previously mentioned. Table 4.3 shows the calculated SFRC shear stress demand ($v_c = V_c/A_g$) and the shear stress carried by the transverse reinforcement at peak shear demand.

Table 4.3: Shear Strength Resisted by Transverse Reinforcement and the SFRC.

Specimen	f'_c (psi)	Fiber Type - V_f	$V_s = \frac{A_s\, d\, (f_y)_{measured}}{s}$			$V_s = \frac{A_s\, d\, (f_s)_{M-P}}{s}$		
			$v_s/\sqrt{f'_c}$	$v_c/\sqrt{f'_c}$	$v_{max}/\sqrt{f'_c}$	$v_s/\sqrt{f'_c}$	$v_c/\sqrt{f'_c}$	$v_{max}/\sqrt{f'_c}$
CB1	7930	HE 55/35 - 1.25%	6.2	6.0	12.2	6.1	6.1	12.2
CB2	8840	HE 55/35 - 1.25%	6.1	3.7	9.8	4.7	5.2	9.9
CB3	8630	RC 55/30 BG - 1.25%	6.1	3.4	9.5	5.7	3.7	9.4
CB4	9260	RC 55/30 BG - 1.00%	6.2	1.0	7.2	3.8	3.4	7.2
CB5	9750	RC 80/30 BP - 1.00%	5.7	2.1	7.8	3.2	4.6	7.8
CB6	7950	HE 55/35 - 1.50%	7.4	0.7	8.1	3.0	5.1	8.1
CB7	9330	RC 80/30 BP - 1.50%	6.9	3.2	10.1	3.8	6.3	10.1
CB8	8490	RC 80/30 BP - 1.50%	7.3	0.9	8.2	3.5	4.7	8.2

Considering the transverse reinforcement reached $(f_y)_{measured}$ resulted in unrealistically low SFRC shear stress demands (v_c). Except for Specimen CB1, which as discussed previously failed prematurely in shear, the shear stress demand on the SFRCs ranged between 3.4 and 5.2, and between 4.7 and $6.3\sqrt{f'_c}$ (psi) for coupling beams with $l_n/h = 3.0$ and 2.0, respectively (see Table 4.3).

The proposed shear stress limits for the different SFRC classes are shown in Table 4.4. Furthermore, Figure 4.25 shows the variation of v_c throughout the range of applied drifts for each specimen, as calculated from strain gauge measurements and the Menegotto-Pinto model. Note that only Specimens CB1 and CB7 sustained a $v_c \geqslant 5\sqrt{f'_c}$ (psi), which led to reduced deformation capacity.

As shown in Figure 4.25, the transverse reinforcement data provide supporting evidence for the recommended SFRC shear stress limits. It should be mentioned that for cases in which drift capacity was less than 6%, the material class was deemed acceptable because beam peak shear stress (v_u) were greater than the limit proposed (see Figure 4.21). The calculated SFRC shear stress using the Menegotto-Pinto model were consistently larger than $3\sqrt{f'_c}$ (psi) and often exceeded $5\sqrt{f'_c}$ (psi). Table 4.4 compares the maximum shear strength contribution of each SFRC class, calculated assuming a stress on the transverse reinforcement equal to 60 ksi, $(f_y)_{measured}$, and $(f_s)_{M-P}$. The SFRC shear strength contributions are maximum values calculated using the data from coupling beam specimens with SFRCs corresponding to each SFRC Class (e.g., Specimens CB7 and CB8 were constructed with a material classified as a Class I SFRC and the maximum shear strength contribution of the SFRC for these two tests was $6.3\sqrt{f'_c}$, psi). From Table 4.4, it seems that considering a stress in the transverse reinforcement equal to 60 ksi led to more realistic estimates of the shear stress demand on the SFRC and is thus recommended for design.

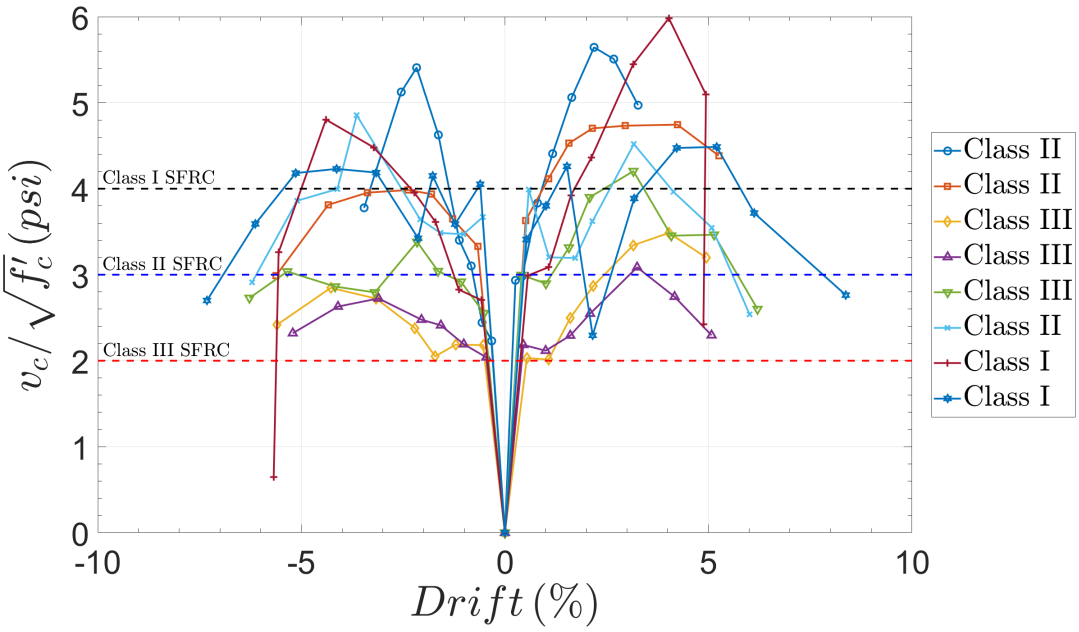

Figure 4.25: Shear Stress Carried by the SFRC ($v_c = v_u - v_s$) with v_s Calculated using $(f_s)_{M-P}$.

Table 4.4: Calculated Shear Stress Contributions and Recommended Limits.

		Peak SFRC Contributions		
		$f_y = 60$ ksi	$(f_y)_{measured}$	$(f_s)_{M-P}$
SFRC Class	Proposed Limits $v_c/\sqrt{f'_c}$	$v_c/\sqrt{f'_c}$	$v_c/\sqrt{f'_c}$	$v_c/\sqrt{f'_c}$
Class I	4.0	4.1	3.2	6.3
Class II	3.0	4.5	3.7	5.2
Class III	2.0	4.2	3.4	3.7

4.3.2 Confinement Reinforcement

Preserving the integrity of the concrete core is essential for a reinforced concrete member to exhibit a ductile response when subjected to large inelastic deformation cycles. In practice, concrete confinement is achieved by the use of closely spaced hoops that provide passive confinement to the concrete core as it tries to expand laterally under compressive loads. As discussed in Section 3.2.1, the confinement reinforcement provisions for columns of special moment resisting frames in ACI 318-14 (ACI Committee 318, 2014) were followed to detail the hoops in the plastic hinge regions (taken as $h/2$ from each support), although a slightly larger spacing than required was used for practical purposes.

In general, smaller strains were measured in the plastic hinge confinement reinforcement compared to those measured in the transverse reinforcement outside the plastic hinges. Nearly all the confinement reinforcement remained elastic even during large deformation cycles (drifts $\geqslant 5.0\%$) for all the coupling beam specimens. Only a few hoops yielded at drifts exceeding 4.0%, e.g., strain gauge S1 in Specimen CB2 (see Figures 4.26 and 4.27). These results indicate that the hoops were effective in providing adequate confinement to the concrete core within the plastic hinge regions.

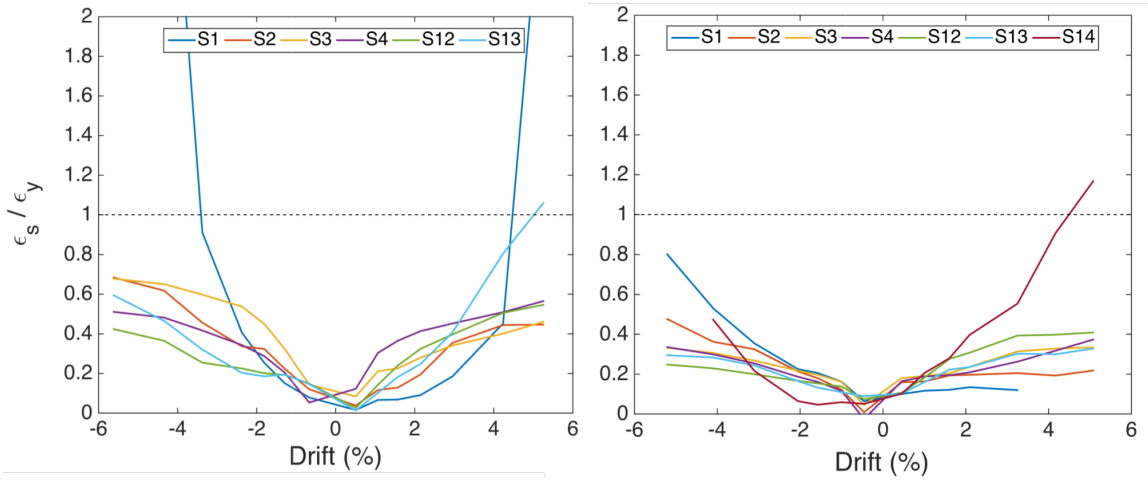

Figure 4.26: Plastic Hinge Confinement Reinforcement Strain Envelopes for Coupling Beams with $l_n/h = 3.0$. Left: Specimen CB2; Right: Specimen CB4.

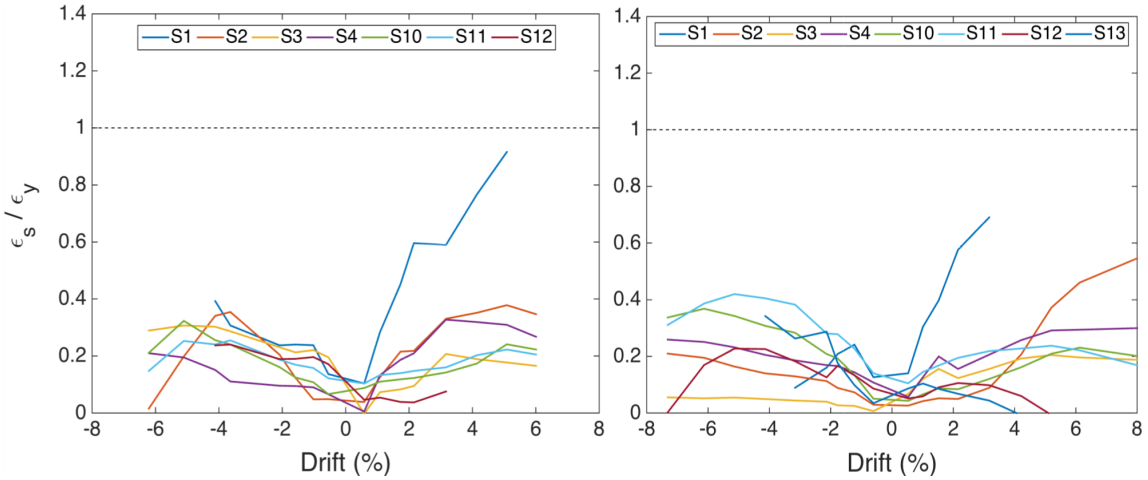

Figure 4.27: Plastic Hinge Confinement Reinforcement Strain Envelopes for Coupling Beams with $l_n/h = 2.0$. Left: Specimen CB6; Right: Specimen CB8.

4.3.3 Longitudinal and Dowel Reinforcement

Strain gauge measurements indicated that yielding of the main longitudinal reinforcement typically initiated at deformations of approximately 0.5–0.75% drift. As the applied lateral displacement further increased, flexural yielding continued spreading into the coupling beams. Reinforcement yielding spread to a distance of $h/2$ from the face of the supports at drifts between approximately 2.0% and 3.0% for coupling beams with $l_n/h = 3.0$. For Specimens with $l_n/h = 2.0$, yielding of the main flexural reinforcement spread past the termination of the U-shaped dowels (approximately $h/5$ from the beam ends) at approximately 1.5 to 2.0% drift. During subsequent drift cycles, the longitudinal reinforcement reached very large strains at the end of the beams. As shown in Figures 4.28 through 4.31, the measured strains in the longitudinal reinforcement were often in the strain-hardening regime of response and, in cases, exceeded 6.0%. Figures 4.28 and 4.29, and Figures 4.30 and 4.31, provide examples of beam-shear versus strain responses for the main longitudinal bars at the end regions of beams with $l_n/h = 3.0$ and 2.0, respectively (see Figures 3.18 and 3.19 for strain gauge location). Furthermore, the normalized strains (ϵ_s/ϵ_y) measured at different locations along the beams are shown in Figure 4.32 through Figure 4.37.

Measurements from the strains gauges on the U-shaped dowels showed that yielding of the dowel reinforcement occurred at drifts of approximately 1.0 and 0.75% for Specimens CB2–CB5 and CB6–CB8, respectively. In general, the strains in the dowel reinforcement were smaller than those in the flexural reinforcement. However, the occurrence of yielding indicates that the dowel reinforcement was properly developed and effective in strengthening the beam-to-wall interface.

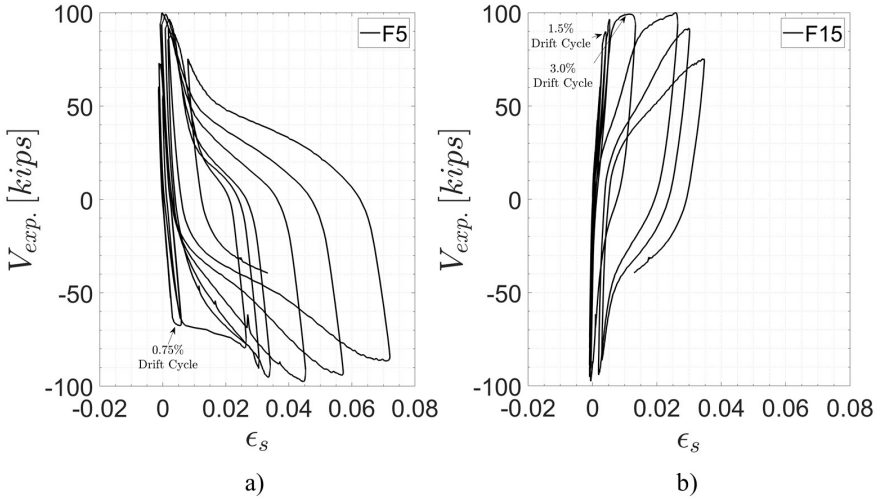

Figure 4.28: Strain Response of Main Flexural Reinforcement-Specimen CB2. a) Beam-Wall Interface; b) h/2 from Support.

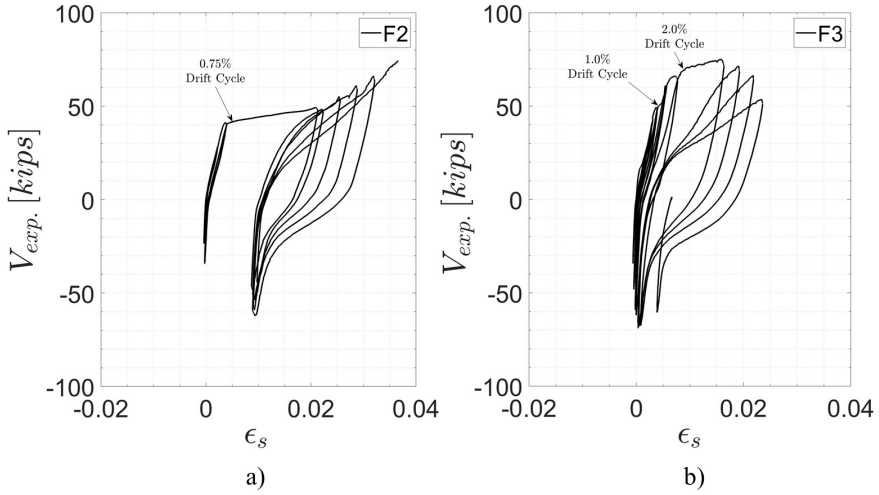

Figure 4.29: Strain Response of Main Flexural Reinforcement-Specimen CB4. a) Beam-Wall Interface; b) h/2 from Support.

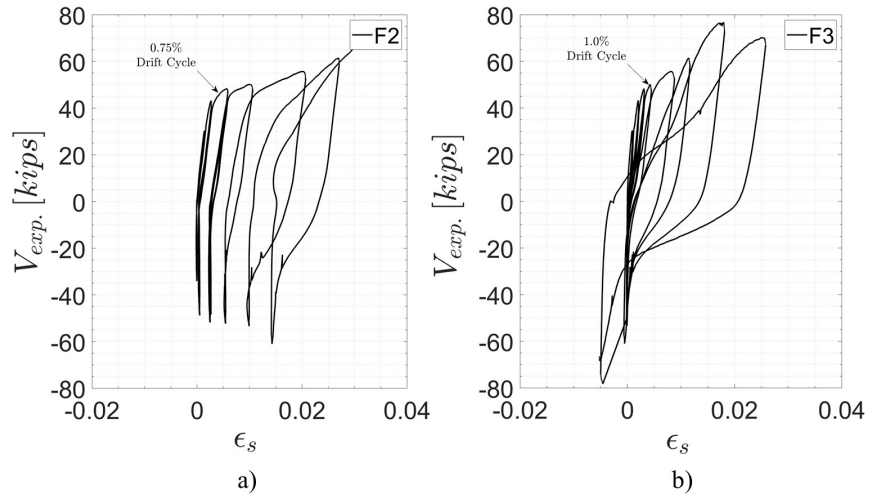

Figure 4.30: Strain Response of Main Flexural Reinforcement-Specimen CB6. a) Beam-Wall Interface; b) h/5 from Support.

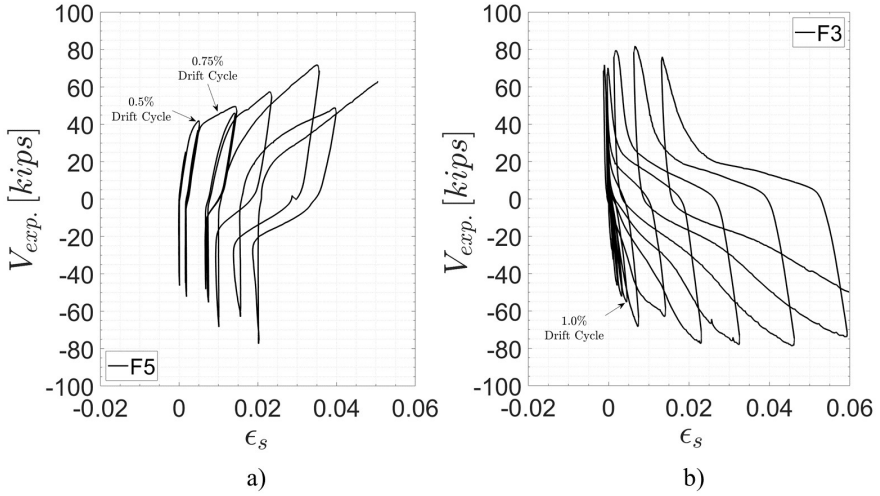

Figure 4.31: Strain Response of Main Flexural Reinforcement-Specimen CB8. a) Beam-Wall Interface; b) h/5 from Support.

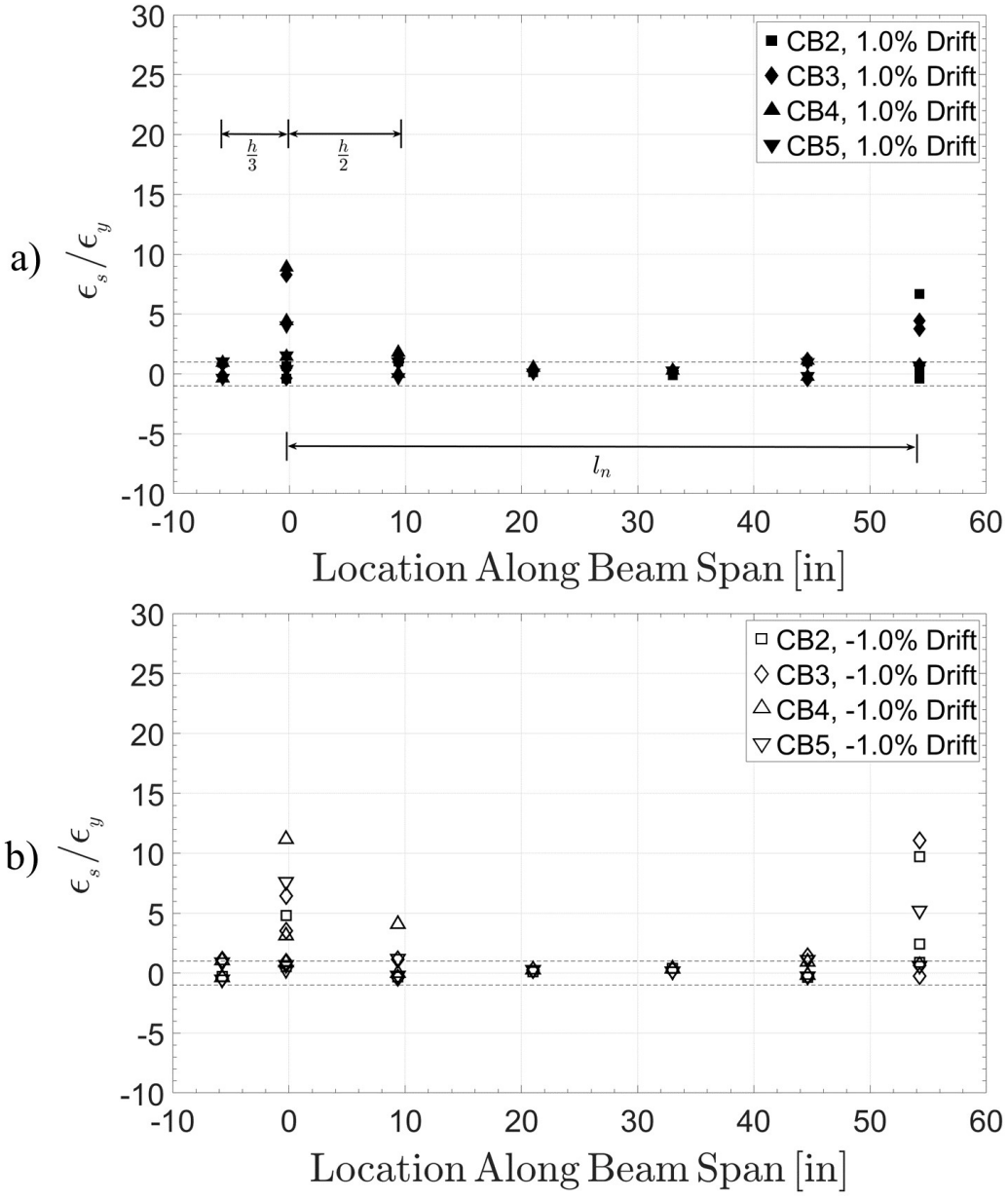

Figure 4.32: Longitudinal Reinforcement Strains at 1.0% Drift (Specimens CB2–CB5). a) Positive Drifts; b) Negative Drifts.

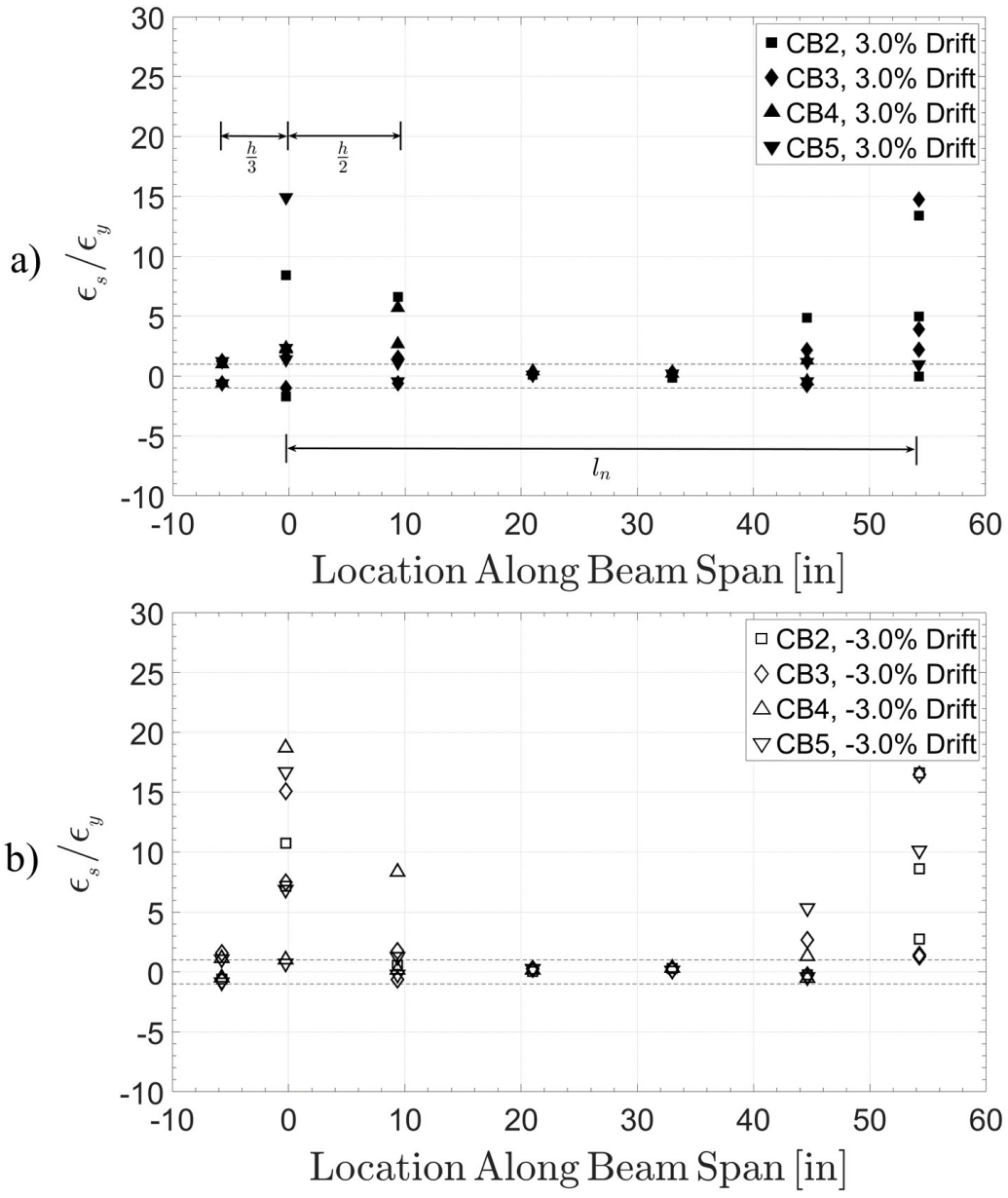

Figure 4.33: Longitudinal Reinforcement Strains at 3.0% Drift (Specimens CB2–CB5). a) Positive Drifts; b) Negative Drifts.

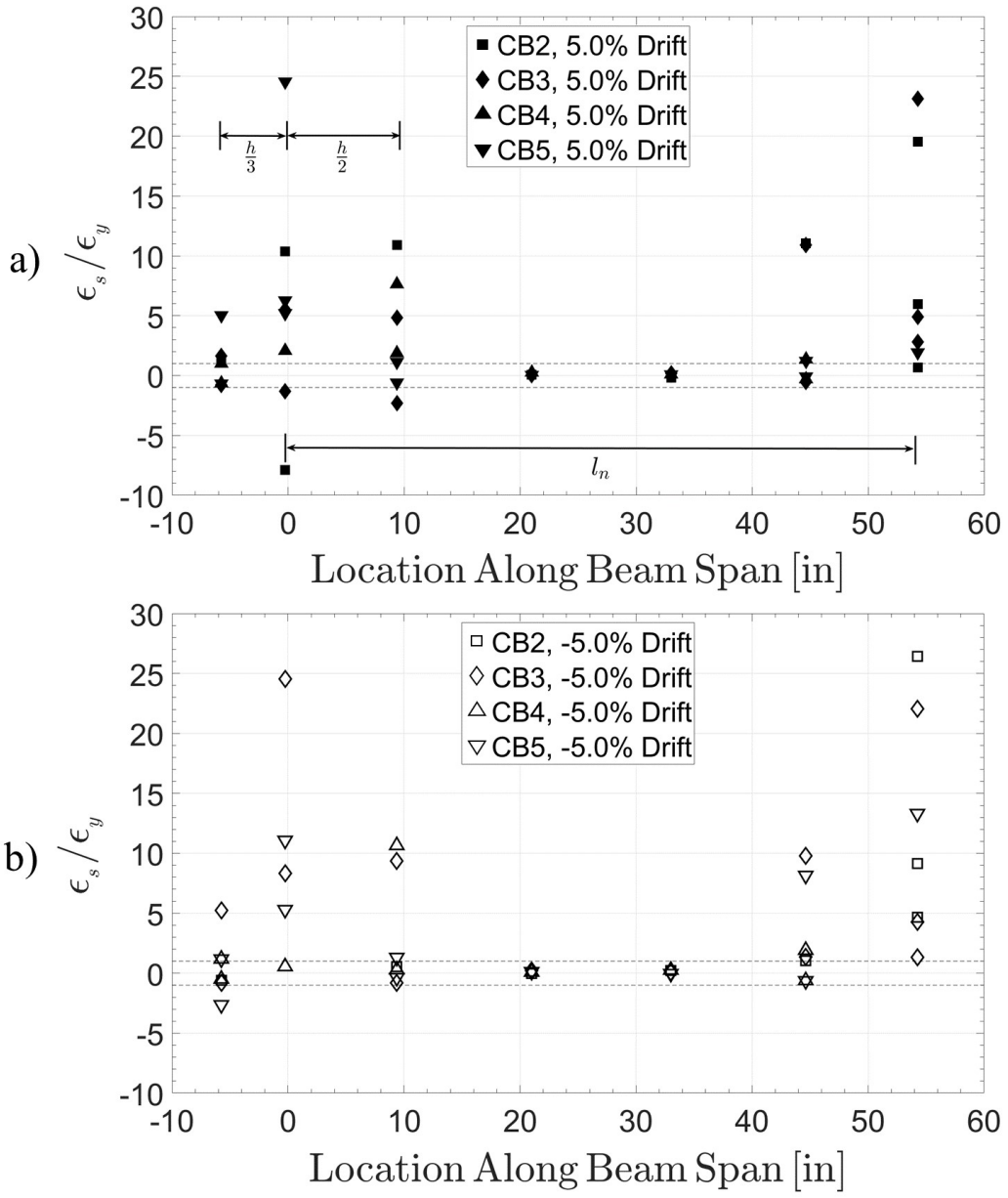

Figure 4.34: Longitudinal Reinforcement Strains at 5.0% Drift (Specimens CB2–CB5). a) Positive Drifts; b) Negative Drifts.

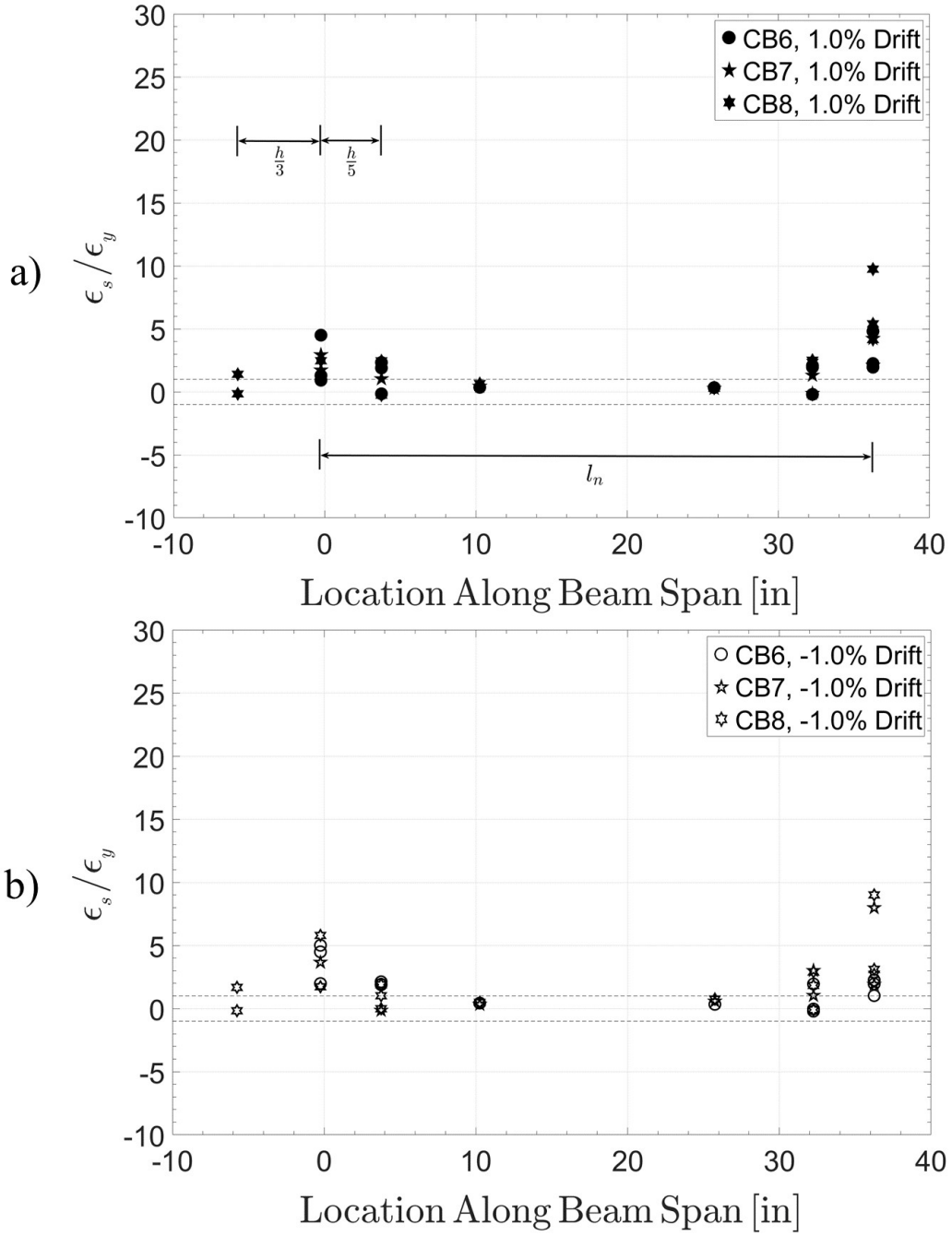

Figure 4.35: Longitudinal Reinforcement Strains at 1.0% Drift (Specimens CB6–CB8). a) Positive Drifts; b) Negative Drifts.

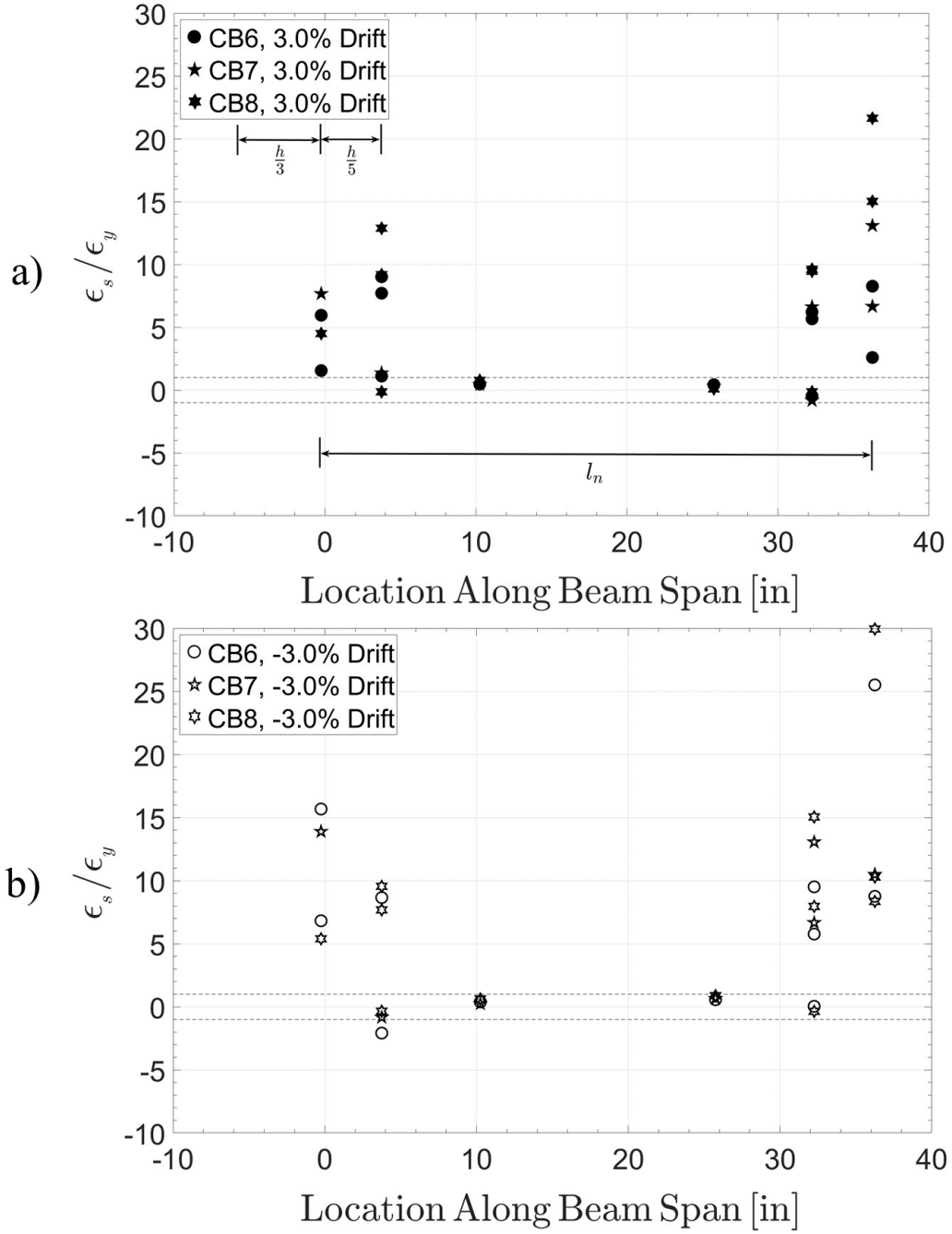

Figure 4.36: Longitudinal Reinforcement Strains at 3.0% Drift (Specimens CB6–CB8). a) Positive Drifts; b) Negative Drifts.

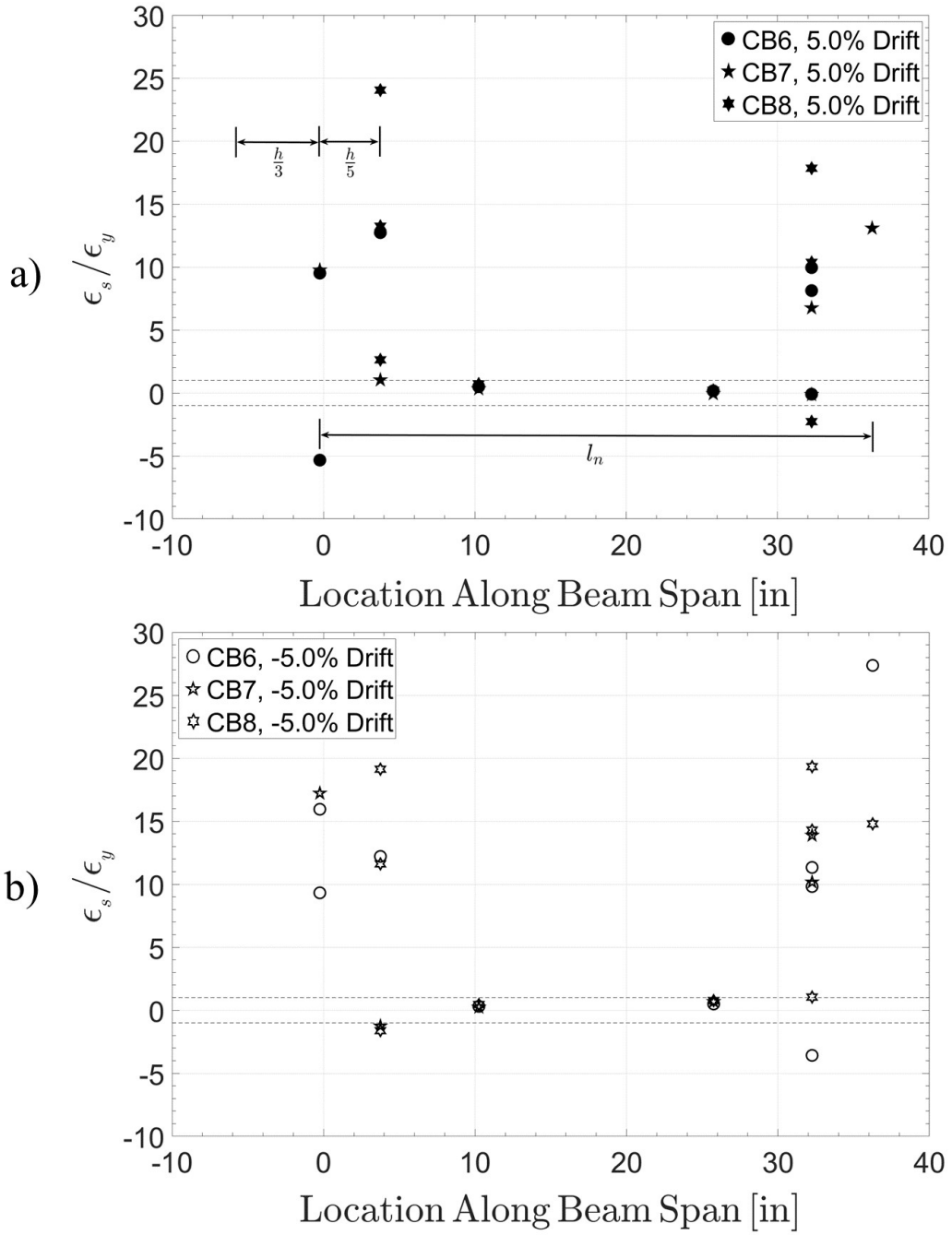

Figure 4.37: Longitudinal Reinforcement Strains at 5.0% Drift (Specimens CB6–CB8). a) Positive Drifts; b) Negative Drifts.

4.4 Curvature Distribution

To quantify and characterize the flexural behavior of the SFRC coupling beams, Optotrak™ markers on each of the marker strips were used to calculate the average curvature of each strip throughout the range of applied lateral drifts (see Appendix Sections A.4–A.5 for marker strip layout and curvature calculation details). Figures 4.38 and 4.39 show representative curvature profiles for coupling beams with aspect-ratio of 3.0 and 2.0, respectively.

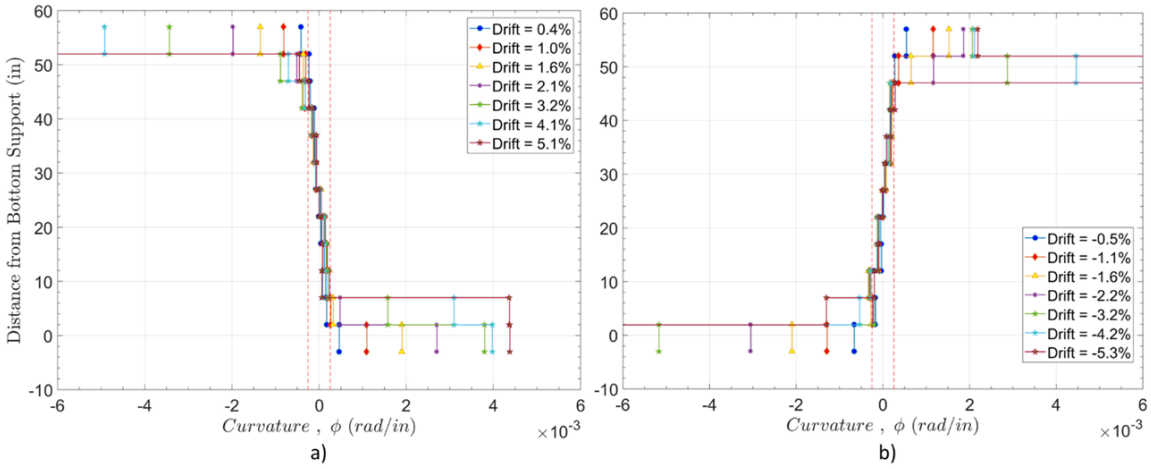

Figure 4.38: Sample Curvature Profiles - Specimen CB5. a) Positive Drifts; b) Negative Drifts.

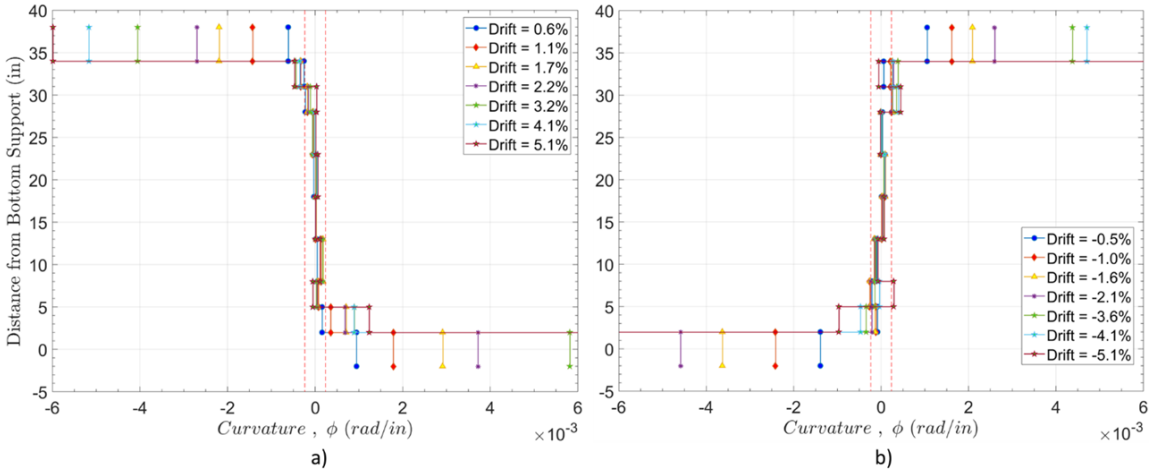

Figure 4.39: Sample Curvature Profiles - Specimen CB6. a) Positive Drifts; b) Negative Drifts.

The vertical red-dashed lines shown in Figures 4.38 and 4.39 mark the approximate theoretical curvature at first yield (ϕ_y), calculated from moment-curvature (M–ϕ) analyses (see Section 4.6.1). First yield curvatures in the range of 2 to 3x10^{-4} rad/in. were calculated considering both zero axial force and the maximum axial force developed while testing the SFRC coupling beams (calculated ϕ_y values are provided in Table 4.5).

As shown in Figures 4.38 and 4.39, curvatures nearly equal to or exceeding ϕ_y occurred approximately within the first 8 to 12 inches from the beam ends. However, most inelastic flexural deformations occurred within the first 5 and 7 inches from the beam ends for coupling beams with aspect ratio of 2.0 and 3.0, respectively. As expected, the curvatures within the mid-span region of the SFRC coupling beams followed a nearly linear distribution and remained below the theoretical yield curvature. Furthermore, the curvatures along the beam length suggested that the inflection point was located near mid-span; see Figures 4.38 and 4.39. For completeness, the curvature profiles shown in Figures 4.38 and 4.39 contain the calculated curvatures in all marker strips, including "effective" curvatures at the beam-wall interfaces. However, these effective curvatures are primarily due to

concentrated rotations as opposed to bending of the SFRC beams (interface bond-slip behavior is discussed in Section 4.5). In some cases, calculated curvatures deviated from the expected curvature distributions; curvature opposite in sign to moment at peak drifts within a cycle, particularly during the larger drift cycles. Two causes for these deviations were: 1) large plastic rotations in a given direction that did not fully reverse upon loading in the opposite direction; and 2) Damage localization causing rotations to occur primarily in a strip while the curvatures in the adjacent strip did not reverse upon loading in the opposite direction. The latter was the case for Strips 8 and 9, second and third strip from the bottom in Figure 4.39b, respectively, in Specimen CB6.

Table 4.5: Theoretical Yield Curvatures.

Specimen		CB2	CB3	CB4	CB5	CB6	CB7	CB8
ϕ_y	$P = 0$	2.49	2.50	2.41	2.43	2.20	2.46	2.07
(rad/in) x10^{-4}	$P = P_{max}$	3.02	2.93	2.77	2.75	2.57	3.01	2.48

4.5 Behavior of Beam-to-Wall Connections

Localized rotations at the connections/joints of reinforced concrete members are often a significant source of flexibility. These localized rotations arise from accumulation of inelastic strains in the reinforcement and bar slip due to deterioration of bond between concrete and steel bars. The latter is exacerbated in members undergoing large displacement reversals, such as coupling beams.

To quantify the response of the precast beam-to-wall connections, Optotrak™ markers located at the support end-blocks and the first row of markers at the beam ends were used to calculate the rotations occurring a the beam-wall interfaces or cold joints. The moment rotation (M–θ_{slip}) response of the beam-to-wall connections of Specimens CB2 to CB5 and Specimens CB6 to CB8 are shown in Figures 4.40 and 4.41, and Figures 4.42 and 4.43, respectively. The moment rotation curves are labeled with the marker strip and the loading direction; for example, $S12-P$ and $S12-N$ stand for marker strip 12 during positive and negative drifts, respectively.

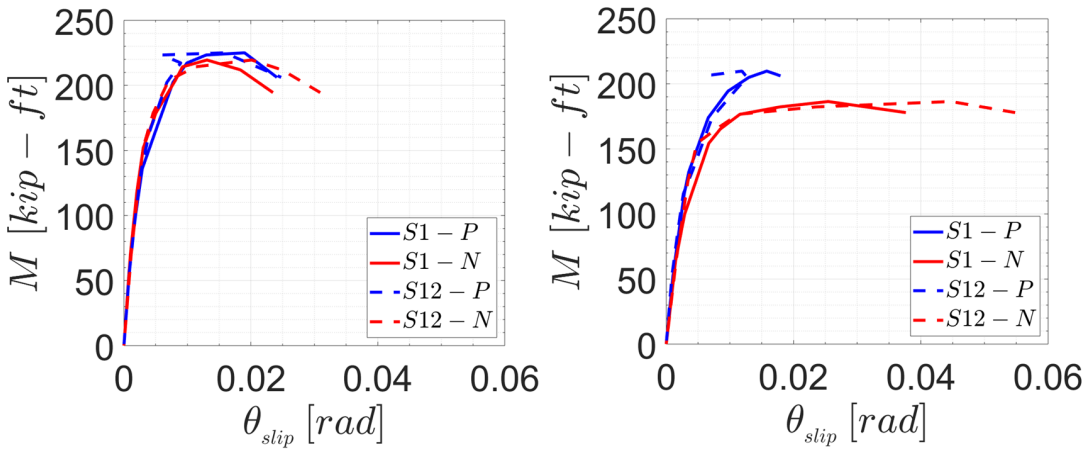

Figure 4.40: Moment Versus Rotation Response at Beam-to-Wall Connections. a) Specimen CB2; b) Specimen CB3.

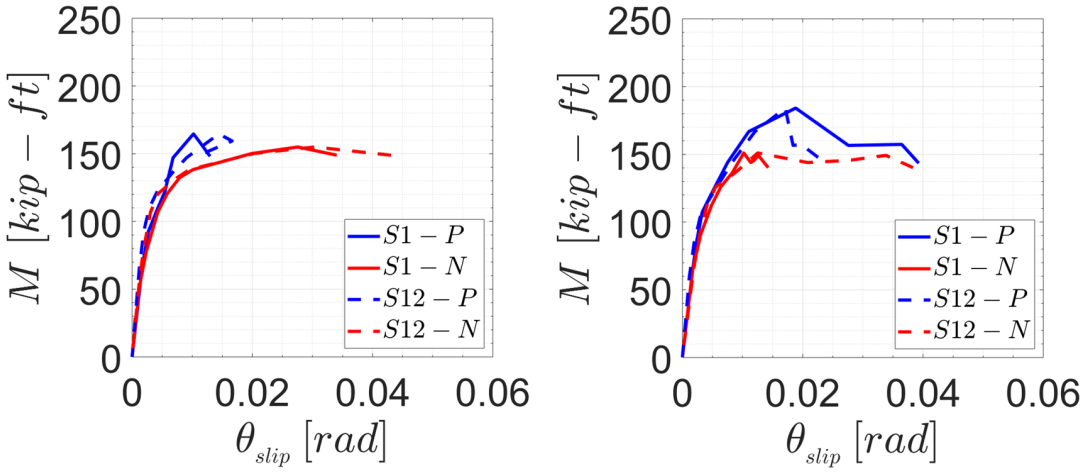

Figure 4.41: Moment Versus Rotation Response at Beam-to-Wall Connections. a) Specimen CB4; b) Specimen CB5.

In general, the connection rotations were larger in the reversed loading direction (negative drifts). Coupling beams with span-to-depth ratio of 3.0 underwent average rotations at peak strength in the range of 1.2 to 3.5%, with average rotation of 1.5% and 2.3% in the positive and negative loading directions, respectively. These average rotations are the average of the two beam-wall connection rotations of each specimen. Specimens CB3 and CB4 exhibited the largest difference in average rotations between the two loading directions. Average rotation at peak strength in the negative loading direction for Specimens CB3 and CB4 were approximately 3.5% and 2.9%, respectively. These rotations were approximately 2.5 times larger than the rotations achieved at peak strength in the opposite direction. The average rotations at the beam-wall interfaces at peak strength of Specimens CB6 to CB8 were in the range of approximately 1.8 to 3.5%, with average rotations at peak strength of 2.4% and 2.8% in the positive and negative loading directions, respectively.

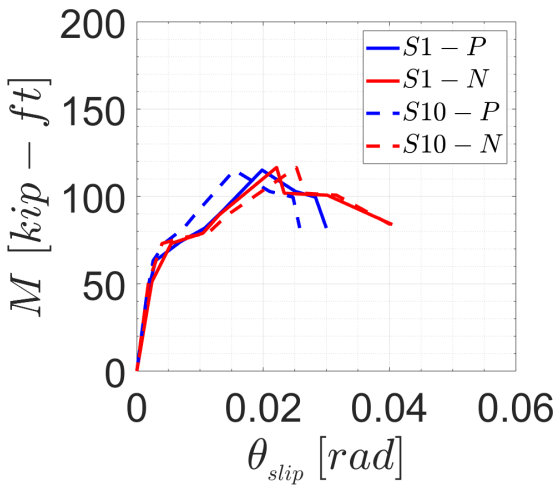

Figure 4.42: Moment-Rotation Response at Beam-to-Wall Connections for Specimen CB6.

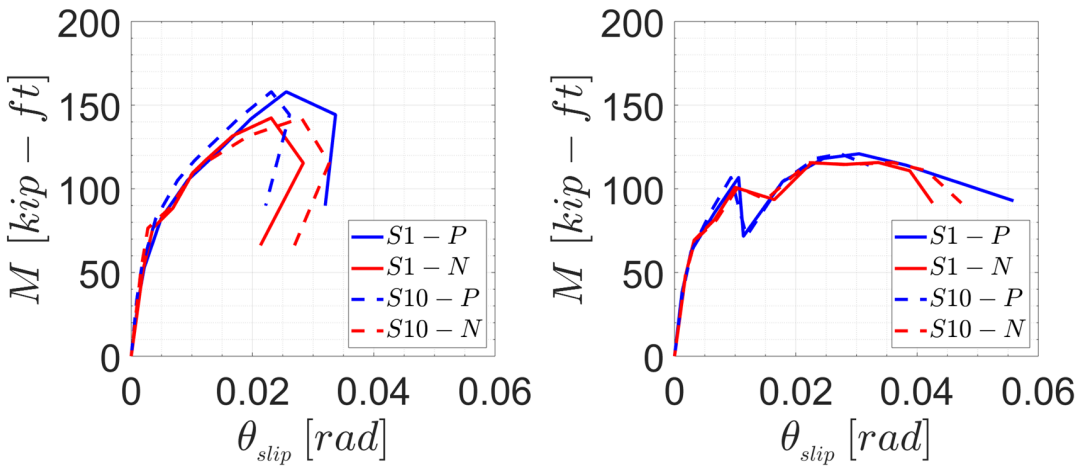

Figure 4.43: Moment-Rotation Response at Beam-to-Wall Connections. a) Specimen CB7; b) Specimen CB8.

The average end rotations versus drift envelope responses for Specimens CB2 to CB8 are shown in Figure 4.44, where the data plotted in black and red correspond to beams with span-to-depth ratio of 3.0 and 2.0, respectively. As shown in Figure 4.44, the relationship between interface rotation and cycle drift was linear. Furthermore, for any given drift, the rotations at the beam-to-wall connections of the specimens with span-to-depth ratio of 2.0 were, on average, larger than those observed for the more slender beams (approximately 20% larger at any given drift), indicating a larger contribution to coupling beam drift.

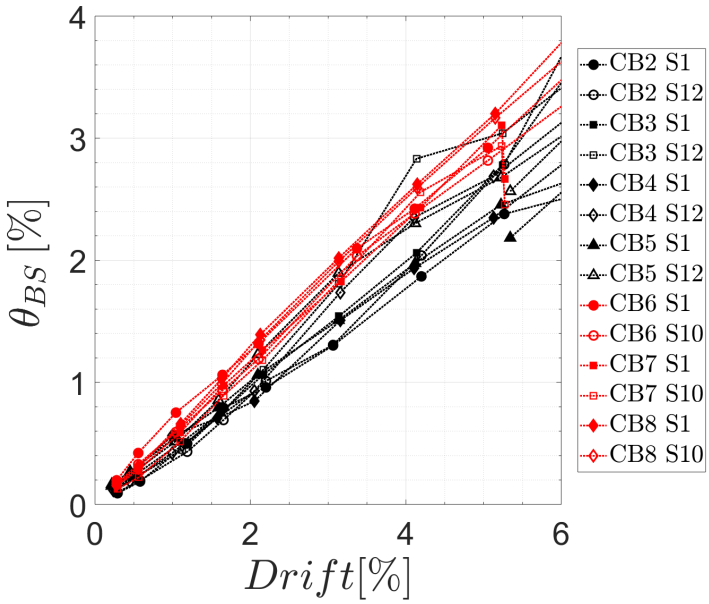

Figure 4.44: Interface Rotation versus Average Cycle Drift.

4.6 Flexural Behavior of SFRC Coupling Beams

In this section, calculated and experimental moment versus curvature responses at critical sections of the coupling beam specimens are discussed. Flexural rigidity values for use in elastic analysis are then discussed. Compressive strain limits for estimation of curvature and rotation capacity of SFRC coupling beam sections and plastic hinge regions are also discussed, followed by an evaluation of plastic hinge length and rotations.

4.6.1 Moment-Curvature Response

Nonlinear sectional analysis, commonly known as Moment-Curvature (M–ϕ) analysis, considers material nonlinear stress-strain responses to model the flexural behavior of reinforced concrete sections. The iterative M–ϕ analysis is typically deformation-controlled, where the controlling deformation is often the concrete maximum compressive strain (ϵ_{cm}). The analysis follows the Bernoulli beam bending assumption that plane sections remain plane after bending, which together with an assumed depth of the neutral axis allows for the definition of a strain gradient over the cross section. Using material constitutive equations, the stresses in the concrete and steel reinforcement are calculated and equilibrium of forces is verified. This process requires iteration by adjusting the assumed depth of the neutral axis until equilibrium is satisfied. Once the depth of the neutral axis is known, the curvature corresponding to the selected ϵ_{cm} and the moment carried by the section are calculated according to basic reinforced concrete mechanics. This iterative process is then repeated for increasing ϵ_{cm} values until the ultimate concrete compressive strain (ϵ_{cu}) is reached. In this study, a maximum $\epsilon_{cm} = 0.012$ was used for the calculation of analytical M–ϕ responses.

4.6.1.1 Concrete Compressive Stress-Strain Model

The compressive stress strain relation of concrete has been extensively studied and various models describing the behavior of unconfined and confined concrete can be

found in the literature, (e.g., Hognestad, 1952; Kent and Park, 1971; Mander et al., 1988; Roy and Sozen, 1964; Sheikh and Uzumeri, 1982). In this study, the compressive behavior of the various SFRCs investigated was modeled using Hognestad's parabola up to peak strength, a linear descending branch for post peak response, and a residual compressive strength. Normalized stress-strain curves for different normalized descending slopes (Z), along with the expressions for each branch, are shown in Figure 4.45.

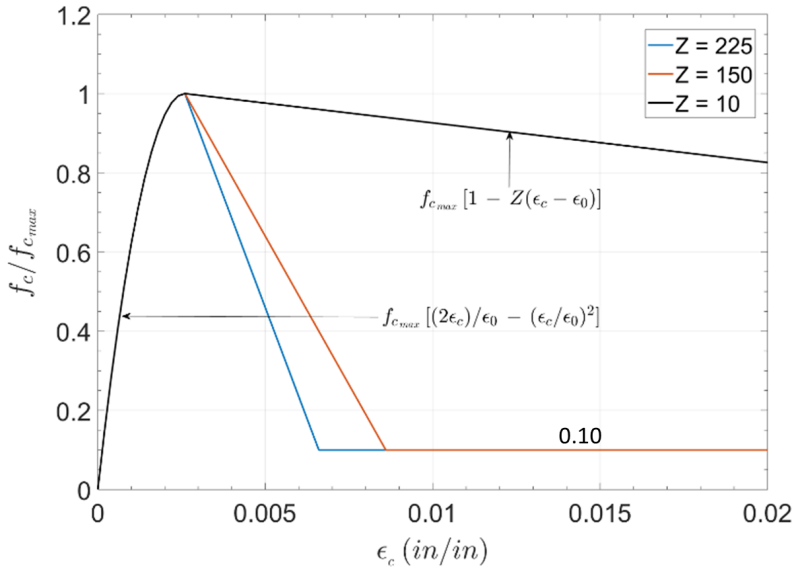

Figure 4.45: Compressive Stress-Strain Response Model.

The following variables define the model: concrete strain, ϵ_c; strain at peak compressive strength, ϵ_0 (taken as 0.0026 given the use of f'_c between 8 and 10 ksi); concrete stress, f_c; concrete compressive strength, f'_c; and the normalized slope of the descending branch, Z. The slope of the descending branch is defined as $Z = \frac{0.5}{\epsilon_{50u} + \epsilon_{50h} - \epsilon_0}$, where ϵ_{50u} is the post-peak strain at a stress equal to half the compressive strength for unconfined concrete, and ϵ_{50h} is the increase in strain at 50% strength decay due to reinforcement confinement (Kent and Park, 1971; Park and Paulay, 1974). Kent and Park proposed the following empirical expression

to estimate ϵ_{50h}, $\epsilon_{50h} = \frac{3}{4}\rho_s\sqrt{\frac{b_c}{s}}$, where ρ_s is the ratio of volume of transverse reinforcement to volume of concrete core measured to the outside of the confining hoops; b_c is the width of the confined core measured to the outside of the hoops; and s is the spacing of the confining hoops. Given the high volume of confinement reinforcement ($\rho_s = 4.7\%$) within the plastic hinge regions of the SFRC coupling beams, calculated Z values were approximately 10. Thus, a Z value of 10 was used to model the SFRC descending branch within the plastic hinge regions. For simplicity, a single compressive stress-strain response was considered for the entire cross-section ($Z = 10$). Even though some difference in behavior between core and cover concrete was expected, the amount of fibers used was expected to provide substantial concrete confinement and delay cover spalling.

4.6.1.2 Steel Reinforcement Stress-Strain Model

The monotonic stress-strain relation of the reinforcement steel was modeled using a piece-wise function to describe the initial elastic region, yield plateau and strain hardening region. The model requires six parameters, namely, yield strength (f_y), Young's modulus (E_s), tensile strength (f_u), fracture strain (ϵ_u), strain at the onset of strain hardening (ϵ_{sh}), and the tangent modulus at the onset of strain hardening (E_{sh}). The model is defined by the following equations:

$$f_s = \begin{cases} E_s * \epsilon_s & \text{if} \quad \epsilon_s \leqslant \epsilon_y \\ f_y & \text{if} \quad \epsilon_y < \epsilon_s \leqslant \epsilon_{sh} \\ f_y + (f_u - f_y) * [2\frac{\epsilon_s - \epsilon_{sh}}{\epsilon_{sm} - \epsilon_{sh}} - (\frac{\epsilon_s - \epsilon_{sh}}{\epsilon_{sm} - \epsilon_{sh}})^2] & \text{if} \quad \epsilon_{sh} < \epsilon_s \leqslant \epsilon_{sm} \\ f_u & \text{if} \quad \epsilon_{sm} < \epsilon_s \leqslant \epsilon_u \\ 0 & \text{if} \quad \epsilon_u < \epsilon_s \end{cases} \tag{4.1}$$

where f_s is the stress carried by the steel reinforcement, ϵ_s is the strain acting on the steel reinforcement and ϵ_{sm} is given by Equation 4.2 and represents the strain at which the tensile strength is achieved. The strain hardening region in this model follows a parabola, and the model is similar to that described by Mander (1983).

The material properties were taken from the experimentally measured values reported in Section 3.7.4 and the parameter E_{sh} was selected by trial and error to fit the experimental curves. Figure 4.46 show experimental and modeled stress versus strain curves for the bars used in Specimen CB4 (#5 bars - solid lines; #4 bars - dashed lines). Because the responses of the different bar sizes were similar for each coupling beam specimen, an average stress versus strain response was used to model the longitudinal reinforcement bars, regardless of the size. Except for Specimen CB7, the average yield strength used in the model was within 5% of the measured bar yield strength (for Specimen CB7 the average model-to-measured bar yield strength was 93%).

$$\epsilon_{sm} = \epsilon_{sh} + 2\left(\frac{f_u - f_y}{E_{sh}}\right) \tag{4.2}$$

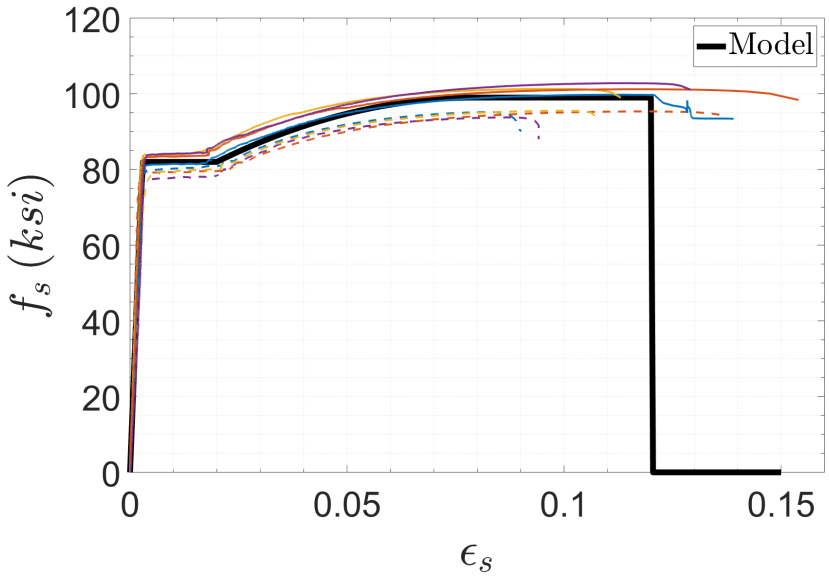

Figure 4.46: Stress-Strain Model and Experimental Responses for Steel Reinforcement (Specimen CB4).

4.6.1.3 SFRC Tensile Stress-Strain Model

The tensile responses of SFRCs obtained through the testing of notched prisms are in terms of tensile stress versus crack opening, which cannot be directly incorporated in a M–ϕ analysis. For modeling purposes, strains were calculated as the crack opening divided by a characteristic gauge length assuming the cracks to be smeared. The characteristic gauge length for each SFRC material was obtained from observations of crack spacing in the plastic hinge regions of coupling beam specimens.

Inspection of the cracking patterns observed within the plastic hinges of the coupling beams showed that flexural cracks had similar widths until initiation of damage localization. Therefore, to estimate the tensile strains for a given SFRC, an average crack spacing was estimated using images of the plastic hinges of the beam with the considered SFRC. The images were analyzed using the open-source software ImageJ (Schneider et al., 2012). A known dimension on each image analyzed was used to set a scale on ImageJ and several measurements of the spacing of flexural cracks were taken to estimate an average crack spacing. The calculated crack spacing for the coupling beam specimens were then used to calculate a characteristic gauge length for each class of SFRC; e.g., the crack spacing observed for Specimens CB7 and CB8, with a Class I SFRC, were averaged to obtain the characteristic gauge length for Class I SFRCs. This analysis led to approximate average crack spacings or characteristic gauge lengths of 3.5, 4.0 and 4.5 in. for Class I, Class II and Class III SFRCs, respectively.

The average tensile stress versus stain response of each SFRC was modeled as a tri-linear piece-wise function. Figure 4.47 shows the tensile response of the SFRC used in Specimen CB4 along with the modeled response. The three points needed to define the tri-linear stress versus strain responses correspond to peak tensile strength $(\epsilon_0, f_{t_{max}})$, post-cracking strength (ϵ_1, f_{t_1}), and the point of zero strength or complete fiber pull-out $(\epsilon_{fp}, 0)$. Table 4.6 summarizes the parameters used to model the tensile behavior of each of the six SFRCs considered in this study.

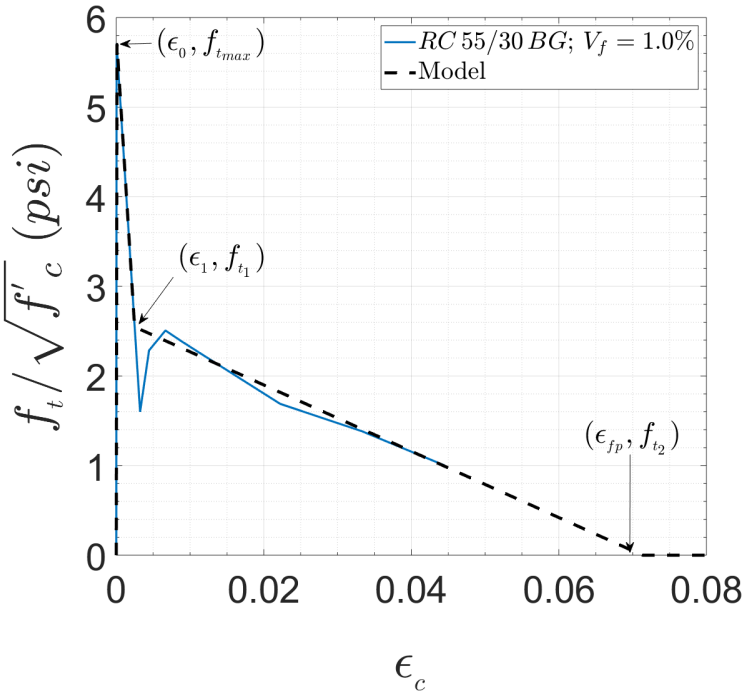

Figure 4.47: SFRC Tensile Stress Versus Strain Model (Specimen CB4).

Table 4.6: SFRC Tensile Response Model Parameters.

Coupling Beam	Fiber Type	V_f (%)	$\frac{f_{t\,max}}{\sqrt{f'_c}}$	ϵ_0 (μ)	$\frac{f_{t_1}}{\sqrt{f'_c}}$	ϵ_1 (μ)	ϵ_{fp} (%)
CB2	HE 55/35	1.25	5.4	100	3.00	2400	7.8
CB3	RC 55/30 BG	1.25	5.2	100	2.80	2000	6.5
CB4	RC 55/30 BG	1.0	5.7	100	2.55	2500	7.1
CB5	RC 80/30 BP	1.0	5.6	100	3.50	1800	6.8
CB6	HE 55/35	1.5	5.6	100	4.20	1400	7.5
CB7 and CB8	RC 80/30 BP	1.5	5.7	100	5.70	100	7.6

4.6.1.4 Flexural Strength

The shear demand of earthquake-resistant coupling beams is linked to the development of plastic hinges at the beam ends. Therefore, calculating accurately the plastic flexural strength is paramount for the seismic design of coupling beams. To this end, nonlinear sectional analysis was used to compute the flexural strength of coupling beam Specimens CB2–CB8. The analysis considered measured mechanical properties for the SFRCs and steel reinforcement by implementing the models described in the preceding sections. Furthermore, the M–ϕ analysis considered the peak axial force developed in each member and two critical sections for calculating the beam flexural strength. The cross-sections considered were: 1) section just after the termination of the U-shaped dowel reinforcement (Section B-B in Figure 4.48); and 2) section at the face of the wall support (Section A-A in Figure 4.48).

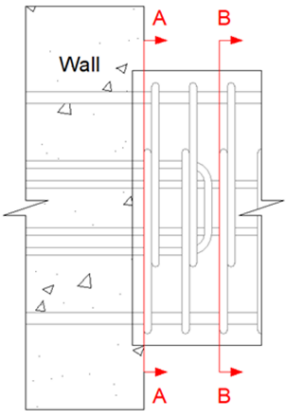

Figure 4.48: SFRC Coupling Beam Critical Sections.

For ease of comparison with measured strengths, the calculated strengths (shown in Table 4.7) are presented in terms of the shear force associated with the development of the plastic flexural strength (M_p) at each section, calculated as $V_u = \frac{2M_p}{l}$, where l was the beam span length l_n or the distance between dowel cut-off sections. The flexural strength of the SFRC coupling beams was taken as the highest moment achieved prior to exceedance of the estimated compressive strain capacity of the SFRC. A detailed discussion on estimating the compressive strain capacity of the SFRCs is provided in Section 4.6.3. Two shear demands were calcualted based on the flexural strength at section A-A and B-B. The shear demand $(V_u)_f$ resulted from M–ϕ analyses that explicitly modeled the tensile behavior of the SFRCs, whereas calculations of V_u neglected the SFRC tensile strength (see Table 4.7).

Table 4.7: Calculated Peak Shear Demands using M–ϕ Analysis.

				M_p at Section B-B Dowel Cut-off Section				M_p at Section A-A Wall Section	
Specimen	f'_c (psi)	P_u (kips)	V_{max} (kips)	$(V_u)_f$ (kips)	V_u (kips)	$\frac{(V_u)_f}{V_{max}}$	$\frac{V_u}{V_{max}}$	V_u (kips)	$\frac{V_u}{V_{max}}$
CB2	8840	144	100	117	111	1.17	1.11	101	1.01
CB3	8630	116	94.6	110	105	1.16	1.11	96.8	1.02
CB4	9260	98.6	75.0	93.4	88.1	1.25	1.17	84.6	1.13
CB5	9750	91.1	82.9	94.9	88.8	1.14	1.07	85.7	1.03
CB6	7950	73.6	78.2	99.8	88.0	1.28	1.13	84.0	1.07
CB7	9330	125	106	130	111	1.23	1.05	104	0.99
CB8	8490	89.9	81.9	111	98.7	1.36	1.21	92.3	1.13
					Average =	1.23	1.12	Average =	1.05

Accounting for the tensile behavior of the SFRCs led to calculated shear demands based on the flexural capacity at Section B-B 15–35% greater than the measured strengths, whereas disregarding the SFRC tension resulted in calculated shear demands 6–20% larger than the measured strengths. The sudden termination of the dowel reinforcement creates a disturbance that weakens the section, which is believed to be one of the reasons for the overestimated shear demands. Furthermore, the close spacing of the reinforcement within the plastic hinge region can affect the distribution of fibers along the cross section, potentially decreasing their effectiveness. The calculated demands based on the flexural strength at section A-A were, on average, 5% greater than the measured strengths. Despite the slight overestimation, M–ϕ analysis resulted in calculated shear demands based on the flexural strength at the beam-wall interface in good agreement with the measured strengths.

4.6.1.5 Experimental Moment Curvature Response

The curvatures calculated for the different marker strips were used to define the M–ϕ responses at the plastic hinges of the specimens (see Appendix A.5 for details on curvature calculations). As discussed in Section 4.4, the point of contraflexure was located approximately at mid-span throughout the tests. Therefore, the moment at any given cross-section can be calculated as the shear force times the distance from mid-span to the cross-section under consideration. Note that the curvatures calculated for the marker strips containing the beam-wall interface are due to reinforcement bond-slip (strain penetration) rotations and thus, not actual curvatures. Instead, the rotations are considered as "apparent" curvatures for the purpose of the following discussion.

Experimental M–ϕ responses were calculated for the dowel cutoff and the beam-wall interface sections at each beam end. For comparison purposes, the experimental M–ϕ curves are plotted along with analytical M–ϕ responses calculated for increasing values of axial force, starting with zero axial force and increments of $0.02 f'_c A_g$. As discussed in Section 4.6.1.4, accounting for the SFRC tensile response in M–ϕ analyses led to an overestimation of the flexural strength and thus, the analytical M–ϕ responses were calculated neglecting the SFRC tensile response. The experimental M–ϕ responses for the top and bottom plastic hinges of Specimens CB2–CB8 are shown in Figure 4.49 through Figure 4.55. Note that in Figures 4.52, 4.53 and 4.55, strength drops corresponding to adjustment of axial restraint are identified with black stars. Also, the maximum compressive strain of the concrete (ϵ_c) for the analytical M–ϕ curves is identified with numbered red dotted lines. In Figures 4.49–4.55 the experimental M–ϕ responses are shown for both the positive (plotted in blue) and negative (plotted in red) loading directions and are identified with a letter P or N for positive and negative loading directions, respectively.

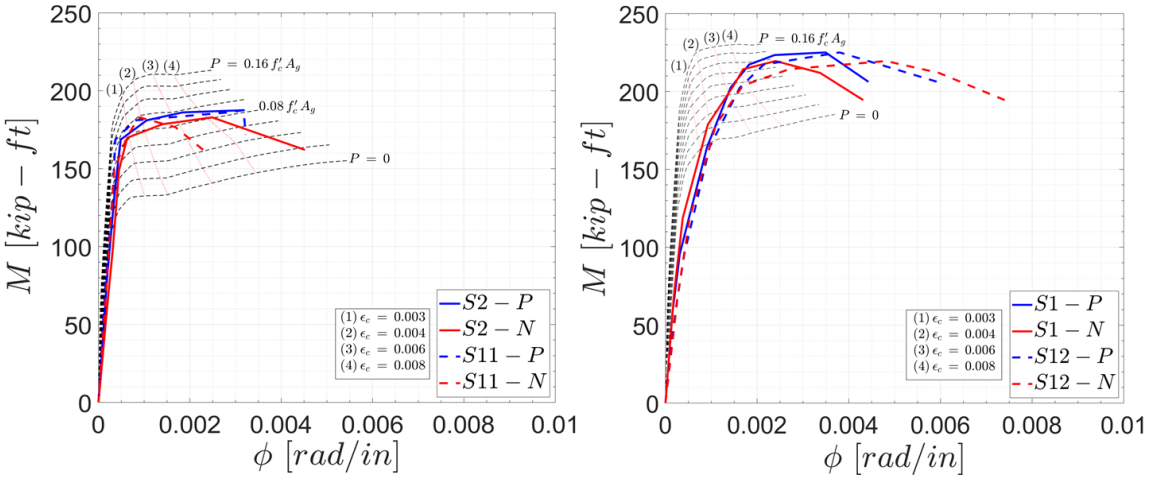

a) Response of the Dowel Cutoff Sections

b) Response of the Beam-Wall Interfaces

Figure 4.49: Experimental Moment Versus Curvature Responses - Specimen CB2.

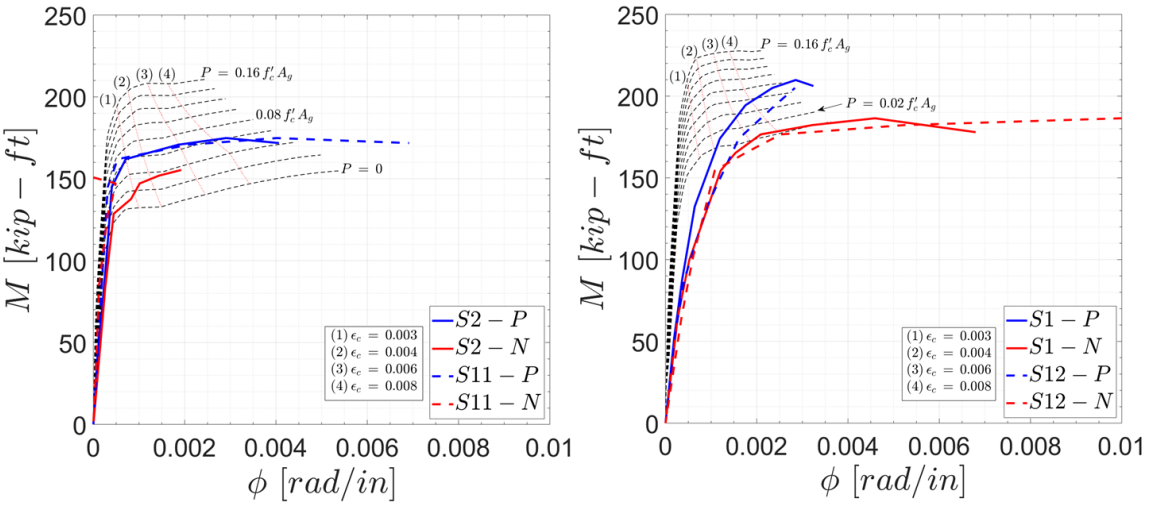

a) Response of the Dowel Cutoff Sections

b) Response of the Beam-Wall Interfaces

Figure 4.50: Experimental Moment Versus Curvature Responses - Specimen CB3.

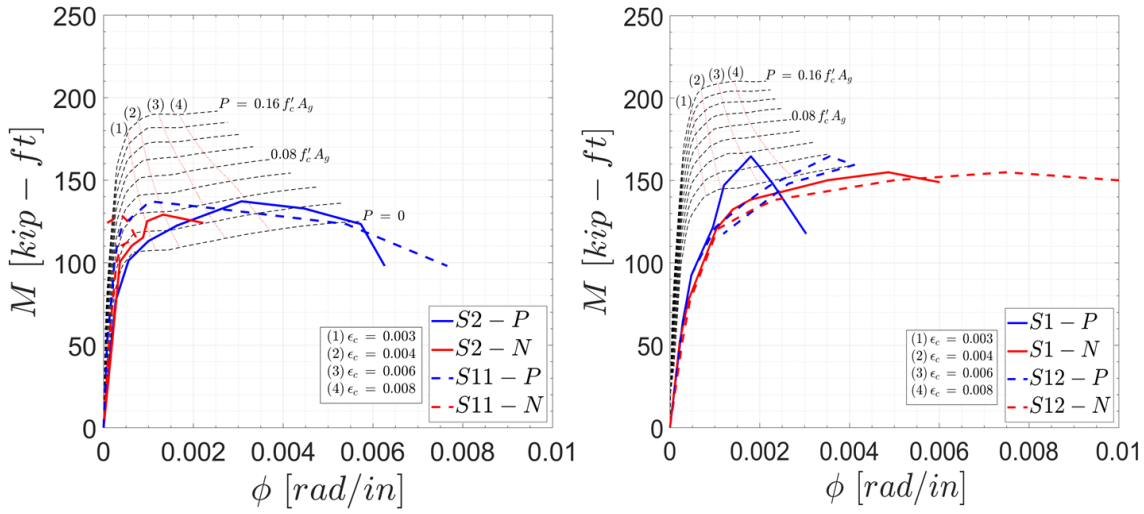

a) Response of the Dowel Cutoff Sections

b) Response of the Beam-Wall Interfaces

Figure 4.51: Experimental Moment Versus Curvature Responses - Specimen CB4.

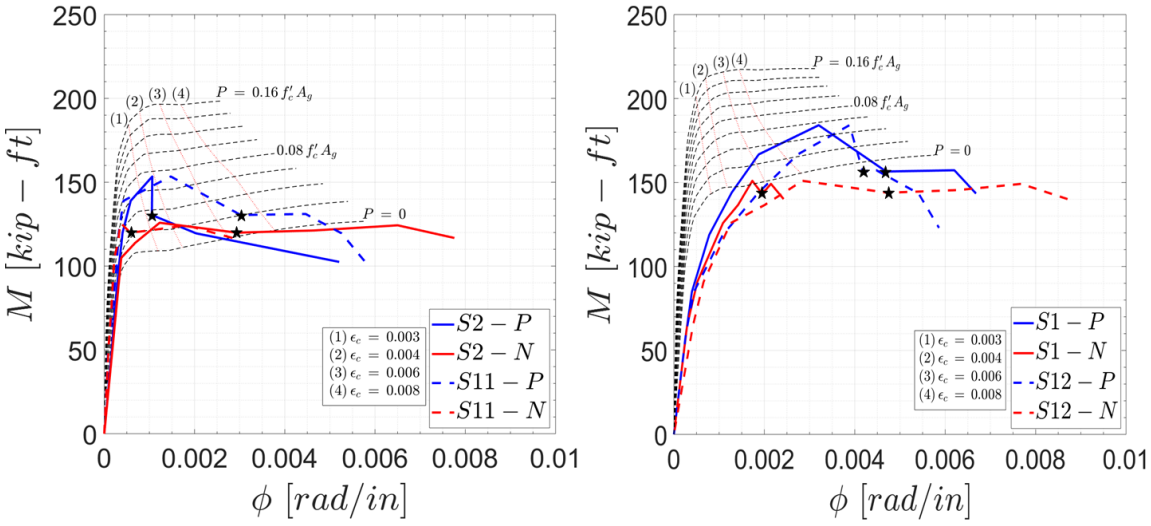

a) Response of the Dowel Cutoff Sections

b) Response of the Beam-Wall Interfaces

Figure 4.52: Experimental Moment Versus Curvature Responses - Specimen CB5.

As expected, the beam-to-wall connections of the precast SFRC coupling beams were significantly more flexible than the sections within the SFRC beams and M–ϕ analysis cannot replicate the effective flexural rigidity of the beam-to-wall connections. In contrast, the flexural rigidity of the dowel cutoff sections are in good agreement with the calculated M–ϕ responses. Furthermore, as shown in Figures 4.49–4.52, the dowel cutoff section underwent large curvatures, well into the inelastic range of response. Maximum curvatures were typically in the range of 0.002 to 0.007 rad/in. and often exceeded the analytical curvatures corresponding to maximum compressive strains of 0.006 and 0.008. These large curvatures at the dowel cutoff sections are consistent with the observed damage and the formation of plastic hinges at the ends of coupling beams with span-to-depth ratio of 3.0. Note that, in some cases, the M–ϕ response exhibited an unusual reverting behavior due to the accumulation of large plastic rotations in the opposite direction, as shown in Figure 4.50 and Figure 4.51.

Given the different marker layout used for Specimens CB6–CB8 ($l_n/h = 2.0$) the experimental M–ϕ responses at the beam ends were calculated using 2 marker strips. Thus, the curvatures for the top and bottom plastic hinges (Top PH and Bottom PH) were calculated using Strips 2 and 3, and Strips 8 and 9, respectively (see Figures A.6 and A.7). This resulted in plastic hinge curvatures calculated over comparable gauge lengths of 5 in. and 6 in. for specimens with span-to-depth ratios of 3.0 and 2.0, respectively. The "apparent" curvatures at the beam-wall interfaces were calculated using gauge lengths of approximately 5.6 and 5.1 in. for specimens with span-to-depth ratio of 3.0 and 2.0, respectively. The behavior of the beam-wall interfaces is most appropriately described in terms of their moment-rotation response, which was discussed in Section 4.5.

The experimental M–ϕ responses for Specimens CB6 through CB8 are shown in Figures 4.53 to 4.55, where the bending moment for the plastic hinge responses corresponds to the moment acting at the dowel cutoff section located approximately at the center of Strip 2 or Strip 9.

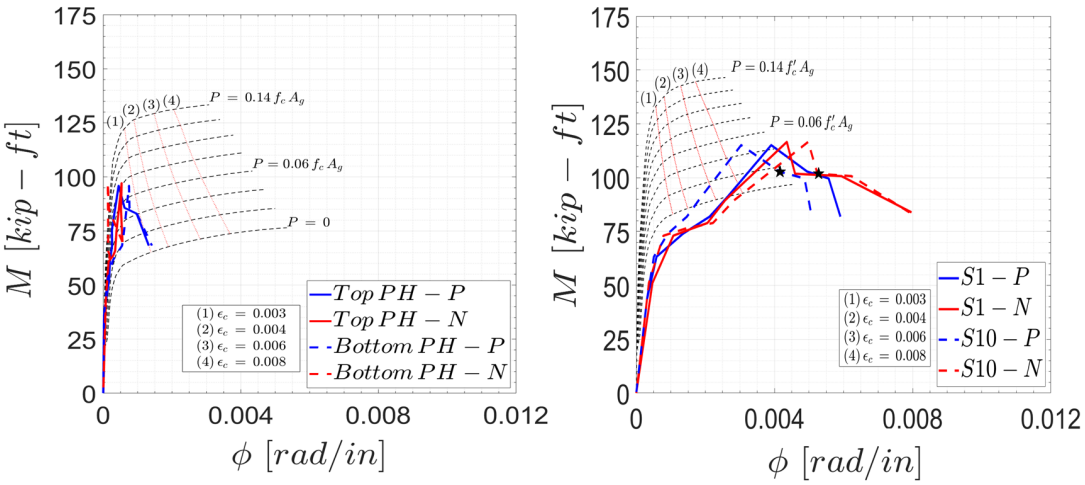

a) Average Response of the First 2 Strips Within SFRC Coupling Beam

b) Response of the Beam-Wall Interfaces

Figure 4.53: Experimental Moment Versus Curvature Responses - Specimen CB6.

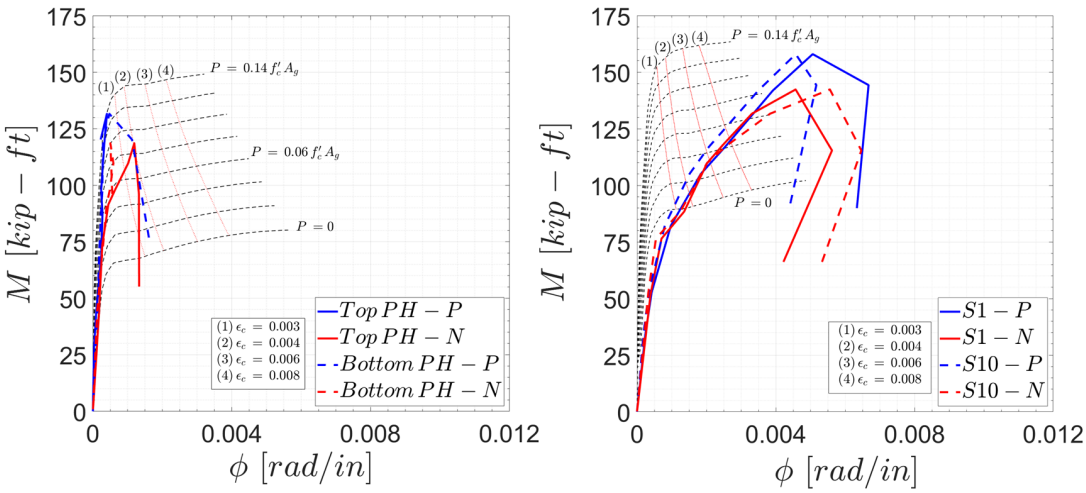

a) Average Response of the First 2 Strips Within SFRC Coupling Beam

b) Response of the Beam-Wall Interfaces

Figure 4.54: Experimental Moment Versus Curvature Responses - Specimen CB7.

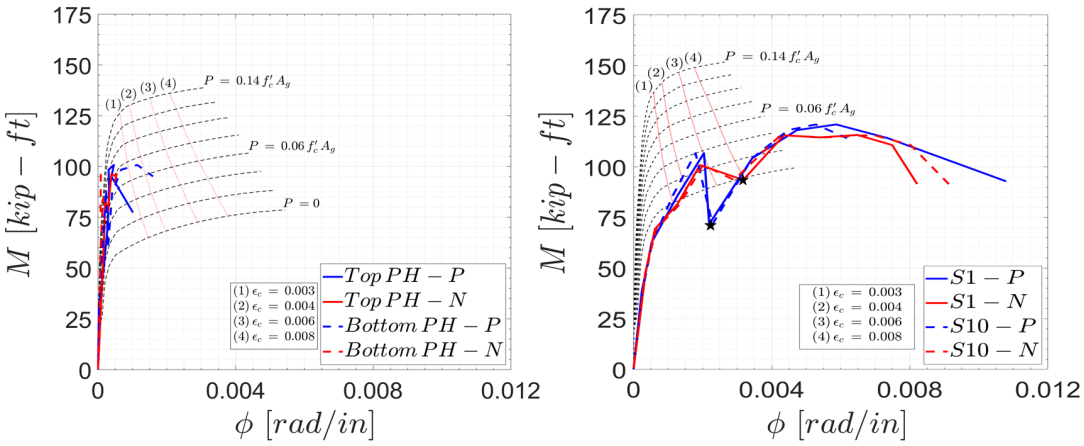

a) Average Response of the First 2 Strips Within SFRC Coupling Beam

b) Response of the Beam-Wall Interfaces

Figure 4.55: Experimental Moment Versus Curvature Responses - Specimen CB8.

Similar to Specimens CB2 to CB5, the analytical M–ϕ responses for Specimens CB6 to CB8 were able to replicate well the flexural rigidity at the dowel cutoff section, but not at the beam-to-wall connections. Comparing the M–ϕ responses of specimens with span-to-depth ratio of 3.0 and 2.0, it is clear that flexure played a much larger role in the behavior of Specimens CB2 to CB5 than in Specimens CB6 to CB8. In fact, the flexural response at the dowel cutoff section of Specimens CB6 to CB8 exhibited little-to-no inelastic flexural deformations.

4.6.2 Flexural Rigidity for Use in Linear Elastic Analysis

Estimating deformation demands on reinforced concrete structures requires proper selection of member effective flexural stiffness (EI_{eff}), considerations for stiffness and strength degradation, and other deformation mechanism such as reinforcement slip and potentially, shear sliding in members subjected to high shear stresses. Nowadays, nonlinear dynamic analyses are commonly used for the design of high-rise structures in regions of high seismicity. However, linear elastic analyses are often used for the design of typical buildings without irregularities. Therefore, realistic effective flexural stiffness for SFRC coupling beams are needed for use in linear elastic analysis of coupled wall systems.

The effective flexural rigidity of the coupling beam specimens was calculated based on the measured shear force and the average relative end displacement due to bending assuming perfect fixity at both ends. The average relative end displacement due to flexural deformations including concentrated rotations at the beam-wall interface, $(\delta_f)_{avg}$, was calculated using the second moment-area theorem and the calculated curvature distribution based on Optotrak™ marker data. The relative end displacement was calculated for both ends of the coupling beams and the average was taken as $(\delta_f)_{avg}$. The effective flexural rigidity was calculated as:

$$EI_{eff} = \frac{V l_n^3}{12 (\delta_f)_{avg}} \tag{4.3}$$

where V is the shear force acting on the beam and l_n is the beam span length. The effective flexural rigidity of Specimens CB2 to CB8, normalized by the flexural rigidity of the gross section (EI_g) throughout the range of applied drifts, is shown in Figure 4.56; where the concrete Young's modulus was calculated as $E = 57000\sqrt{f'_c}$.

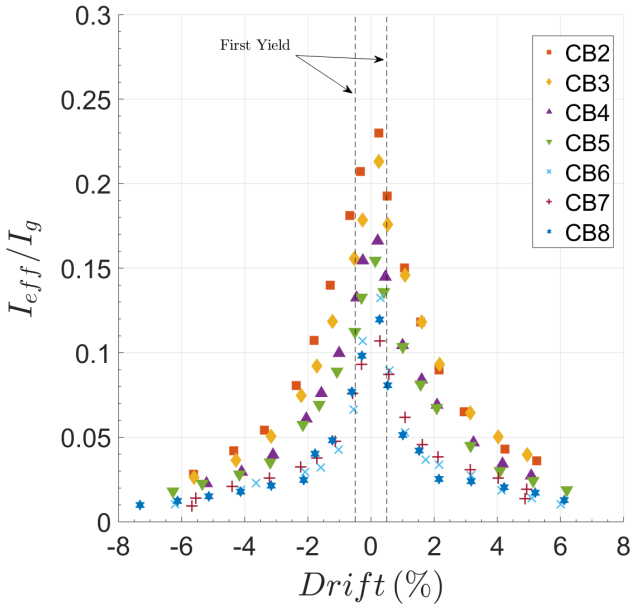

Figure 4.56: Effective Flexural Rigidity for Equivalent Linear Elastic Analysis.

The effective, cracked elastic, flexural stiffness at first yield for the SFRC coupling beams ranged from 0.08 to 0.19 $\mathrm{EI_g}$, which is approximately between $\frac{1}{4}$ to $\frac{2}{3}$ of the effective flexural rigidity recommended in ASCE/SEI 41-13 of $0.3\mathrm{EI_g}$ (American Society of Civil Engineers, 2014). Flexural rigidity values at first yield for Specimens CB2 to CB5 are similar to the findings of Elwood and Eberhard (2009) from a study on over 300 columns, indicating that $\mathrm{EI_{eff}}$ for members subjected to axial loads below $0.1f'_c\,A_g$ is approximately $0.2\mathrm{EI_g}$. In contrast, Specimens CB6 to CB8 exhibited a smaller effective stiffness, approximately $0.08\mathrm{EI_g}$, which is attributed to a higher contribution of bar-slip deformations to the overall response. Despite the lower effective stiffness of Specimens CB6 to CB8, the precast SFRC coupling beams reported herein exhibited effective flexural stiffness comparable to those of coupling beams with and without diagonal bars from multiple studies, as summarized in Son Vu et al. (2014). Moreover, the effective flexural stiffness are also in good agreement with those for SFRC coupling beams of $0.2\,\mathrm{EI_g}$ and 0.13 to $0.2\,\mathrm{EI_g}$ reported by Lequesne (2011) and Setkit (2012), respectively. In conclusion, for linear elastic

analysis, an effective, cracked leastic, flexural stiffness of approximately $0.1EI_g$ and between 0.15 to $0.2EI_g$ are appropriate for precast SFRC coupling beams without diagonal bars and with span-to-depth ratios of 2.0 and 3.0, respectively.

4.6.3 SFRC Compressive Strain Limits

Estimating experimentally limiting compressive strains for concrete in members subjected to large displacement reversals proves to be a challenging endeavor primarily due to the accumulation of tensile strains and resulting elongation of the member and extensive damage sustained by concrete in plastic hinges. The discussion presented herein aims to estimate limiting in-place concrete compressive strains for the different SFRCs investigated in this study. For this analysis, two limiting compressive strains were defined, i.e., the first crushing strain limit and the ultimate compressive strain of the SFRC. Crushing strain limits ($\epsilon_{UB_{cr}}$ or $\epsilon_{LB_{cr}}$ for upper- and lower-bound estimates, respectively) were defined as the maximum average compressive strain corresponding to first concrete crushing within the plastic hinges and the ultimate strains (ϵ_{UB_u} or ϵ_{LB_u} for upper- and lower-bound estimates, respectively) were defined as the maximum average compressive strain sustained up to the second-to-last drift cycle prior to a strength loss of 20%. The calculated strains at the second-to-last cycle sustaining a shear force $V \geqslant 0.8\,V_{max}$ were preferred over those corresponding to later cycles because the calculated strains for the later cycles were excessively large and unreliable due to extensive damage sustained by the plastic hinges.

Despite the large shear demands the specimens were subjected to and their low span-to-depth ratios, data indicated that a linear strain gradient provides a reasonable estimate of the strain distribution along the cross section of the beams with span-to-depth ratio of 3.0 (see Figure 4.57, where the location of the calculated strains is measured from the left column of markers shown in Figure A.10 of Appendix A.5). In contrast, strain linearity was not appropriate for the beams with span-to-depth ratio of 2.0 (Specimens CB6 to CB8).

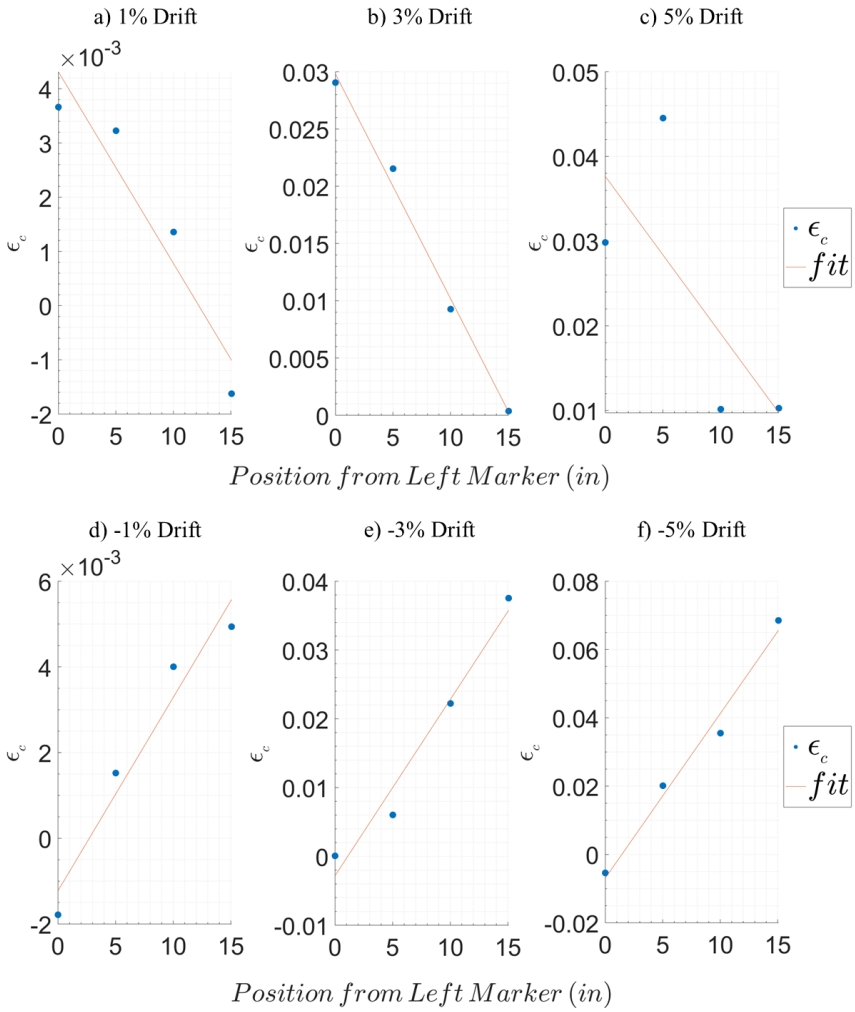

Figure 4.57: Sample Strain Profile and Linear Fit - Top Plastic Hinge of Specimen CB2.

For coupling beams with $l_n/h = 3.0$, linear extrapolation was used to calculate the strains occurring at the edges of the beams. Towards the end of the tests, most of the damage concentrated near the section corresponding to the dowel reinforcement cut-off; therefore, the strains at the top and bottom plastic hinges of Specimens CB2 to CB5 were calculated with the Optotrak™ markers of Strips 2 and 11, respectively. Note that Specimen CB1 was not included in this analysis due to its premature

shear failure. Coupling beams with $l_n/h = 2.0$ exhibited a higher concentration of damage at the beam-wall interfaces. Therefore, the compressive strains at the beam ends were calculated based on the 2^{nd} row of markers within the beams and the markers on the adjacent support. Because the interfaces were located between the markers considered for the analysis, all deformations were assumed to occur within the coupling beam, i.e., the end blocks were assumed rigid. This approach resulted in strains calculated over the same gauge length for all coupling beams (approximately 5 in).

Concrete cracking and spalling sometimes compromised measurements from Optotrak™ markers, particularly during the late cycles at large displacements. In such cases, the average plastic hinge curvatures were calculated using markers that were not compromised by the extensive damage to the concrete. Moreover, accumulation of average tensile strains due to increasing cyclic displacements and cracks not perfectly closing upon displacement reversal may result in compression zones with measured tensile strains. Further, in some cases, large tensile strains near the center of the cross section resulted in linear fits shifted towards positive (tensile) strains, leading to a similar shift in the strains calculated at the edge of the concrete (see Figure 4.58). Despite the poor linear fits shown in Figure 4.58, in general, linear fits approximated well the average strains along the depth of the beams.

Linearity of the strain profiles was evaluated using Pearson's linear correlation coefficients (r). Correlation coefficients were calculated for linear fits of the strains occurring within marker strips 2 and 11 of Specimens CB2–CB5 (refer to Figure A.10 for marker strip locations). Twelve fits were selected per coupling beam at drifts of +/- 1.0, 3.0 and 5.0%, resulting on 48 different linear fits and corresponding r-values. Figure 4.59 shows a distribution plot of the calculated r coefficients that supports the assumption of linearity for Specimens CB2 to CB5. Moreover, the curvatures calculated using linear fits ($\phi_{lin-fit}$) were in good agreement with those calculated using only the strains at the location of the outer markers (ϕ_{2pt}), as shown in Figure 4.60. Therefore, it was considered reasonable to use $\phi_{lin-fit}$ to calculate the strains at the beam edges.

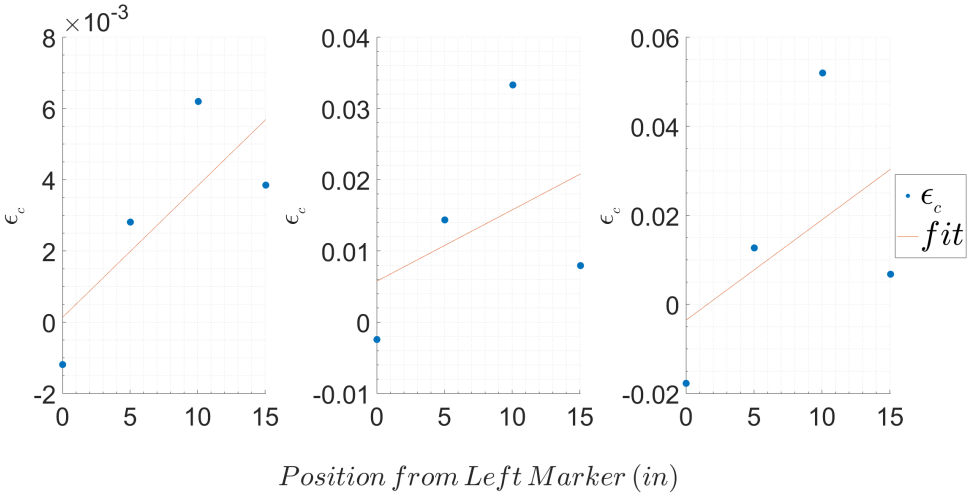

Figure 4.58: Strain Profile and Linear Fit - Top Plastic Hinge of Specimen CB4.

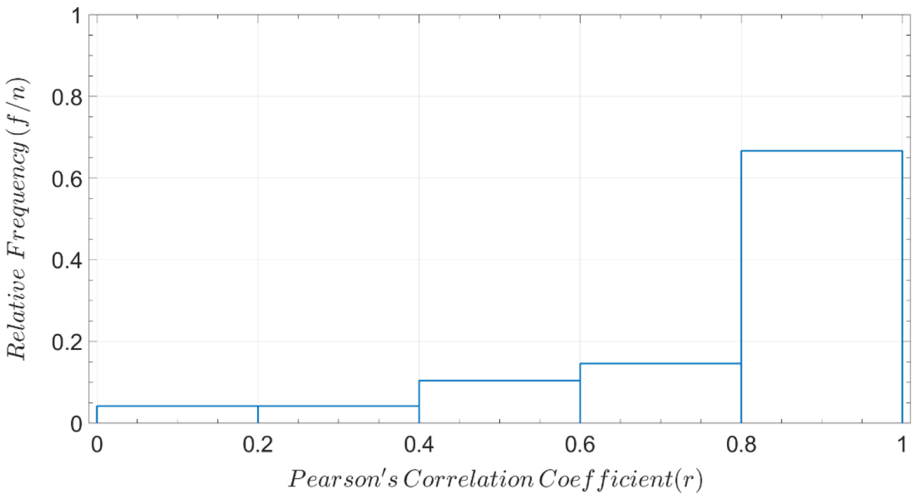

Figure 4.59: Pearson's Correlation Coefficients for Strain Profile Linear Fits ($f =$ frequency; $n =$ sample size).

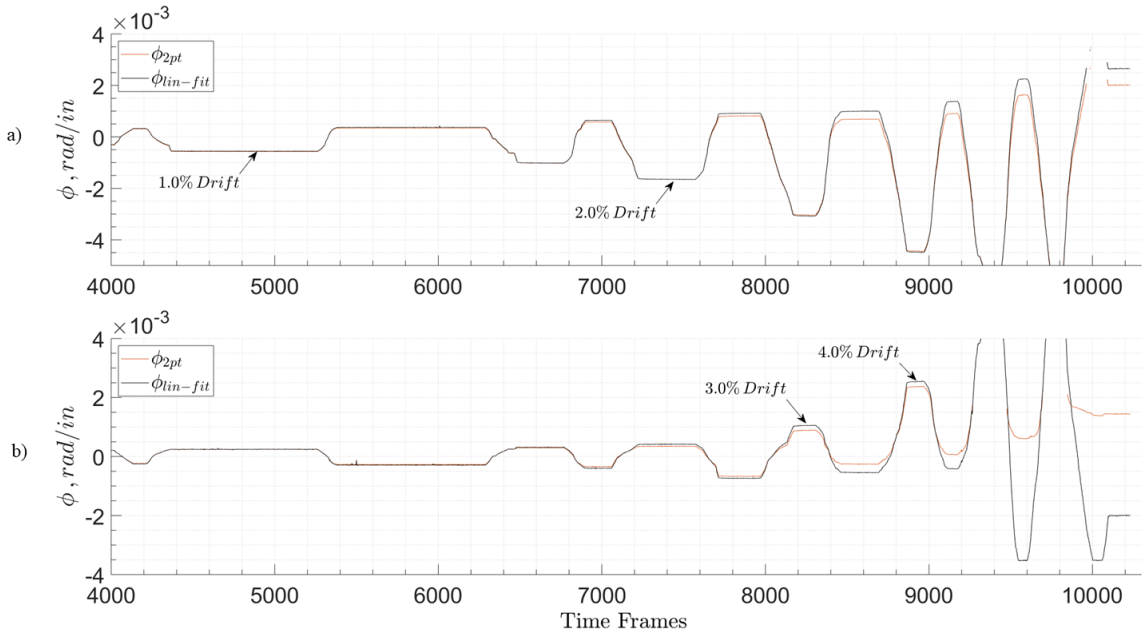

Figure 4.60: Calculated Curvatures - Specimen CB4. a) Top Hinge (Strip 2); b) Bottom Hinge (Strip 11).

Due to the damage and accumulation of tensile strains, an adjustment was required to estimate the actual compressive strain sustained by the concrete within the plastic hinges. Consider the beam shown in Figure 4.61. Upon loading reversal, the open flexural cracks begin to close while closed cracks on the opposite edge of the beam begin to open. Eventually, over a deformation range, moment is carried across the open crack by the tension and compression of the flexural reinforcement, with a corresponding decrease in stiffness. As soon as the flexural cracks on the compression side are closed, compression starts being transferred through the concrete as the compression zone gets engaged. Consequently, an increase in flexural stiffness must be reflected in the moment-rotation hysteresis upon crack closing. If closing of flexural cracks is identified for each loading cycle, then, closure of flexural cracks provides a realistic reference point for the calculation of compressive strains in the concrete. Crack closure was thus assumed to correspond to the state of zero

compressive strain in the SFRC at the beam edge. The change in strain beyond crack closure was thus taken equal to the compressive strain in the concrete.

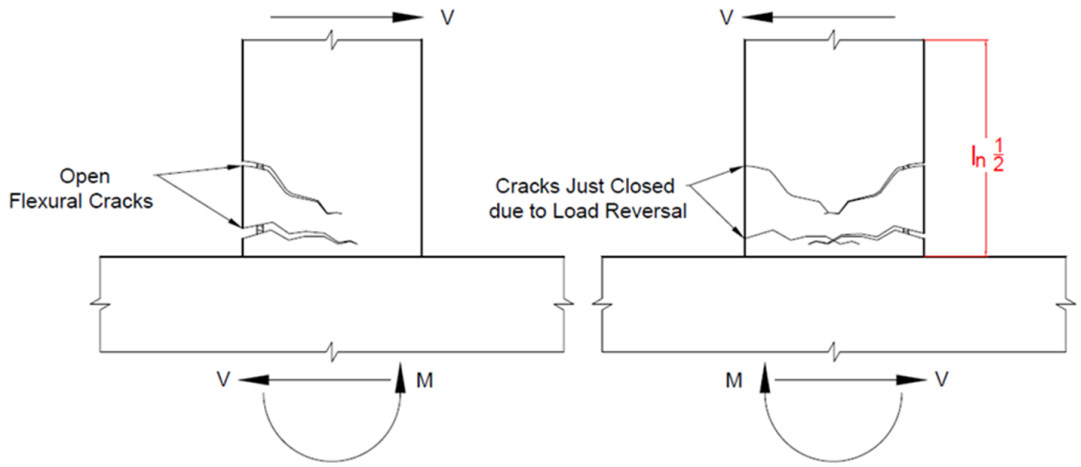

Figure 4.61: Opening and Closing of Flexural Cracks during Reversed Cyclic Displacements.

To identify the instant at which the compressive strain in the SFRC was assumed to be zero, the plastic hinge moment-rotation (M–θ) hysteresis for Specimens CB2 to CB5 was examined to identify increases in stiffness in the reloading stages of each drift cycle. The point at which the stiffness of the M–θ hysteresis began to increase was identified for each loading direction, using tangents corresponding to the maximum and minimum average slopes, as shown in Figure 4.62. The slopes throughout a given M–θ cycle were calculated as linear fits of ten consecutive data points. The intersection of these tangents was then assumed to coincide with the closing of flexural cracks and thus, the instant of zero compressive strain at the beam edge. Strains estimated following this approach are considered upper-bound estimates of the compressive strain (ϵ_c) at each drift cycle.

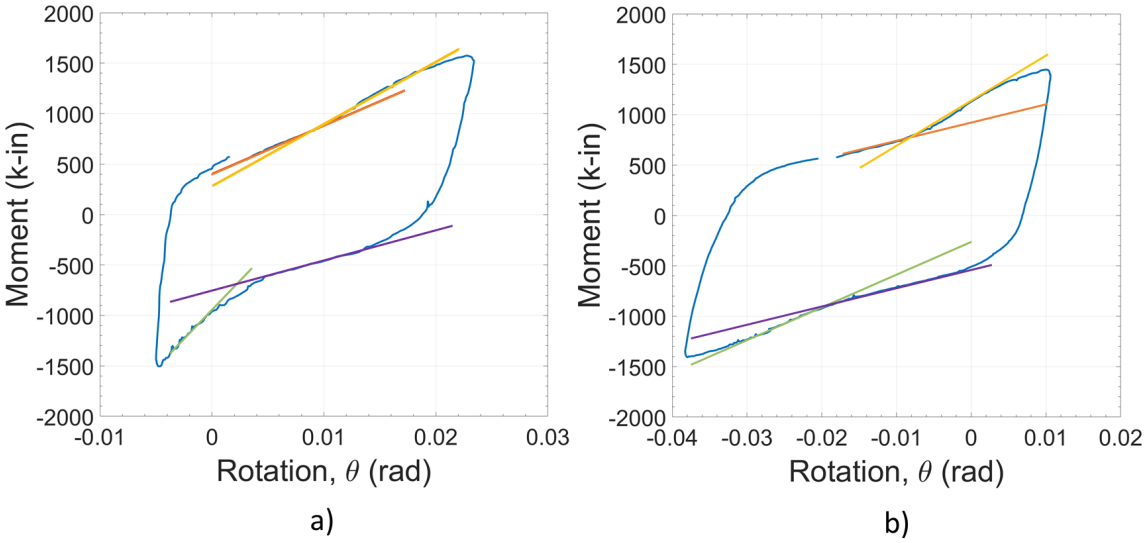

Figure 4.62: Tangents used to Calculate Upper-Bound Compressive Strain in Specimen CB5. a) Bottom Hinge; b) Top Hinge.

For lower-bound estimates of the compressive strain, a second instant of zero strain was considered. By the time the section achieves its maximum flexural stiffness in a given a cycle, the concrete in the compression zone has already been strained in compression. Therefore, the point at which the slope of the hysteresis loop is maximum was also considered a point of zero compressive strain, leading to a lower-bound estimate of the SFRC compressive strain. An example of the location of the reference points used for the calculation of upper-bound (diamond marker) and lower-bound (star marker) compressive strains is presented in Figure 4.63a. Figure 4.63b, on the other hand, shows the calculated compressive strains throughout a given cycle for the top right edge of Specimen CB5 (i.e., to the right of markers 10 and 14 shown in Figure A.10). The strains ϵ_L and ϵ_R in Figure 4.63b correspond to the calculated strains at the left and right edges of the beam, respectively.

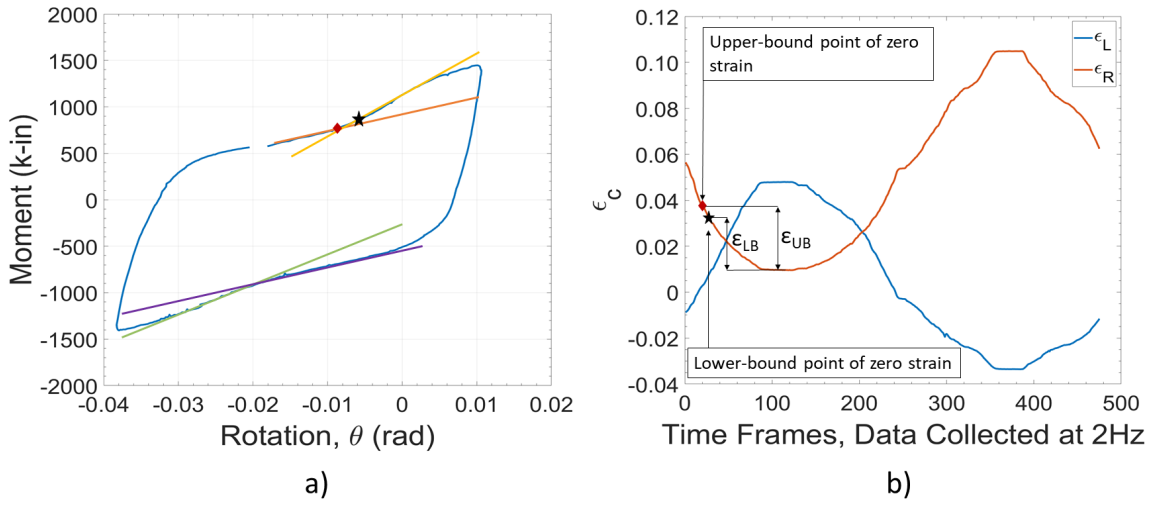

Figure 4.63: Determination of Lower- and Upper-Bound Compressive Strains. a) Points Corresponding to Zero Compressive Strain on a M–θ Cycle; b) Calculated Strains at Beam Edges.

According to the described analysis, the upper-bound and lower-bound compressive strains ($\epsilon_{c_{UB}}$ and $\epsilon_{c_{LB}}$, respectively) were calculated at each side of the top and bottom plastic hinges of Specimens CB2 to CB5. Figures 4.64 through 4.67 show the calculated upper- and lower-bound compressive strains for Specimens CB2 to CB5, where ϵ_{TL} and ϵ_{TR} are the calculated strains at the left and right sides of the top plastic hinge, respectively. Similarly, ϵ_{BL} and ϵ_{BR} correspond to the calculated strains at the bottom plastic hinge (left and right sides with respect to the marker grid, see Figure A.10).

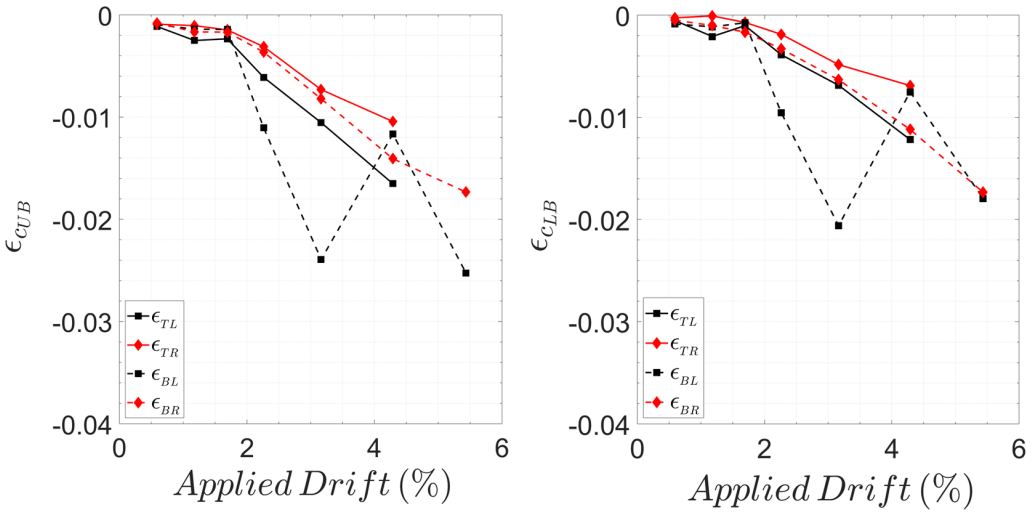

Figure 4.64: Calculated Compressive Strains - Specimen CB2. a) Upper-bound Estimate; b) Lower-bound Estimate.

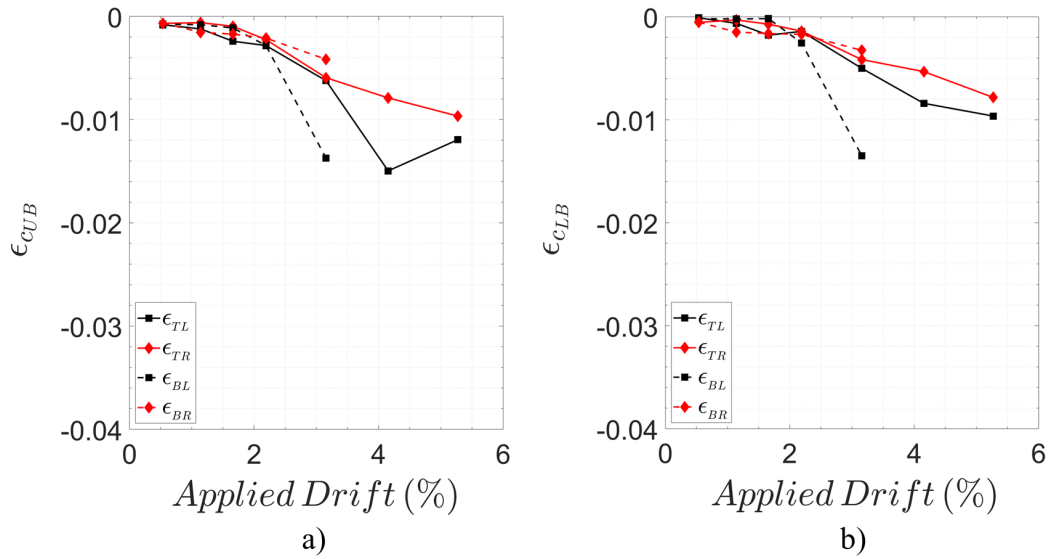

Figure 4.65: Calculated Compressive Strains - Specimen CB3. a) Upper-bound Estimate; b) Lower-bound Estimate.

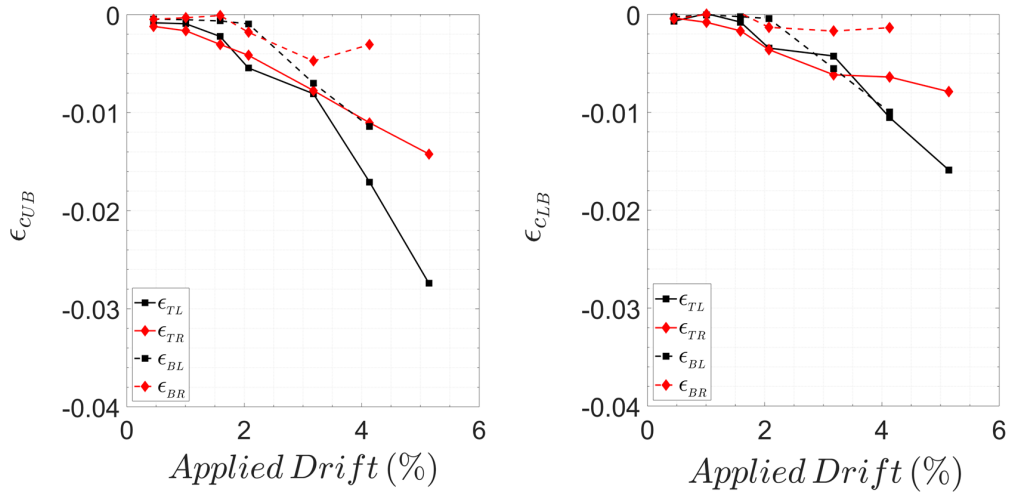

Figure 4.66: Calculated Compressive Strains - Specimen CB4. a) Upper-bound Estimate; b) Lower-bound Estimate.

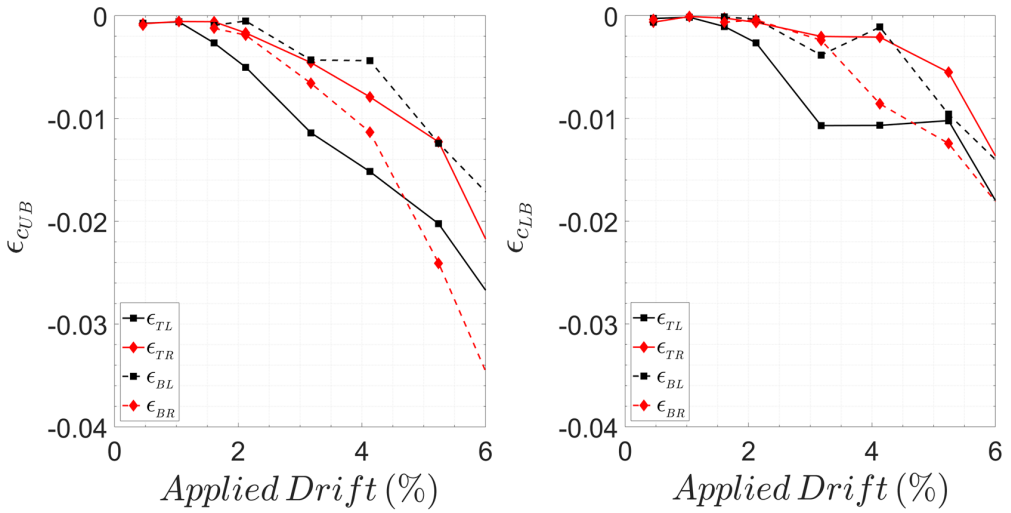

Figure 4.67: Calculated Compressive Strains - Specimen CB5. a) Upper-bound Estimate; b) Lower-bound Estimate.

As discussed at the beginning of this section, a different approach was taken to calculate the compressive strains for the specimens with aspect-ratio of 2.0 (i.e. Specimens CB6 to CB8) because the procedure described for the more slender beams was not applicable to these specimens. The compressive strains reported herein were calculated at the location of the outermost markers, not at the edges of the beams and thus, are considered a lower-bound estimate of the compressive strains at the edges. Figures 4.68 through 4.69 show the calculated average compressive strains for Specimens CB6 to CB8.

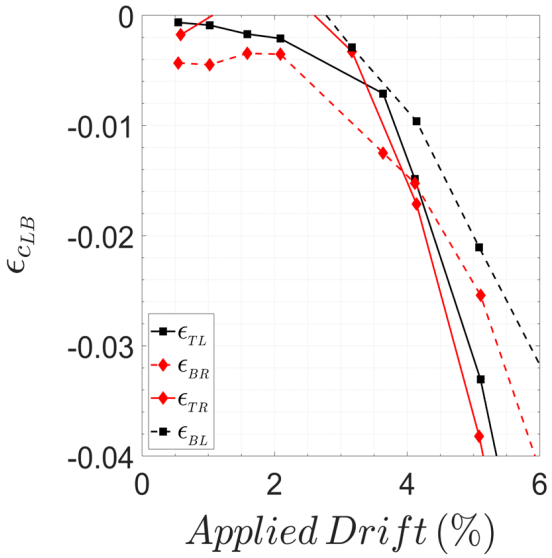

Figure 4.68: Calculated Lower-Bound Compressive Strains - Specimen CB6.

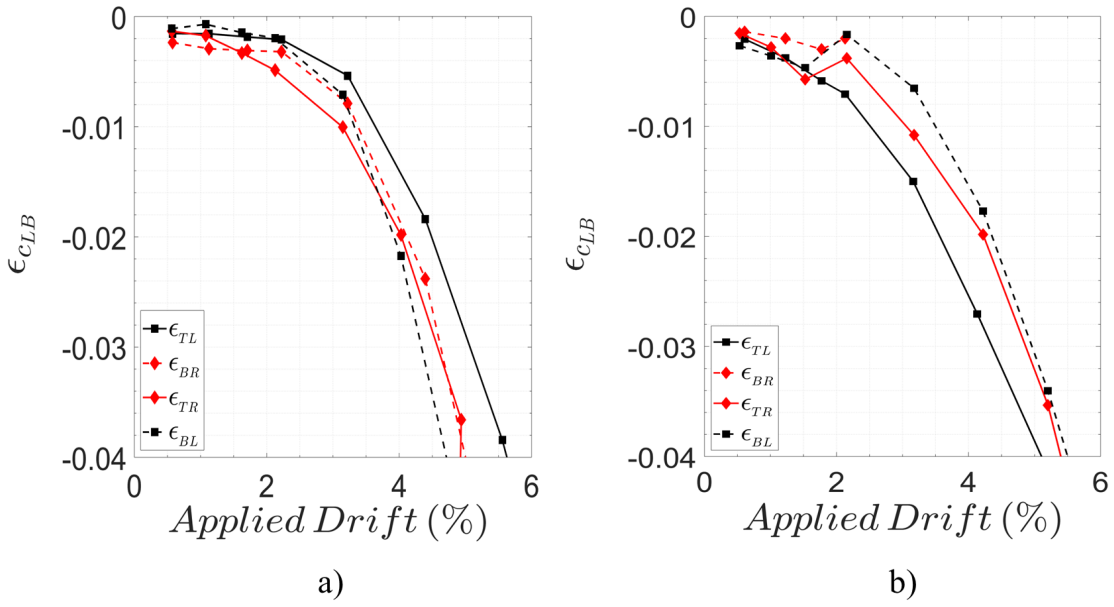

Figure 4.69: Calculated Lower-Bound Compressive Strains. a) Specimen CB7; b) Specimen CB8.

Despite the challenges discussed thus far, in most cases reasonable limit compressive strain estimates were calculated for the investigated SFRCs. To identify the drift at which crushing of the compression zone was first noticed and thus, estimate the corresponding crushing strain from the curves shown in Figures 4.64 through 4.69, changes in the compressive strain versus drift responses were investigated. For this purpose, two best-fit lines were drawn over the average compressive strain versus drift responses, as shown in Figure 4.70; one of the two lines corresponded to a linear fit of the average compressive strain at 0.5, 1.0, and 1.5% drift, and the second line to a linear fit of the compressive strains at 4.0, 5.0, and 6.0% drift. The intersection of the two lines was assumed to correspond to the strain at which significant softening of the compression zone began to occur and was taken as a reasonable estimate of the drift at which onset of crushing occurred. Furthermore, drifts corresponding to concrete crushing determined from the strain-drift

responses agreed well with the drifts at which evidence of crushing could be observed. Sample images showing the approximate drifts at which initial crushing was identified at all four corners of Specimen CB5 are provided in Figure 4.71.

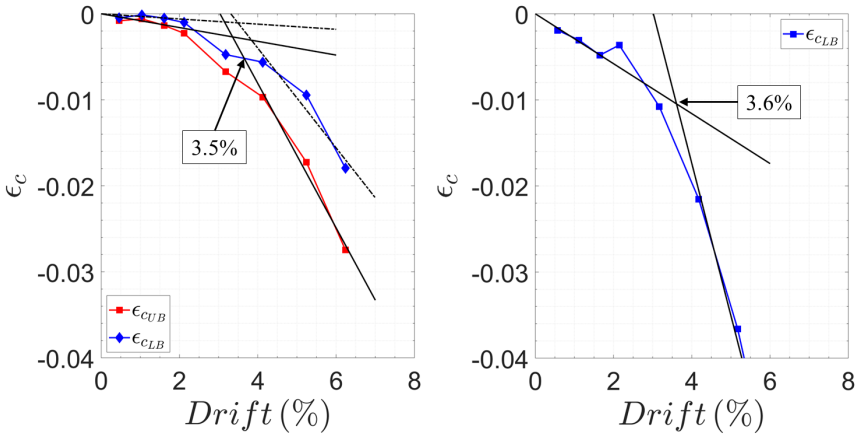

Figure 4.70: Average Concrete Compressive Strain versus Drift. a) Specimen CB5 Upper- and Lower-Bound Strains; and b) Specimen CB8 Interface Lower-Bound Strains.

The SFRC compressive strain limits calculated at each corner of the coupling beam specimens, including the drift cycle corresponding to first crushing and ultimate state, are provided in Table 4.8. Once again, top left (TL), top right (TR) and so on are with respect to the Optotrak™ marker grid shown in Figure A.10 (see also Appendix A.4). Note that because the damage shown in Figure 4.71 is on the back side of Specimen CB5, the directions are inverted; i.e., the left edge of the beam corresponds to the right edge with respect to the Optotrak™ marker layout.

Based on the calculated compressive strains, a strain of 0.006 seems to be reasonable as a measure of the strain at the onset of concrete cover crushing. On the other hand, ultimate strain capacity limits of 0.02 and 0.012 for Class I, and Class II and III SFRCs, respectively, seem appropriate for determining expected flexural strength and corresponding curvature.

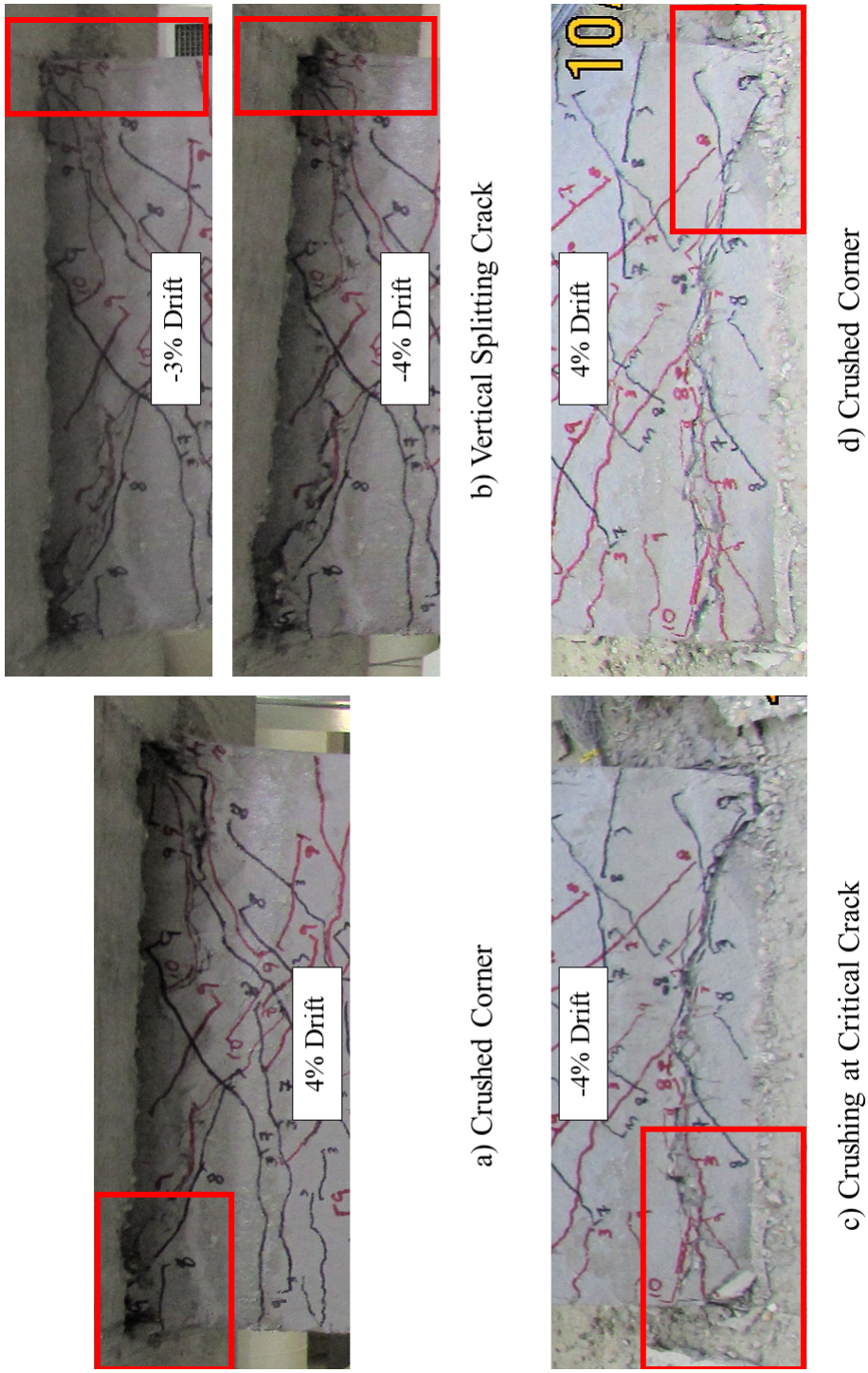

Figure 4.71: Evidence of Crushing - Specimen CB5.

Table 4.8: SFRC Limiting Compressive Strain in Plastic Hinge Regions.

$l_n/h = 3.0$							
Specimen	Location	$\epsilon_{UB_{cr}}$	$\epsilon_{LB_{cr}}$	Drift (%)	ϵ_{UB_u}	ϵ_{LB_u}	Drift (%)
CB2	TL	-0.011	-0.007	-3%	-0.017	-0.012	-5%
	TR	-0.007	-0.005	3%	-0.010	-0.007	4%
	BL	-0.012	-0.008	4%	-0.012	-0.008	4%
	BR	-0.008	-0.006	-3%	-0.017	-0.017	-5%
	Average =	-0.009	-0.006	-	-0.014	-0.011	-
CB3	TL	-0.006	-0.005	-3%	-0.015	-0.010	-5%
	TR	-0.006	-0.004	3%	-0.008	-0.005	4%
	BL	-0.014	-0.013	3%	-	-	4%
	BR	-	-	-	-	-	-5%
	Average =	-0.009	-0.008	-	-0.011	-0.007	-
CB4	TL	-0.008	-0.004	-3%	-0.027	-0.016	-5%
	TR	-0.008	-0.006	3%	-0.011	-0.006	4%
	BL	-0.007	-0.006	3%	-0.011	-0.010	4%
	BR	-0.005	-0.002	-3%	-	-	-5%
	Average =	-0.007	-0.004	-	-0.017	-0.011	-
CB5	TL	-0.015	-0.011	-4%	-0.020	-0.011	-5%
	TR	-0.008	-0.002	4%	-0.012	-0.006	5%
	BL	-0.004	-0.001	4%	-0.012	-0.010	5%
	BR	-0.011	-0.009	-4%	-0.024	-0.012	-5%
	Average =	-0.010	-0.006	-	-0.017	-0.010	-

$l_n/h = 2.0$					
Specimen	Location	$\epsilon_{LB_{cr}}$	Drift (%)	ϵ_{LB_u}	Drift (%)
CB6	TL	-0.007	-3% $\rightarrow$ $-$4%	-0.015	-4%
	TR	-0.004	3%	-0.017	4%
	BL	-0.004	4%	-0.010	4%
	BR	-0.013	-2% $\rightarrow$ $-$3%	-0.015	-4%
	Average =	-0.007	-	-0.014	-
CB7	TL	-0.006	-3% $\rightarrow$ $-$4%	-0.019	-4%
	TR	-0.010	3% $\rightarrow$ 4%	-0.020	4%
	BL	-0.007	3% $\rightarrow$ 4%	-0.022	4%
	BR	-0.008	-2% $\rightarrow$ $-$3%	-0.024	-4%
	Average =	-0.008	-	-0.021	-
CB8	TL	-0.015	-2%	-0.041	-5%
	TR	-0.011	3% $\rightarrow$ 4%	-0.035	5%
	BL	-0.007	3%	-0.034	5%
	BR	-	-3%	-	-5%
	Average =	-0.011	-	-0.037	-

4.6.4 Spread of Plasticity and Plastic Hinge Rotation Capacity

The design of the SFRC coupling beam specimens considered the potential plastic hinge region to extend into the beams a distance of $h/2$ from the supports, following the work by Lequesne (2011) and Setkit (2012). To quantify the spread of plasticity in the SFRC coupling beams, the curvatures calculated over the length of each specimen, as well as the strains measured on the longitudinal reinforcement, were used. As previously discussed in Section 4.4, curvatures exceeding ϕ_y were mostly concentrated within the first two marker strips at the ends of the beams corresponding to 12 in. ($\frac{2h}{3}$) and 8 in. ($\frac{4h}{9}$) for coupling beams with span-to-depth ratio of 3.0 and 2.0, respectively. However, the largest plastic deformations occurred within the first strip at each end. Considering the spread of plasticity to extend up to the centroid of the second marker strip from the beam ends results in lengths of 9.5 in. ($\approx \frac{h}{2}$) and 6.5 in. ($\approx \frac{h}{3}$) for coupling beams with span-to-depth ratios of 3.0 and 2.0, respectively. The spread of plasticity was further confirmed by the strains measured on the longitudinal bars (Figures 4.32 through 4.37).

Strain gauges located on the bars anchored in the end-blocks indicate that reinforcement yielding penetrated into the supports a distance of at least $\frac{h}{3}$, or in terms of maximum bar diameter (d_b), approximately $8\,d_b$, $10\,d_b$ and $12\,d_b$ for Specimens CB2 and CB3, Specimens CB4 and CB5, and Specimens CB6 through CB8, respectively. Similar observations were reported by Lequesne (2011).

4.6.4.1 Plastic Hinge Rotation

In general, the plastic hinges exhibited stable flexural responses with wide hysteresis loops and minor pinching. Prior to a strength loss of 20%, coupling beams with $l_n/h = 3.0$ (except for Specimen CB1) underwent maximum rotations in the range of 2.3 to 4.4% rad within the first marker strip adjacent to the beam-wall interfaces (within beam, excluding interface). However, much larger rotations were observed at the beam-wall interfaces, ranging from 3.2 to 7.8% rad. In contrast, the specimens with aspect ratio of 2.0 underwent much smaller flexural rotations within the beams. Maximum flexural rotations for Specimens CB6 through CB8 were in the range of 0.6 to 1.0% rad, whereas the rotations at the interfaces ranged from 3.2 to 4.2% rad. The shear force versus rotation hysteresis shown in Figures 4.72 through 4.75 compare the responses of the interfaces and the beam ends for selected coupling beam specimens. These responses provide examples of the different behaviors observed, e.g., the non-reversing and accumulating rotations shown in Figure 4.72b, and slightly pinched loops for specimens with $l_n/h = 2.0$ shown in Figures 4.74 and 4.75 (S1, S2, and so on refer to the marker strips; see Appendix A.4).

The response of the specimens with span-to-depth ratio of 2.0 exhibited slightly more pinched hysteresis loops, as was expected due to their shorter shear span. In addition, Figures 4.74 and 4.75 clearly show that reinforcement bond-slip dominated the response of these specimens with significantly smaller flexural deformation demands within the beam compared to the more slender specimens.

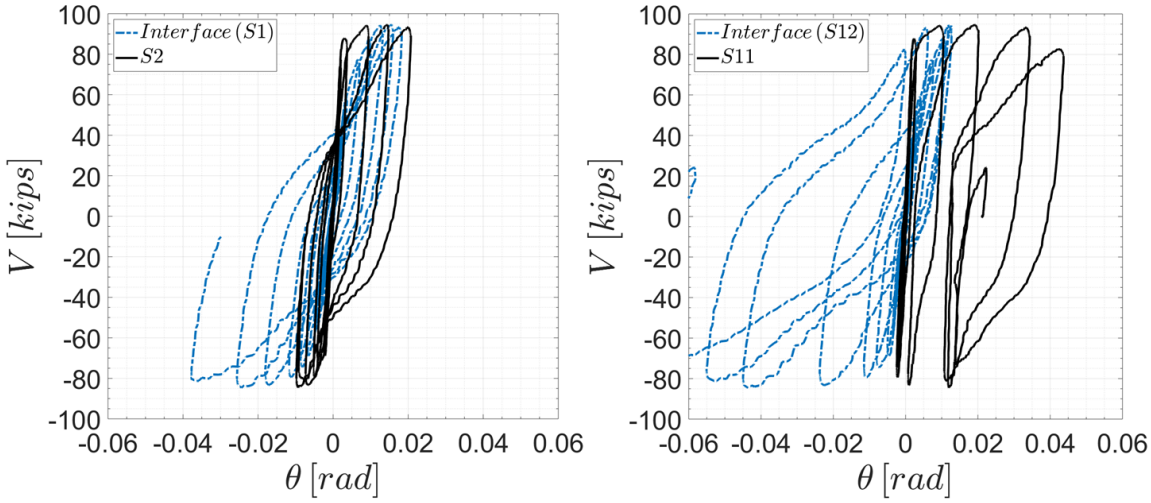

a) Top Plastic Hinge

b) Bottom Plastic Hinge

Figure 4.72: Shear Versus Rotation Response - Specimen CB3.

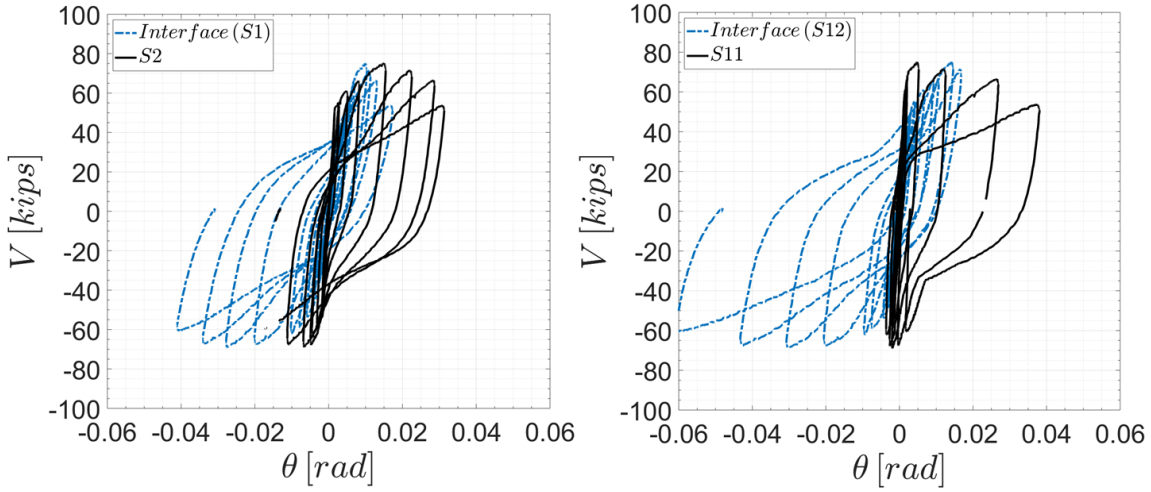

a) Top Plastic Hinge

b) Bottom Plastic Hinge

Figure 4.73: Shear Versus Rotation Response - Specimen CB4.

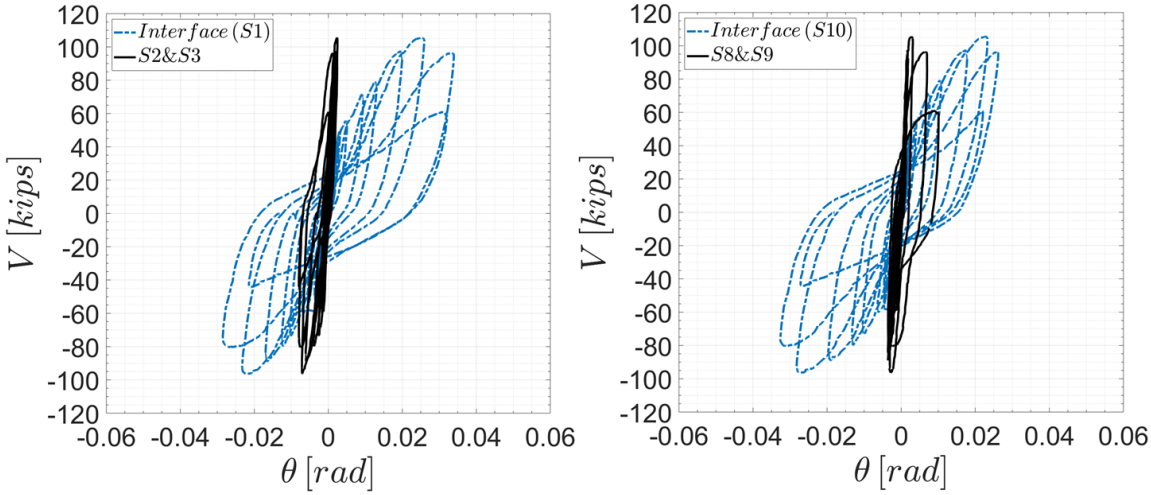

a) Top Plastic Hinge

b) Bottom Plastic Hinge

Figure 4.74: Shear Versus Rotation Response - Specimen CB7.

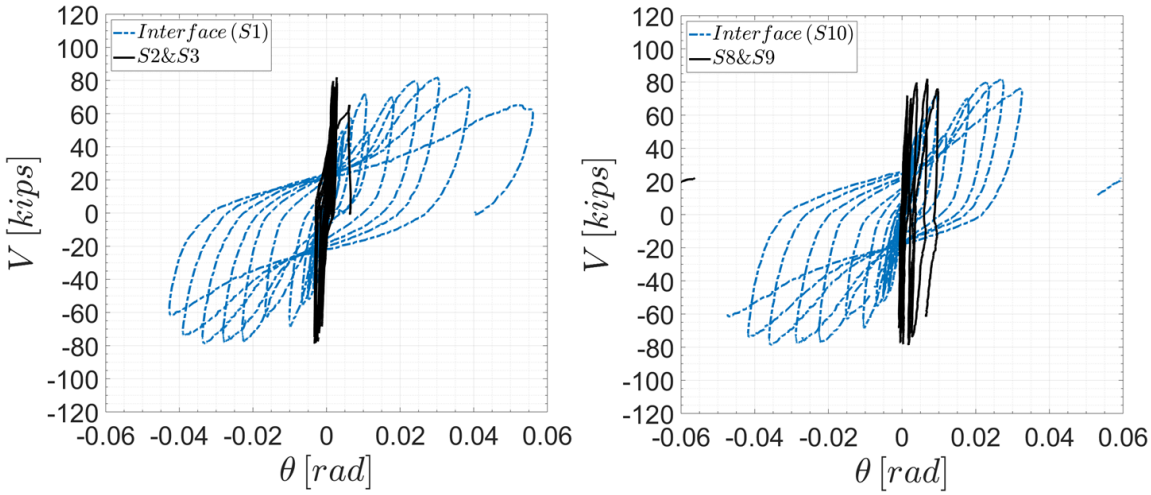

a) Top Plastic Hinge

b) Bottom Plastic Hinge

Figure 4.75: Shear Versus Rotation Response - Specimen CB8.

4.7 Shear Behavior of SFRC Coupling Beams

Shear deformations in flexural members are often neglected because they do not account for a significant portion of the response. However, it has been shown that shear deformations can be significant in deep flexural members; e.g., Saatcioglu and Ozcebe (1989). Furthermore, previous studies on coupling beams have shown that shear deformations can account for 20 to 40% of the total deformation and thus, they require proper consideration in analysis and design (Lequesne, 2011 and Setkit, 2012). Therefore, shear deformations should be considered in analysis and design of deep flexural members expected to sustain inelastic displacement reversals under high shear stresses, such as coupling beams.

4.7.1 Shear Response Outside Plastic Hinges

4.7.1.1 Shear Strains and SFRC Shear Strength Contribution

As expected, the steel fibers were effective in controlling crack growth and encouraging the development of a dense array of cracks throughout the beams (see crack patterns in Section 4.1). Furthermore, crack spacing and width varied for the different SFRCs depending on their post-cracking tensile response. To further evaluate the suitability of each class of SFRC for resisting shear stresses, the shear strains and strength of each coupling beam were investigated. Refer to Appendix A.4 for details on the calculation of shear strains.

The region outside the plastic hinges (mid-span region, taken as $l_n - h$), underwent relatively uniform shear strains at each drift increment, essentially behaving within the cracked-elastic range (Figures 4.76 and 4.77), except for the last cycle applied to Specimen CB1. Therefore, calculated shear strains for the marker strips within the mid-span region of the beams were averaged to quantify the magnitude of the average shear strains (γ_{avg}). Figure 4.78 shows the average shear strains calculated at different drift levels for all coupling beams.

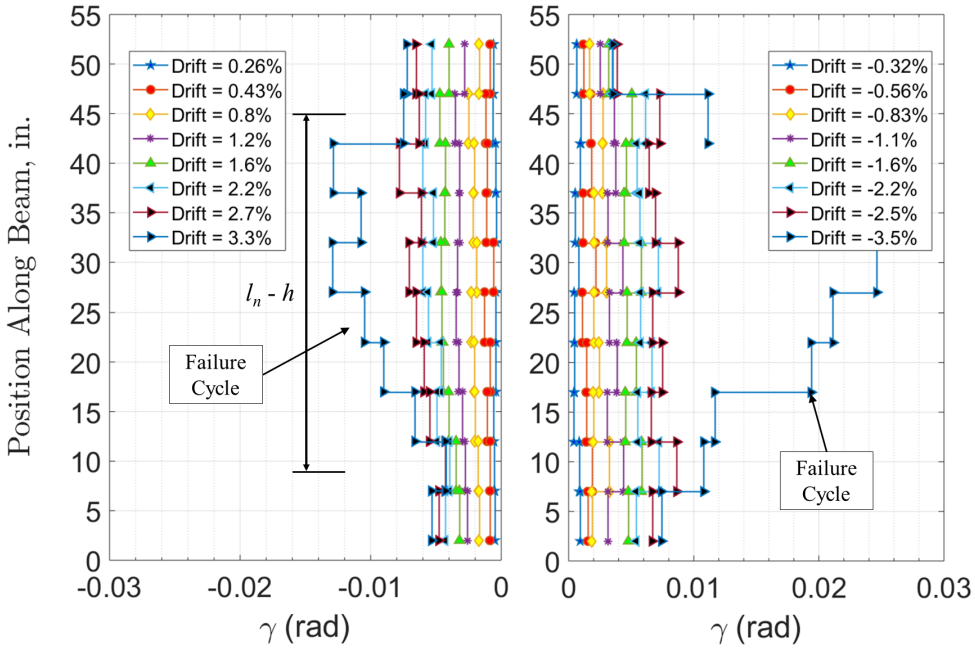

Figure 4.76: Shear Strain Distribution - Specimen CB1.

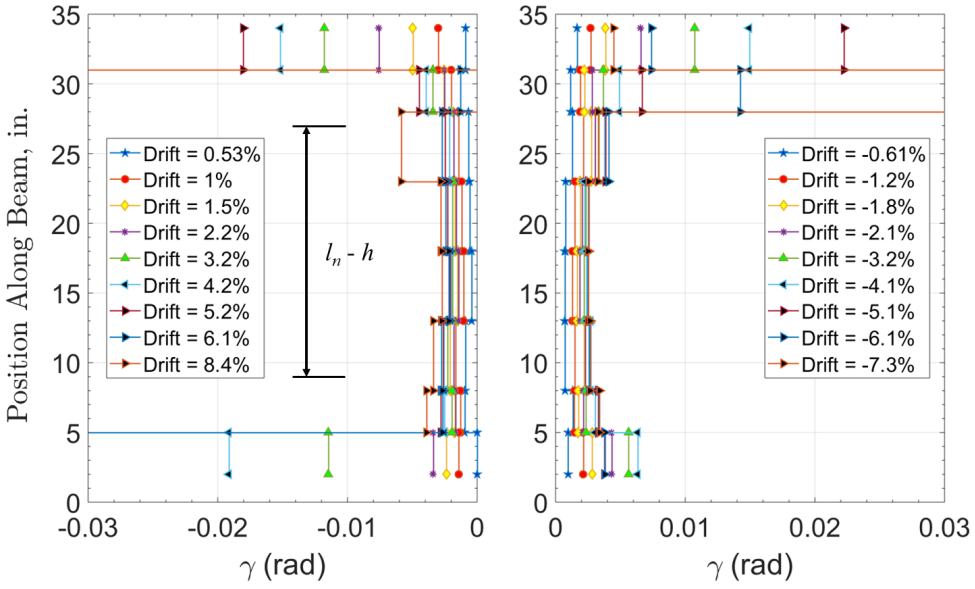

Figure 4.77: Shear Strain Distribution - Specimen CB8.

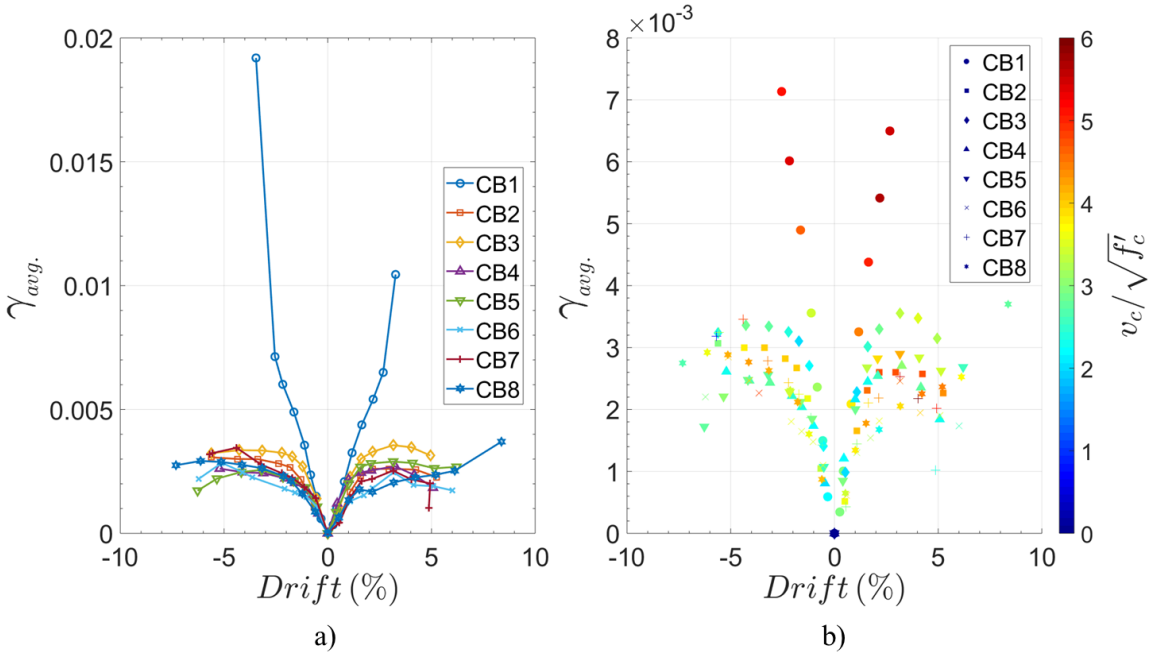

Figure 4.78: Average Shear Strains Outside Plastic Hinges (γ_{avg} in rad).

Except for Specimen CB1, which failed in shear, average shear strains in the mid-span region of all SFRC coupling beams remained below 0.004 rad, which corresponded to minimal shear-related damage. Furthermore, as shown in Figure 4.78b, the intensity or magnitude of the SFRC shear stresses, v_c, remained between approximately 2.0 and $4.5\sqrt{f'_c}$ (psi). Figure 4.79 (Specimens CB2 through CB4) and Figure 4.80 (Specimens CB5 through CB8) show the applied shear stress (v) and the contributions from the transverse reinforcement (v_s), calculated from strain gauge readings, and the SFRC (v_c) normalized by $\sqrt{f'_c}$ (psi). Refer to Section 4.3.1 for a discussion on calculation of the SFRC shear stress contribution.

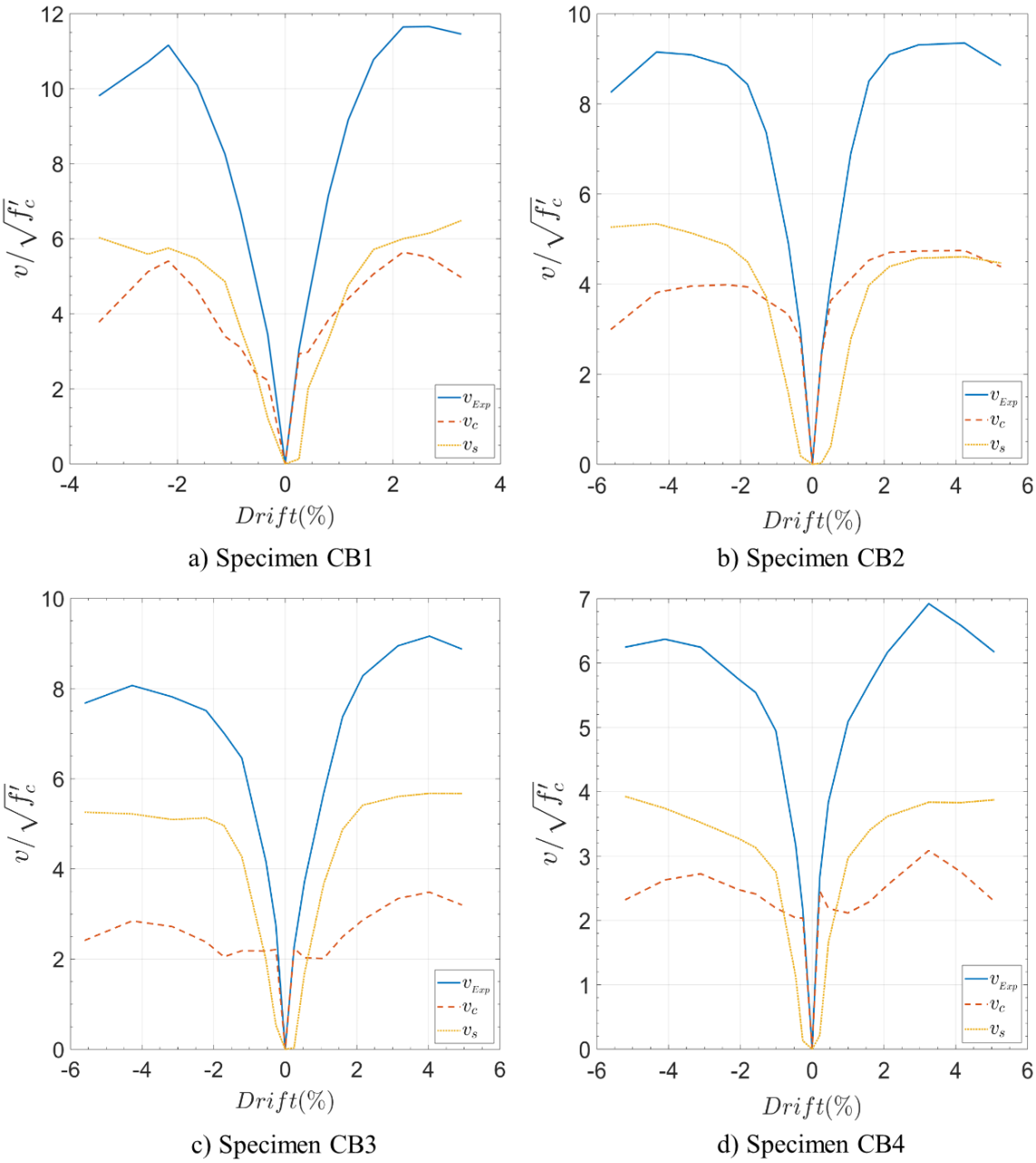

Figure 4.79: Coupling Beam Shear Stress Contributions - Specimens CB1 through CB4 ($\sqrt{f'_c}$ in psi units).

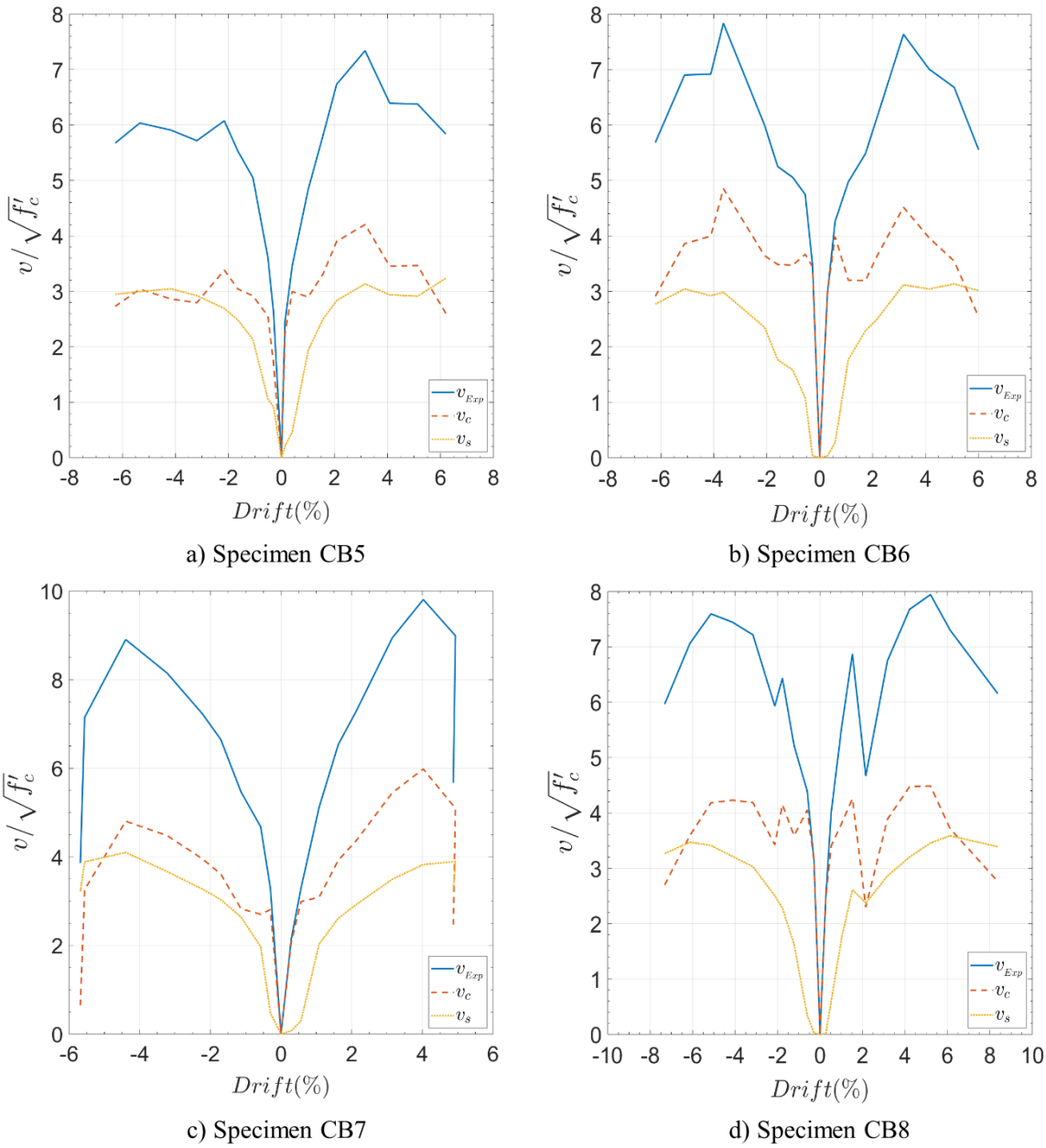

a) Specimen CB5

b) Specimen CB6

c) Specimen CB7

d) Specimen CB8

Figure 4.80: Coupling Beam Shear Stress Contributions - Specimens CB5 through CB8 ($\sqrt{f'_c}$ in psi units).

As seen in Figure 4.80d, the Class I SFRC used in Specimen CB8 often carried approximately $4.0\sqrt{f'_c}$ (psi) of the total shear demand up to a deformation of at least 5.0% drift. Similarly, the Class II SFRC used in Specimen CB6 carried shear stresses greater than $3.0\sqrt{f'_c}$ (psi) up drifts exceeding 5.0% (Figure 4.80b), while the shear stresses carried by the Class III SFRCs used in Specimens CB4 and CB5 were greater than $2.0\sqrt{f'_c}$ (psi) throughout the range of applied drifts (see Figures 4.79d and 4.80a). On the other hand, in Specimen CB1 shown in Figure 4.79a, shear stresses above $5.0\sqrt{f'_c}$ (psi) led to extensive shear damage and premature failure. This specimen was constructed with a class II SFRC.

In summary, the data presented herein provide supporting evidence for limiting the shear stress contribution of SFRC in flexural members, as was previously recommended in Sections 4.2 and 4.3.1. Moreover, for design of SFRC coupling beams, it is recommended that the SFRC shear strength contribution do not exceed 4.0, 3.0, and $2.0\sqrt{f'_c}$ for Class I, Class II and Class III SFRCs, respectively.

4.7.1.2 Effective Shear Stiffness

It is common to account for the change in stiffness due to cracking and up to first yield by considering an effective, cracked-elastic shear stiffness. Comparison of the V-γ_{avg} hysteresis of the mid-span regions of the SFRC coupling beams shows that the assumption of linear cracked-elastic behavior is reasonable. As shown in Figure 4.81, the hysteresis loops of Specimens CB4 and CB8 remained within approximately $\pm$ 0.004 rad and upon comparison with the response of Specimen CB1, shear responses within this range of strains can be simplified to a linear, cracked-elastic response. Similar shear responses were observed at the mid-span regions of Specimens CB2, CB3, and CB5 through CB7.

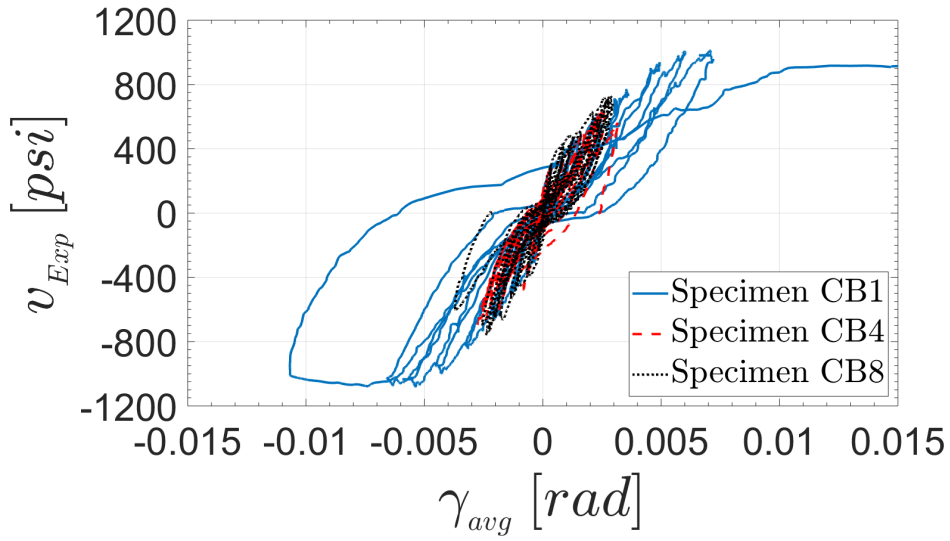

Figure 4.81: Mid-span region Shear Response Comparison - Specimens CB1, CB4 and CB8.

The effective shear stiffness ($G_{eff}\ A_g$) of the SFRC coupling beams was calculated as the secant stiffness of the V-γ_{avg} responses of the mid-span region of the beams. The variation of the secant stiffness throughout the range of applied drift demands is shown in Figure 4.82

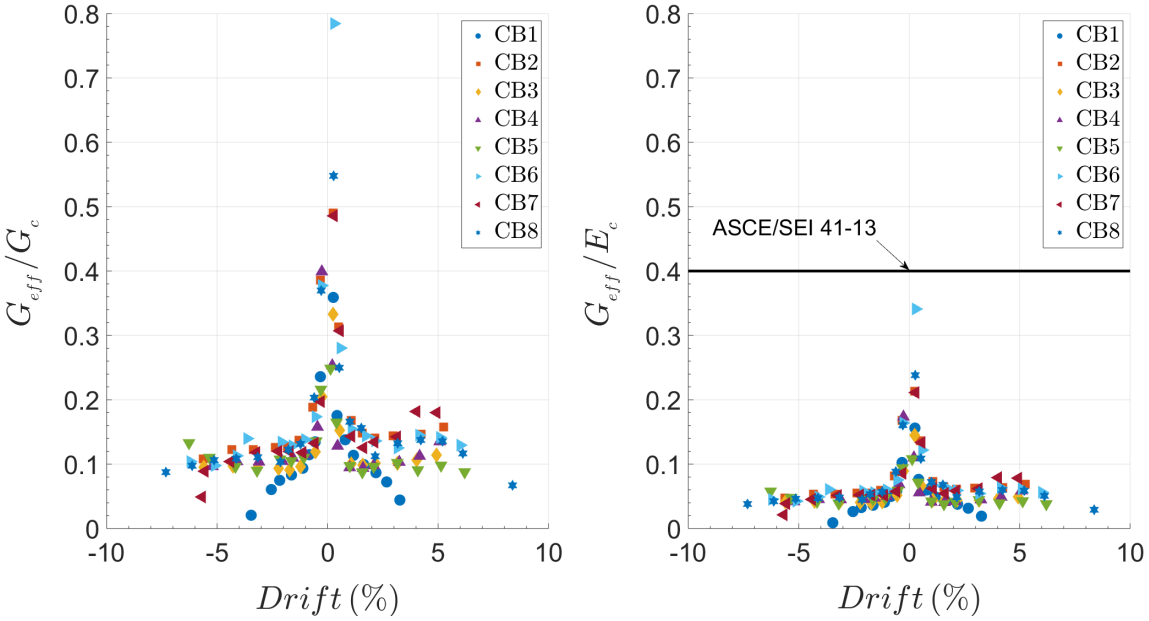

Figure 4.82: Effective Secant Shear Stiffness. a) Effective-to-Uncracked Shear Moduli Ratio; b) Effective Shear Modulus as Fraction of the Young's Modulus of Concrete.

As expected, the shear stiffness of SFRC coupling beams significantly softens after cracking. The SFRC coupling beams exhibited, on average, effective shear moduli 8 to 14% of the uncracked-elastic concrete shear modulus ($G_c = \frac{E_c}{2(1+\nu)}$, where $E_c = 57000\sqrt{f'_c}$, psi). In contrast, the shear rigidity recommended for analysis in ASCE/SEI 41-13 is $0.4E_c\,A_w$ (American Society of Civil Engineers, 2014), which is essentially the uncracked shear rigidity. The experimental results indicate that for drift demands $\geqslant 0.75\%$, the average effective shear rigidity is approximately 13% of the uncracked shear rigidity, that is, $0.05E_c\,A_w$. Similar results where reported by Lequesne (2011) and Setkit (2012).

Note that in this study, the shear stresses were calculated based on the gross cross-sectional area ($A_g = b\,h$), whereas the effective rigidity in ASCE/SEI 41-13 considers the area as $A_w = b_w\,d$, where b_w and d are the web width and effective depth, respectively (the effective depth, d, is measured from the extreme

compression fiber to the centroid of the tension reinforcement or can be taken as $0.8h$). Therefore, being rigorous with the definition of shear rigidity, there is a discrepancy on the shear rigidity values reported herein; however, the difference is minor since the ratio d/h for the SFRC coupling beams of this study was in the range of 0.85 to 0.9.

4.7.2 Shear Behavior of Plastic Hinges

Shear sliding after several cycles beyond flexural yielding was the predominant failure mechanism of the SFRC coupling beams. The formation of a sliding plane within plastic hinges of flexural members requires the coalescence of flexural cracks formed during cycles of reverting displacements. Thus, shear sliding is dependent on the rotation and shear stress demands, amount of reinforcement crossing the sliding plane, as well as the loading history. Onset of strength degradation in the test specimens was due to the formation of sliding planes at the critical sections near the termination of the dowel reinforcement. Therefore, to better understand the failure mechanism of SFRC coupling beams and the factors affecting the onset of shear sliding, the shear responses of the plastic hinges of the SFRC coupling beam specimens were studied.

Sample plastic hinge shear responses are shown in Figures 4.83 through 4.85. Note that although the deformations at the interfaces are strictly sliding displacements, not actual shear strains (γ), "apparent" shear distortions in the top beam-wall interface were calculated over the distance between Optotrak™ markers on the top end-block and the first row of markers within the beams. The markers containing the bottom interface were placed closer than intended and thus, the "apparent" shear distortion was calculated using the gauge length of the first marker strip; on average, the gauge lengths were approximately 5.6 and 5.1 in. for the beam-wall interfaces of specimens with span-to-depth ratio of 3.0 and 2.0, respectively. Shear strains within the SFRC plastic hinges were calculated over gauge lengths of 5.0 and 6.0 in. for specimens with span-to-depth ratio of 3.0 and 2.0, respectively; see marker strip layout in Appendix A.4.

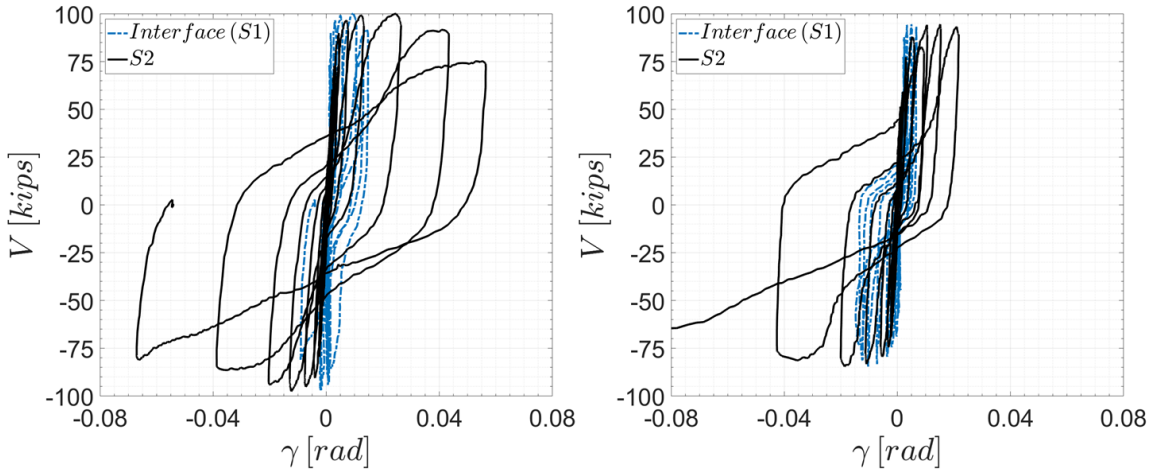

a) Specimen CB2 b) Specimen CB3

Figure 4.83: Plastic Hinge Shear Response. a) Specimen CB2; b) Specimen CB3.

SFRC coupling beams with span-to-depth ratio of 3.0 developed well defined plastic hinges and sliding concentrated at the dowel cut-off sections. Consequently, sliding at the beam-wall interfaces was less pronounced, as shown in Figure 4.83. As expected, the shear force versus distortion ($V-\gamma$) hysteresis was pinched. The responses shown in Figure 4.83 are representative of the shear behavior observed in SFRC coupling beam with $l_n/h = 3.0$.

Contrary to the behavior of Specimens CB2 through CB5, Specimens CB6 through CB8 underwent interface sliding greater than the sliding observed at the critical crack near the dowel cut-off. Moreover, the responses of coupling beams with span-to-depth ratio of 2.0 exhibited significantly more pinched loops than the those of the more slender beams. Sample shear responses are shown in Figures 4.84 and 4.85 (Specimens CB7 and CB8, respectively).

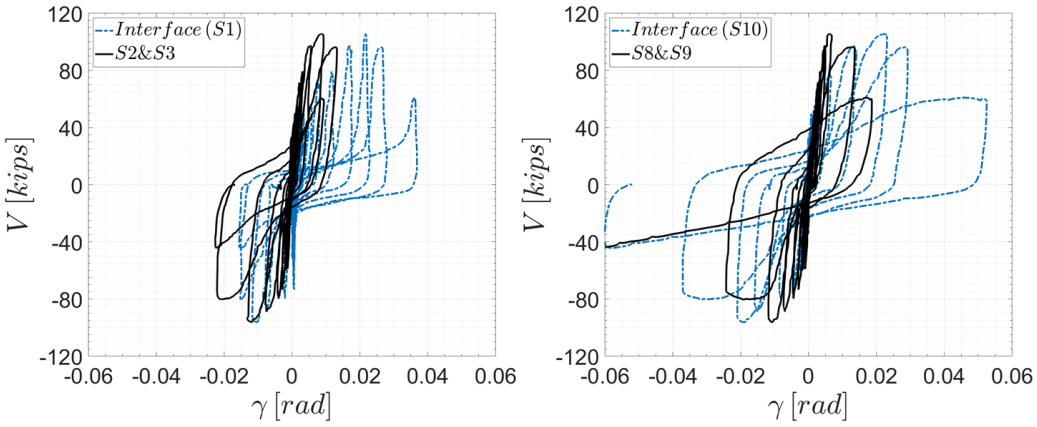

a) Specimen CB7 – Top Hinge

b) Specimen CB7 – Bottom Hinge

Figure 4.84: Plastic Hinge Shear Response - Specimen CB7.

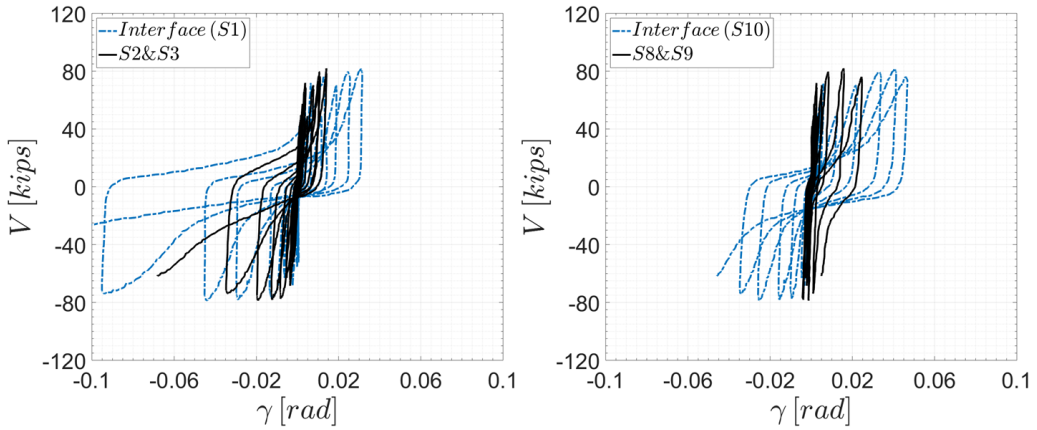

a) Specimen CB8 – Top Hinge

b) Specimen CB8 – Bottom Hinge

Figure 4.85: Plastic Hinge Shear Response - Specimen CB8.

Plastic hinge sliding displacements prior to a strength loss of approximately 20% were in the range of 0.2 to 0.4 in. and 0.1 to 0.2 in. for specimens with span-to-depth ratio of 3.0 and 2.0, respectively. Furthermore, at the beam-wall interfaces of Specimens CB6 through CB8 ($l_n/h = 2.0$), maximum sliding displacements were between approximately 0.2 and 0.4 in., comparable to the observed sliding at the dowel cut-off section of Specimens CB2 through CB5. On average, sliding displacements at the dowel cut-off critical crack accounted for approximately 8–10% of the total drift during cycles of 2.0% drift or larger. In contrast, there was significantly less interface sliding in the specimens with span-to-depth ratio of 3.0 compared to the specimens with span-to-depth ratio of 2.0. On average, interface sliding during cycles of 2.0% drift or greater accounted for approximately 3.0% and 17.0% of the total drift for specimens with span-to-depth ratio of 3.0 and 2.0, respectively. As expected, flexure played a much larger role in the overall response of the more slender beams, leading to greater damage within the beam ends. Consequently, sliding in these specimens occurred primarily along the critical crack at the dowel cut-off sections. Moreover, the amount of reinforcement crossing the interface of Specimens CB6–CB8 was approximately 40-50% less than that of Specimens CB2–CB5. Therefore, interface sliding was expected to be greater in the specimens with span-to-depth ratio of 2.0.

Investigation of the shear distortion versus plastic hinge rotation envelopes (γ–θ_{PH}) for the marker strips containing the sliding planes near the dowel cut-off sections indicated that shear distortions increased with increasing θ_{PH}. As shown in Figure 4.86, the plastic hinge shear-rotation responses exhibited significant variation among the coupling beam specimens. The scatter is attributed primarily to changes in shear demands, axial load, and the unsymmetrical behavior of some of the specimens, e.g., Specimens CB3 and CB4 (see Figures 4.72, 4.73 and 4.83). The observed variability is significantly reduced if the average response of the two loading directions is considered, as shown in Figure 4.87.

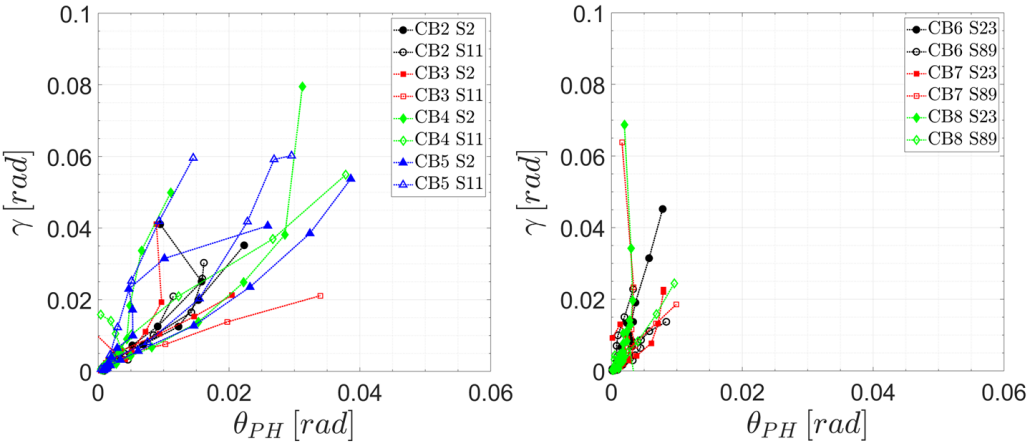

a) b)

Figure 4.86: Plastic Hinge Shear Strain-Rotation Responses. a) Specimens with $l_n/h = 3.0$; b)Specimens with $l_n/h = 2.0$.

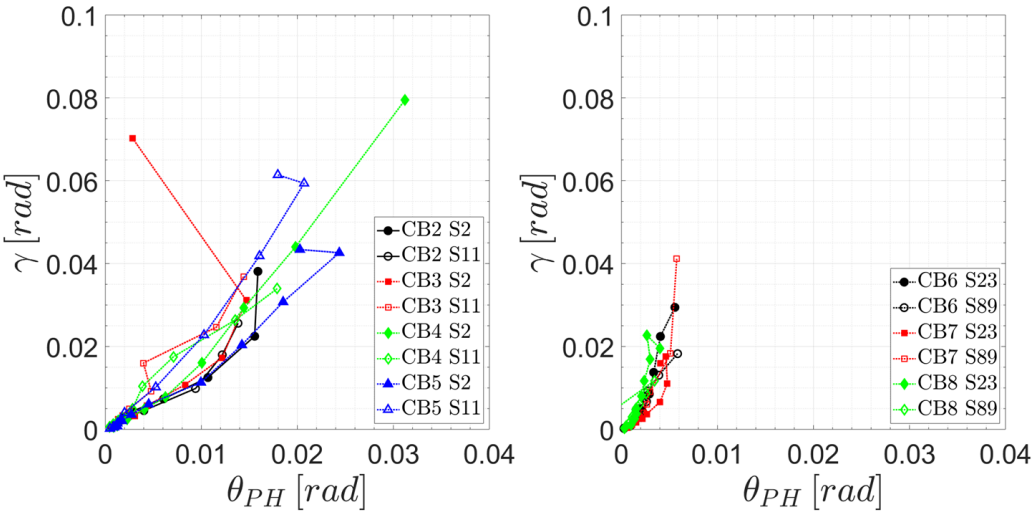

a) b)

Figure 4.87: Plastic Hinge Shear Strain-Rotation Average Responses. a) Specimens with $l_n/h = 3.0$; b)Specimens with $l_n/h = 2.0$.

Linear regressions on the average responses (average of both positive and negative loading) for Specimens CB2 through CB5 ($l_n/h = 3.0$) suggest $\gamma/\theta_{PH} \approx 2.0$. In contrast, the plastic hinges of Specimens CB6 through CB8 ($l_n/h = 2.0$) exhibited a behavior dominated by sliding shear displacements, as evidenced by the rapid increase in shear deformations with a small increment in rotation demand (see Figure 4.86b and Figure 4.87b). Furthermore, plastic hinge rotations for Specimens CB6 through CB8 remained below 1.0%.

4.7.2.1 Onset of Shear Sliding

Given that shear sliding is dependent on both rotation reversals and magnitude, the shear-rotation response was investigated to identify the onset of shear sliding. For the purpose of identifying the onset of shear sliding, the shear-rotation response was evaluated in terms of the ratio of the change in shear distortion to the change in rotation ($\delta\gamma/\delta\theta$) within the plastic hinges and the corresponding shear stresses. Figure 4.88 shows a pair of shear versus distortion cycles illustrating the definition of $\delta\gamma$; note that $\delta\theta$ was calculated the same way for the rotation hysteresis cycles. Shear-to-rotation ratios as a function of the average peak shear stress for each displacement cycle of Specimens CB2 through CB5 and CB6 through CB8 are shown in Figure 4.89 and Figure 4.90, respectively.

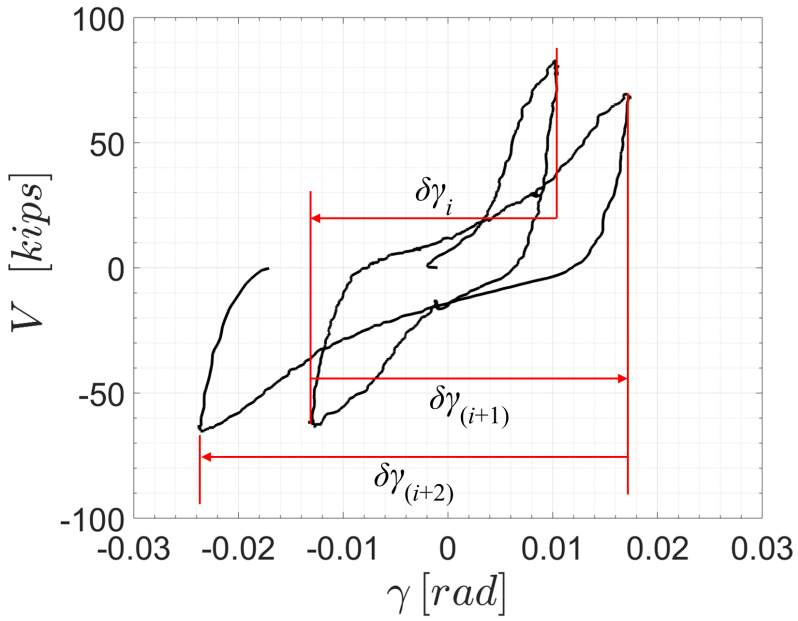

Figure 4.88: Definition of Changes in Shear Strain for Two Consecutive Hysteresis Cycles.

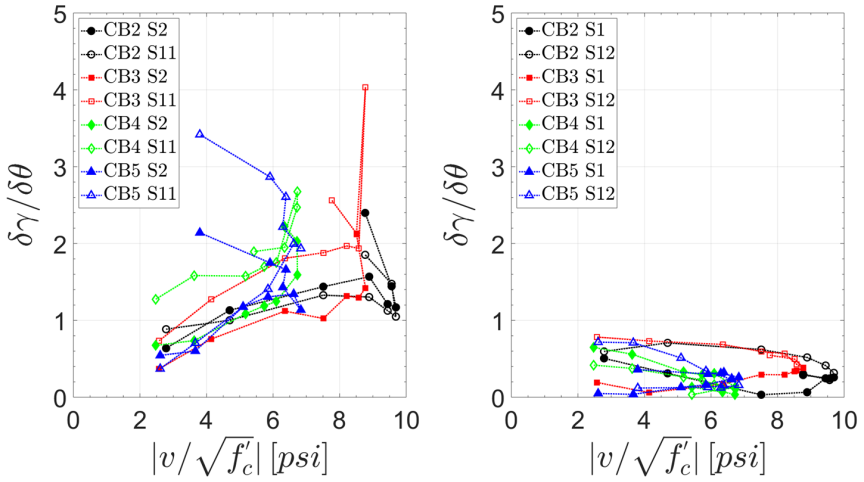

Figure 4.89: Shear-Rotation Change Ratio Versus Shear Stress in SFRC Plastic Hinges - Specimens with $l_n/h = 3.0$. a) Dowel Cut-Off Section; b) Beam-Wall Interfaces.

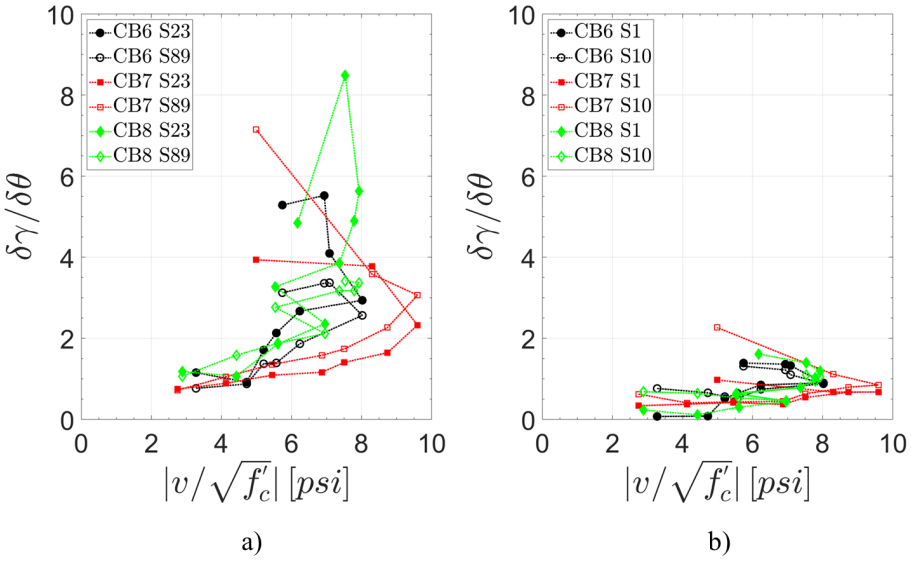

Figure 4.90: Shear-Rotation Change Ratio Versus Shear Stress in SFRC Plastic Hinges - Specimens with $l_n/h = 2.0$. a) Dowel Cut-Off Section; b) Beam-Wall Interfaces.

As shown in Figures 4.89a and 4.90a, the shear strain-to-rotation ratio continuously increased with displacement cycles. However, sliding displacements within the plastic hinges became dominant for displacement cycles beyond the point at which peak strength occurred. A similar trend is observed for the interfaces of Specimens CB6 through CB8; however, the shear strain-to-rotation ratio exhibited little variation at the interfaces of the more slender coupling beams. This was due to the limited sliding that occurred at the interfaces of Specimens CB2 through CB5 compared to the sliding at the dowel cut-off sections. Note that the shear strain-rotation ratios for Specimens CB6 through CB8 at the dowel cut-off section were larger than those for the more slender coupling beams. The larger $\delta\gamma/\delta\theta$ ratios are a consequence of the significantly smaller rotations developed in the plastic hinges of the shorter beams and not due to larger sliding displacements. Similarly, the smaller $\delta\gamma/\delta\theta$ ratios for the beam-wall interfaces was due to the large concentrated rotations in Specimens CB6 through CB8.

4.7.3 Shear Friction Analysis

The lack of diagonal reinforcement in the SFRC coupling beams provided the conditions necessary for the development of shear sliding failures. Therefore, to further investigate the shear sliding behavior of the coupling beams, the well known shear-friction analogy (Birkeland and Birkeland, 1966 and Mast, 1968) was used to analyze the shear sliding capacity at the dowel cut-off sections and the beam-to-wall interfaces. Shear-friction is typically used whenever shear must be transferred at an interface such as the joint of new and old concrete (e.g., Bass et al., 1989), concrete-to-steel interfaces, shear at the base of structural walls (e.g., Wood, 1990), and between crack surfaces in monolithic concrete. The analogy assumes shear is transferred across the crack solely due to friction between the crack faces, as one crack face slides relative to the other, neglecting any contribution from reinforcement dowel action. As the crack faces slide relative to each other, the roughness of the crack surfaces results in a separation of the crack faces, leading to the development of tension in the reinforcement bars crossing the crack and consequently providing a clamping effect across the crack. This clamping effect provides compression normal to the crack faces, giving rise to the frictional resistance. Shear friction provisions in ACI 318-14 define the nominal shear strength across the assumed shear plane as:

$$V_n = \mu \left(A_{vf} f_y + P \right) \tag{4.4}$$

where μ is the surface friction coefficient, A_{vf} is the area of reinforcement across the shear plane, f_y is the reinforcement yield strength, and P is any external compression acting normal to the shear plane.

The shear friction coefficient at the dowel cut-off sections and beam-wall interfaces was evaluated by setting V_n equal to the applied shear in Equation 4.4 at a given drift. Similarly, the axial force P was taken as the axial force acting on the coupling beam concurrently with V, and the reinforcement stress was taken as the measured yield strength, $(f_y)_{measured}$. Since shear-friction relies on the clamping effect of the reinforcement in tension, only half of the coupling beam longitudinal reinforcement was considered to contribute to the development of frictional resistance—calculated stresses for the flexural reinforcement confirmed that about half of the reinforcement at any given drift demand was in compression, even while tensile strains were being measured due to the accumulation of plastic strains. Note that the dowel reinforcement was not considered in the calculation of $A_{vf}\, f_y$ at the plastic hinge critical crack because the shear planes within the beam typically formed at the dowel cut-off sections.

Re-arranging Equation 4.4, the effective friction coefficient (μ_{Eff}) was calculated as:

$$\mu_{Eff} = \frac{V}{A_{vf}\,(f_y)_{measured} + P} \tag{4.5}$$

Figures 4.91–4.97 show the sliding responses at the critical cracks and interfaces of Specimens CB2 through CB8. The responses are shown in terms of the effective shear friction coefficient and the sliding displacement $(\delta_{sliding})$. Furthermore, four curves are shown in each plot, corresponding to the response of both ends of the beams during the positive (solid markers) and negative (hollow markers) drifts. The sliding displacements were calculated based on the shear distortions previously calculated for marker strips S1, S2, S11 and S12 for coupling beams with span-to-depth ratio of 3.0 and S1, S2–S3, S8–S9, and S10 for coupling beams with span-to-depth ratio of 2.0, as:

$$\delta_{sliding} = \gamma_{s_i}\, h_{s_i} \tag{4.6}$$

where h_{s_i} is the height or distance between marker rows of the i^{th} marker strip corresponding to γ_{s_i}.

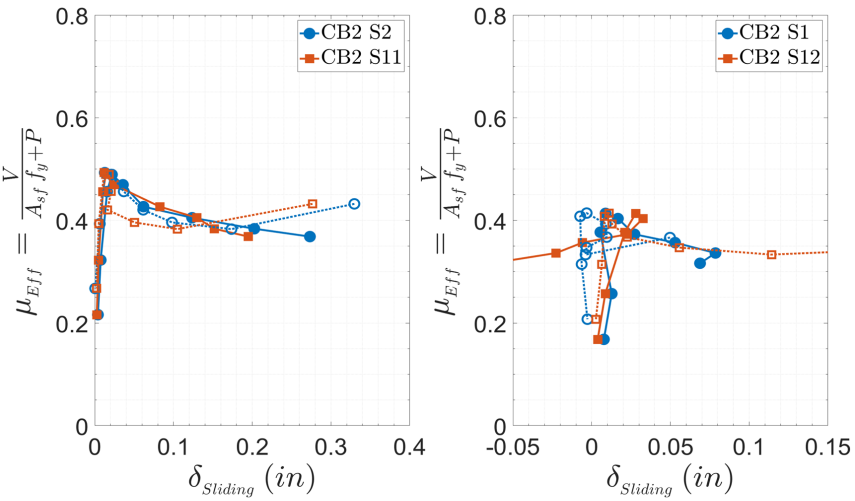

a) Response within SFRC Plastic Hinge

b) Interface Response

Figure 4.91: Specimen CB2 - Shear Friction-Sliding Response. Solid and hollow markers correspond to positive and negative drifts, respectively.

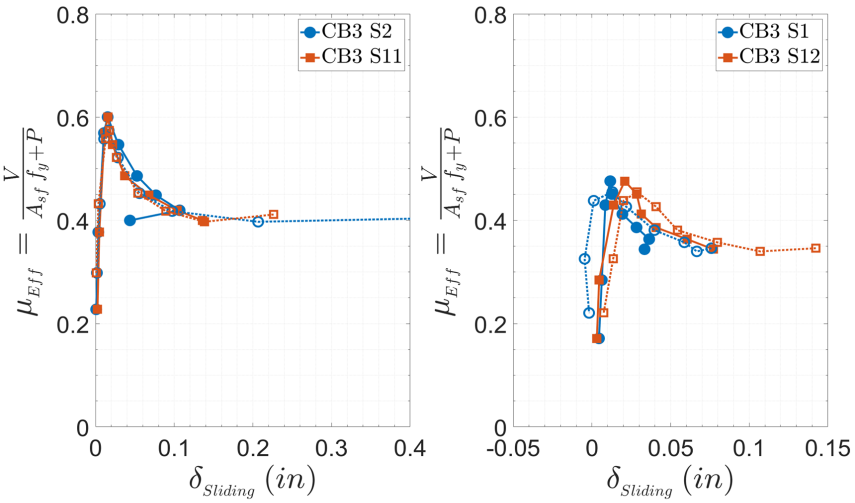

a) Response within SFRC Plastic Hinge

b) Interface Response

Figure 4.92: Specimen CB3 - Shear Friction-Sliding Response. Solid and hollow markers correspond to positive and negative drifts, respectively.

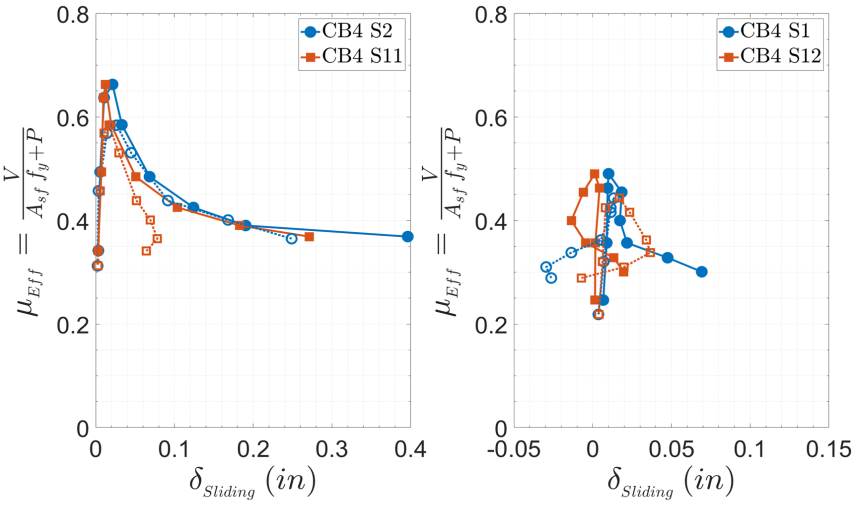

a) Response within SFRC Plastic Hinge b) Interface Response

Figure 4.93: Specimen CB4 - Shear Friction-Sliding Response. Solid and hollow markers correspond to positive and negative drifts, respectively.

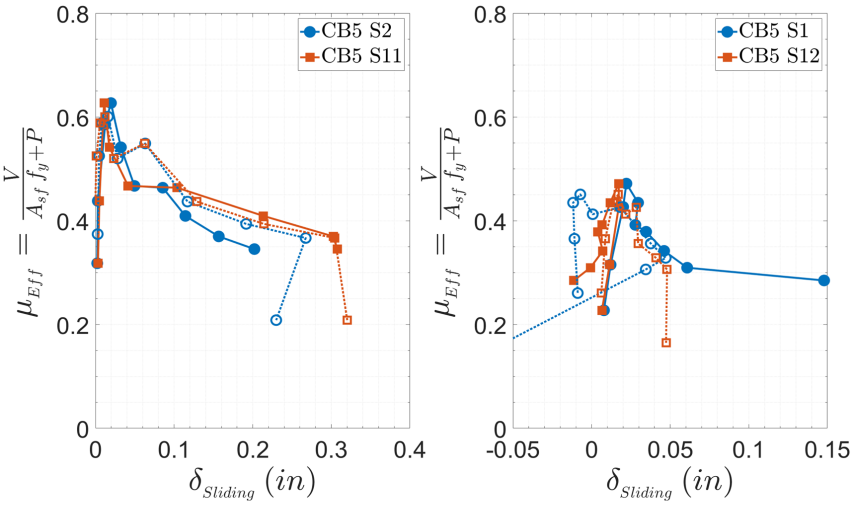

a) Response within SFRC Plastic Hinge b) Interface Response

Figure 4.94: Specimen CB5 - Shear Friction-Sliding Response. Solid and hollow markers correspond to positive and negative drifts, respectively.

The shear plane in the SFRC coupling beams was formed by the coalescence of flexural cracks formed during loading in opposite directions as opposed to a shear plane in direct shear; therefore, smaller effective shear frictions coefficients are expected compared to those corresponding to shear transfer across a crack in monolithic concrete. As seen in Figures 4.91–4.94, the peak effective shear friction coefficients for Specimens CB2 through CB5 ($l_n/h = 3.0$) ranged from 0.49 to 0.66, much smaller than the shear friction coefficient recommended by ACI 318-14 (1.4 for shear transfer across a crack in monolithic concrete). Furthermore, considering nominal yield strength instead of the measured yield strength leads to peak μ_{Eff} in the range of 0.59 to 0.88. At the beam-to-wall interfaces, peak μ_{Eff} ranged from 0.41 to 0.49, also smaller than 0.6 recommended for concrete placed against hardened concrete not intentionally roughened (ACI Committee 318, 2014). However, if the reinforcement nominal yield strength is considered (60 ksi), peak μ_{Eff} are in the range of approximately 0.50 to 0.65, closer to 0.6, as recommended in ACI 318-14.

Note that for Specimens CB2, CB4 and CB5, the response of the bottom interface (marker strip S12) exhibited smaller sliding displacements as the drift demands kept increasing, resulting in odd curves moving towards negative or smaller sliding displacements (see Figures 4.91b, 4.93b and 4.94b). This behavior was due to sliding occurring along different planes during each loading direction. For example, sliding along the bottom interface (S12) occurred during negative drift cycles (hollow markers) and upon reversal, sliding concentrated in the critical crack near the dowel cut-off section (S11), requiring the interface to slide much less, thus accumulating sliding displacement towards the negative drift direction.

Figures 4.95 through 4.97 show the effective shear friction coefficient versus shear sliding response for Specimens CB6 through CB8 with $l_n/h = 2.0$. Sliding was significant at both the dowel cut-off sections and beam-wall interfaces of Specimens CB6 through CB8. Furthermore, interface sliding at peak strength and at a strength decay of approximately 20% were approximately 4 times larger than that in the specimens with span-to-depth ratio of 3.0. Peak effective friction coefficients were significantly larger than those for Specimens CB2 through CB5, ranging from approximately 0.96 to 1.17 at the dowel cut-off sections and 0.77 to 0.89 at the beam-

wall interfaces. The quantity $A_{vf}\,(f_y)_{measured}$ for Specimens CB6 through CB8 was approximately 40 to 60% of the corresponding value for Specimens CB2 through CB5. Therefore, the calculated shear-friction coefficients for Specimens CB6 through CB8 were expected to be larger, given that the peak strengths were relatively similar. Moreover, if the reinforcement nominal yield strength (60 ksi) is considered, peak μ_{Eff} for the interfaces and plastic hinges of Specimens CB6 through CB8 would be in the range of approximately 0.88 to 1.04 and 1.11 to 1.40, respectively.

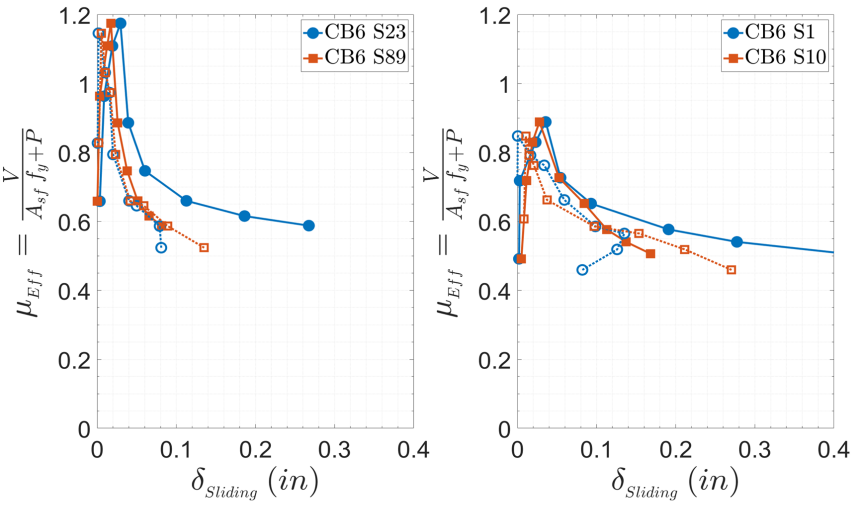

a) Response within SFRC Plastic Hinge

b) Interface Response

Figure 4.95: Specimen CB6 - Shear Friction-Sliding Response. Solid and hollow markers correspond to positive and negative drifts, respectively.

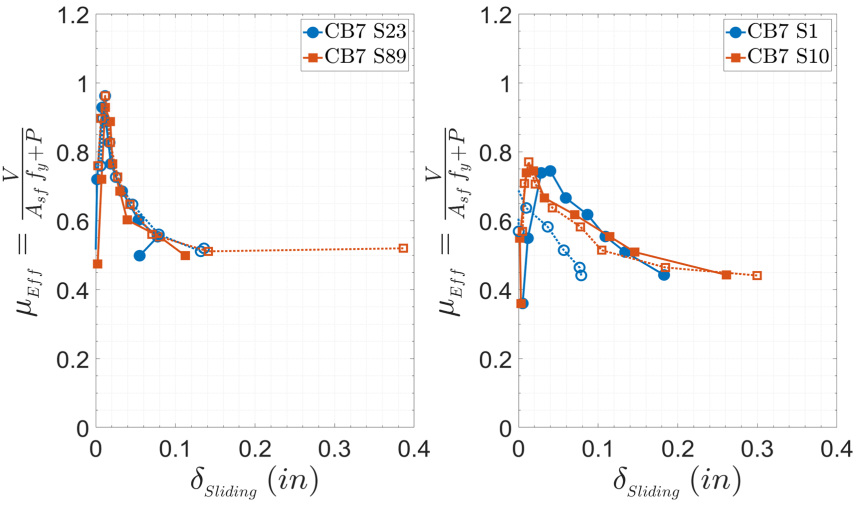

a) Response within SFRC Plastic Hinge b) Interface Response

Figure 4.96: Specimen CB7 - Shear Friction-Sliding Response. Solid and hollow markers correspond to positive and negative drifts, respectively.

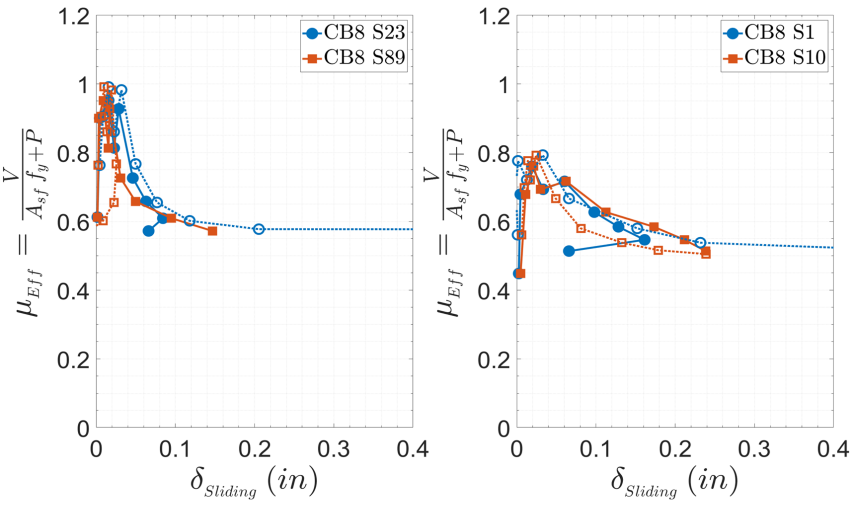

a) Response within SFRC Plastic Hinge b) Interface Response

Figure 4.97: Specimen CB8 - Shear Friction-Sliding Response. Solid and hollow markers correspond to positive and negative drifts, respectively.

Shear-friction coefficients of 0.40 and 0.60 are recommended for frictional analysis along the dowel cut-off section of SFRC coupling beams with span-to-depth ratio of 3.0 and 2.0, respectively. Sliding behavior at the beam-wall interfaces was similar to that of the dowel cut-off section. Therefore, similar shear-friction coefficients of 0.35 and 0.55 were found to be appropriate for interfaces between walls and precast SFRC coupling beams with span-to-depth ratio of 3.0 and 2.0, respectively. Note that these friction coefficients are peak values calculated assuming a constant axial compression equal to the peak axial force developed in each coupling beam specimen and are lower than those previously discussed. In conclusion, interface sliding for the beams with span-to-depth ratio of 2.0 was approximately 4 times larger than the interface sliding of the beams with span-to-depth ratio of 3.0 (this was expected due to the smaller shear span of Specimens CB6 through CB8). Additionally, coupling beams with reinforcement detailed such that μ_{Eff} is similar to the recommended values should exhibit a similar shear sliding behavior.

4.8 Axial Force and Elongations

As the beams undergo cycles of reverting displacements, accumulation of plastic strains in the flexural reinforcement results in significant beam elongations. In coupled walls systems, the walls and slabs provide restraint against coupling beam elongation, leading to the development of axial compression in the coupling beams. Therefore, the effect of axial compression on the behavior of coupling beams should be considered in design. In the component tests, the steel links keeping both end-blocks parallel during testing (see Figure 3.12) provided an axial restraint intended to simulate that provided by walls and slabs in coupled wall systems.

The total elongation of the beams was calculated using the Optotrack™ markers on the end-blocks of each specimen. The elongation of the beam due primarily to flexural rotations within the beam, on the other hand, was calculated using the first row of markers on each end of the beams. The difference of these elongations is, roughly, the elongation due to concentrated rotations at the interfaces. The total elongation of the coupling beams (δ_L) was used to calculate average axial strains,

$\epsilon_L = \delta_L / l_n$. As seen on Figure 4.98, the maximum average axial strains ranged from approximately 0.40 to 0.70% and from 0.70 to 0.90% for coupling beams with aspect ratio of 3.0 and 2.0, respectively. Figure 4.98b shows the relative contribution of the average longitudinal strain associated to rotations at the beam-wall interfaces ($(\epsilon_L)_{Wall}$) to ϵ_L versus applied drift. Consistent with the greater rotation demands at the beam-wall interfaces for the beams with aspect ratio of 2.0, the elongation of these beams was primarily due to the accumulation of plastic strains at the beam-wall interfaces (approximately in the range of $55\% \leqslant (\epsilon_L)_{Wall}/\epsilon_L \leqslant 85\%$). In contrast, for the more slender beams the elongation $(\epsilon_L)_{Wall}$ was in the range of 15 to 65% of the total average elongation.

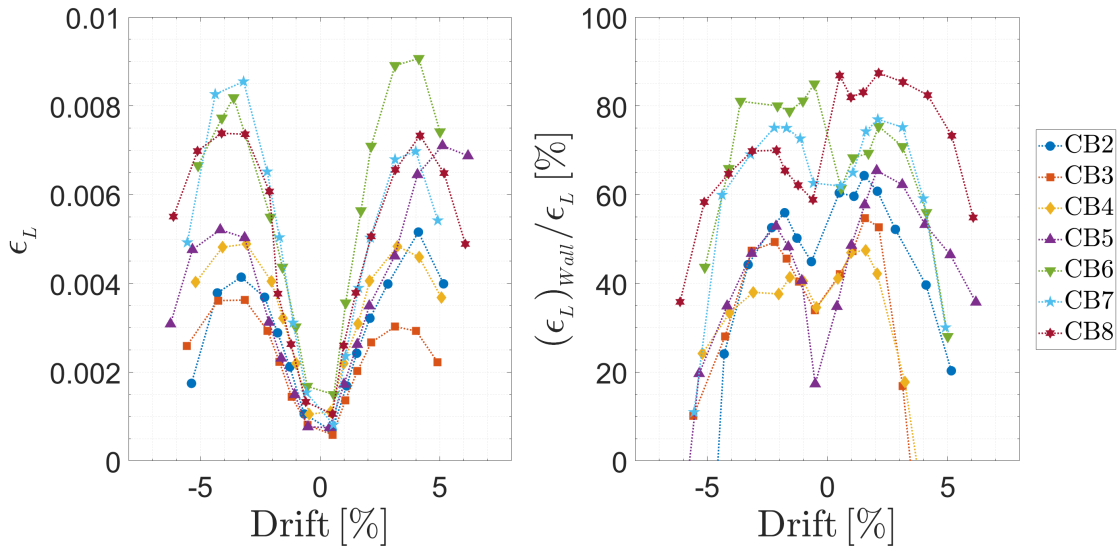

Figure 4.98: Average Axial Strain Versus Drift Envelopes for Specimens CB2 through CB8.

The axial compressive force developed due to restraint against axial expansion can be significant and its presence increases the flexural strength of the beams and, consequently, their shear demand. Thus, reasonable values of axial compression must be considered in design to avoid underestimating the peak shear demand in coupling beams. Figure 4.99, shows the normalized axial force P versus ϵ_L for Specimens CB2 through CB8. In Figure 4.99, the filled and hollow markers correspond to displacements in the positive and negative loading directions, respectively. Furthermore, the markers plotted in red and black correspond to beams with span-to-depth ratio of 3.0 and 2.0, respectively.

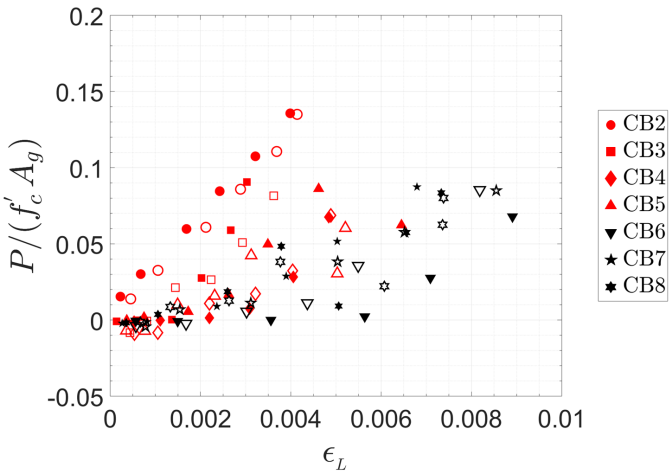

Figure 4.99: Coupling Beam Axial Force versus Longitudinal Strains.

The peak axial force developed in the SFRC coupling beams ranged from approximately 0.09 to 0.15 $f'_c A_g$ and a fairly linear correlation to the average axial strain was observed for each individual specimen. In general, the stiffness of the provided axial restraint was similar for Specimens CB4 through CB8. On the other hand, Specimens CB2 and CB3 had greater axial restraint, approximately 4 and 2 times the restraint of Specimens CB4 through CB8 (comparison based on the slopes of the responses shown in Figure 4.99). Part of the variability is attributed to variations on initial tightening of the steel links providing the restraint. Furthermore, sudden axial force drops, such as that exhibited by Specimen CB5, were due to loosening

of the link bolts to reduce the axial force and maintain the shear demand close to the intended value.

Since beam elongations are primarily due to accumulation of plastic strains while the beams undergo inelastic displacement cycles, both flexural and bond-slip rotations contribute to the overall elongation of the beams. Therefore, ϵ_L was related to the drift due to rotations at the beam-wall interfaces (θ_{BS}) plus the drift due to flexural rotations within the SFRC coupling beams ($\frac{\delta_F}{l_n}$), i.e., $\theta_{S+F} = \theta_{BS} + \frac{\delta_F}{l_n}$. Figures 4.99a and b, show ϵ_L as a function of the total drift due to rotations at the beam-wall interfaces plus the rotations within the SFRC coupling beams for beams with span-to-depth ratio of 3.0 and 2.0, respectively.

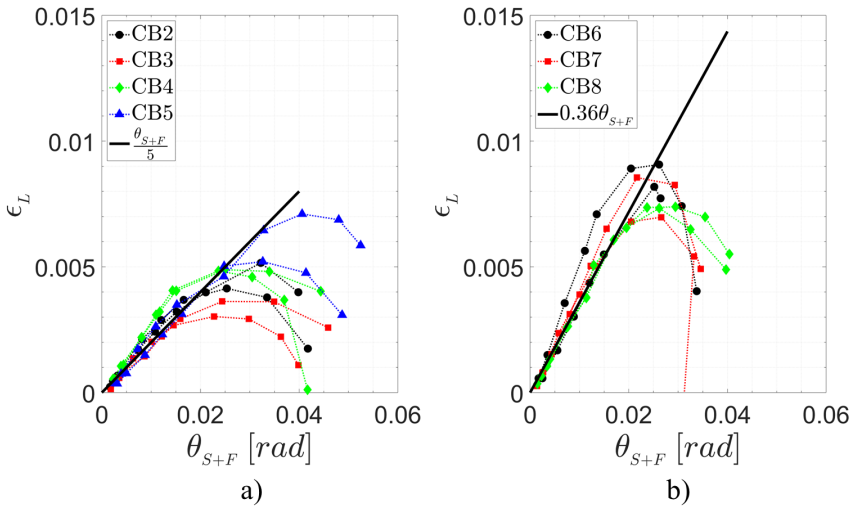

Figure 4.100: Coupling Beam Axial Force versus Longitudinal Strains.

The average axial strain was found to be proportional to the flexural and concentrated rotations up to rotations of approximately 2.0 to 2.5%. For θ_{S+F} exceeding approximately 3.0 and 2.5% for beams with span to depth ratio of 3.0 and 2.0, respectively, beam elongation began to reduce. The larger drops in elongations were due to the extensive damage and pronounced shear sliding displacements.

The peak elongations exhibited by the test beams were within those exhibited by the coupling beams in the coupled wall specimens tested by Lequesne (2011), which

ranged between 0.5 to 1.7%. Therefore, assuming the axial restraint exhibited by the tests beams is representative of that in coupled wall systems, an axial compression of $0.1f'_c A_g$ seems reasonable for use when calculating the coupling beam expected flexural strength and shear demand.

4.9 Drift Component Analysis

The relative contributions of flexural, shear, and reinforcement slip deformations to the applied drift were quantified in order to evaluate their contribution as applied drift was increased during the tests. Based on the curvatures and shear distortions calculated for each marker strip on the beams (see Appendix Sections A.4–A.5 for marker and strip layouts, and calculation details), the lateral displacement corresponding to each deformation mechanism was calculated. The lateral displacements due to flexural deformations were calculated using the 2^{nd} moment-area theorem. The first moment of the areas under the curvature diagram was calculated with respect to both beam ends, and the average tangential deviation was taken as the lateral displacement resulting from the curvature distribution at the specific drift under consideration; no corrections for end-block rotations were considered in this analysis because end-block rotations were small, thus resulting in corrected drifts typically within 6% of the uncorrected drifts (see Appendix A.1 for a discussion on end-block rotations). At a given drift level, the tangential deviation δ_F was calculated as,

$$\delta_F = \sum \phi_i \, (h_s)_i \, \bar{x}_i \tag{4.7}$$

where ϕ_i is the average curvature of the i^{th} strip, $(h_s)_i$ is the height of the i^{th} strip, and $\bar{x}_i$ is the distance from the centroid of the i^{th} strip to the beam end considered. The lateral displacement due to concentrated rotations at the beam-to-wall interfaces were calculated separately as the interface rotation times the beam length. Therefore, only the curvatures calculated for the strips within the coupling beams were considered to contribute to δ_F. The lateral displacement due to shear deformations, δ_V, was calculated using the average shear distortion for each marker

strip as follows,

$$\delta_V = \sum (\gamma_s)_i \, (h_s)_i \tag{4.8}$$

where $(\gamma_s)_i$ is the average shear distortion of the i^{th} strip. For this analysis, no distinction was made between shear sliding and displacements due to shear distortions on the beam. Instead, both effects were considered as shear contributions. Figure 4.101 through Figure 4.104 show the relative contributions of the deformation mechanisms to the applied lateral drifts in each of the coupling beam specimens.

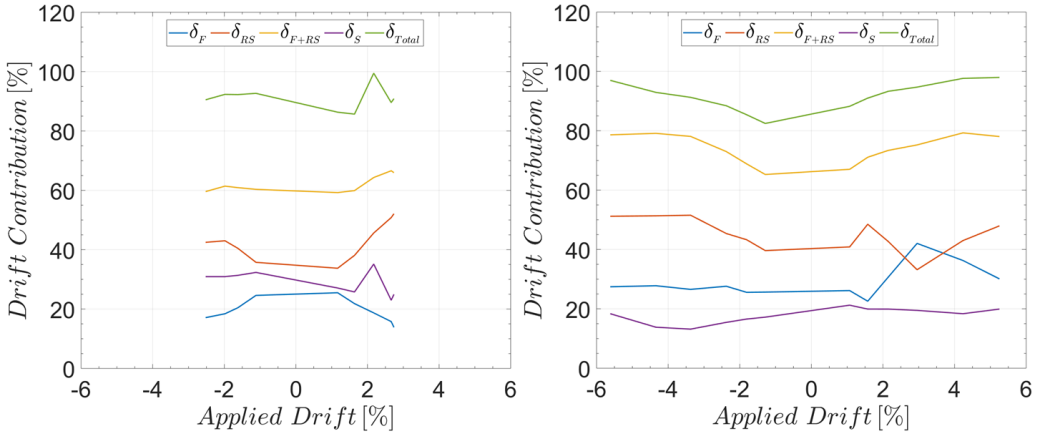

a) Specimen CB1 b) Specimen CB2

Figure 4.101: Relative Contributions to Drift. a) Specimen CB1; b) Specimen CB2.

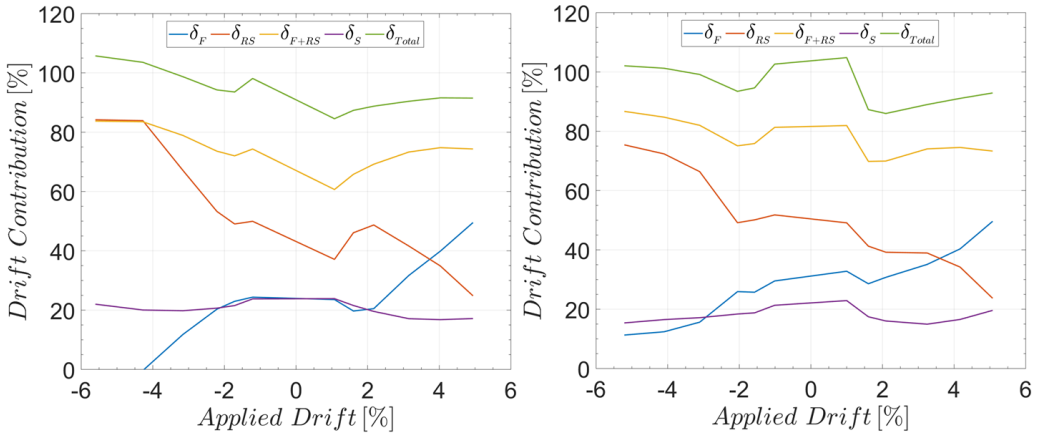

a) Specimen CB3 b) Specimen CB4

Figure 4.102: Relative Contributions to Drift. a) Specimen CB3; b) Specimen CB4.

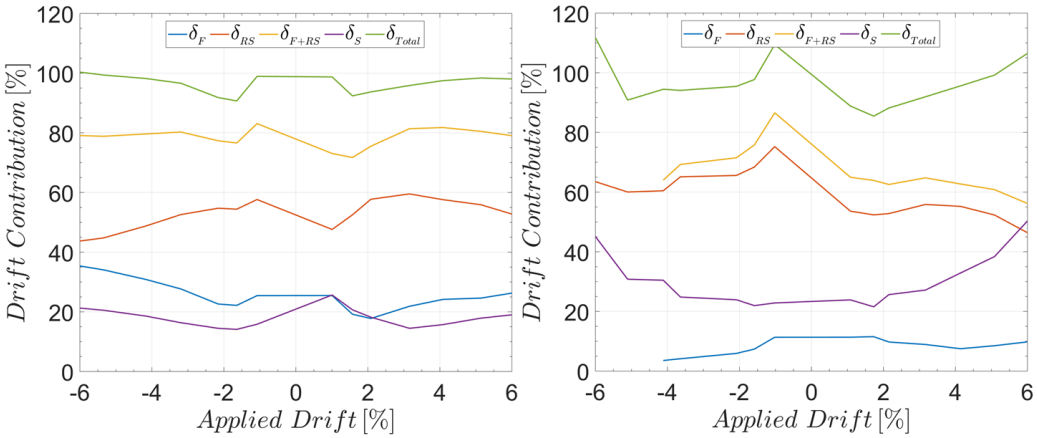

a) Specimen CB5 b) Specimen CB6

Figure 4.103: Relative Contributions to Drift. a) Specimen CB5; b) Specimen CB6.

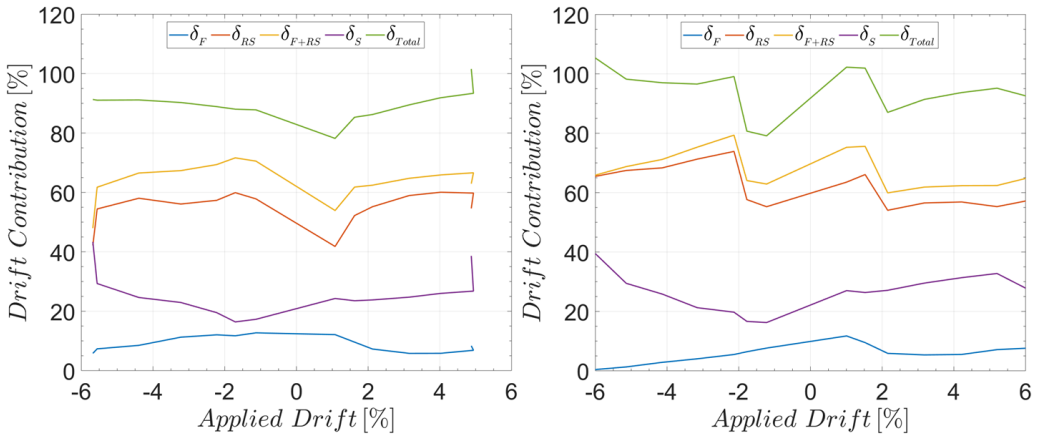

a) Specimen CB7 b) Specimen CB8

Figure 4.104: Relative Contributions to Drift. a) Specimen CB7; b) Specimen CB8.

Table 4.9 summarizes the relative contributions of the deformation mechanisms to the applied drift for each coupling beam specimen. The contributions shown represent the average contribution of the different mechanisms to the applied drifts for each specimen across the range of applied displacements. In addition, Tables 4.10, 4.11, and 4.12 summarize the average drift contributions of each deformation mechanism during the 1.0%, 3.0%, and 5.0% drift cycles, respectively.

Table 4.9: Average Contribution of Deformation Mechanisms to Drift Demand.

	Average Contribution to Lateral Drift			
Specimen	Shear	Flexure	Reinforcement Slip	Total
CB1	29%	20%	42%	91%
CB2	18%	29%	45%	92%
CB3	20%	22%	52%	94%
CB4	18%	28%	49%	95%
CB5	18%	26%	53%	97%
CB6	30%	8%	59%	97%
CB7	26%	9%	55%	90%
CB8	27%	6%	62%	94%

Table 4.10: Lateral Drift Contributions for 1.0% Drift Cycle.

	Average Contribution to Lateral Drift			
Specimen	Shear	Flexure	Reinforcement Slip	Total
CB1	30%	25%	35%	89%
CB2	19%	26%	40%	85%
CB3	24%	24%	44%	91%
CB4	22%	31%	50%	104%
CB5	21%	25%	53%	99%
CB6	23%	11%	64%	99%
CB7	21%	12%	62%	95%
CB8	10%	22%	61%	92%

Table 4.11: Lateral Drift Contributions for 3.0% Drift Cycle.

	Average Contribution to Lateral Drift			
Specimen	Shear	Flexure	Reinforcement Slip	Total
CB2	16%	34%	42%	93%
CB3	18%	22%	54%	95%
CB4	16%	25%	53%	94%
CB5	15%	25%	56%	96%
CB6	26%	7%	60%	93%
CB7	24%	9%	66%	98%
CB8	25%	5%	64%	94%

Table 4.12: Lateral Drift Contributions for 5.0% Drift Cycle.

	Average Contribution to Lateral Drift			
Specimen	Shear	Flexure	Reinforcement Slip	Total
CB2	19%	29%	50%	97%
CB3	20%	25%	55%	99%
CB4	17%	30%	50%	98%
CB5	19%	29%	50%	99%
CB6	35%	6%	56%	97%
CB7	28%	7%	64%	99%
CB8	31%	4%	61%	97%

On average, the deformation mechanisms accounted for 90% to 97% of the applied lateral drift. Clearly, drift contributions from reinforcement slip at the interfaces played a major role on the behavior of the precast SFRC beams. Concentrated rotations at the beam-wall interfaces accounted for approximately 40-50% of the applied lateral drift in the specimens with aspect-ratio of 3.0 and approximately 60% in the specimens with aspect-ratio of 2.0. As expected, contributions from flexural deformations were largest (approximately 20 to 30%) in Specimens CB2 through CB5 with $\frac{l_n}{h} = 3.0$, whereas in the beams with aspect ratio of 2.0, flexural deformations accounted for less than 10% of the applied drift. Moreover, the average shear contributions to drift were approximately 20% for Specimens CB2 through CB5 ($\frac{l_n}{h} = 3.0$) and 26 to 30% for Specimens CB6 through CB8 ($\frac{l_n}{h} = 2.0$).

4.10 Energy Dissipation

It is well established that coupling beams play a major role in the behavior of earthquake-resistant coupled wall systems. In addition to the improved coupled-wall lateral stiffness and strength provided by the coupling action of the beams, coupling beams are expected to dissipate a substantial amount of the energy imparted to the structure by the ground motions. Energy dissipation in reinforced concrete flexural members is attributed to mechanisms such as concrete cracking,

friction between cracked surfaces, and inelastic reinforcement deformations. The energy dissipated by the coupling beams during a given drift cycle can be calculated as the area enclosed by the shear force versus displacement hysteresis loop. To evaluate the energy dissipation capacity of the SFRC coupling beams, energy dissipated per drift cycle was calculated for each specimen and is shown in Figure 4.105.

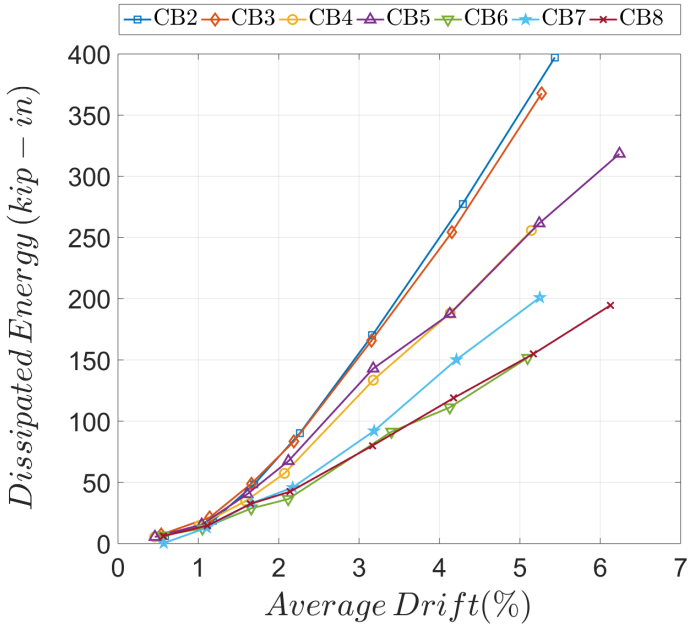

Figure 4.105: Energy Dissipated per Drift Cycle.

A continuous increment in the dissipated energy was observed for all the coupling beam specimens that exhibited ductile behavior (i.e., Specimens CB2 through CB8). To better compare the energy dissipation capacity of the SFRC coupling beams, the energy dissipated by the specimens was normalized by the energy dissipated by an equivalent elasto-plastic system. For this purpose, the energy dissipated in each displacement cycle of the coupling beams was normalized using an elasto-plastic system reaching the same peak force and displacement. The stiffness of the elasto-plastic system was selected to be equal to the effective stiffness (i.e., peak-to-peak stiffness) of the first cycle to 0.5% drift for each coupling beam

specimen. This is consistent with the approach taken by Lequesne (2011) and Setkit (2012), and thus allows for a direct comparison of the results. Furthermore, first yield of flexural reinforcement was identified during the 0.5% and 0.75% drift cycle for the coupling beam specimens. Thus, the SFRC coupling beam stiffness during the 0.5% drift cycle approximately corresponds to the stiffness at first yield. Figure 4.106a shows a sample hysteresis loop taken from Specimen CB5 corresponding to the 6.0% drift cycle and the equivalent elasto-plastic loop used for normalization.

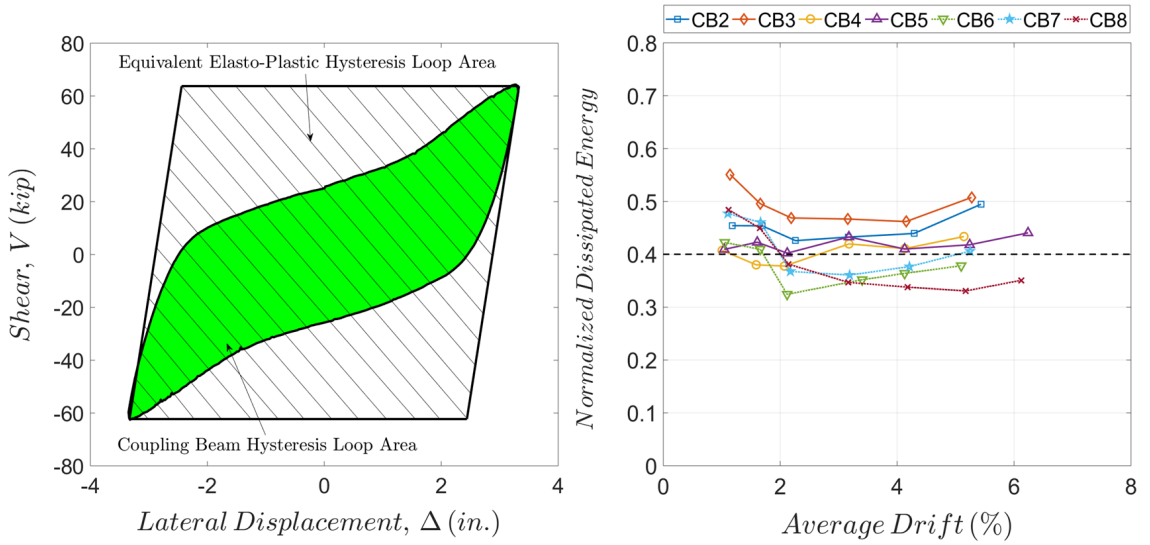

a) Coupling Beam and Equivalent Elasto-Plastic Hysteresis Loop

b) Normalized Dissipated Energy per Drift Cycle

Figure 4.106: Normalized Dissipated Energy. a) Coupling Beam and Equivalent Elasto-Plastic Hysteresis Loops; b) Normalized Energy per Drift Cycle.

Figure 4.106b shows the variation of normalized dissipated energy for cycles of 1.0% drift and greater. The specimens with span-to-depth ratio of 3.0 and 2.0 are plotted in Figure 4.106b with solid and dotted lines, respectively. In general, the SFRC coupling beams exhibited very good energy dissipation capacity with little to no deterioration of the energy dissipating mechanisms. The normalized energy dissipated during each displacement cycle remained approximately constant,

with average values of 0.44 and 0.39 for coupling beams with $l_n/h = 3.0$ and 2.0, respectively. Specimens CB2 through CB5 (span-to-depth ratio of 3.0) exhibited normalized dissipated energies between 0.40 and 0.49 throughout the range of applied displacements. On the other hand, the normalized dissipated energy ranged from 0.38 to 0.41 for Specimens CB6 through CB8 (span-to-depth ratio of 2.0). These results are in good agreement with results reported by Lequesne (2011) and Setkit (2012). Table 4.13, adapted from Lequesne (2011) and Setkit (2012), presents the average normalized dissipated energy (for drifts beyond 1.0%) for several coupling beam specimens reported in the literature, including the specimens reported herein. These results support that SFRC coupling beams with well-confined plastic hinge regions exhibit energy dissipation capacities comparable to well-detailed diagonally reinforced concrete coupling beams.

Table 4.13: Normalized Dissipated Energy for RC and SFRC Coupling Beams.

Researchers	Year	l_n/h	Axial Force (Y/N)	FRC (Y/N)	Diagonal Bars (Y/N)	Normalized Dissipated Energy
*Shiu et al.	1978	2.50	N	N	Y	0.50
*Tegos et al.	1988	2.00	Y	N	Y	0.35
*Naish et al.	2009	2.40	N	N	Y	0.55
**Setkit, M.	2012	2.75	Y	N	Y	0.45
*Lequesne, R.	2010	1.75	Y	Y	Y	0.40
**Setkit, M.	2012	3.30	Y	Y	Y	0.45
**Setkit, M.	2012	3.30	Y	Y	N	0.40
**Setkit, M.	2012	2.75	Y	Y	Y	0.43
**Setkit, M.	2012	2.75	Y	Y	Y	0.40
**Setkit, M.	2012	2.75	Y	Y	N	0.35
Current study	2016	3.00	Y	Y	N	0.45
Current study	2016	3.00	Y	Y	N	0.49
Current study	2016	3.00	Y	Y	N	0.40
Current study	2016	3.00	Y	Y	N	0.42
Current study	2016	2.00	Y	Y	N	0.38
Current study	2016	2.00	Y	Y	N	0.41
Current study	2016	2.00	Y	Y	N	0.38

* Adapted from Lequesne (2011); ** Adapted from Setkit (2012)

5 DESIGN AND MODELING RECOMMENDATIONS

5.1 SFRC Tensile and Flexural Response Evaluation

As presented in the literature review (Section 2.1), the mechanical properties of fiber reinforced concretes (FRCs) are dependent on the fiber aspect ratio (l_f/d_f), type of mechanical anchorage (e.g., hooks, undulations, or twists), fiber tensile strength (f_u), and fiber volume fraction (V_f). Therefore, designers considering FRC in their designs must be able to select the appropriate fiber reinforcing parameters that will result in an FRC with the desired mechanical properties. For this purpose, the tensile and flexural responses of FRCs with hooked steel fibers were studied. In the following sections, relations between SFRC peak post-cracking strength and fiber reinforcing parameters are evaluated. Also, an empirical model for the estimation of peak post-cracking strength based on fiber volume fraction, aspect ratio and tensile strength is presented.

5.1.1 Relationship Between Tensile Post-Cracking Strength and Fiber Reinforcing Parameters

One of the most important parameters that define the tensile behavior of SFRCs is the peak post-cracking strength, f_{pc}. Thus, the relationship between f_{pc} and the fiber reinforcing parameters, i.e., V_f, l_f/d_f, and f_u, was investigated.

5.1.1.1 Post-Cracking Tensile Strength Versus Fiber Volume Fraction

The results from direct tension tests discussed in Section 3.7.2 and results reported in Tameemi and Lequesne (2015) were analyzed to establish relations between peak post-cracking strength and fiber volume fraction. Average response results were considered for each fiber investigated, i.e., RC 80/30 BP, RC 55/30 BG, and HE 55/35 fibers. Also, to eliminate the influence of concrete strength (e.g., its influence on fiber bond behavior), the ratio of the peak post-cracking strength to the first cracking strength ($R_{pc} = f_{pc}/f_{cr}$) was considered in the analysis. A summary of the

average first cracking and peak post-cracking tensile strength of the investigated SFRCs is provided in Table 5.1. Note that in Table 5.1, first cracking and peak post-cracking strength values for most SFRCs reinforced with RC 80/30 BP fibers are not reported because the reported R_{pc} values for each V_f are average values of SFRC samples with significantly different compressive strengths (e.g. 6 and 10 ksi). Therefore, only the average strength ratio is reported.

Table 5.1: SFRC Average Tensile Responses.

Fiber Type	V_f (%)	l_f/d_f	f_{cr} (psi)	f_{pc} (psi)	$R_{pc} = \frac{f_{pc}}{f_{cr}}$
HE 55/35	1.00	64	570	329	0.58
HE 55/35	1.25	64	498	293	0.59
HE 55/35	1.50	64	503	367	0.73
RC 55/30 BG*	0.50	55	462	60	0.13
RC 55/30 BG*	0.75	55	419	130	0.31
RC 55/30 BG†	1.00	55	477	245	0.51
RC 55/30 BG	1.25	55	482	244	0.51
RC 55/30 BG*	1.50	55	418	255	0.61
RC 80/30 BP*	0.50	79	-	-	0.61
RC 80/30 BP*	0.75	79	-	-	0.85
RC 80/30 BP†	1.00	79	-	-	0.88
RC 80/30 BP	1.25	79	572	614	1.07
RC 80/30 BP†	1.50	79	-	-	1.14

* Reported by Tameemi and Lequesne (2015)
† Values Include Samples from Current Study and Tameemi and Lequesne (2015)

To investigate the effect of V_f on the peak post-cracking strength of SFRCs, the influence of the fiber aspect ratio and strength, l_f/d_f and f_u, respectively, must be removed from the data. To accomplish this, R_{pc} values for each SFRC were normalized by the peak post-cracking strength ratio exhibited by the SFRC reinforced with the same fiber at a $V_f = 1.5\%$; e.g., R_{pc} values for SFRCs reinforced with RC 80/30 BP fibers were divided by the R_{pc} corresponding to RC 80/30 BP fibers at a $V_f = 1.5\%$. The strength ratio for an SFRC reinforced with a given fiber at a $V_f = 1.5\%$ is henceforth referred to as $(R_{pc})_{1.5\%}$.

Regression analyses were used to define three simple models describing the influence of the fiber dosage on the normalized peak post-cracking strength ratios ($\frac{f_{pc}}{f_{cr}(R_{pc})_{1.5\%}}$[†]). Note that for structural applications, such as coupling beam design, volume fractions below 1.0% are generally not adequate. Therefore, the model expressions were obtained by least squares linear regressions neglecting the data for SFRCs reinforced at a 0.5% volume fraction. However, the reported errors and coefficients of determination (R^2) were calculated accounting for the data of SFRCs at a 0.5% volume fraction as a measure of the model accuracy throughout the full range of fiber volume fractions considered. The regression models are shown in Figure 5.1, where two linear models and a power-law model are compared. Also, Figure 5.1 shows the 95% confidence prediction bounds for the power-law model.

[†] Given that the reported R_{pc} values are average ratios of SFRCs with different compressive strengths, f_{cr} for the SFRC reinforced at a 1.5% volume fraction was not necessarily the same as f_{cr} for the SFRCs reinforced at a different V_f. Thus, the ratio $\frac{f_{pc}}{f_{cr}(R_{pc})_{1.5\%}}$ was strictly not equal to $\frac{f_{pc}}{(f_{pc})_{1.5\%}}$.

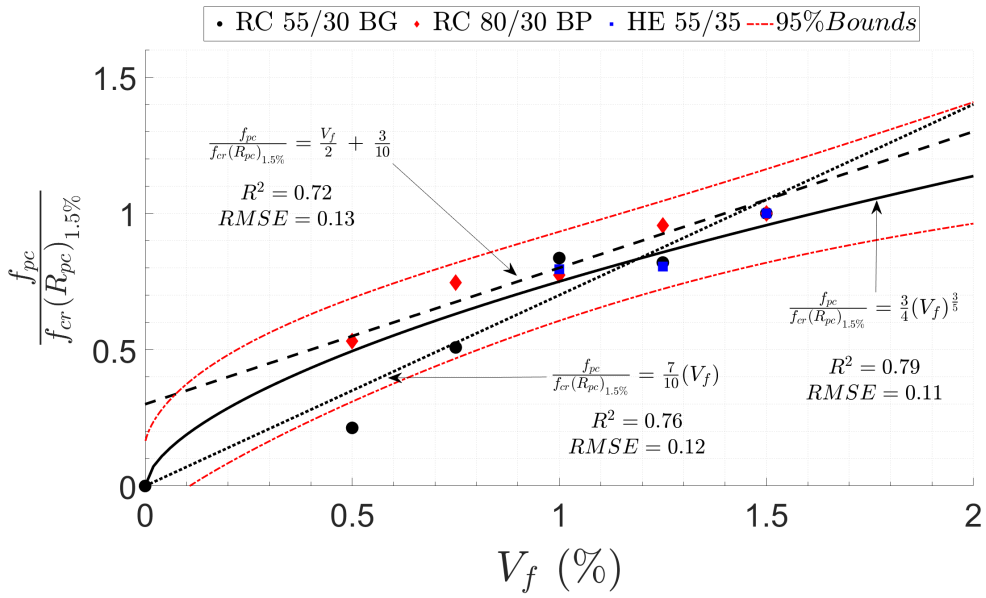

Figure 5.1: Influence of Fiber Volume Fraction on SFRC Peak Post-Cracking Tensile Strength.

As shown in Figure 5.1, both the zero intercept linear model and the power-law model seem to fit the data better; however, all the models are fairly similar in terms of how well they estimate the SFRC peak post-cracking strength ratio as a function of V_f. Due to mixing constraints and associated challenges in achieving a uniform fiber distribution, further increments in fiber volume fraction beyond approximately 1.5% are expected to lead to smaller increases in peak post cracking strength. Therefore, despite the similarities between these models, the power-law model (Equation 5.1) is believed to better represent the expected relationship between the peak post-cracking strength ratio and V_f.

$$\frac{f_{pc}}{f_{cr}\,(R_{pc})_{1.5\%}} = \frac{3}{4}(V_f)^{\frac{3}{5}} \tag{5.1}$$

5.1.1.2 Peak Post-Cracking Strength Versus Fiber Tensile Strength and Aspect Ratio

The tensile strength of SFRCs is known to increase with fiber aspect ratio. In SFRCs reinforced with hooked fibers, the peak post-cracking strength is largely influence by mechanical anchorage and thus, the tensile strength of the fiber also influences peak post-cracking strength. Now that a relationship between the peak post-cracking strength and the fiber content has been selected, the effect of fiber aspect ratio and fiber tensile strength (f_u) was investigated. To accomplish this, the following expression was assumed to describe the peak post-cracking strength of the SFRCs,

$$\frac{f_{pc}}{f_{cr}} = F_{(V_f)}\ (R_{pc})_{1.5\%} \tag{5.2}$$

where $F_{(V_f)}$ is the function obtained from the regression analysis discussed in the preceding paragraphs to account for the effect of V_f on the post-cracking strength.

Each of the fibers considered in this study had a different aspect ratio and tensile strength. Therefore, three different aspect ratios with corresponding tensile strengths were considered. Due to the limited data available, the post-cracking strength ratio $(R_{pc})_{1.5\%}$ was assumed proportional to the square-root of the fiber aspect ratio times the normalized fiber tensile strength, as shown in Equation 5.3.

$$(R_{pc})_{1.5\%} = \Psi \sqrt{\frac{l_f}{d_f}\ \frac{f_u}{(f_u)_{min}}} \tag{5.3}$$

where $(f_u)_{min}$ is the lowest fiber tensile strength considered in this study from among commercially available fibers, i.e., 160 ksi, and Ψ is a constant. The relationship between the peak post-cracking strength ratio of the SFRCs reinforced at a 1.5% volume fraction is shown in Figure 5.2. The constant Ψ can be taken as 0.08, which leads to reasonable agreement with the experimental data, as shown in Figure 5.2.

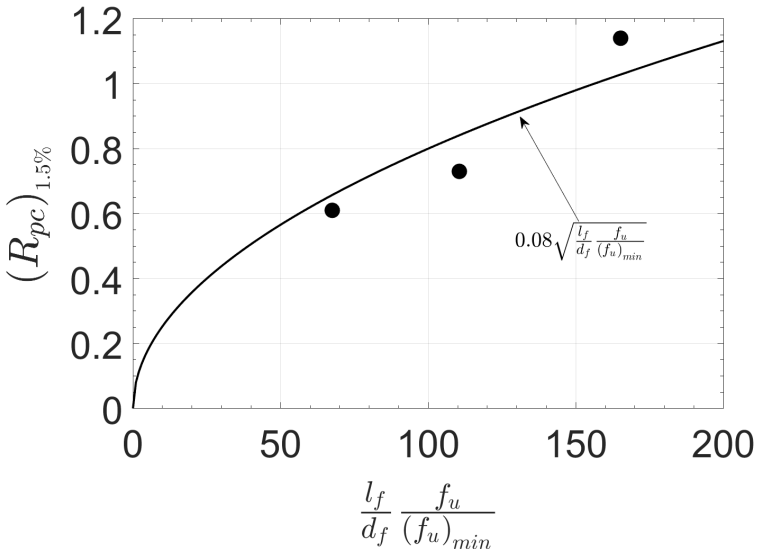

Figure 5.2: Relation Between $(R_{pc})_{1.5\%}$ and Fiber Aspect Ratio and Tensile Strength.

The peak post-cracking strength ratio can thus be estimated as,

$$R_{pc} = \frac{f_{pc}}{f_{cr}} = 0.06(V_f)^{\frac{3}{5}}\sqrt{\frac{l_f}{d_f}\frac{f_u}{f_{u_{min}}}} \tag{5.4}$$

where $f_{u_{min}}$ =160 ksi. Given the limited data, the proposed model is restricted to hooked steel fibers with $160\,ksi \leqslant f_u \leqslant 330\,ksi$; $55 \leqslant \frac{l_f}{d_f} \leqslant 80$; and $0.5\% \leqslant V_f \leqslant 1.5\%$.

5.1.1.3 Calculated Peak Post-Cracking Strength Ratios

To evaluate the accuracy of Equation 5.4, post-cracking strength ratios were calculated and compared to the experimental post-cracking strength ratios. Figure 5.3 shows the experimental and calculated f_{pc}/f_{cr} ratios. The red-dashed lines in Figure 5.3 are the $\pm$20% bounds.

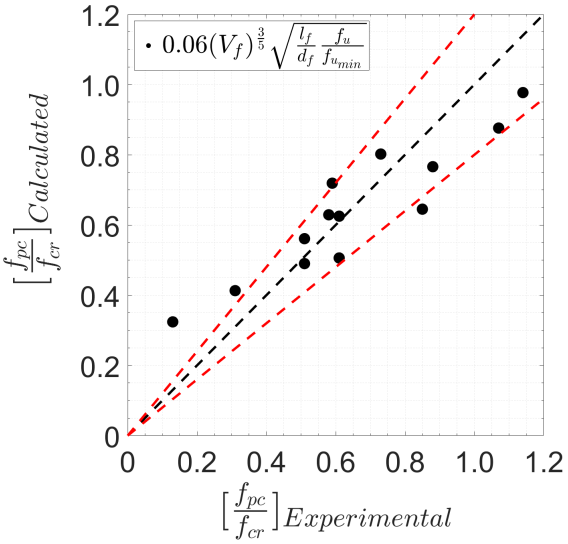

Figure 5.3: Experimental and Calculated Tensile Strength Ratios.

As shown in Figure 5.3, most of the calculated peak post-cracking strength ratios are within 20% of experimental values.The average ratio of calculated-to-experimental tensile peak post-cracking strength ratio was 1.00 with a coefficient of variation of 17.8%.

5.2 SFRC Tensile Versus Flexural Response

The tensile response of fiber reinforced concrete is typically used to characterize the performance of the composite; however, it is also a challenging material property to properly characterize. Due to the challenges associated with direct tension tests and the lack of a standardized direct tension test for SFRCs, there is a large variability in the results and testing methods published in the literature, which prevents meaningful comparisons between reported results (for further details on the challenges of direct tension tests of FRC and the variability of results see Naaman, 2007a, 2017). For most applications, the performance of SFRCs is assessed through standardized flexural tests such as ASTM C1609 and BS EN 14651:2005.

For design purposes, it is useful to estimate the flexural response of SFRCs based on the required tensile response, or the tensile response based on a given flexural response. Some guidance can be found in the literature on relationships between the tensile and flexural response of FRCs (Vandewalle, 2003; Naaman, 2007a; ACI Committee 544, 2018). The following discussion will focus on relating the tensile response of SFRCs, as measured by the direct tension tests discussed in Section 3.7.2, to the modulus of rupture and a residual strength based on bending tests per ASTM C1609 (2012). The modulus of rupture (MOR) for FRCs is defined as the equivalent elastic stress at peak post-cracking strength.

Consider an SFRC beam with depth h, width b and flexural stresses along the beam cross-section, as shown in Figure 5.4a. The stresses acting on the beam at peak post-cracking flexural strength can be modeled assuming linear[1] compressive stresses up to the concrete compressive strength and uniform tensile stress with an intensity equal to the SFRC peak-post cracking strength (f_{pc}), as shown in Figure 5.4b.

[1] The assumed shape of the compression stress block, i.e., linear, parabolic, or rectangular, has little influence on the flexural analysis (Naaman, 2007a).

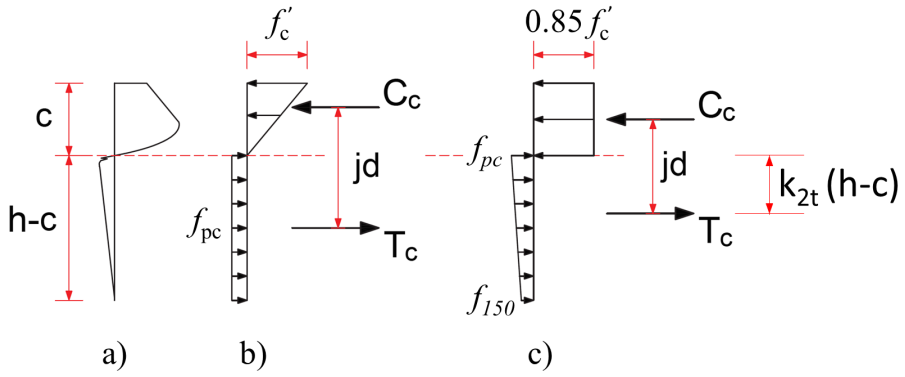

Figure 5.4: Stress Distributions for SFRC Bending Analysis; a) "Real" Stresses; b) Assumed Stresses at Peak Post-Cracking Strength; c) Assumed Stresses at Residual Strength ($\delta = \frac{L}{150}$).

At peak post-cracking flexural strength and enforcing equilibrium on the cross-section shown in Figure 5.4b, it can be shown that the neutral axis depth ratio ($\frac{c}{h}$) and the modulus of rupture can be calculated as:

$$\frac{c}{h} = \frac{f_{pc}}{\frac{f_c'}{2} + f_{pc}} \tag{5.5a}$$

$$MOR = f_{pc}\left(1 - \frac{c}{h}\right)\left(3 + \frac{c}{h}\right) = \frac{f_c'}{2}\left[\left(\frac{c}{h}\right)^2 + 3\frac{c}{h}\right] \tag{5.5b}$$

To estimate the residual flexural strength ($f_{E_{150}}$) corresponding to a deflection of $\frac{1}{150}$ of the span length ($\delta = \frac{L}{150}$), a uniform compressive stress block with intensity of $0.85f_C'$ and a linear tensile stress distribution were assumed, as shown in Figure 5.4c. The residual tensile strength (f_{150}) was taken as the tensile stress at a crack opening corresponding to a beam deflection of $\frac{L}{150}$ (w_{150}). On average, the results from bending tests for all the investigated SFRCs indicate that the crack width at peak post-cracking strength (w_{pc}) was in the range of approximately 0.028 to 0.053 in. and $w_{150} \approx 0.2$in (COV= 3.8%), based on the equivalent stress versus crack width response obtained from un-notched beam tests. For further details on flexural and tensile responses, see Section 3.7 and Appendices B.2 and B.3.

The change on the assumed tensile stress distribution between the two loading stages (Figure 5.4b and Figure 5.4c) is based on the experimental tensile responses. The response up to peak post-cracking strength can be approximated by a constant stress equal to f_{pc}, whereas the response at larger deformation demands will be well into the softening branch of the SFRC tensile response and thus, a linearly decreasing tensile stress distribution is more appropriate. Enforcing equilibrium with the stresses shown in Figure 5.4c, the neutral axis depth can be calculated as,

$$\frac{c}{h} = \frac{f_{pc} + f_{150}}{2\left(0.85f'_c\right) + f_{pc} + f_{150}} \;=\; \frac{f_{Avg.}}{0.85f'_c + f_{Avg.}} \tag{5.6a}$$

where $f_{Avg.} = \frac{f_{pc}+f_{150}}{2}$. The location of the tensile stress resultant with respect to the neutral axis is given by,

$$k_{2t}(h-c) = \frac{f_{pc} + 2f_{150}}{3\left(f_{pc} + f_{150}\right)}(h-c) \;=\; \left[\frac{2}{3} - \frac{f_{pc}}{6f_{Avg.}}\right](h-c) \tag{5.6b}$$

The moment at a deflection of $\frac{L}{150}$ and the internal lever arm (jd) are calculated as,

$$M_{150} = \left(0.85f'_c\, b\, c\right)\, jd; \quad jd = \frac{c}{2} + k_{2t}\,(h-c) \tag{5.6c}$$

and the residual strength (equivalent elastic flexural stress) is given by,

$$f_{E_{150}} = \frac{6\,M_{150}}{b\,h^2} \;=\; 0.85f'_c\,\frac{c}{h}\left[\frac{3c}{h} + \left(1 - \frac{c}{h}\right)\left(4 - \frac{f_{pc}}{f_{Avg.}}\right)\right] \tag{5.6d}$$

Equations 5.5 and 5.6 can be used to estimate the flexural response based on a known tensile post-cracking strength and a residual tensile stress at a crack width of 0.2 in (f_{pc} and f_{150}, respectively), or to estimate f_{pc} and f_{150} based on the peak equivalent flexural stress (MOR) and the equivalent flexural stress at $\delta = \frac{L}{150}$ ($f_{E_{150}}$) from bending tests on un-notched beams. Estimating the flexural response

from f_{pc} and f_{150} is straightforward because the neutral axis depth can be easily calculated with Equations 5.5a and 5.6a. However, estimating the tensile response from flexure (MOR and $f_{E_{150}}$) requires solving first a quadratic expression for the ratio c/h corresponding to the modulus of rupture (Equation 5.5b) and then, f_{pc} can be obtained from Equation 5.5a. The calculated f_{pc} value is then used in order to solve Equations 5.6a and 5.6d for c/h and $f_{Avg.}$ (or f_{150}).

The calculated strengths from the described analysis were compared to the experimental responses of the investigated SFRCs and the results are shown in Figure 5.5. The red markers in Figures 5.5a and b correspond to series of tests where the beams were tested at a much older age than the tension specimens. Note that, the stresses shown on Figures 5.5a and 5.5b are equivalent flexural stresses (f_E) and tensile stresses (f_t), respectively, and the dashed lines represent ±20% error bounds.

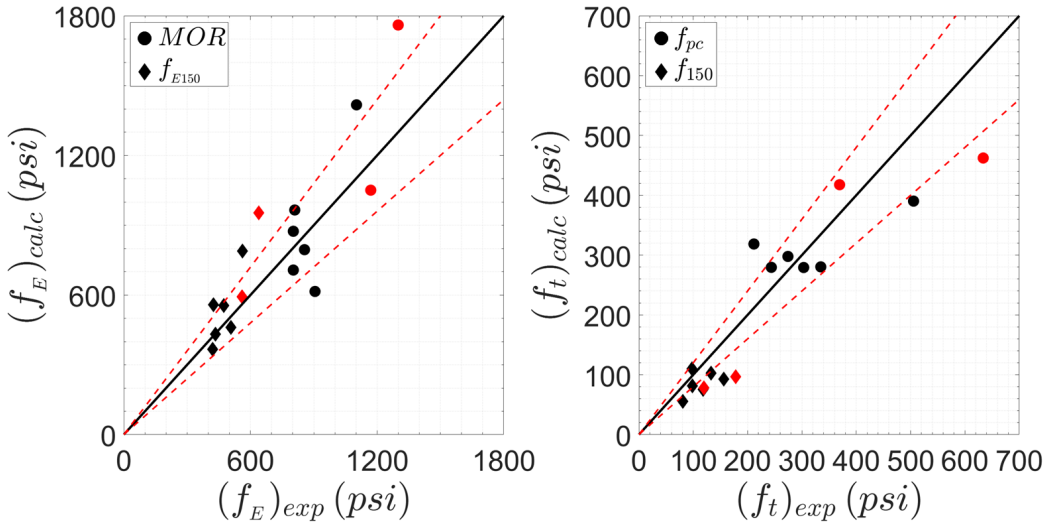

Figure 5.5: Comparison of Calculated and Experimental Flexural and Tensile Stresses; a) Flexural Stress from Tensile Response; b) Tensile Stress from Flexural Response.

Calculated peak post-cracking and residual flexural strengths from tensile stresses ranged from approximately 70% to 130% and 90% to 140% of the experimental values, respectively; however, the average $\frac{\mathrm{MOR}_{\mathrm{calc}}}{\mathrm{MOR}_{\mathrm{exp}}} \approx 1.0$ with a COV $\approx 22\%$, and $\frac{(f_{\mathrm{E}_{150}})_{\mathrm{calc}}}{(f_{\mathrm{E}_{150}})_{\mathrm{exp}}} \approx 1.1$ with a COV $\approx 20\%$. Likewise, estimating the tensile response from flexural stresses resulted in calculated stresses ranging from approximately 80% to 150% and 60% to 110% of the experimental values, for tensile peak post-cracking and residual strengths, respectively. On average, $\frac{(f_{\mathrm{pc}})_{\mathrm{calc}}}{(f_{\mathrm{pc}})_{\mathrm{exp}}} \approx 1.04$ with a COV $\approx 26\%$ and $\frac{(f_{150})_{\mathrm{calc}}}{(f_{150})_{\mathrm{exp}}} \approx 0.8$ with a COV $\approx 25\%$. As expected, there is a large variability in the SFRC responses; however, as seen in Figure 5.5, most of the calculated stresses are reasonable estimates (within 20%) of the average measured flexural and tensile stresses.

In the absence of a standardized FRC tensile test and keeping in mind the large variability of the tensile response, results from ASTM C1609 bending tests can be used to obtain a rough estimate of the SFRC tensile response. For this purpose, the crack width corresponding to f_{150} may be taken as 0.2in which, based on experiments, seemed to show little variation. On the other hand, the crack width at tensile peak post-cracking strength is more difficult to estimate and experimental values show great variability. Therefore, as a rough estimate, the tensile response can be assumed to be linear, in which case the peak post-cracking strength may be assumed to occur at zero crack width, as shown in Figures 5.4c and 5.6. Further guidance on estimating the tensile response of SFRCs from their flexural response is provided in 544.4R-18: Guide for Design with Fiber-Reinforced Concrete (ACI Committee 544, 2018).

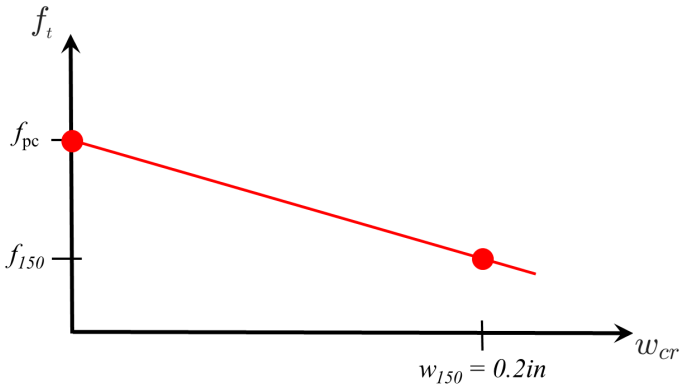

Figure 5.6: Assumed Tensile Response for Calculation of Flexural Strength of ASTM C1609 Beams at a Midspan Deflection of $\frac{L}{150}$.

5.3 Design of SFRC Coupling Beams

5.3.1 Dowel Reinforcement Cut-off

Because of the precast design of the SFRC coupling beams, the beam-to-wall connection, i.e., cold joint, was reinforced with U-shaped dowels to strengthen the joint and encourage inelastic deformations to occur within the coupling beam. Further, even if the SFRC coupling beam is cast-in-place, it is likely that the SFRC would be stopped at the intersection with the wall. In the test coupling beams, the design of the dowel reinforcement was intended to lead to nearly simultaneous yielding at the beam-wall interface and within the coupling beam itself. Selection of the area and extension of the dowel reinforcement can be determined as follows. Considering the moment capacity and demand diagram in Figure 5.7, the dowel cutoff distance X_{dowel} can be calculated as:

$$\frac{M_{P-Interface}}{l_n/2} = \frac{M_{P-Interface} - M_{P-Dowel}}{X_{dowel}} \rightarrow X_{Dowel} = (1 - \frac{M_{P-Dowel}}{M_{P-Interface}}) \frac{l_n}{2} \qquad (5.7)$$

where $M_{P-Interface}$ and $M_{P-Dowel}$ are the plastic moment capacity at the beam-wall interface and a section right after the termination of the dowel reinforcement, respectively. The ratio of the calculated plastic moment capacities at the two sections ($\frac{M_{P-Dowel}}{M_{P-Interface}}$) for the specimens tested in this study was approximately 9/10 and the shear demands corresponding to the development of their flexural strength at the dowel cutoff sections ($V_{P-Dowel}$) were between 3 to 10% higher than the calculated shear demand corresponding to the development of the moment capacity at the beam-wall interface ($V_{P-Interface}$).

The experimental coupling beams in this study were designed with a dowel cutoff distance equal to 9 and 8 bar diameters (d_b) for specimens with aspect ratio of 3.0 and 2.0, respectively, to encourage the formation of plastic hinges within $h/2$ from the supports (i.e. expected plastic hinge region). This dowel cutoff distance was most successful for specimens with span-to-depth ratio of 3.0 for which well-defined plastic hinges formed within $h/2$ from the supports. Spreading of inelastic deformations away from the beam-wall interfaces, on the other hand, was very limited for the beams with span-to-depth ratio of 2.0. Given the adequate performance of the experimental beams, a dowel cutoff distance of at least $8d_b$ and resulting in $0.9 \leqslant \frac{V_{P-Interface}}{V_{P-Dowel}} \leqslant 1.0$ is recommended for the design of SFRC coupling beams.

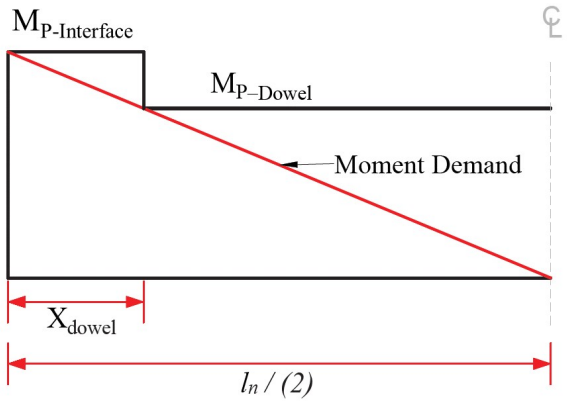

Figure 5.7: Coupling Beam Moment Capacity/Demand Diagram.

5.3.2 Plastic Sectional Analysis

The nonlinear sectional analysis discussed in Section 4.6.1 showed very good agreement with the measured strengths of the SFRC coupling beams. Thus, a simple plastic sectional analysis can be used to reasonably estimate the expected flexural strength and consequently the shear demand of these elements. Such an analysis and recommended assumptions are discussed next.

To consider the effects of SFRC on the flexural strength of the beams, several assumptions must be made. Given the superior deformation capacity of SFRCs over conventional concrete (see Section 4.6.3), the SFRC ultimate strain capacity can be assumed as $\epsilon_{cu} = 0.02$ and $\epsilon_{cu} = 0.012$ for Class I, and Class II and III SFRCs, respectively, as opposed to 0.003 specified in ACI 318 (see Section 4.2 for a discussion on SFRC performance classification). In addition, the possibility of modeling the tensile behavior of SFRCs as a tensile stress block, acting over a portion of the tension side of the flexural member, was investigated. Based on the measured strains and observed fractures in the longitudinal reinforcement of the SFRC coupling beams, the tension reinforcement is assumed to achieve strain hardening. To account for tensile strain hardening, an elasto-plastic stress-strain response was assumed for the reinforcement taking $f_u = 1.1(f_y)_{measured}$ and $f_u = (f_y)_{measured}$ for reinforcing bars in tension and compression, respectively (see Section 3.7.4).

For design, the axial restraint provided by the stiff walls of coupled wall systems can be accounted for by an axial force of $0.1f'_c A_g$. This level of axial compression is consistent with the axial forces developed in the coupling beam component tests reported herein and in the work of Lequesne (2011) and Setkit (2012). The assumptions made for the sectional analysis are:

1. Euler-Bernoulli beam bending - plane section remain plane after bending.
2. Concrete compression zone can be modeled using Whitney's stress block.
3. Maximum concrete compressive strain $\epsilon_{cu} = 0.02$ and $\epsilon_{cu} = 0.012$ for Class I, and Class II and III SFRCs, respectively.
4. Elastoplastic stress-strain response for the steel reinforcement with a maximum stress of $1.1(f_y)_{measured}$ and $(f_y)_{measured}$ for bars in tension and compression, respectively.
5. SFRC tensile stress block with intensity of $\alpha\sqrt{f'_c}$ acting over a depth equal to $\beta_t(h - c)$ (Figure 5.8).

Figure 5.8 shows a schematic of the sectional analysis with the internal stresses and forces, the strain profile, and applied axial force (P) assumed for a given cross section. A discussion on the development of the tensile stress block is provided in the following section.

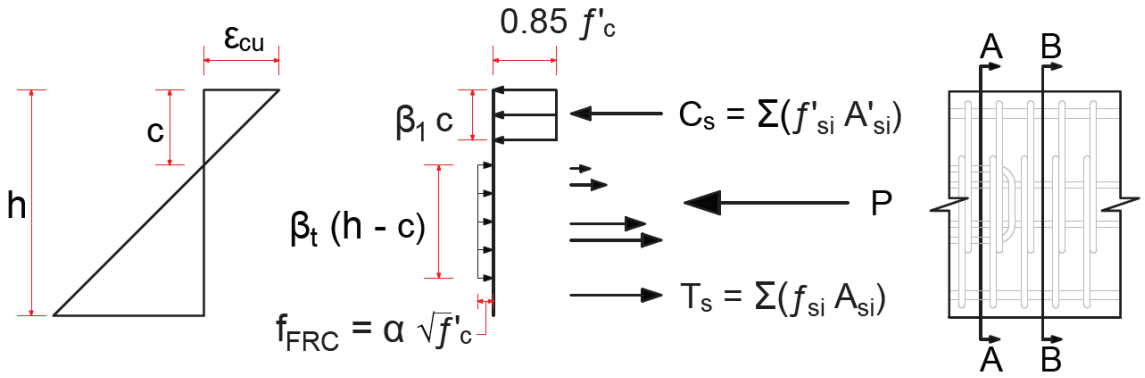

Figure 5.8: Assumed Strain Distribution and Internal Forces.

5.3.2.1 Development of Tensile Stress Block

Having characterized the tensile response of the different SFRCs used for the construction of the coupling beam specimens, an average tensile response for each class of SFRC (i.e., Class I, Class II and Class III SFRCs) was established. The measurements recorded during tensile tests of SFRC notched prisms only allow for defining these average responses in terms of tensile stress versus crack opening, which cannot be directly incorporated in a sectional analysis. To incorporate a material response in a sectional analysis, stress-strain responses are needed. However, strains can be estimated using the calculated crack openings and a gauge length that is characteristic of each SFRC Class.

To estimate the appropriate gauge length, the strains in the material are assumed to be reasonably estimated by effectively "smearing" the flexural crack over the crack spacing observed in the SFRC within the plastic hinges of the coupling beam specimens. Moreover, it is also implied that the flexural cracks in the SFRC

at a given load have approximately the same width. Inspection of the cracking observed within the plastic hinges of the coupling beams tested showed that the flexural cracks had similar widths prior to initiation of damage localization; damage localization typically occurred at deformations larger than that corresponding to peak strength. To estimate the average crack spacing for each class of SFRC, images of the beams plastic hinges cast with each SFRC were analyzed using the open-source software ImageJ (Schneider et al., 2012). The software was calibrated using a known dimension on each image analyzed and several measurements of the spacing of flexural cracks were taken. The approximate average crack spacing for each class of SFRC were 3.5, 4.0 and 4.5 in. for Class I, Class II, and Class III SFRCs, respectively.

The purpose of this analysis was to develop an equivalent uniform tensile stress that can be incorporated in a plastic sectional analysis, as shown in Figure 5.8. To achieve this, average tensile stress-strain responses for each class of SFRC were generated based on the average response of tension specimens for each SFRC considered in this study. The average SFRC tensile responses and their respective models are shown in Figure 5.9, and are assumed to adequately represent the stresses developed in the concrete under tension. The solid lines in Figure 5.9 are the calculated average response based on the results of the tension prisms corresponding to each class of SFRC with strains calculated using the average crack spacings discussed in the previous paragraph. The dotted lines are extrapolated assuming the descending slope of the response remains constant, and the black-dashed lines correspond to the modeled average responses. The key points of the modeled SFRC tensile responses are provided in Table 5.2, where ϵ_0, ϵ_1 and ϵ_{fp} are the strains corresponding to peak strength, strength immediately after first cracking, and strain at zero stress (fiber pull-out), respectively. Similarly, $f_{t_{max}}$) and f_{t_1} are the peak tensile stress and the stress just after first cracking, respectively.

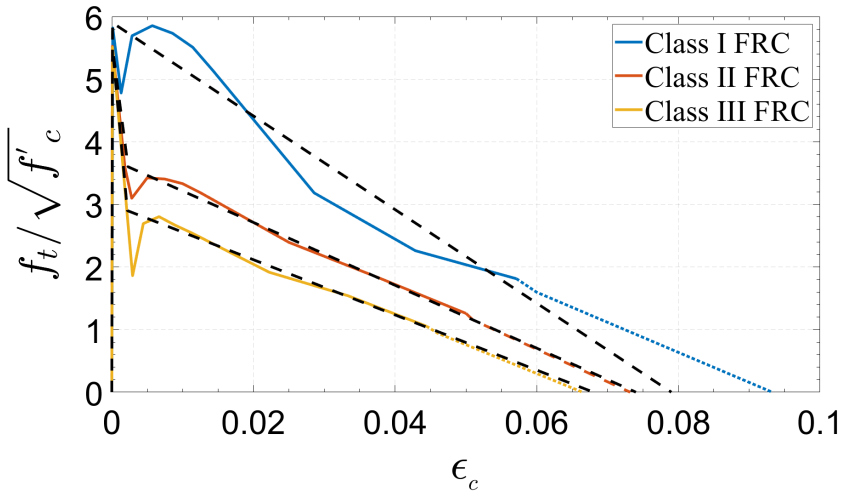

Figure 5.9: Measured and Modeled SFRC Average Tensile Responses.

Table 5.2: Stresses and Strains for Modeling the Average Response of Each SFRC Class.

SFRC Performance Class	$\frac{f_{t_{max}}}{\sqrt{f'_c}}$	ϵ_0 (μ)	$\frac{f_{t_1}}{\sqrt{f'_c}}$	ϵ_1 (μ)	ϵ_{fp} (%)
Class I	5.9		N/A	N/A	7.9
Class II	5.5	$\frac{f_{t_{max}}}{E_c}$	3.6	2300	7.4
Class III	5.5		2.9	2200	6.8

A statically equivalent tensile stress block must yield the same net tensile force in the concrete acting at the same distance from the neutral axis as the actual stress resultant. To ensure these two conditions are reasonably satisfied, a similar approach to that used to develop Whitney's compressive stress block (Whitney, 1942) was followed. Integrating the average response, the parameters k_{1t} and k_{2t} (shown in Figure 5.10) for the tensile response of the SFRCs were calculated as,

$$k_{1t} = \frac{\int_0^{\epsilon_{max}} f_t(\epsilon)d\epsilon}{f_{t_{max}}\,\epsilon_{max}} \quad \text{and} \quad k_{2t} = \frac{\int_0^{\epsilon_{max}} \epsilon\, f_t(\epsilon)d\epsilon}{\epsilon_{max}\int_0^{\epsilon_{max}} f_t(\epsilon)d\epsilon} \tag{5.8}$$

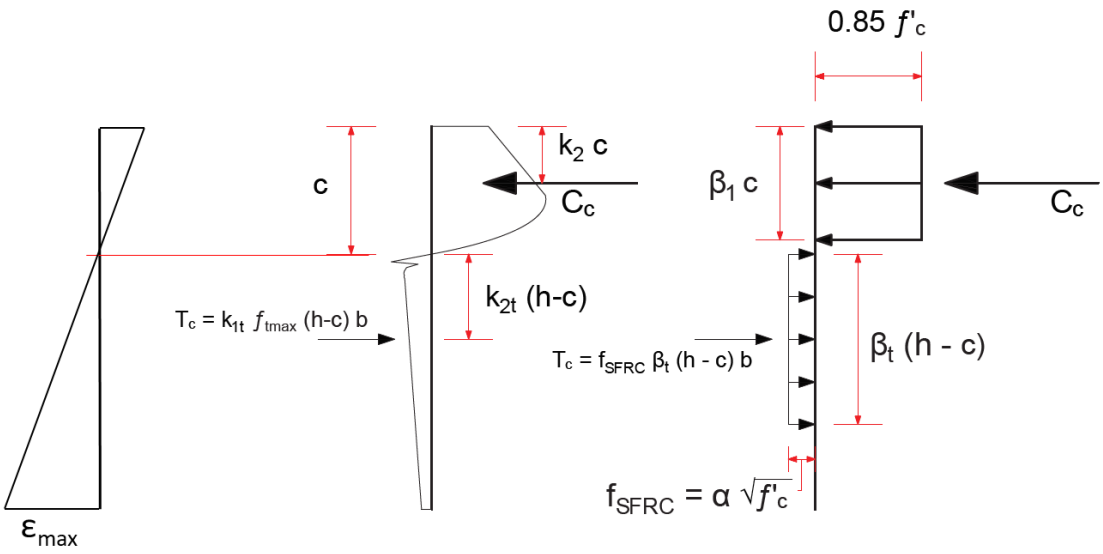

Figure 5.10: SFRC Stress Distributions and Corresponding Stress Blocks.

Ensuring that the resultant of the tensile stress block acts at the same location as the resultant of the average stress distribution, it follows that $\beta_t = 2k_{2t}$. The intensity of the tensile stress block, f_{SFRC}, is obtained by equating the tension resultants of the stress block and the average response, which leads to $\alpha = \frac{k_{1t}}{\beta_t}\frac{f_{tmax}}{\sqrt{f'_c}}$. The plastic sectional analysis described in Section 5.3.2 was used to calculate the peak flexural strength of Specimens CB2 through CB8 and to calculate the tensile stress block parameters corresponding to peak strength. For the analysis, the average SFRC tensile responses were modeled as shown in Figure 5.9, and the axial force measured during the tests at peak strength was considered. Table 5.3 shows the calculated stress block parameters for Specimens CB2 through CB8, while the calculated strengths are discussed in the following section.

Table 5.3: Tensile Stress Block Parameters at Peak Flexural Strength.

Specimen SFRC Class	CB2 II	CB3 III	CB4 III	CB5 III	CB6 II	CB7 I	CB8 I
k_{1t}	0.61	0.48	0.46	0.46	0.53	0.77	0.72
k_{2t}	0.46	0.45	0.45	0.45	0.44	0.45	0.43
β_t	0.93	0.90	0.89	0.89	0.89	0.90	0.87
$\alpha\,(\sqrt{f'_c})$	3.62	2.95	2.86	2.86	3.30	5.05	4.86

Based on the analysis and experimental data, tensile stress block parameters $\beta_t = 0.9$ and α of 5.0, 3.5, and $2.9\sqrt{f'_c}$ for Class I, II, and Class III SFRCs, respectively, seem reasonable to model the tensile behavior of SFRCs with hooked fibers.

5.3.2.2 Validation of Proposed Sectional Analysis

To validate the sectional analysis and the tensile stress block developed in the preceding section, the expected flexural strength of Specimens CB2 through CB8 was calculated and compared to the experimental strengths. Additionally, two possible β_t values, either 0 or 0.9, were considered to quantify the effect of SFRCs on calculating coupling beam flexural strength.

On average, the calculated flexural strengths using the tensile stress block are approximately 14% higher than the experimental SFRC coupling beam strengths, while disregarding the tensile strength contribution of the SFRC led to calculated strengths in better agreement with the experimental results (see Table 5.4 and Figure 5.11). Note that results in Table 5.4 and Figure 5.11 are expressed in terms of the shear corresponding to the calculated flexural strengths. As shown in Figure 5.11, good agreement between calculated and experimental strengths were obtained by neglecting the SFRC tensile response. This may be due to early damage concentration due to termination of the dowel reinforcement and a preferential fiber alignment towards a plane normal to the beam longitudinal axis caused by the heavy amount of transverse reinforcement provided.

Table 5.4: Calculated Shear Demands for SFRC Coupling Beams.

					No SFRC Tension				SFRC Tension	
					Wall Section		Dowel Section		Dowel Section	
Specimen	f'_c (psi)	l_n/h	$\frac{P}{f'_c A_g}$	V_{Exp} (kips)	V_{Calc} (kips)	$\frac{V_{Calc}}{V_{Exp}}$	V_{Calc} (kips)	$\frac{V_{Calc}}{V_{Exp}}$	V_{Calc} (kips)	$\frac{V_{Calc}}{V_{Exp}}$
CB2	8840	3.0	0.143	100	98.3	0.98	109	1.09	114	1.14
CB3	8630	3.0	0.107	94.6	93.4	0.99	103	1.08	107	1.13
CB4	9260	3.0	0.078	75.0	80.7	1.08	84.8	1.13	90.9	1.21
CB5	9750	3.0	0.830	82.9	83.2	1.00	87.8	1.06	94.0	1.13
CB6	7950	2.0	0.077	78.2	77.3	0.99	79.6	1.02	82.9	1.06
CB7	9330	2.0	0.122	106	102	0.96	111	1.05	118	1.12
CB8	8490	2.0	0.095	81.9	84.4	1.03	89.0	1.09	96.6	1.18
					Average =	1.00	Average =	1.07	Average =	1.14
					COV =	3.8%	COV =	3.3%	COV =	4.2%

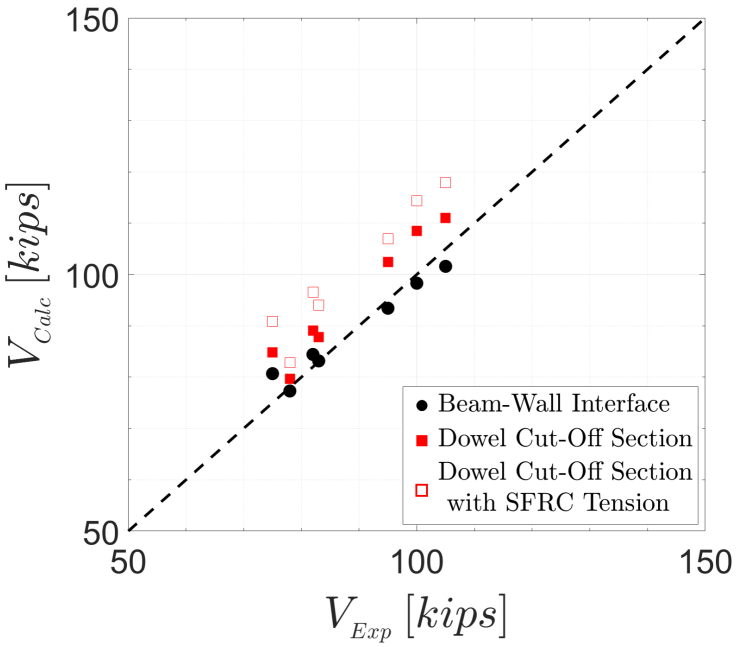

Figure 5.11: Calculated and Experimental Coupling Beam Shear Demands.

5.4 Modeling Shear-Drift Response Envelopes

Typical design practice for high-rise coupled wall systems relies on nonlinear dynamic analysis. For such analyses, one of the most practical and computationally efficient approaches for modeling the response of flexural members consists of simple "lumped plasticity" models. In such models, the flexural member consists of a linear elastic beam element and inelastic rotational and/or shear springs at the ends.

Backbone curves of reinforced concrete members can be modeled as tri-lineal force-deformation response envelopes consisting of a linear cracked-elastic region up to an effective yield strength, $(V_y)_{eff.}$, a second linear segment with reduced stiffness up to peak strength (V_{max}), and a third linear segment for strength decay up to the member deformation capacity. In this study, the deformation capacity of SFRC coupling beams was determined as the maximum deformation prior to a strength loss greater than 20%; thus, the third envelope point defining the post-peak decaying response was taken as $V = 0.8V_{max}$.

The following sections discuss the modeling approach considered for the strength and deformation mechanisms of SFRC coupling beams with the goal of modeling the shear versus drift backbone response.

5.4.1 SFRC Coupling Beam Strength

Strength calculations for modeling the envelope response of SFRC coupling beams followed the plastic sectional analysis discussed in Section 5.3.2. Flexural strengths were calculated for the cross-section at the beam-wall interface, as this section typically controls the strength of the SFRC coupling beams. Therefore, the tensile stresses carried by the SFRC were not considered. In the following discussion, strength is expressed in terms of the shear associated with a given flexural strength.

The effective yield strength was calculated as the first yield strength ($V_y^{1^{st}}$) plus a percentage of the difference between V_{max} and $V_y^{1^{st}}$. Note that no axial force is considered in the calculation of $V_y^{1^{st}}$ given the limited beam axial expansion up to that point. Based on the measured coupling beam responses, the effective yield strength can be reasonably estimated as,

$$(V_y)_{eff.} = \frac{1}{3}\left(V_{max} - V_y^{1^{st}}\right) + V_y^{1^{st}} \tag{5.9}$$

Calculating the peak flexural strength and corresponding deformation requires the selection of an appropriate limiting compressive strain for the concrete. Therefore, based on the analysis discussed in Section 4.6.3, it is proposed that ϵ_{cu} be taken as 0.02 and 0.012 for Class I SFRCs and Class II–III SFRCs, respectively. Moreover, the average axial force acting on each coupling beam at peak strength during each loading direction was considered as the axial force for peak strength calculations. For design purposes, it is recommended that an axial force of $0.1f'_cA_g$ be considered for calculations corresponding to peak strength.

5.4.2 Reinforcement Bond-Slip Response

5.4.2.1 Bond-Slip Model

The effect of reinforcement slip can be easily implemented in a "lumped plasticity" model by means of a nonlinear rotational spring. To explicitly account for reinforcement bond-slip many different models with varying levels of complexity are available in the literature, e.g., Otani and Sozen (1972), Eligehausen et al.

(1982), Alsiwat and Saatcioglu (1992), Lehman and Moehle (2000), and Sezen and Setzler (2008). As discussed in Section 4.9, reinforcement slip at the precast connections was the predominant deformation mechanism of the SFRC coupling beam specimens. Therefore, accurately capturing the bond-slip behavior is essential for modeling the response of SFRC coupling beams. For this purpose, a simple bond-slip model was considered in this study, based on the model described in Sezen and Setzler (2008) and Lehman and Moehle (2000).

As shown in Figure 5.12, the adopted bond-slip model consists of a uniform bond stress (τ_e) acting over the elastic bar segment and a lower uniform bond stress (τ_i) acting over the inelastic portion of the bar. The model considers the bond stresses acting over embedded bar lengths l_{de} and l_{di} for the elastic and inelastic segments, respectively. The embedment lengths are dependent on the magnitudes of the bond stresses τ_e and τ_i and are defined as:

$$l_{de} = \frac{f_y \, d_b}{4 \, \tau_e} \tag{5.10a}$$

$$l_{di} = \frac{\left(f_s(\epsilon_s) - f_y\right) \, d_b}{4 \, \tau_i} \tag{5.10b}$$

Integration of the reinforcement strains over the embedment lengths results in the total slip displacement and is given by,

$$\delta_{slip} = \begin{cases} \frac{\epsilon_s \, d_b}{8} \frac{f_s(\epsilon_s)}{\tau_e} & \text{for } \epsilon_s \leqslant \epsilon_y \\ \frac{\epsilon_y \, l_{de}}{2} + \epsilon_y \, l_{di} + \left[\frac{(\epsilon_s - \epsilon_y) \, l_{di}}{2}\right] & \text{for } \epsilon_s > \epsilon_y \end{cases} \tag{5.10c}$$

where $f_s(\epsilon_s)$ is the reinforcement stress at a given strain ϵ_s, and d_b is the largest bar diameter in the outermost layer of reinforcement. Once the reinforcement slip has been calculated, the corresponding rotation (θ_{slip}) is calculated assuming the rotation occurs about the neutral axis, as shown in Figure 5.12e.

$$\theta_{slip} = \frac{\delta_{slip}}{d - c} \tag{5.11}$$

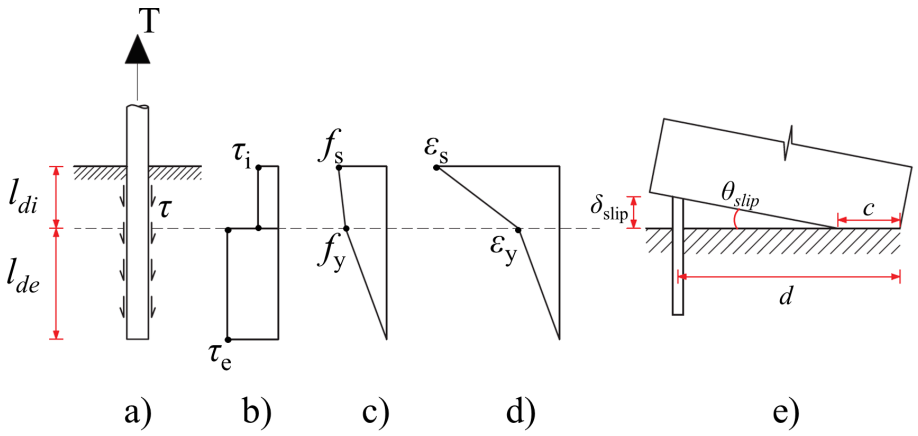

Figure 5.12: Reinforcement Bond-Slip Model. a) Embedded Bar in Tension; b) Assumed Bond Stresses; c) Bar Stresses; d) Bar Strains; and e) Bar-Slip Rotation.

5.4.2.2 Calculated Bond Strengths

Measurements from strain gauges F1 and F2, and F12 and F13 were used to estimate bond strength using Equation 5.12 (see Figure 5.14 for strain gauge locations near the beam wall-interface). From strain gauge measurements, reinforcement stresses were calculated using the modified Menegotto-Pinto model (Sakai and Mahin, 2004) described in Section 4.3. Enforcing equilibrium on the differential bar length shown in Figure 5.13, the governing equation describing the bond stress is given by,

$$\tau(x) = \frac{d_b \left[f_s\,(x + dx) - f_s\,(x) \right]}{4\,dx} \tag{5.12}$$

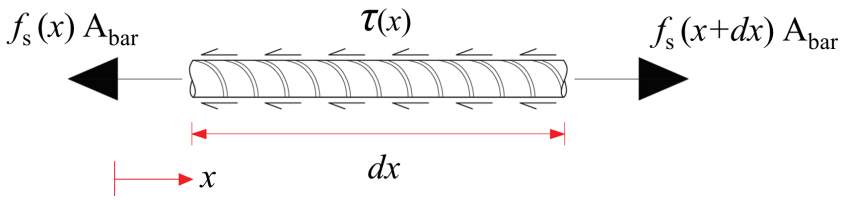

Figure 5.13: Stresses/Forces Acting on Differential Bar Length.

Bond stress calculations were performed over a constant length equal to the distance between two consecutive strain gauges. In the test beams, the strain gauges considered for bond stress calculations were located approximately 5.5 and 6.0 in. for beams with span-to-depth ratio of 2.0 and 3.0, respectively. Note that for Specimens CB6 trough CB8 the strain gauges corresponding to F12 and F13 in Figure 5.14 were F14 and F15, respectively.Figure 5.15 shows the calculated bond stress versus strain response for the outermost bars of Specimens CB3 through CB5 (the black solid line corresponds to $\tau_i = 4\sqrt{f'_c}$, psi). It should be mentioned that one or more damaged strain gauges in the other specimens did not allow calculation of bond stress between two consecutive strain gauges.

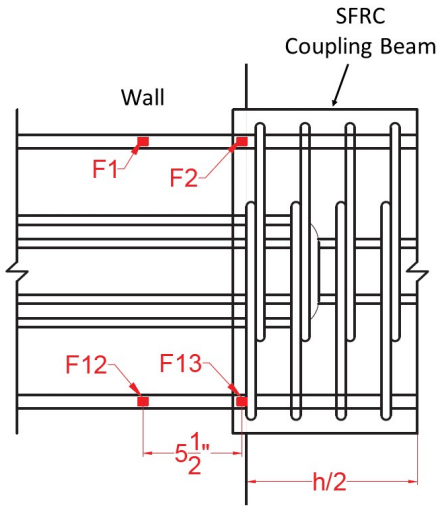

Figure 5.14: Location of Strain Gauges Used for Bond Stress Calculations in Specimens with Span-to-Depth Ratio of 3.0.

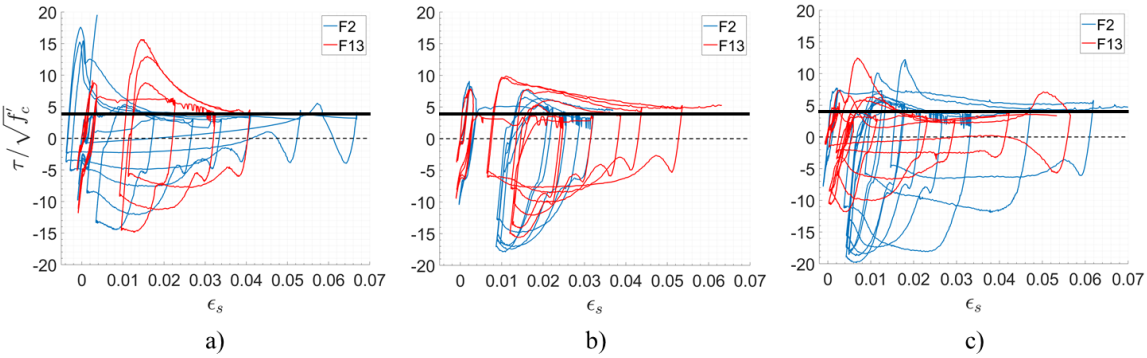

Figure 5.15: Calculated Bond Stress Response.
a) Specimen CB3; b) Specimen CB4; and c) Specimen CB5.

A detailed analysis of the calculated bond stress responses revealed unrealistic calculated bar behavior during unloading and reloading. Figure 5.16a shows a bond stress versus strain cycle where red, black, and yellow markers indicate whether the calculated bar stresses for the two consecutive gauges were both tensile, both compressive, or of opposite sign, respectively. Upon unloading, there are regions where the stresses calculated at the beam-wall interface (from gauges F2 and F13) were in tension while those within the development length (F1 and F12) were in compression; this behavior is unrealistic. Figure 5.16b shows calculated stresses from readings of strain gauges F1 and F2, where segments AB and BC correspond to unloading from compression and loading to tension, respectively. Despite their similar unloading stiffness, strain gauge measurements at the beam-wall interface changed at a faster rate, leading to the anomalous behavior. Therefore, only the data for which the calculated bar stresses were both in tension for consecutive gauges may be relied on to provide insight on the bond stress response.

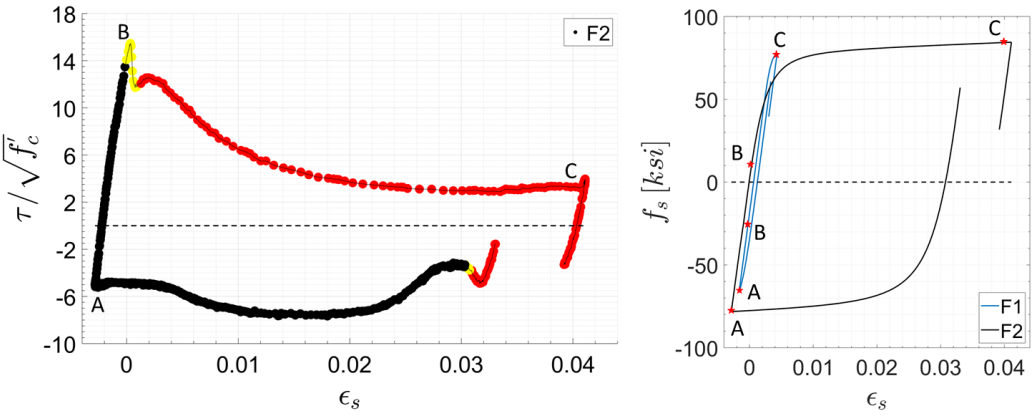

Figure 5.16: Bond Stress Response During 3.0% Drift Cycle of Specimen CB3. a) Bond Stress versus Strain; b) Calculated Bar Stresses.

The elastic bond strength was estimated based on the stresses calculated from strain gauges F1 and F12 and the distance from the bar end to the location of the strain gauge (approximately 15 inches). The resulting peak bond stresses prior to exceeding the yield strain were in the range of 10.5 to $12.2\sqrt{f'_c}$ (psi), comparable to other published values (e.g., Lehman and Moehle, 2000; Sezen and Setzler, 2008). Therefore, the bond strength for the elastic portion of the bar, τ_e, was taken as $12\sqrt{f'_c}$ (psi). On the other hand, the calculated bond stresses for the inelastic portion of the bars for Specimens CB3 through CB5 were in the range of 3.5 to $5.0\sqrt{f'_c}$ (psi) during large inelastic excursions. As shown in Figure 5.15, a bond strength τ_i of $4.0\sqrt{f'_c}$ (psi) seems more appropriate for the specimens with span-to-depth ratio of 3.0.

The strain gauges within the end-blocks of the specimens with span-to-depth ratio of 2.0 (gauges F1 and F14) were damaged and thus no data were collected, except for Specimen CB8. Bond stress calculations from gauges F1 and F2 of Specimen CB8 were possible for drift cycles below 2.0% drift and the analysis suggests a much lower bond strength τ_i than for Specimens CB3 through CB5 ($\tau_i \approx 1.2\sqrt{f'_c}$, psi). Furthermore, for the same drift level the measured strains at approximately

$10d_b$ into the supports were greater for Specimen CB8 than for the more slender coupling beams (Figure 5.17a). The larger bar strains in Specimen CB8, as well as the larger interface rotations in the other specimens with an aspect ratio of 2.0 (shown in Figure 5.17b), suggest a higher bond deterioration in the bars of these specimens compared with the specimens with an aspect ratio of 3.0.

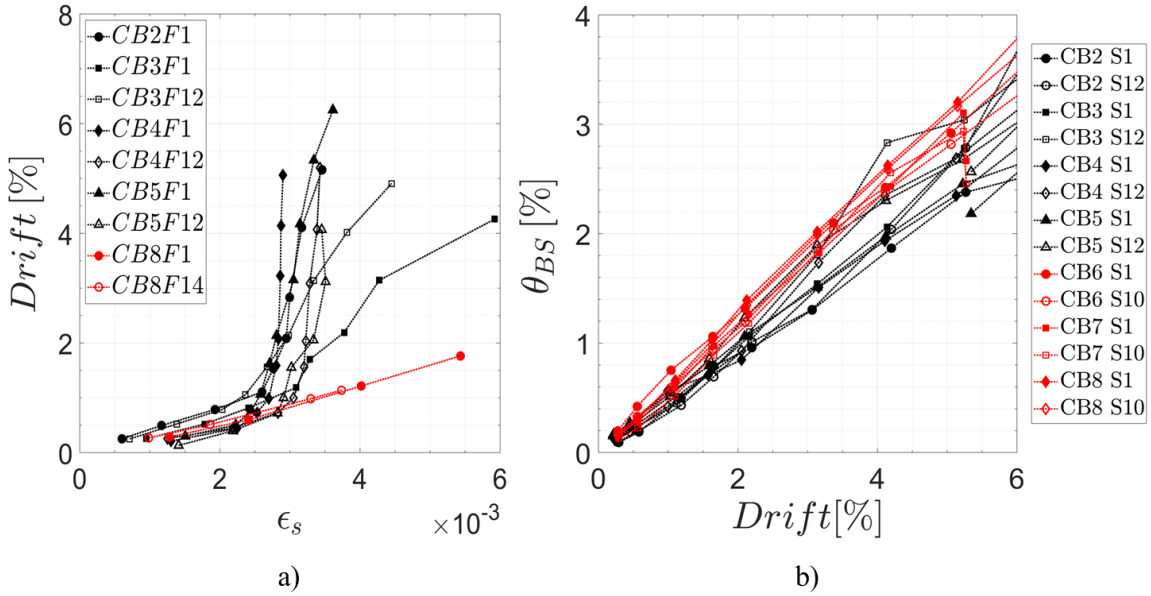

Figure 5.17: Increased Role of Slip in Coupling Beams with $l_n/h = 2.0$. a) Applied Drift Versus Measured Strains within the Support; and b) Rotations Due to Bond-Slip Versus Drift.

Despite the limitations of the presented analysis, there is supporting evidence of greater bond deterioration occurring on members with smaller span-to-depth ratios. Given the limited data, a simple variation of the uniform bond strength (τ_i) with beam span-to-depth ratio is proposed, as shown in Figure 5.18. Note, however, that the bond model discussed herein is not intended to describe in detail the reinforcement bond-slip behavior, but to allow for simple calculation of the rotations due to reinforcement slip.

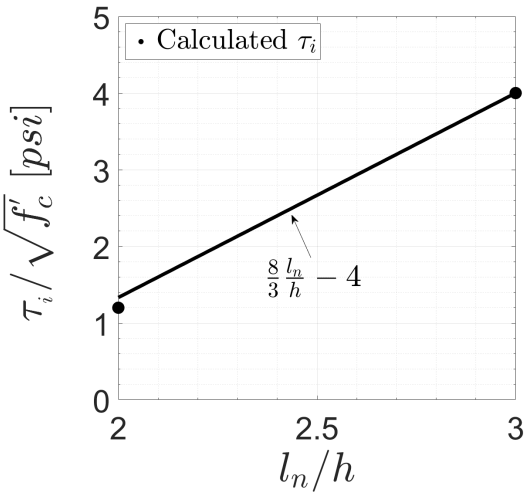

Figure 5.18: Proposed Variation of Uniform Bond Strength τ_i for SFRC Coupling Beams.

5.4.2.3 Calculated Versus Experimental Bar Slip and Interface Rotations

To evaluate the accuracy of the bond-slip model, the calculated bar slippages (δ_{slip}) were compared to the gap opening calculated near the corners of the coupling beams using the Optotrak™ markers. The gap opening calculated near a beam corner was assumed to be at the same location of the outermost bar. Although there was a small difference on the location of outermost markers and the outermost reinforcement bar ($\approx 1/4$ in. for Specimens CB2 through CB5), the gap openings calculated with the Optotrack™ data provide an estimate of the reinforcement slip for the outermost bars. Figure 5.19 shows the calculated and experimental slip responses for Specimens CB2 through CB5, where τ_e and τ_i were taken as $12\sqrt{f'_c}$ and $4\sqrt{f'_c}$ (psi), respectively. Similar to the notation used in Section 4.6.3, top left (TL), top right (TR) and so forth refer to the Optotrak™ marker grid shown in Figure A.10. The exact location of the gauges in Specimen CB5 were not recorded and thus, the comparisons shown in Figure 5.19d are based on the best estimate of the strain gauge locations according to the magnitude and sign of measured strains.

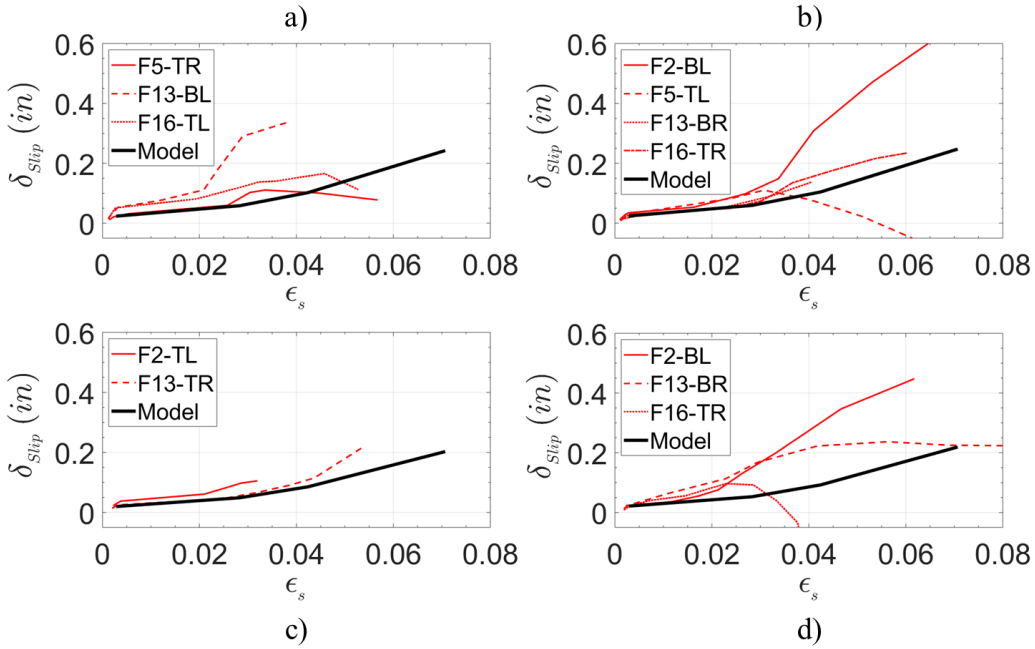

Figure 5.19: Experimental and Modeled Reinforcement Slip Responses. a) Specimen CB2; b) Specimen CB3; c) Specimen CB4; and d) Specimen CB5.

In general, the measured gap openings are larger than the calculated values and exhibit considerable variability. As shown in Figure 5.19, the simple and practical bond-slip model provides a reasonable lower bound estimate of the expected reinforcement slip for the precast SFRC coupling beams reported in this study. A comparison of the calculated and experimental slip for Specimens CB6–CB8 was not included due to a larger discrepancy between the Optotrak™ marker and reinforcement bar locations. However, a comparison of the calculated and measured rotations due to reinforcement slip was possible for all specimens; as well as two other specimens tested by others, as shown in Figure 5.20 and summarized in Table 5.5. The hollow markers in Figure 5.20 correspond to measured rotations for a given loading direction, whereas solid markers correspond to the average rotation of both loading directions. In addition, the red dotted lines mark the $\pm 20\%$ bounds.

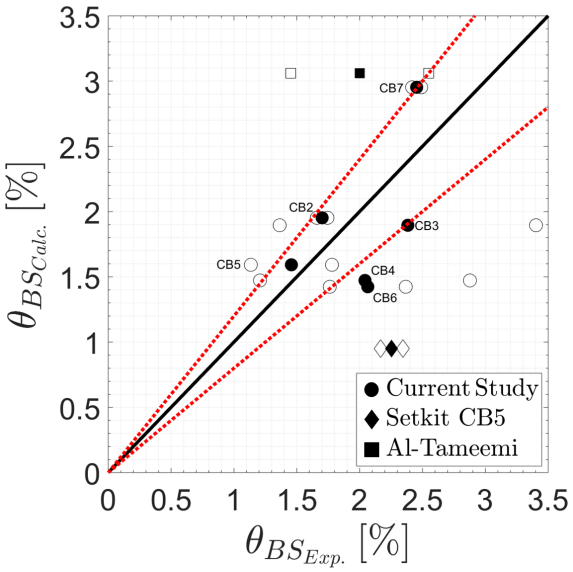

Figure 5.20: Calculated and Measured Slip Rotations at Peak Strength.

As shown in Figure 5.20, there is significant scatter on the calculated and experimental reinforcement-slip rotations, especially when loading directions are considered independently. However, given the inherent variability in bond strength, as well as its dependence on the axial load magnitude, displacement history, and the shear associated with the moment capacity of the interface versus that at the dowel cut-off section ($V_{\text{P-Interface}}/V_{\text{P-Dowel}}$), the model presented is believed to lead to reasonable estimates of the rotation due to reinforcement-slip without the need for complex or computationally intensive models. It should be mentioned that for the case of the coupling beam reported in Setkit (2012), the ratio $V_{\text{P-Interface}}/V_{\text{P-Dowel}}$ was significantly lower than for the other specimens, which led to a larger concentration of rotations at the beam-wall interface.

Table 5.5: Calculated and Experimental Reinforcement-Slip Rotations at Peak Strength.

	Positive Loading		Negative Loading		Average
Specimen	$(\theta_{BS})_{Exp.}$	$(\theta_{BS})_{Calc.}/(\theta_{BS})_{Exp.}$	$(\theta_{BS})_{Exp.}$	$(\theta_{BS})_{Calc.}/(\theta_{BS})_{Exp.}$	Ratio
CB2	1.7%	1.12	1.7%	1.18	1.15
CB3	1.4%	1.39	3.4%	0.56	0.80
CB4	1.2%	1.22	2.9%	0.51	0.72
CB5	1.8%	0.89	1.1%	1.40	1.09
*CB6	1.8%	0.81	2.4%	0.60	0.69
CB7	2.4%	1.22	2.5%	1.19	1.20
*CB8	2.9%	0.54	3.4%	0.45	0.49
**Setkit CB5	2.2%	0.44	2.3%	0.41	0.42
Al-Tameemi	1.5%	2.11	2.6%	1.20	1.53
	Average =	1.33	Average =	1.01	1.08
	COV =	31.5%	COV =	37.3%	27.2%

* Excluded from average and COV calculations due to changes in axial restraint.

** Excluded from average and COV calculations due to lower $V_{P-Interface}/V_{P-Dowel}$ capacity ratio.

5.4.3 Flexural Response

Despite the short spans typical of coupling beams, flexural deformations play an important role on the behavior of coupling beams under displacement reversals. As discussed in Section 4.9, flexural deformations within the coupling beam can account for about 30% of the overall displacement demand for beams with span-to-depth ratios of 3.0 and larger. Typically, "lumped plasticity" models account for flexural deformations with a combination of a linear elastic beam element and rigid-plastic rotational springs to account for the nonlinear flexural response of plastic hinges. The following sections discuss how the flexural deformations of SFRC coupling beams can be accounted for in a "lumped plasticity" model.

5.4.3.1 Elastic Beam Element with Shear Deformations

Elastic flexural deformations are modeled with an Euler-Bernoulli beam element. However, to account for the shear deformations of the SFRC coupling beams, the stiffness matrix of the Euler-Bernoulli beam element must be modified. For this purpose, the shear flexibility was added to the bending flexibility. The modified stiffness matrix that accounts for shear deformations was then obtained from the flexibility matrix. The lateral displacements due to elastic flexure and shear can thus be calculated as,

$$\delta_E = \delta_{FE} + \delta_{SE} = \frac{V l_n^{\,3}}{12EI}(1 + 2g) \tag{5.13}$$

where g is a non-dimensional parameter defined as $g = \frac{6EI}{GAL^2}$ (taking the shear shape factor equal to 1.0). To account for the reduced stiffness of cracked concrete, effective flexural and shear stiffness are used, as opposed to gross sectional properties. As discussed in Section 4.7.1.2, an effective shear stiffness $GA_{eff} = 0.05E_cA_g$ provides a reasonable estimate of the shear stiffness for the experimental SFRC coupling beams (concrete elastic modulus is taken as $E_c = 57000\sqrt{f'_c}$, psi). The effective flexural rigidity to be used in analyses that explicitly model the effect of reinforcement bond-slip separate from flexural deformations is discussed in the following section.

5.4.3.2 Effective Flexural Rigidity of SFRC Coupling Beams

Current design practice for high-rise buildings relying on coupled walls for lateral strength and stiffness often relies on advanced nonlinear analyses and performance-based seismic design methodologies. For such analyses, detailed component models able to capture the hysteresis behavior of RC members are used. Component models aiming to model flexural deformations and bond-slip deformations separately (e.g., using a rotational spring for bond-slip rotations at connection interfaces) must employ EI_{eff} values different than those intended to include the effect of bond-slip. Therefore, the effective flexural rigidity exhibited by the SFRC coupling beams

was determined from the experimental M–ϕ responses within the coupling beam presented in Section 4.6.1.5.

The yield moment (M_y) was defined as the smaller of the calculated moment at first yield of the flexural reinforcement as computed by M–ϕ analysis of the section after the termination of the U-shaped dowel reinforcement (Section B-B in Figure 4.48). The yield curvature (ϕ_y) was then selected as the curvature corresponding to M_y on the experimental M–ϕ curves. As shown in Figure 5.21, both the top and bottom plastic hinges in the positive and negative loading directions were considered for each SFRC coupling beam and thus, the average ϕ_y was chosen for estimating EI_{eff}. With both M_y and ϕ_y determined, the effective flexural rigidity was calculated as $EI_{eff} = \frac{M_y}{\phi_y}$.

For comparison purposes, the flexural rigidity of each beam was also calculated using the measured shear force and curvature distribution at first yield, similar to the analysis discussed in Section 4.6.2. For this purpose, the curvatures measured within the SFRC beam were used to calculate the lateral displacement due to flexure excluding concentrated rotations at the beam-wall interfaces ($(\delta_f)_{avg}$) and the effective flexural rigidity was calculated as $EI_{eff} = \frac{V l^3}{12 (\delta_f)_{avg}}$, where l was the distance between the first and last row of Optotrak™ markers within the SFRC beams (approximately 50 and 32 in. for beams with span-to-depth ratio of 3.0 and 2.0, respectively). Table 5.6 summarizes the calculated flexural rigidity for each specimen and Figure 5.21 compares the calculated effective rigidities with the values obtained from the experimental M–ϕ curves for Specimen CB4 and Specimen CB6 with span-to-depth ratios of 3.0 and 2.0, respectively.

Table 5.6: Effective Flexural Rigidity of SFRC Coupling Beams.

Specimen	M_y (kip-ft)	$(\phi_y)_{avg}$ $(\frac{rad}{in} \times 10^{-4})$	$\frac{M_y/(\phi_y)_{avg}}{EI_g}$	$\frac{V l^3/(12(\delta_f)_{avg})}{EI_g}$
CB2	105	2.7	0.30	0.33
CB3	105	2.7	0.30	0.30
CB4	80.7	2.5	0.24	0.23
CB5	82.0	2.4	0.25	0.24
CB6	45.3	0.9	0.41	0.29
CB7	52.0	1.6	0.24	0.21
CB8	43.1	0.9	0.37	0.28

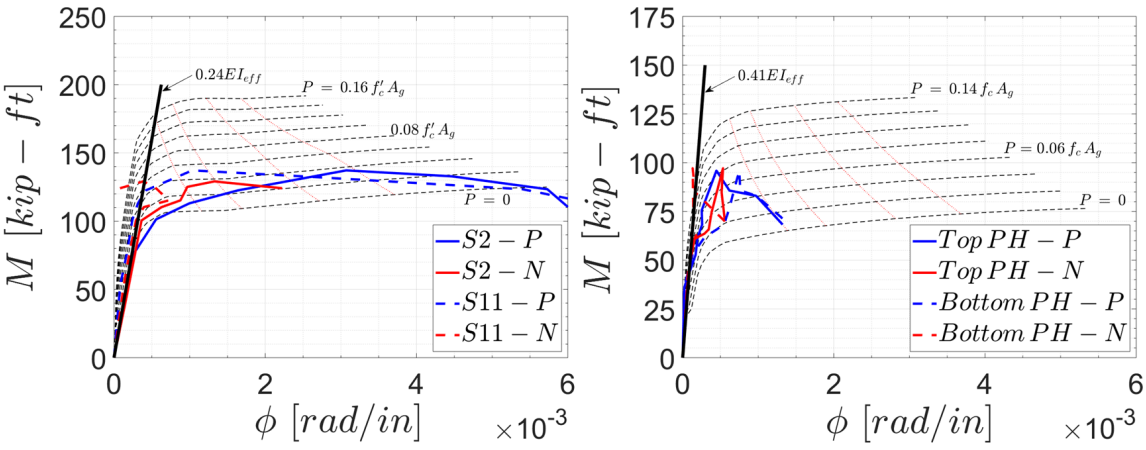

a) Effective Flexural Rigidity - Specimen CB4

b) Effective Flexural Rigidity - Specimen CB6

Figure 5.21: Plastic Hinge Flexural Rigidity. a) Specimen CB4; b) Specimen CB6.

Coupling beam effective flexural rigidity ranged from 0.21 to $0.41EI_g$, with average values of $0.27EI_g$ and $0.30EI_g$ for specimens with span-to-depth ratio of 3.0 and 2.0, respectively. Therefore, for nonlinear analyses, the effective rigidity recommended in ASCE/SEI 41-13 of $0.30EI_g$ leads to reasonable estimates of the cracked-elastic flexural rigidity for cases where bond-slip rotations are modeled separately.

5.4.3.3 Plastic Hinge Model - Inelastic Flexure

As displacement demands exceed the beam yield displacement, flexural plastic hinges form at each end of the coupling beam. To account for the additional lateral displacement due to these plastic rotations, it is assumed that plastic hinges extend over a length (l_p) from the face of the supports into the beams and that the curvature is constant over the plastic hinge length, as shown on Figure 5.22. The plastic hinge length was calibrated with the measured coupling beam responses, where $\phi_y = \frac{(M_y)_{eff.}}{EI_{eff}}$ and ϕ_u were calculated from a sectional analysis at the dowel cutoff cross-section (see Section 5.4.1). Applying the second moment-area theorem on the curvature distribution shown in Figure 5.22, the plastic flexural displacement (δ_{FP}) is calculated as,

$$\delta_{FP} = [\phi_u - \phi_y]\, l_p (l_n - l_p) \tag{5.14a}$$

and the experimental δ_{FP} was calculated as,

$$\delta_{FP} = \delta_F - \frac{V {l_n}^3}{12EI_{eff}} \tag{5.14b}$$

where δ_F is the total displacement due to flexural deformations calculated per Equation 4.7 (see Section 4.9).

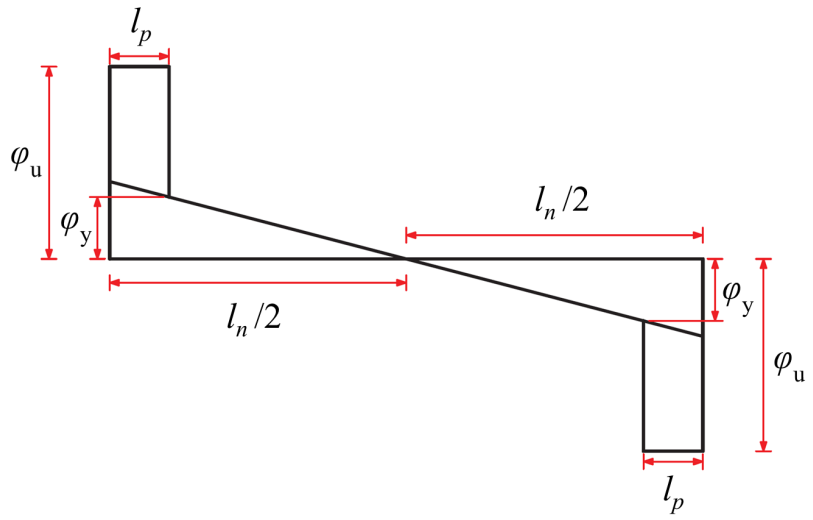

Figure 5.22: Assumed Curvature Distribution.

Analysis of the coupling beam responses suggest that a plastic hinge length of 0.4h is appropriate for coupling beams with span-to-depth ratios of 3.0 (h is the coupling beam depth).

As discussed in Section 4.6.1.5, coupling beams with span-to-depth ratio of 2.0 did not undergo large flexural rotations; their behavior was dominated by reinforcement slip and shear sliding. Consequently, the ultimate curvature capacity assumed for the plastic hinge model was not experimentally achieved, thus resulting in a very small calculated plastic hinge length. However, this does not indicate that there was no spread of flexural yielding (see Section 4.6.4). To account for the decreased plastic flexure demand within coupling beams with $2.0 \leqslant l_n/h < 3.0$, it is proposed that the plastic hinge length be varied with the coupling beam span-to-depth ratio as shown in Figure 5.23. For Coupling beams with $l_n/h = 3.0$, l_p is taken as 0.4h. Note that this analysis assumes that at peak strength, the flexural rotation capacity corresponding to the maximum compressive concrete strain is reached (refer to Section 5.4.1).

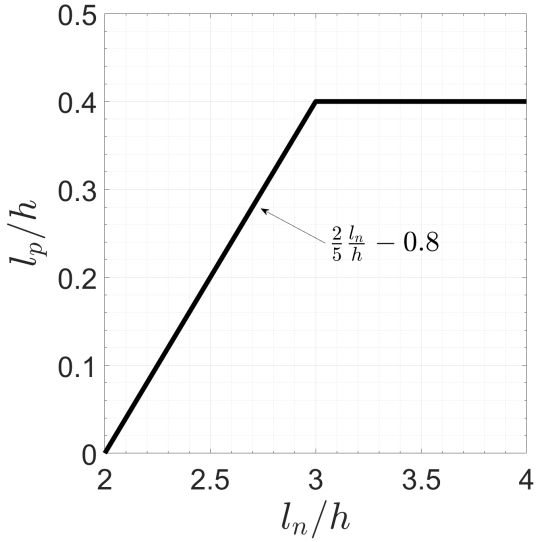

Figure 5.23: Proposed Plastic Hinge Length for SFRC Coupling Beams.

5.4.4 Shear-Sliding Displacements

Sliding across the beam-wall interfaces and within the plastic hinges must be considered to accurately model the response envelope of SFRC coupling beams. For this purpose, the total drift due to sliding displacements ($\frac{\Delta_{sliding}}{l_n}$) was related to the drift due to reinforcement slip plus flexure ($\theta_{S+F} = \theta_{BS} + \frac{\delta_F}{l_n}$), where δ_F is the total lateral displacement due to elastic and plastic flexural deformations. The relationship between sliding displacements and θ_{S+F} is shown in Figure 5.24. For comparison purposes, Specimen CB5 tested by Setkit (2012), with span-to-depth ratio of 3.3, was included in Figure 5.24a.

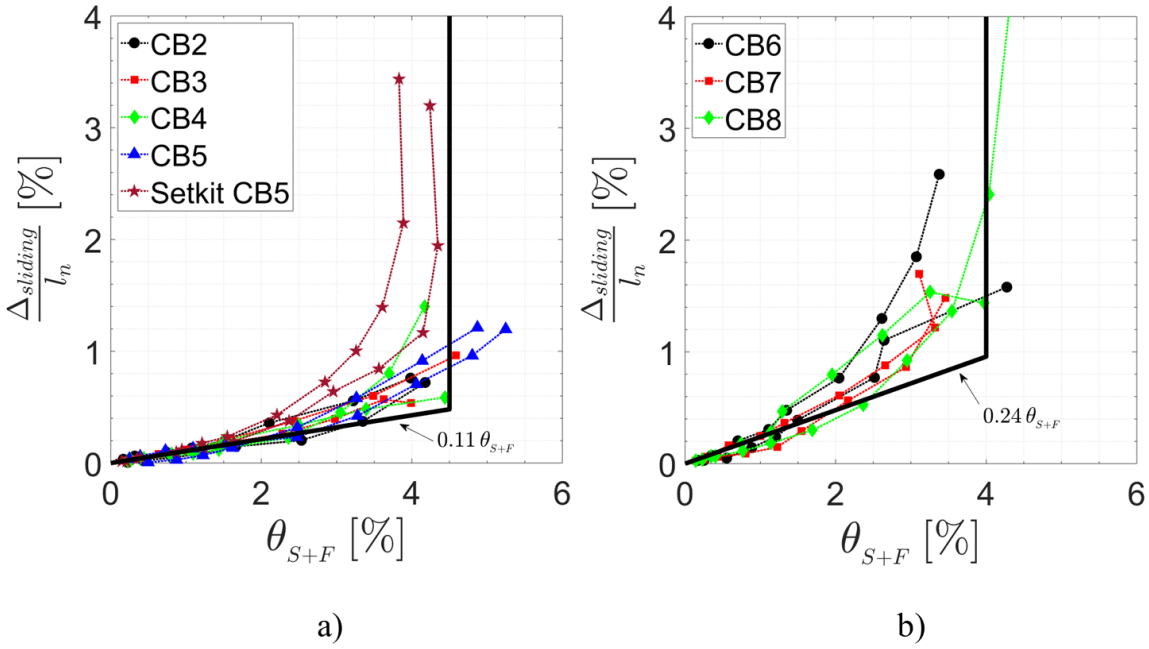

Figure 5.24: Relationship Between Drift Due To Sliding Displacements and Drift Due To Bar Slip Plus Elastic and Plastic Flexural Deformations (θ_{S+F}). a) Coupling Beams with $l_n/h \geqslant 3.0$; and b) Coupling Beams with $l_n/h = 2.0$.

As expected, sliding displacements increased as rotation increased. Further, the shear-sliding mechanism deteriorated as the beams underwent cycles of reverting displacements, leading to a faster increase of sliding displacements at large rotations. Regression analyses suggest that the nonlinear relationship between $\frac{\Delta_{sliding}}{l_n}$ and θ_{S+F} can be reasonably approximated by an expression of the form $A\,(\theta_{S+F})^{1.6}$; however, for simplicity, the relationship was considered bilinear with a limiting drift or rotation value for θ_{S+F}. The black lines shown in Figure 5.24 are the best fit linear models for Specimens CB2 through CB8 (best fit for cycles up to approximately 3.0% drift) with the recommended limiting value for θ_{S+F}. Limiting the combined drift contribution of flexure and reinforcement-slip is deemed reasonable considering the greater flexibility of shear-sliding relative to the former two deformation mechanisms at large rotations.

Once shear-sliding overtook the response, the drift contribution of the other deformation mechanism increased only marginally. Therefore, the proposed empirical shear sliding model is given by,

$$\frac{\Delta_{sliding}}{l_n} = a\,\theta_{S+F} \leqslant \min\left(a\,(\theta_{S+F})_{max},\ \frac{0.5\,in}{l_n}\right) \tag{5.15}$$

where the ratio $a = \frac{\Delta_{sliding}/l_n}{\theta_{S+F}}$ and $(\theta_{S+F})_{max}$ are dependent on the coupling beam span-to-depth ratio. The upper limit of $\Delta_{sliding} = 0.5\,in.$ is based on maximum total sliding displacement at peak strength for the test specimens. For SFRC coupling beams designed following the design recommendation presented in this document, the proposed empirical model for a and $(\theta_{S+F})_{max}$ is shown in Figure 5.25. The hollow markers shown in Figure 5.25b mark the average value of Specimens CB2 through CB5 and Specimens CB6 and CB8; Specimen CB7 was excluded because the shear stress demand was approximately 25% higher than the recommended peak shear stress demand ($8\sqrt{f'_c}$, psi) for coupling beams with span-to-depth ratio of 2.0.

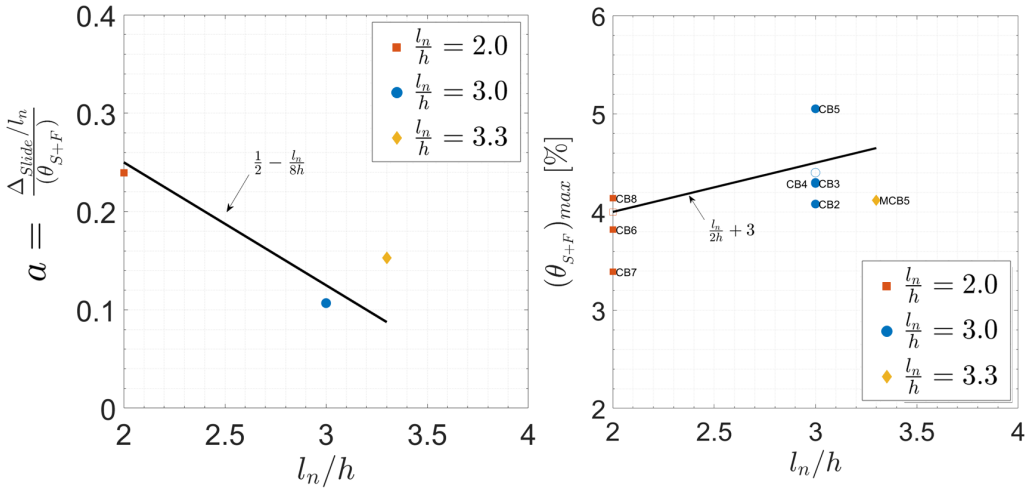

Figure 5.25: Shear-Sliding Empirical Model for SFRC Coupling Beams. a) Variation of Model Slope; and b) Proposed Slip plus Flexure Drift Contribution Limit.

Note that Specimen CB5 tested by Setkit (2012) (diamond marker on Figure 5.25), deviates from the behavior observed for the coupling beams of this study. The ratio of the shear corresponding to the development of the plastic flexural strength at the beam-wall interface to the shear corresponding to the development of the plastic flexural strength at the dowel cut-off section, $V_{P-Interface}/V_{P-Dowel}$, was, on average, 0.82 for Specimen CB5 tested by Setkit (2012), whereas for the specimens of this study this ratio ranged between 0.91 and 0.96. Therefore, the difference in behavior is attributed to a weaker -beam-wall interface relative to the dowel cut-off section, resulting in higher deformation demands at the wall face.

Shear sliding is dependent on the amount of reinforcement crossing the sliding plane and thus, it is closely related to the frictional resistance (see Section 4.7.3 for details). As discussed in Section 4.7.2, sliding at the beam-wall interfaces was more pronounced for the members with span-to-depth ratio of 2.0. However, interface sliding was similar in these specimens to the sliding observed at the dowel cut-off section of the more slender beams. Therefore, sliding behavior at the interfaces and dowel cut-off sections was assumed to be identical, following an average sliding response. It was observed that the total sliding displacement at a 20% strength decay for Specimens CB2 trough CB8 was similar, leading to similar average sliding displacements per sliding plane, $(\delta_{sliding})_{avg.}$, as shown on Figure 5.26.

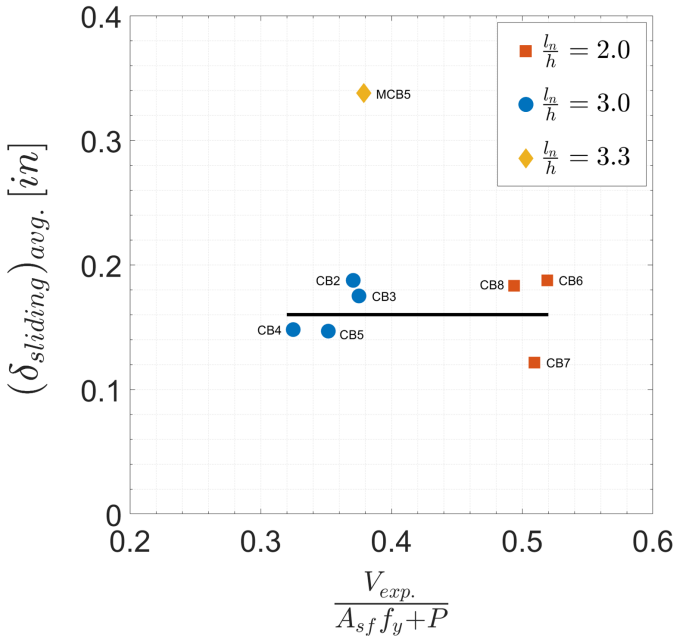

Figure 5.26: Average Sliding Displacement versus Normalized Frictional Strength (μ_{Eff}) at a 20% Strength Decay.

For modeling purposes, four sliding planes are considered, two beam-wall interfaces and a sliding plane at each dowel cut-off section. As shown in Figure 5.26, for a range of effective friction coefficients (approximately $0.3 \leqslant \mu_{Eff} \leqslant 0.5$), the average sliding displacement at a strength decay of approximately 20% can be taken as 0.16in. per sliding plane, for a total sliding displacement $\Delta_{sliding} = 0.64$in. Prior to achievement of peak strength sliding displacements are small. However, sliding becomes predominant for cycles beyond peak strength. Therefore, sliding was considered for drift calculations at peak strength and at a 20% strength decay. At peak strength, the shear-sliding drift was calculated based on θ_{S+F}. However, the drift capacity of the beams was calculated based on the assumed maximum sliding displacement of 0.64in and the proposed empirical shear-sliding model.

5.4.5 Rotational Spring And Drift Calculations

The proposed lumped plasticity model for SFRC coupling beams without diagonal bars consists of zero-length rotational springs at the beam ends and a linear elastic element with effective flexural and shear stiffness, as shown in Figure 5.27. The rotational springs follow the moment-rotation response shown in Figure 5.28 and accounts for all the inelastic deformations (i.e., plastic flexure, reinforcement slip, and shear sliding), while elastic flexure and shear are modeled with the linear-elastic beam element discussed in Section 5.4.3.1.

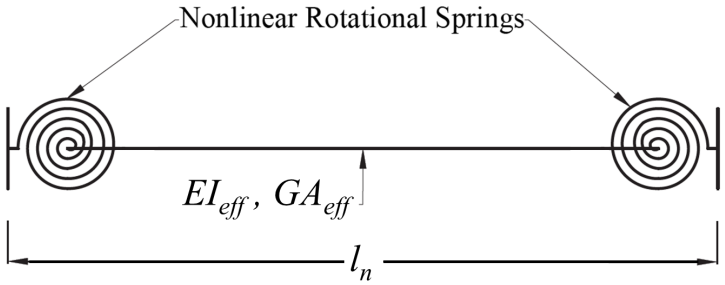

Figure 5.27: Lumped Plasticity Model for SFRC Coupling Beams.

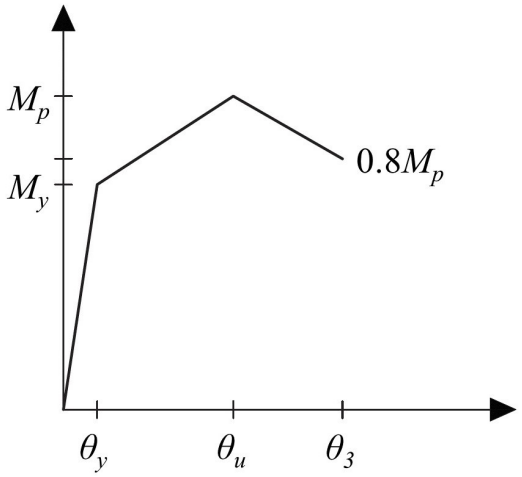

Figure 5.28: Inelastic Rotational Spring Response.

Three key points define the rotational spring response, namely, yield strength (M_y), plastic or ultimate strength (M_p), and 20% strength decay with their corresponding rotations, θ_y, θ_u, and θ_3, respectively. Strengths are calculated per the sectional analysis discussed in Section 5.4.1 and the rotations as:

$$\theta_y = (\theta_{slip})_y = \frac{(\delta_{slip})_y}{d-c} = \frac{\epsilon_y f_y}{8\tau_e}\frac{d_b}{d-c} \tag{5.16a}$$

$$\theta_u = (\theta_{slip})_p + \frac{\delta_{FP}}{l_n} + \frac{(\Delta_{slidig})_p}{l_n} \tag{5.16b}$$

$$\theta_3 = \frac{(\Delta_{slidig})_3}{l_n} + (\theta_{S+F})_{max} - \frac{0.8\,\delta_{FE}}{l_n} \tag{5.16c}$$

where $(\theta_{slip})_p$ is the rotation due to bond-slip at peak strength, calculated based on the reinforcement strain corresponding to a tensile stress of $f_u = 1.1(f_y)_{measured}$; δ_{FP}/l_n is the rotation due to plastic flexural deformations (Equation 5.14a); δ_{FE}/l_n is the rotation due to elastic flexural deformations at peak strength, i.e., $V_p l_n^3/(12EI_{eff})$; $(\Delta_{slidig})_p/l_n$ is the total chord rotation due to sliding displacement at peak strength (Equation 5.15); $(\Delta_{slidig})_3 = 4(\delta_{sliding})_{avg.} = 0.64$in.; and the parameters a and $(\theta_{S+F})_{max}$ are the shear sliding model parameters given by (Figure 5.25),

$$a = \frac{1}{2} - \frac{l_n}{8h} \qquad \text{for} \qquad 2.0 \leqslant \frac{l_n}{h} \leqslant 3.3 \tag{5.17a}$$

$$(\theta_{S+F})_{max} = \frac{l_n}{2h} + 3 \qquad \text{for} \qquad 2.0 \leqslant \frac{l_n}{h} \leqslant 3.3 \tag{5.17b}$$

The inelastic rotational spring envelope, combined with the linear elastic element, allows the calculation of the shear versus drift envelope response of SFRC coupling beams without diagonal bars and can be easily implemented in commercial software. The total chord rotation or drift angles at yield, peak, and 20% strength decay are

calculated as,

$$\Theta_y = \frac{(V_y)_{eff}\, l_n^2}{12EI_{eff}}\left(1 + 2\frac{6EI_{eff}}{GA_{eff}L^2}\right) + \theta_y \tag{5.18a}$$

$$\Theta_u = \frac{V_p l_n^2}{12EI_{eff}}\left(1 + 2\frac{6EI_{eff}}{GA_{eff}L^2}\right) + \theta_u \tag{5.18b}$$

$$\Theta_3 = \theta_3 + \frac{0.8\,\delta_{FE}}{l_n} + \frac{0.8V_p}{GA_{eff}} * (l_n - 2X_{dowel}) \tag{5.18c}$$

For the calculation of Θ_3, elastic shear displacements are considered only for the beam segment between the two dowel cut-off sections because the sliding displacements calculated from the proposed empirical model already take into account shear deformations between the beam-wall interface and dowel cut-off section. Therefore, elastic shear deformations are calculated over a distance equal to $l_n - 2X_{dowel}$, where X_{dowel} is the distance from the support to the dowel cut-off section as defined in Section 5.3.1. Lastly, the load-displacement behavior of SFRC coupling beams is assumed the same for both loading directions, as shown in Figure 5.29.

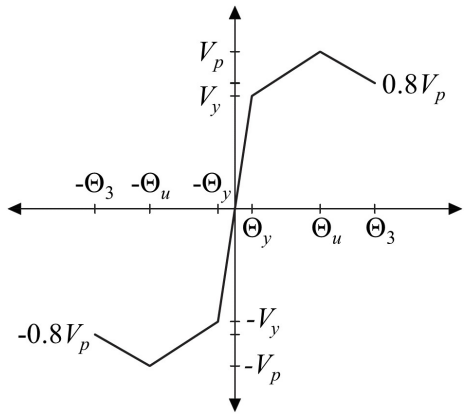

Figure 5.29: Shear Force Versus Drift Backbone Model.

5.4.6 Modeled vs. Experimental Backbone Curves

To validate the model discussed in the preceding sections, the shear versus drift response of 10 SFRC coupling beams without diagonal bars were calculated and compared to the measured responses; seven of the coupling beams were discussed in detail in Chapter 4, two were tested by Setkit (2012) with span-to-depth ratios of 3.3 and 2.75, and one other by Post and Al-Tameemi (2017) with span-to-depth ratio of 2.25. The calculated backbones for specimens with span-to-depth ratios of 3.0 and 2.0 are shown in Figure 5.30 and Figures 5.31a through c, respectively. The response of the specimen tested by Post and Al-Tameemi (2017) is shown in Figure 5.31d ($l_n/h = 2.25$), whereas responses of the two specimens tested by Setkit (2012) are shown in Figure 5.32. A summary of the calculated shear forces and drifts corresponding to peak strength and 20% strength decay is provided in Table 5.7.

Table 5.7: Calculated Response Summary.

At Peak Strength								Drift Capacity		
Specimen	$\frac{P}{f'_c A_g}$	Shear Strength		$V_{Calc.}/V_{Exp.}$	Average Drift		$\frac{(\Theta_u)_{Calc.}}{(\Theta_u)_{Exp.}}$	Average Drift		$\frac{(\Theta_3)_{Calc.}}{(\Theta_3)_{Exp.}}$
		$V_{Exp.}$	$V_{Calc.}$		$(\Theta_u)_{Exp.}$	$(\Theta_u)_{Calc.}$		$(\Theta_3)_{Exp.}$	$(\Theta_3)_{Calc.}$	
CB2	14.3%	100	98.3	0.98	3.7%	4.1%	1.10	5.5%	5.9%	1.09
CB3	10.7%	94.6	93.4	0.99	4.0%	4.1%	1.01	5.6%	5.9%	1.05
CB4	7.8%	75.0	80.7	1.08	3.6%	3.8%	1.05	5.8%	5.9%	1.01
CB5	8.3%	82.9	83.2	1.00	*3.9%	3.9%	1.00	6.3%	5.9%	0.94
CB6	7.7%	78.2	77.3	0.99	**3.4%	2.3%	0.68	5.7%	6.0%	1.06
CB7	12.2%	106	102	0.96	4.2%	4.0%	0.97	5.3%	6.0%	1.14
CB8	9.5%	81.9	84.4	1.03	*3.3%	2.5%	0.74	6.2%	6.0%	0.96
Setkit CB5	8.4%	116	118	1.02	4.2%	4.4%	1.04	6.8%	5.8%	0.86
Setkit CB6	5.0%	126	131	1.04	4.1%	4.7%	1.16	6.5%	5.5%	0.85
Al-Tameemi CB1	8.2%	112	116	1.04	3.1%	4.5%	1.43	5.8%	6.1%	1.05
			Average =	1.01		Average =	1.11		Average =	1.00
			COV =	3.4%		COV =	14.1%		COV =	9.7%

* Average of the drift before and after axial load adjustment; thus, not included in COV calculation.

** Lower axial restraint led to slower development of axial load; thus, not included in COV calculation.

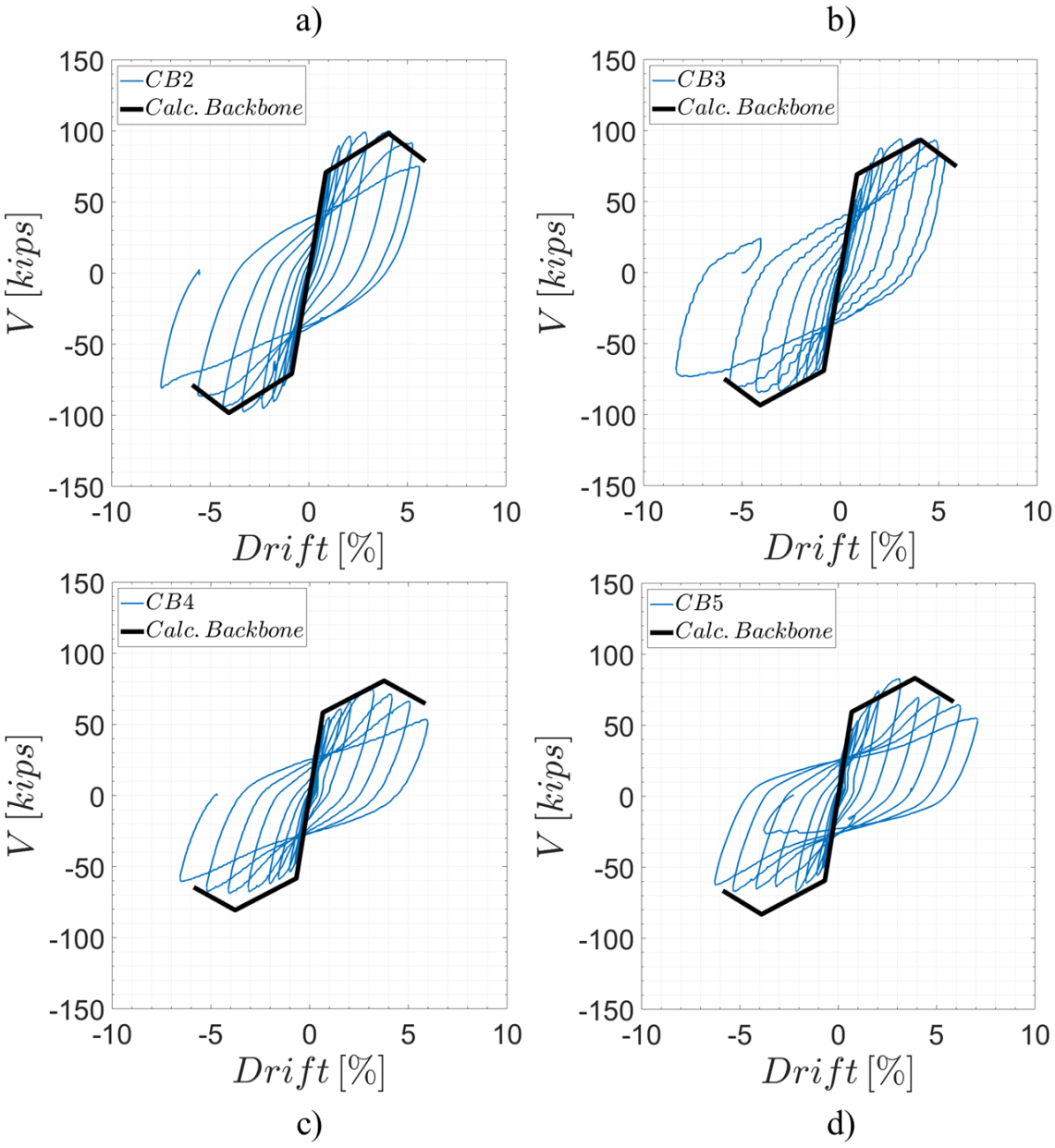

Figure 5.30: Calculated SFRC Coupling Beam Backbone Responses ($l_n/h = 3.0$).

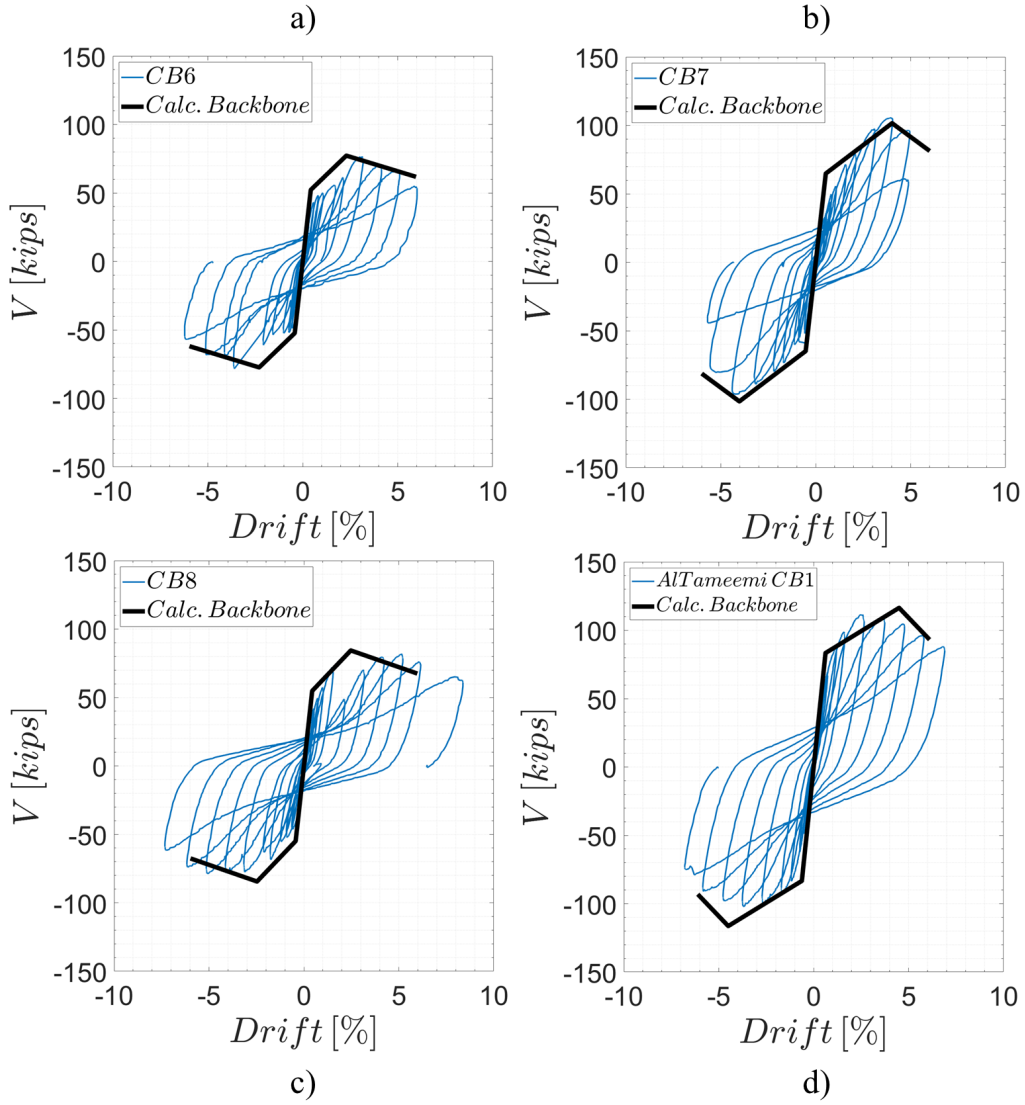

Figure 5.31: Calculated SFRC Coupling Beam Backbone Responses ($l_n/h = 2.0$ and 2.25).

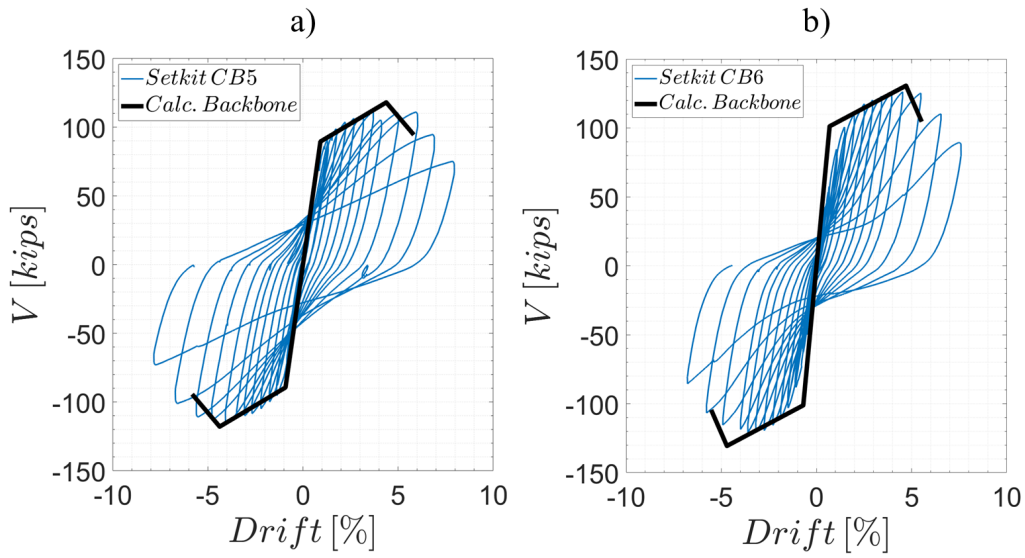

Figure 5.32: Calculated Backbone Responses for SFRC Coupling Beams tested by Setkit (2012). a) $l_n/h = 3.3$; and b) $l_n/h = 2.75$.

The variation in axial restraint, i.e., the adjustments and tightness of the steel arms providing the axial restraint in the test specimens, is believed to be the reason for the significant discrepancy between the calculated and measured drift at peak strength for Specimens CB6 and CB8. Furthermore, the discrepancy between the calculated and measured drift capacity of the specimens tested by Setkit (2012) is attributed to a weaker wall section relative to the dowel cut-off section. The weaker wall section of these specimens resulted in increased rotations and sliding at the beam-wall connections and delayed damage within the SFRC beam, thus resulting in a higher drift capacity than predicted by the model.

Despite the uncertainty due to the axial restraint, the simple lumped plasticity model was able to replicate satisfactorily the response of SFRC coupling beams with span-to-depth ratios in the range of 2.0 to 3.3 and no diagonal bars, as shown in Figures 5.30 through 5.32. Calculated peak shear forces are in good agreement with measured strengths and calculated drift capacities are within 15% of the experimental values with a COV≈10%. In contrast, the drift at peak strength is less accurately predicted and has greater variability (COV≈15%) due to the effect of axial restraint on development of axial force.

A graphic comparison of the modeled and measured strengths and deformations are provided in Figures 5.33a and b, respectively. The markers in blue correspond to the approximate yield strength compared to the calculated first yield strength; black markers correspond to peak strength; and the red markers in Figure 5.33b correspond to the drift at approximately 20% strength loss. Moreover, the dotted red lines correspond to ±10% error bounds. As shown in Figure 5.33, for most cases the proposed model led to calculated strengths and drifts within 10% of the measured responses for the three key points considered.

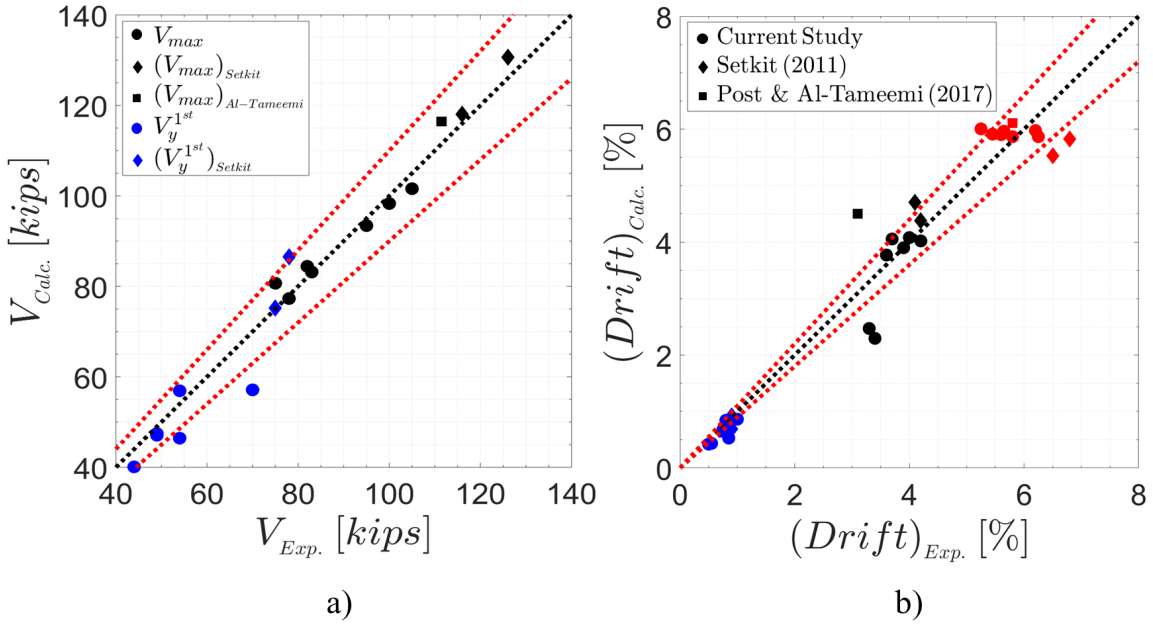

Figure 5.33: Comparison of Calculated and Measured Response. a) Shear Strength; and b) Lateral Drift.

In conclusion, despite the simplicity of the model and the axial restraint variability, the proposed lumped plasticity model resulted in good agreement with the measured coupling beam responses. Furthermore, the model provides a practical approach for nonlinear modeling of SFRC coupling beams without diagonal bars that follow the design recommendations discussed herein.

6 SUMMARY AND CONCLUSIONS

6.1 Study Summary

Medium- and high-rise buildings in regions of high seismicity often rely on coupled wall systems for lateral stiffness, strength, and energy dissipation. The performance of coupled walls, however, is greatly affected by the behavior of the coupling beams. Current design provisions and practice for reinforced concrete coupling beams typically result in diagonally-reinforced coupling beams with intricate reinforcement detailing that include large amounts of diagonal and transverse reinforcement. Consequently, diagonally-reinforced concrete coupling beams are challenging and time-consuming to construct. Results from previous studies on steel fiber-reinforced concrete (SFRC) coupling beams (e.g., Lequesne, 2011; Setkit, 2012) showed great potential for the simplification of reinforcement detailing through the use of SFRCs. In particular, elimination of diagonal reinforcement and reductions in transverse reinforcement was shown to be possible in coupling beams with aspect ratios of 2.75 and 3.33 by using a strain-hardening SFRC reinforced with a specific high-strength (330 ksi) hooked steel fiber at a 1.5% volume fraction.

For SFRC coupling beams to be widely implemented in practice and design provisions included in ACI 318, there is need for a better understanding of the behavior of SFRC coupling beams without diagonal bars constructed with various SFRCs (different types of fibers and dosages), as well as recommendations that link SFRC material behavior and coupling beam performance. The study reported herein was aimed at addressing these needs. The main objectives of this study were:

I- Evaluate the strength, deformation, and energy dissipation capacity of coupling beams without diagonal bars and constructed with various SFRCs.

II- Investigate the feasibility of using tensile strain-softening SFRCs for coupling beams without diagonals bars.

III- Characterize the tensile, flexural, and compressive response of various SFRCs to develop performance-based classification criteria for their use in coupling beams.

IV- Provide modeling and design recommendations for SFRC coupling beams without diagonal bars.

To accomplish the study objectives, eight large-scale, precast SFRC coupling beams were tested under large displacement reversals. The coupling beams were constructed using a simplified reinforcement detailing relative to the provisions in ACI 318-14 and each with one of six different SFRC mixtures. The experimental variables considered were coupling beam span-to-depth ratio, fiber type and dosage, and peak shear stress demand. Five of the specimens had a span-to-depth ratio of 3.0 and were designed to resist peak shear stresses ranging from 6 to $12\sqrt{f'_c}$ (psi). The remaining three specimens had a span-to-depth ratio of 2.0 and were designed for peak shear stress demands of approximately 8 to $10\sqrt{f'_c}$ (psi).

To establish a link between the mechanical properties of the SFRCs and the structural performance of the coupling beams, a series of material tests were conducted on companion SFRC specimens. In this study, three types of hooked steel fibers and three different fiber volume fractions (1.0%, 1.25% and 1.5%) were investigated, for a total of six SFRC mixtures. The flexural, tensile, and compressive behavior of the different SFRCs was investigated through bending tests of notched and un-notched beams, direct tension tests on notched prisms, and cylinder compression tests, respectively. Analysis of results from coupling beam tests led to recommendations for the flexural and shear design, as well as for modeling the shear versus drift envelope response of SFRC coupling beams without diagonal bars. To model the backbone shear versus drift response, an empirical model that accounts for inelastic flexural deformations, shear-sliding behavior at large drifts, and concentrated rotations at the beam-wall interface caused by reinforcement slip was developed.

6.1.1 Summary of Coupling Beam Tests

Eight SFRC coupling beams were tested under reversed displacement cycles of increasing magnitude with peak shear stress demands between 7 and $12\sqrt{f'_c}$ (psi). Except for Specimen CB1, which experienced a premature shear failure, the precast SFRC coupling beams exhibited stable hysteresis and drift capacity between approximately 5.5 and 6.2% drift. In this study, drift capacity was defined as the largest drift achieved prior to a cycle in which a strength decay greater than 20% occurred. Additionally, the SFRC coupling beams without diagonal bars exhibited energy dissipating capacity similar to that of well-detailed diagonally-reinforced coupling beams.

The behavior of the SFRC coupling beams was dominated by concentrated rotations at the beam-wall connections and, for the beams with span-to-depth ratio of 3.0, the formation of plastic hinges at the beam ends. Moreover, the behavior and deformation capacity exhibited by the SFRC coupling beams with span-to-depth ratio of 3.0 demonstrated that strain-softening SFRCs can be successfully used for coupling beam design, contingent upon limiting coupling beam shear stresses and using an SFRC meeting or exceeding the proposed material performance criteria (details provided as part of the conclusions in Section 6.2). For coupling beams with span-to-depth ratio of 2.0, however, flexural deformations within the coupling beam accounted for less than approximately 10% of the applied drift during cycles of amplitude greater than or equal to 1.0% drift. Ultimately, strength degradation and failure were due to the formation of shear-sliding planes at the dowel cut-off sections.

6.1.2 Summary of Analytical Work

The flexural response of the investigated SFRCs was related to coupling beam span-to-depth ratio, peak shear stress, and drift capacity to establish minimum SFRC performance criteria for coupling beam design. As a result, SFRC performance classes were proposed based on the flexural response exhibited by the SFRCs in ASTM C1609-12 four-point bending tests. Regression analyses were used to

develop an empirical model relating the tensile peak post-cracking strength of the investigated SFRCs to the fiber volume fraction, tensile strength, and aspect ratio. However, given the limited data set, the model is limited to SFRCs reinforced with hooked-steel fibers where failure is governed by fiber pull-out, and to the range of fiber reinforcing parameters considered in this study. The proposed model showed good agreement between calculated and experimental peak post-cracking strength and thus, it can be used for preliminary selection of fiber type and dosage to achieve a target SFRC flexural performance.

The shear versus drift response of SFRC coupling beams without diagonal bars was modeled as a tri-linear response comprised of a cracked-elastic region, a hardening region, and a decaying branch up to a strength loss of 20%. For this purpose, a simple lumped plasticity model that accounts for inelastic deformations due to flexure, shear-sliding, and reinforcement slip was proposed. Good agreement was obtained between calculated and measured shear versus drift envelope responses.

6.2 Conclusions and Recommendations

The following conclusions and recommendations are based on the results obtained from the coupling beam tests, as well as the SFRC material tests. Thus, these are limited to SFRCs exhibiting tensile and flexural properties meeting or exceeding those exhibited by the SFRCs investigated in this study.

1. SFRC coupling beams with span-to-depth ratios greater than or equal to 2.0 subjected to displacement reversals can achieve drift capacities of at least 5.0% and exhibit stable hysteresis when subjected to peak shear stress demands between 6 and $10\sqrt{f'_c}$ (psi).

2. The main contribution to drift for all the SFRC coupling beams was rotations at the beam-wall connections due to reinforcement slip, which accounted for approximately 50 to 60% of the applied drift for cycles of 1.0% drift and larger. The second most significant deformation mechanism was either inelastic

rotations or shear-sliding near the beam ends for coupling beams with span-to-depth ratio of 3.0 and 2.0, respectively.

3. Strength decay and eventual failure of SFRC coupling beams was typically due to sliding across a through-depth crack at the dowel cut-off sections. In most cases, shear sliding became significant during cycles of approximately 4.0% drift and larger.

4. The use of RC 80/30BP fibers at a 1.5% volume fraction resulted in a hardening behavior under direct tension and significant deflection hardening under four-point bending (in both notched and un-notched beams). This SFRC exhibited the best post-cracking performance among the SFRCs investigated, achieving peak equivalent post-caking flexural strength (f_{pc}) at least 20% greater than its first caking strength (f_{cr}) and a residual strength at a mid-span deflection of L/150 (f_{150}), where L is the beam span length, greater than 40% of its peak post-cracking strength.

5. The experimental results presented herein indicate that the use of an SFRC that meets or exceeds the performance of RC 80/30BP at a 1.5% volume fraction (i.e., a Class I SFRC) should result in drift capacities of approximately 6.0% for coupling beams with span-to-depth ratios between 2.0 and 3.0 when peak shear stress is limited to 8 and $10\sqrt{f'_c}$ (psi), respectively.

6. Experimental results from coupling beams with span-to-depth ratio of 3.0 constructed with SFRCs exhibiting softening behavior under direct tension, such as Class II ($f_{pc} \geqslant f_{cr}$ and $f_{150} \geqslant 0.4 f_{pc}$ based on ASTM C1609-12 tests) or Class III SFRCs ($f_{pc} \geqslant 0.8 f_{cr}$ and $f_{150} \geqslant 0.4 f_{pc}$), showed that drift capacities of 6.0% may be achieved if coupling beam peak shear stress is limited to 8 and $6\sqrt{f'_c}$ (psi) for Class II and Class III SFRCs, respectively.

7. Strain-softening SFRCs, such as Class II and Class III SFRCs, should not be used for the design of coupling beams with span-to-depth ratios less than 3.0 until further experimental data supporting their use are available. These lower

performing SFRCs may not provide sufficient shear strength and deformation capacity to allow shorter coupling beams to exhibit adequate strength and drift capacity.

8. Experimental results showed that SFRC shear stress demands exceeding $5\sqrt{f'_c}$ (psi) can lead to reduced deformation capacity (Specimen CB7) and may lead to premature shear failure (Specimen CB1). Therefore, it is recommended that the coupling beam transverse reinforcement be designed such that the SFRC shear strength contribution does not exceed 4, 3, and $2\sqrt{f'_c}$ (psi) for Class I, Class II, and Class III SFRCs, respectively. For design calculation purposes, the yield strength of the transverse reinforcement should be limited to 60 ksi.

9. Transverse confinement reinforcement detailed per the provisions for columns of Special Moment Frames in ACI 318-14 proved adequate for confining the plastic hinge regions of SFRC coupling beams and should be provided over a length equal to half the beam depth from the supports.

10. The use of U-shaped dowel reinforcement at the beam-to-wall connection proved effective in strengthening the cold joint and contributed to the spread of plasticity into the precast SFRC beams. This was achieved by terminating the dowel reinforcement at a distance away from the beam-wall connection such that the ratio of the shear associated with the development of the plastic flexural strength at the wall to the shear associated with the development of the plastic flexural capacity at the dowel cut-off section ranged between 0.9 and 1.0.

The following conclusions and modeling recommendations are made based on the study of the deformation mechanisms of SFRC coupling beams and the analytical studies conducted.

1. Plastic sectional analysis using Whitney's stress block for the concrete in compression, an elastic-perfectly plastic steel model with ultimate strength

equal to 1.0 and 1.1 times the measured reinforcement yield strength for bars in compression and tension, respectively, resulted in calculated plastic flexural strengths in excellent agreement with experimental results. On average, the ratio of calculated-to-experimental peak strength was 1.00 with a COV of approximately 4%. For design purposes, it is recommended that an axial force of $0.1f'_c A_g$ be considered for calculating the shear demand corresponding to the development of the beam plastic flexural strength.

2. Including the tensile behavior of SFRCs in sectional analyses resulted in calculated coupling beam strengths approximately 15% greater than experimental strengths. On the other hand, coupling beam flexural strengths calculated neglecting the tensile strength of the SFRC were in good agreement with measured strengths. Therefore, despite its simplicity, including a tensile stress block in a sectional analysis to account for the tensile contribution of SFRCs is not recommended.

3. The backbone shear versus drift response of SFRC coupling beams without diagonal bars was successfully modeled as a tri-linear response with cracked elastic, hardening, and strength decaying regions. For this purpose, a simple lumped plasticity model was used, consisting of a linear-elastic beam element with zero-length rotational springs at its ends that account for inelastic deformations due to bending, bar slip, and shear sliding.

4. Analysis of the calculated strains within the plastic hinges of SFRC coupling beams indicate that first signs of concrete cover crushing typically occurred at a strain of approximately 0.006. Furthermore, the average compressive strain corresponding to the second-to-last cycle prior to a strength decay greater than 20% was approximately 0.02 and 0.012 for Class I, and Class II and Class III SFRCs, respectively.

5. Measured flexural deformations within the coupling beam accounted for approximately 20–30% of the applied drift for SFRC coupling beams with span-to-depth ratio of 3.0 for cycles of 1.0% drift and larger. For beams with

span-to-depth ratio of 2.0, on the other hand, flexure accounted for 10% or less of the applied drift. Furthermore, experimental results suggest that, at peak strength, a plastic hinge length of $0.4h$ is appropriate for coupling beams with span-to-depth ratio of 3.0. Coupling beams with span-to-depth ratio of 2.0, however, had limited inelastic flexural deformations within the beam itself and thus, these deformations can be neglected for modeling purposes. To model the backbone response of SFRC coupling beams while accounting for the reduction of flexural demands in coupling beams with span-to-depth ratios between 3.0 and 2.0, it is recommended that the plastic hinge length (l_p) be linearly interpolated.

6. Coupling beam test data were used to calculate uniform bond strength over elastic and inelastic bar segments to model the bar slip response at the beam-wall interfaces. The data supported the use of a bond strength (τ_e) of $12\sqrt{f'_c}$ (psi) over the elastic bar portion and a bond strength (τ_i) of 4.0 and $1.2\sqrt{f'_c}$ (psi) over the inelastic bar portion for beams with span-to-depth ratio of 3.0 and 2.0, respectively. The larger flexural stiffness of coupling beams with an aspect ratio of 2.0 resulted in increased deformation demands at the beam-wall connections and thus, faster reinforcement bond deterioration. For beams with span-to-depth ratios between 3.0 and 2.0, linear interpolation is recommended for calculating τ_i.

7. The relationship between drift due to shear sliding and drift due to beam and concentrated interface rotations (θ_{S+F}) can be assumed linear up to peak strength. However, beyond peak strength, damage began to localize at the dowel cut-off section, allowing sliding deformations to rapidly increase with minimal changes in beam and interface rotations. It was found that the expression, $\frac{l_n}{2h} + 3$ [%] led to reasonable estimates of the maximum drift due to beam and concentrated interface rotations, where l_n and h are the coupling beam span-to-depth ratio and depth, respectively.

8. For a range of calculated shear friction coefficients between approximately 0.3

and 0.5, the average sliding displacement corresponding to a 20% coupling beam strength loss showed little variation and was, on average, 0.16 in. per sliding plane. For SFRC coupling beams such as those reported herein, sliding is expected to occur at the beam-wall connections and at dowel cut-off sections. Therefore, four sliding planes can be considered for calculating the drift associated with sliding deformations in SFRC coupling beams without diagonal bars.

9. The proposed lumped plasticity model led in most cases to calculated strengths and corresponding drifts at first yield, peak strength, and 20% strength loss within 10% of the measured responses for the coupling beams reported herein, as well as SFRC coupling beams without diagonal bars tested in previous studies.

6.3 Recommendations for Future Work

This study provided new information that allows a better understanding of the behavior of SFRC coupling beams with aspect ratios of 3.0 and 2.0 and no diagonal bars, as well as guidance on minimum SFRC performance requirements for their use in coupling beam design. However, it is proposed that the following studies be conducted in the future:

1. Further material tests on SFRCs reinforced with fibers, including a broader range of tensile strengths, aspect ratios, and anchorage configurations, would allow improvements to the proposed model relating the peak post-cracking strength of SFRCs to the fiber reinforcing parameters, including considerations for the type of fiber mechanical anchorage. Additional work towards the development of a standard test for the tensile response of SFRCs is also needed.

2. The behavior of the beam-wall interface is of major importance in the response of SFRC coupling beams with span-to-depth ratios of 3.3 or less. Further

experimental and analytical studies should be conducted to better understand and simulate the influence of reinforcement slip on coupling beam behavior.

3. Failure of SFRC coupling beams without diagonal bars is governed by shear sliding after several cycles of inelastic displacement reversals. Delaying the onset of shear sliding failure can lead to increased drift capacity. Thus, further coupling beam tests aimed at investigating reinforcement detailing alternatives to delay the onset of shear sliding are recommended.

REFERENCES

ACI Committee 318. (1999). "*Building Code Requirements for Structural Concrete (ACI 318-99)*". American Concrete Institute. Farmington Hills, MI.

ACI Committee 318. (2008). "*Building Code Requirements for Structural Concrete (ACI 318-08)*". American Concrete Institute. Farmington Hills, MI.

ACI Committee 318. (2014). "*Building Code Requirements for Structural Concrete (ACI 318-14) and Commentary (ACI 318R-14)*". American Concrete Institute. Farmington Hills, MI.

ACI Committee 318. (2019). "*Building Code Requirements for Structural Concrete (ACI 318-19) and Commentary (ACI 318R-19)*". American Concrete Institute. Farmington Hills, MI.

ACI Committee 544. (2018). "*544.4R-18: Guide for Design with Fiber-Reinforced Concrete*". American Concrete Institute. Farmington Hills, MI.

Adebar, Perry; Mindess, Sidney; St.-Pierre, Daniel, and Olund, Brent. (1997). "*Shear Tests of Fiber Concrete Beams without Stirrups*". ACI Structural Journal 94(1): 68–76.

Ahmad, S. H., and Shah, S. P. (1982). "*Stress-Strain Curves of Concrete Confined by Spiral Reinforcement*". ACI Journal Proceedings 79(6):484–490.

Alsiwat, Jaber M, and Saatcioglu, Murat. (1992). "*Reinforcement anchorage slip under monotonic loading*". ASCE Journal of Structural Engineering 118(9):2421–2438.

American Society of Civil Engineers. (2014). "*ASCE/SEI 41-13: Seismic Evaluation and Retrofit of Existing Buildings*". American Society of Civil Engineers. Reston, VA.

ASTM A370. (2014). "*Standard Test Methods and Definitions for Mechanical Testing of Steel Products*". American Society for Testing and Materials 1–50.

ASTM A615. (2016). "*Standard Specification for Deformed and Plain Carbon-Steel Bars for Concrete Reinforcement*". American Society for Testing and Materials 1–7.

ASTM C1609. (2012). "*Standard Test Method for Flexural Performance of Fiber-Reinforced Concrete (Using Beam With Third-Point Loading)*". American Society for Testing and Materials 1–8.

ASTM C39. (2016). "*Standard Test Method for Compressive Strength of Cylindrical Concrete Specimens*". American Society for Testing and Materials 1–7.

Balaguru, Perumalsamy N, and Shah, S. P. (1992). "*Fiber-Reinforced Cement Composites*". McGraw Hill, Inc. New York.

Barney, G. B.; Shiu, K .N.; Rabbat, B. G.; Fiorato, A. E.; Russell, H. G., and Corley, W. G. (1980). "*Behavior of Coupling Beams Under Load Reversals*". Portland Cement Association. Skokie, Illinois. Report RD068.01B.

Bass, Robert A.; Carrasquillo, Ramon L., and Jirsa, James O. (1989). "*Shear transfer across new and existing concrete interfaces*". ACI Structural Journal 86(4):383–393.

Batson, G.; Jenkins, E., and Spatney, R. (1972). "*Steel Fibers as Shear Reinforcement in Beams*". ACI Journal 69(10):640–644.

Benzoni, Gianmario; Ohtaki, T; Priestley, MJN, and Seible, Frieder. (1996). "*Seismic Performance of Circular Reinforced Concrete Columns Under Varying Axial Load*". Proceedings of the 4th Caltrans Seismic Research Workshop. 10. January 1996.

Bertero, Vitelmo V., and Popov, E. P. (1975). "*Hysteretic Behavior of Reinforced Concrete Flexural Members with Special Web Reinforcement*". U.S. National Conference on Earthquake Engineering. 316–326.

Birkeland, Philip W., and Birkeland, Halvard W. (1966). "*Connections in Precast Concrete Construction*". ACI Journal Proceedings 63(3):345–368.

Brown, Russell H., and Jirsa, James O. (1971). "*Reinforced Concrete Beams Under Load Reversals*". ACI Journal Proceedings 68(5):380–390.

BS EN 14651:2005. (2005). "*Test method for metallic fibre concrete : measuring the flexural tensile strength (limit of proportionality (LOP), residual).*". British Standards Institution.

Canbolat, Afsin B.; Parra-Montesinos, Gustavo J., and Wight, James K. (2005). "*Experimental Study on Seismic Behavior of High-Performance Fiber-Reinforced Cement Composite Coupling Beams*". ACI Structural Journal 102(1):159–166.

Choi, Kyoung-Kyu; Park, Hong-Gun, and Wight, James K. (2007). "*Shear Strength of Steel Fiber-Reinforced Concrete Beams without Web Reinforcement*". ACI Structural Journal 104(1):12–22.

Cox, H. L. (1952). "*The elasticity and strength of paper and other fibrous materials*". British Journal of Applied Physics 3(3):72–79.

Dinh, Hai H.; Parra-Montesinos, Gustavo J., and Wight, James K. (2010). "*Shear Behavior of Steel Fiber-Reinforced Concrete Beams without Stirrup Reinforcement*". ACI Structural Journal 107(05):597–606.

Dinh, Hai H.; Parra-Montesinos, Gustavo J., and Wight, James K. (2011). "*Shear Strength Model for Steel Fiber Reinforced Concrete Beams without Stirrup Reinforcement*". Journal of Structural Engineering, ASCE 137(10):1039–1051.

Dodd, L L, and Restrepo-Posada, J I. (1995). "*Model for predicting cyclic behavior of reinforcing steel*". Journal of Structural Engineering, ASCE 121(3):433–445.

Eligehausen, Rolf; Popov, Egor P., and Bertero, Vitelmo V. (1982). "*Local bond stress-slip relationships of deformed bars under generalized excitations: experimental results and analytical model*". Earthquake Engineering Research Center, University of California - Berkeley. Berkeley, CA.

Elwood, Kenneth J., and Eberhard, Marc O. (2009). "*Effective Stiffness of Reinforced Concrete Columns*". ACI Structural Journal 106(4):476–484.

Ezeldin, A. Samer, and Balaguru, Perumalsamy N. (1992). "*Normal- and High-Strength Fiber-Reinforced Concrete under Compression*". Journal of Materials in Civil Engineering, ASCE 4(4):415–429.

Fanella, David A., and Naaman, Antoine E. (1985). "*Stress-Strain Properties of Fiber Reinforced Mortar in Compression*". ACI Journal Proceedings 82(4):475–483.

Foltz, Raymond R; Guerra, Jesse M, and Lafave, James M. (2008). "*Behavior of High-Performance Fiber-Reinforced Cementitious Composites for RC Coupling Beams in Earthquake-Resistant Structural Wall Systems*". 14th World Conference on Earthquake Engineering.

Galano, Luciano, and Vignoli, Andrea. (2000). "*Seismic behavior of short coupling beams with different reinforcement layouts*". ACI Structural Journal 97(6):876–885.

Gopalaratnam, Vellore S., and Shah, S P. (1987a). "*Failure Mechanisms and Fracture of Fiber Reinforced Concrete*". ACI Special Publication, SP-105-1 1–26.

Gopalaratnam, Vellore S., and Shah, Surendra P. (1987b). "*Tensile Failure of Steel Fiber-Reinforced Mortar*". Journal of Engineering Mechanics 113(5):635–652.

Hannant, D J. (1978). "*Fibre Cements and Fibre Concretes*". Wiley - Interscience. New York.

Harries, Kent; Mitchell, Dennis; Redwood, Richard, and Cook, William. (1997). "*Seismic design of coupled walls - a case for mixed construction*". Canadian Journal of Civil Engineering 24(3):448–459.

Harries, Kent A.; Fortney, Patrick J.; Shahrooz, Bahram M., and Brinen, Paul J. (2005). "*Practical design of diagonally reinforced concrete coupling beams - Critical review of ACI 318 requirements*". ACI Structural Journal 102(6):876–882.

Harries, Kent A.; Gong, Bingnian, and Shahrooz, Bahram M. (2000). "*Behavior and Design of Reinforced Concrete, Steel, and Steel-Concrete Coupling Beams*". EERI, Earthquake Spectra 16(4):775–799.

Harries, Kent A, and Shahrooz, Bahram M. (2005). "*Hybrid Coupled Wall Systems*". Concrete International 27(5):45–52.

Hjelmstad, Keith D, and Popov, Egor P. (1983). "*Cyclic Behavior and Design of Link Beams*". Journal of Structural Engineering, ASCE 109(10):2387–2403.

Hognestad, Eivind. (1952). "*Inelastic Behavior in Tests of Eccentrically Loaded Short Reinforced Concrete Columns*". ACI Journal 24(2):117–139.

Johnston, Colin D. (1974). "*Steel Fiber Reinforced Mortar and Concrete: A Review of Mechanical Properties*". ACI Special Publication SP-44-7:127–142.

Johnston, Colin D., and Coleman, Ronald A. (1974). "*Strength and Deformation of Steel Fiber Reinforced Mortar in Uniaxial Tension*". ACI Special Publication SP-44-10: 177–194.

Kent, Dudley Charles, and Park, Robert. (1971). "*Flexural Members with Confined Concrete*". Journal of the Structural Division, ASCE 97(ST 7):1969–1990.

Khuntia, Madhusudan; Stojadinovic, Bozidar, and Goel, Subhash C. (1999). "*Shear Strength of Normal and High-Strength Fiber Reinforced Concrete Beams without Stirrups*". ACI Structural Journal 96(2):282–289.

Kopczynski, Cary, and Whiteley, Mark. (2016). "*Lincoln Square Expansion. Steel Fiber Reinforced Concrete Solves Seismic Design Challenge*". Structure Magazine (March 2016):42–44.

Krstulovic-Opara, Neven, and Malak, Sary. (1997). "*Tensile Behavior of Slurry Infiltrated Mat Concrete (SIMCON)*". ACI Materials Journal 94(1):39–46.

Lankard, David R. (1984). "*Slurry Infiltrated Fiber Concrete (SIFCON): Properties and Applications*". Potential for Very High Strength Cement Based Materials, Proceedings, Material Research Society. vol. 42. 277–286.

Lehman, Dawn E, and Moehle, Jack P. (2000). "*Seismic Performance of Well-Confined Concrete Bridge Columns*". Pacific Earthquake Engineering Research Center, PEER 1998/01.

Lequesne, Remy; Setkit, Monthian; Kopczynski, Cary; Ferzli, Joe; Cheng, Min-Yuan; Parra-Montesinos, Gustavo, and Wight, James K. (2011). "*Implementation of High-Performance Fiber Reinforced Concrete Coupling Beams in High-Rise Core-Wall Structures*". Advances in FRC Durability and Field Applications, ACI Special Publication, SP-280-7. vol.280. 94–105.

Lequesne, Rémy; Parra-Montesinos, Gustavo J., and Wight, James K. (2009). "*Test of a Coupled Wall with High Performance Fiber Reinforced Concrete Coupling Beams*". Thomas T. C. Hsu Symposium: Shear and Torsion of Concrete Structures, ACI Special Publication. SP-265 16.

Lequesne, Rémy D. (2011). "*Behavior and design of high-performance fiber-reinforced concrete coupling beams and coupled-wall systems*". Ph.D. thesis. The University of Michigan, Ann Arbor, MI.

Lequesne, Rémy D.; Parra-Montesinos, Gustavo J., and Wight, James K. (2013). "*Seismic Behavior and Detailing of High-Performance Fiber-Reinforced Concrete Coupling Beams and Coupled Wall Systems*". Journal of Structural Engineering, ASCE 139(8):1362–1370.

Lequesne, Rémy D.; Parra-Montesinos, Gustavo J., and Wight, James K. (2016). "*Seismic Response of Fiber-Reinforced Concrete Coupled Walls*". ACI Structural Journal 113(3):5–10.

Lequesne, Rémy D.; Setkit, Monthian; Parra-Montesinos, Gustavo J., and Wight, James K. (2010). "*Seismic Detailing and Behavior of Coupling Beams with High-Peformance Fiber-Reinforced Concrete*". Antoine E. Naaman Symposium: Four Decades of Progress in Prestressed Concrete, Fiber Reinforced Concrete and thin Laminate Composites, ACI Special Publication, SP-272.. 14.

Li, Bing. (2012). "*Initial Stiffness of Reinforced Concrete Columns and Walls*". 15th World Conference on Earthquake Engineering. 10.

Li, Victor C. (1993). "*From Micromechanics to Structural Engineering - The Design of Cementitious Composites for Civil Engineering Applications*". Journal of Structural Mechanics and Earthquake Engineering, JSCE 10(2):37–48.

Liao, Wen-Cheng C.; Chao, Shih-Ho H.; Park, Sang-Yeol, and Naaman, Antoine E. (2006). "*Self-Consolidating High Performance Fiber Reinforced Concrete (SCHPFRC) - Preliminary Investigation*". University of Michigan. Ann Arbor, MI.

Luisoni, Cesar J.; Someson, Hector M., and Ungaro, Miguel A. (1970). "*Verificacion Experimental de un Calculo Plastico y otro Elastico de una Pared de Corte*". IV Simposio Panamericano de Estructuras. vol. 5. 230–286.

Mander, J. B.; Priestley, M. J. N., and Park, R. (1988). "*Theoretical Stress-Strain Model For Confined Concrete*". Journal of Structural Engineering, ASCE 114(8):1804–1826.

Mander, John Barrie. (1983). "*Seismic Design of Bridge Piers*". Ph.D. thesis. University of Canterbury, New Zealand.

Mansur, M. A.; Chin, M S, and Wee, T H. (1999). "*Stress-Strain Relationship of High-Strength Fiber Concrete in Compression*". Journal of Materials in Civil Engineering, ASCE 11(1):21–29.

Mast, Robert F. (1968). "*Auxiliary Reinforcement in Concrete Connections*". Journal of the Structural Division 94(6):1485–1504.

Menegotto, M., and Pinto, P. E. (1973). "*Method of Analysis for Cyclically Loaded R. C. Plane Frames Including Changes in Geometry and Non-Elastic Behavior of Elements under Combined Normal Force and Bending*". Proc. of IABSE Symposium on Resistance and Ultimate Deformability of Structures Acted on by Well Defined Repeated Loads. 15–22.

Mirsayah, Amir A., and Banthia, Nemkumar. (2002). "*Shear Strength of Steel Fiber-Reinforced Concrete*". ACI Materials Journal 99(5):473–479.

Motter, Christopher; Fields, Dave; Hooper, John; Klemencic, Ron, and Wallace, John. (2014). "*Large-Scale Testing of Steel Reinforced Concrete (SRC) Coupling Beams Embedded Into Reinforced Concrete Shear Walls*". 10th U.S. National Conference on Earthquake Engineering. 10.

Naaman, A.E. (2007a). "*Deflection-Softening and Deflection-Hardening FRC Composites: Characterization and Modeling*". ACI Special Publication 248:53–66.

Naaman, Antoine E. (1985). "*Fiber Reinforcement for Concrete*". American Concrete Institute, Concrete International 7(3):21–25.

Naaman, Antoine E. (1999). "*Fibers With Slip-Hardening Bond*". High Performance Fiber Reinforced Cement Composites 3 (HPFRCC 3), Proceedings of the Third International RILEM Workshop. 371–385.

Naaman, Antoine E. (2003). "*Strain hardening and deflection hardening fiber reinforced cement composites*". High Performance Fiber Reinforced Cement Composites 4 (HPFRCC 4), Proceedings of the Fourth International RILEM Workshop. 95–113.

Naaman, Antoine E. (2007b). "*High Performance Fiber Reinforced Cement Composites: Classification and Applications*". CBM-CI International Workshop. 389–401.

Naaman, Antoine E. (2017). "*Fiber Reinforced Cement and Concrete Composites*". Techno Press 3000. Sarasota, Florida, USA.

Naaman, Antoine E; Moavenzadeh, Fred, and McGarry, Frederick J. (1974). "*Naaman et al. (1974).pdf*". Journal of the Engineering Mechanics Division, ASCE 100(EM2):397–413.

Naaman, Antoine E., and Reinhardt, H. W. (1995). "*Characterization of High Performance Fiber Reinforced Cement Composites*". High Performance Fiber Reinforced Cement Composites 2 (HPFRCC 2), Proceedings of the Second International RILEM Workshop. 1–24.

Naaman, Antoine E., and Reinhardt, H. W. (2006). "*Proposed classification of HPFRC composites based on their tensile response*". Materials and Structures 39(5):547–555.

Naaman, Antoine E., and Shah, Surendra P. (1976). "*Pull-Out Mechanism in Steel Fiber-Reinforced Concrete*". Journal of the Structural Division, ASCE 102(8):1537–1548.

Naish, David; Fry, Andy; Klemencic, Ron, and Wallace, John. (2013a). "*Reinforced Concrete Coupling Beams — Part I : Testing*". ACI Structural Journal 110(6):1057–1066.

Naish, David; Fry, Andy; Klemencic, Ron, and Wallace, John. (2013b). "*Reinforced Concrete Coupling Beams — Part II : Modeling*". ACI Structural Journal 110(6): 1067–1075.

Naish, David; Fry, J Andrew; Klemencic, Ron, and Wallace, John. (2009). "*Experimental Evaluation and Analytical Modeling of ACI 318-05/08 Reinforced Concrete Coupling Beams Subjected to Reversed Cyclic Loading*". University of California Los Angeles. Los Angeles, California. UCLA-SGEL Report 2009/06.

Narayanan, R., and Darwish, I. Y. S. (1987). "*Use of Steel Fibers as Shear Reinforcement*". ACI Structural Journal 84(3):216–227.

Nataraja, M.C.; Dhang, N., and Gupta, A.P. (1999). "*Stress-strain curves for steel-fiber reinforced concrete under compression*". Cement and Concrete Composites, Elsevier 21(5-6):383–390.

NDI Measurement Sciences. (2014). "*Optotrak Certus User Guide*". Northern Digital Inc. Waterloo, Ontario, Canada.

Otani, Shunsuke, and Sozen, Mete. (1972). "*Behavior of multistory reinforced concrete frames during earthquakes*". University of Illinois, Urbana-Champaign.

Otter, Duane E., and Naaman, Antoine E. (1988). "*Properties of Steel Fiber Reinforced Concrete Under Cyclic Load*". ACI Materials Journal 85(4):254–261.

Park, R., and Paulay, T. (1974). "*Reinforced Concrete Structures*". John Wiley & Sons, Inc.. Hoboken, NJ, USA.

Park, Wan-Shin, and Yun, Hyun-Do. (2005). "*Seismic behaviour of steel coupling beams linking reinforced concrete shear walls*". Engineering Structures, Elsevier 27(7): 1024–1039.

Parra-Montesinos, G. J.; Wight, J. K.; Kopczynski, C.; Lequesne, R. D.; Setkit, M.; Conforti, A., and Ferzli, J. (2017a). "*Earthquake-resistant fibre-reinforced concrete coupling beams without diagonal bars*". FRC 2014 Joint ACI-fib International Workshop: Fibre-reinforced concrete: From design to structural applications, ACI Special Publication, SP 310-43. 461–470.

Parra-Montesinos, G.J.; Wight, J. K.; Kopczynski, C.; Lequesne, R. D.; Setkit, M.; Conforti, A., and Ferzli, J. (2017b). "*Elimination of Diagonal Reinforcement in Earthquake-Resistant Coupling Beams through Use of Fiber-Reinforced Concrete*". Proceedings of the First ACI & JCI Joint Seminar: Design of Concrete Structures Against Earthquake and Tsunami, ACI Special Publication, SP 313-4. 8.

Parra-Montesinos, G.J.; Wight, J.K.; Kopczynski, C.; Lequesne, R.; Setkit, M.; Conforti, A., and Ferzli, J. (2014). "*High-Performance Fiber Reinforced Concrete Coupling Beams: From Research to Practice*". Tenth U.S. National Conference on Earthquake Engineering.

Parra-Montesinos, Gustavo J. (2005). "*High-Performance Fiber-Reinforced Cement Composites: An Alternative for Seismic Design of Structures*". ACI Structural Journal 102(5):668–675.

Parra-Montesinos, Gustavo J. (2006). "*Shear Strength of Beams with Deformed Steel Fibers*". American Concrete Institute, Concrete International 28(11):57–66.

Parra-Montesinos, Gustavo J, and Chompreda, Praveen. (2006). "*Use of High-Performance Fiber Reinforced Cement Composites for Increasing Shear Strength and Displacement Capacity in Reinforced Concrete Flexural Members*". 8th US National Conference on Earthquake Engineering. 1–10.

Parra-Montesinos, Gustavo J.; Wight, James K, and Setkit, Monthian. (2010). "*Earthquake-Resistant Coupling Beams without Diagonal Reinforcement*". Concrete International 32(12):36–40.

Paulay, T., and Binney, J. R. (1974). "*Diagonally Reinforced Coupling Beams Of Shear Walls*". ACI Special Publication SP 42(26):579–598.

Paulay, Thomas. (1970). "*An Elasto-Plastic Analysis of Coupled Shear Walls*". ACI Journal Proceedings 67(11):915–922.

Paulay, Thomas. (1971). "*Coupling Beams of Reinforced Concrete Shear Walls*". Journal of the Structural Division, Proceedings ASCE 97(3):843–862.

Paulay, Thomas, and Santhakumar, Arumbakkam R. (1976). "*Ductile Behavior of Coupled Shear Walls*". Journal of the Structural Division, ASCE 102(1):93–108.

Pérez-Irizarry, Angel L, and Parra-Montesinos, Gustavo J. (2017). "*Seismic Behavior of Coupling Beams Constructed with Various Types of Steel Fiber Reinforced Concrete*". 16th World Conference on Earthquake Engineering. 1–12.

Post, Gregory, and Al-Tameemi, Mohamed. (2017). "*Comparison of Seismic Behavior of a Fiber Reinforced Concrete Coupling Beam with that of a Diagonally Reinforced Concrete Coupling Beam*". University of Wisconsin - Madison.

Richart, Frank Erwin; Brandtzæg, Anton, and Brown, Rex Lenoi. (1928). "*A study of the failure of concrete under combined compressive stresses*". University of Illinois, Engineering Experiment Station, Bulletin No. 185. Urbana-Champaign, IL.

Roy, H. E. H., and Sozen, Mete A. (1964). "*Ductility of Concrete*". Proceedings of the International Symposium on Flexural Mechanics of Reinforced Concrete, ASCE-ACI. 213–235.

Saatcioglu, Murat, and Ozcebe, Guney. (1989). "*Response of Reinforced Concrete Columns to Simulated Seismic Loading*". ACI Structural Journal 86(1):3–12.

Sakai, Junichi, and Mahin, Stephen A. (2004). "*Analytical Investigations of New Methods for Reducing Residual Displacements of Reinforced Concrete Bridge Columns*". Pacific Earthquake Engineering Research Center. Berkely, CA. PEER Report 2004/02.

Santhakumar, A. R. (1974). "*The Ductility of Coupled Shear Walls*". Ph.D. thesis. University of Canterbury. Christchurch, New Zealand.

Schneider, Caroline A; Rasband, Wayne S, and Eliceiri, Kevin W. (2012). "*NIH Image to ImageJ: 25 years of image analysis*". Nature Methods 9(7):671–675.

Setkit, Monthian. (2012). "*Seismic Behavior of Slender Coupling Beams constructed with High-Performance Fiber-Reinforced Concrete*". Ph.D. thesis. University of Michigan, Ann Arbor, MI.

Sezen, Halil, and Setzler, Eric J. (2008). "*Reinforcement slip in reinforced concrete columns*". ACI Structural Journal 105(3):280–289.

Shah, Surendra P. (1992). "*Do Fibers Increase the Tensile Strength of Cement-Based Matrix?*" ACI Materials Journal 88(6):595–602.

Shah, Surendra P., and Rangan, B. Vijay. (1970). "*Effects of Reinforcements on Ductility of Concrete*". Journal of the Structural Division 96(ST6):1167–1184.

Shah, Surendra P., and Rangan, B. Vijaya. (1971). "*Fiber Reinforced Concrete Properties*". ACI Journal 68(2):126–137.

Sheikh, Shamim A, and Uzumeri, S. M. (1982). "*Analytical Model for Concrete Confinement in Tied Columns*". Journal of the Structural Division, ASCE 108(ST 12):2703–2722.

Shiu, K .N.; Barney, G. B.; Fiorato, A. E., and Corley, W. G. (1978). "*Reversing Load Tests of Reinforced Concrete Coupling Beams*". Central American Conference on Earthquake Engineering. 239–249.

Sirijaroonchai, Kittinun; El-Tawil, Sherif, and Parra-Montesinos, Gustavo. (2010). "*Behavior of high performance fiber reinforced cement composites under multi-axial compressive loading*". Cement and Concrete Composites 32(1):62–72.

Son Vu, Ngoc; Li , Bing, and Beyer, Katrin. (2014). "*Effective stiffness of reinforced concrete coupling beams*". Engineering Structures 76:371–382.

Susetyo, Jimmy; Gauvreau, Paul, and Vecchio, Frank J. (2011). "*Effectiveness of Steel Fiber as Minimum Shear Reinforcement*". ACI Structural Journal 108(4):488–496.

Swamy, R. N., and Bahia, H. M. (1985). "*The Effectiveness of Steel Fibers as Shear Reinforcement*". American Concrete Institute, Concrete International 7(3):35–40.

Tameemi, Waleed Ali Hasan, and Lequesne, Rémy D. (2015). "*Correlations Between Compressive, Flexural, and Tensile Behavior of Self-Consolidating Fiber Reinforced Concrete, SM Report No. 114*". University of Kansas. Lawrence, KS.

Tassios, Theodosios P.; Moretti, Marina, and Bezas, Antonios. (1996). "*On the behavior and ductility of reinforced concrete coupling beams of shear walls*". ACI Structural Journal 93(6):711–720.

Tegos, I. A., and Penelis, G. Gr. (1988). "*Seismic Resistance of Short Columns and Coupling Beams Reinforced With Inclined Bars*". ACI Structural Journal 85(1):82–88.

Thomas, Job, and Ramaswamy, Ananth. (2007). "*Mechanical Properties of Steel Fiber-Reinforced Concrete*". Journal of Materials in Civil Engineering 19(5):385–392.

Vandewalle, L. (2003). "*Final recommendation of RILEM TC 162-TDF: Test and design methods for steel fibre reinforced concrete sigma-epsilon-design method*". Materials and Structures, RILEM 36(262):560–567.

Wafa, Faisal F., and Ashour, Samir A. (1992). "*Mechanical Properties of High-Strength Fiber Reinforced Concrete*". ACI Materials Journal 89(5):449–455.

Weiler, B.; Grosse, C., and Reinhardt, H. W. (1999). "*Debonding Behaviour of Steel Fibres with Hooked Ends*". High Performance Fiber Reinforced Cement Composites 3 (HPFRCC 3), Proceedings of the Third International RILEM Workshop. 423–433.

Whitney, Charles S. (1942). "*Plastic Theory of Reinforced Concrete Design*". Transactions of the American Society of Civil Engineers 107(1):251–282.

Wight, James K., and Sozen, Mete A. (1975). "*Strength Decay of RC Columns under Shear Reversals*". Journal of the Structural Division, Proceedings ASCE 101(ST5): 1053–1065.

Wood, Sharon L. (1990). "*Shear Strength of Low-Rise Reinforced Concrete Walls*". ACI Structural Journal 87(1):99–107.

Appendices

A.1 Drift Calculation with Support Rotations

The support conditions of the coupling beam specimens are not an idealized fixed support. Thus, drifts calculations must account for any rotation of the end supports. Figure A.1 shows the deformed shape of a coupling beam with the bottom and top blocks rotated by an angle α_B and α_T, respectively. The corrected coupling beam drift was calculated per Equation A.1,

$$\text{drift} = \frac{\Delta}{l_n} + \frac{\alpha_T + \alpha_B}{2} \tag{A.1}$$

where Δ is the relative lateral displacement of the end blocks, l_n is the span length of the coupling beam, and α_B and α_T are the rotation of the end blocks in radians. Positive Δ, α_T, and α_B are as shown in Figure A.1.

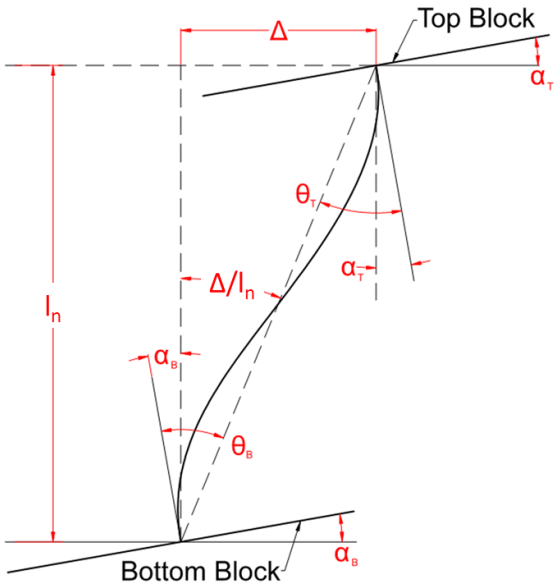

Figure A.1: Coupling Beam Chord Rotation with Support Rotation.

A.2 Four-Point Flexural Tests

For notched beam samples, the crack opening at the location of the notch end was estimated based on the location data collected for the markers. The crack opening of each notched beam specimen can be calculated using Equation A.2, where D_{Top} is the distance in inches from the bottom of the beam to the uppermost row of markers, Nd is the notch depth in inches, θ_L and θ_R are the angles of rotation (rad) of the column of markers to the left and right of the notch, respectively (taken as positive as shown in Figure A.2), ΔX_{Top} is the distance between the two top markers and $(\Delta X_{Top})_0$ is equal to ΔX_{Top} at the initial time, t_0. Figure A.2 illustrates the geometry and variables used to calculate the crack opening.

$$w_{cr} = (D_{Top} - Nd)(\theta_L + \theta_R) + \Delta X_{Top} - (\Delta X_{Top})_0 \tag{A.2}$$

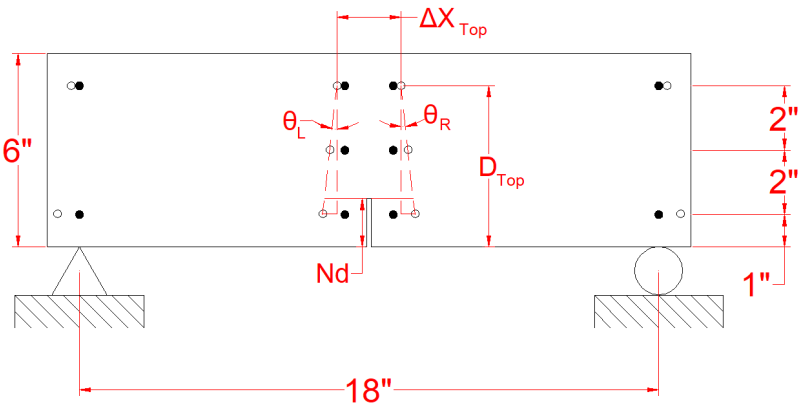

Figure A.2: Crack Opening Calculation Schematic (Notched Beams).

To calculate the crack opening of un-notched samples, the location of the first crack in the concrete was needed. The start of the crack was estimated using a combination of inspection of the tested sample, separation of the markers in the bottom row of markers, as well as the calculated rotations on each column of markers. Once the approximate location of the crack was determined, the rotations

of the columns of markers closest to the crack location were selected to calculate the crack opening. Figure A.3 shows the rotated marker columns due to flexural deformations and the variables used to calculate the crack opening for un-notched beams. To avoid having a heavily congested drawing only the marker columns 1, 2 and 6 are identified.

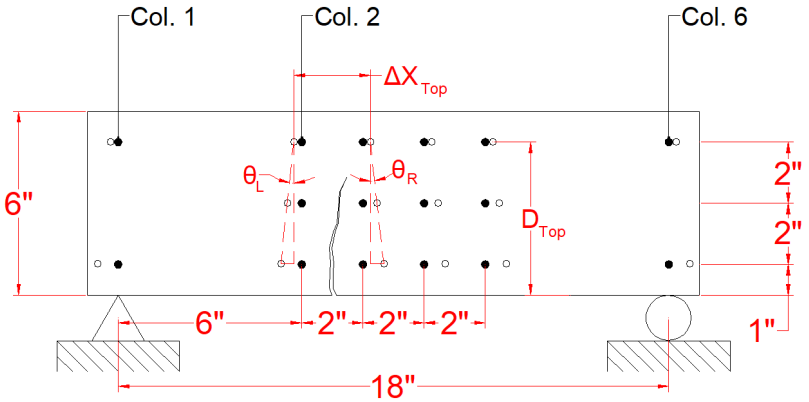

Figure A.3: Crack Opening Calculation Schematic (Un-notched Beams).

The calculation of the crack opening was very similar to that for the notched beams. However, due to the varying location of the crack, the rotations and distance between markers used to calculate the crack opening varied for each specimen. That is, ΔX_{Top}, θ_L and θ_R correspond to the distance between marker columns, rotation of the left marker column and rotation of the right marker column, respectively, using the columns of markers closest to the crack. In some samples, one or both of the columns of markers closest to the crack would result in anomalous crack opening calculations due to markers falling off. Whenever this occurred the next closest column or columns of markers were used for the calculation of the crack opening. The crack opening for the beam samples was calculated according to Equation A3.

$$w_{cr} = D_{Top}(\theta_L + \theta_R) + \Delta X_{Top} - (\Delta X_{Top})_0 \tag{A.3}$$

A.3 Direct Tensile Tests

To estimate the crack opening in the specimens while taking into account any rotation on each side of the notch during testing, the data from the markers were used to define two planes (above and below the notch). Three points in space are needed to define each of these planes. Thus, to define the plane above the notch (Figure A.4), the coordinates of marker 1 and marker 7 were used in conjunction with a third point, A, defined by the average of markers 3 and 5 (Figure A.4). The equation for a plane is defined as shown in Equation A.4.

$$ax + by + cz = d \tag{A.4}$$

To calculate coefficients a, b and c, two vectors on the plane must be known; for example, vectors $\overline{71}$ and $\overline{A1}$ as shown in Figure A.4. The vectors, coefficients and constant for the plane above the notch are calculated according to Equations A.5, A.6 and A.7 respectively. These calculations were performed for each time instant throughout the test allowing the definition of a plane for each time instant.

$$\overline{71} = \begin{bmatrix} X_7 - X_1 \\ Y_7 - Y_1 \\ Z_7 - Z_1 \end{bmatrix} ; \overline{A1} = \begin{bmatrix} X_A - X_1 \\ Y_A - Y_1 \\ Z_A - Z_1 \end{bmatrix} \tag{A.5}$$

$$\overline{71} \times \overline{A1} = \begin{bmatrix} a_{Top} \\ b_{Top} \\ c_{Top} \end{bmatrix} \tag{A.6}$$

$$d_{Top} = \begin{bmatrix} a_{Top} \\ b_{Top} \\ c_{Top} \end{bmatrix} \cdot \begin{bmatrix} X_1 \\ Y_1 \\ Z_1 \end{bmatrix} \tag{A.7}$$

The resulting plane equation is,

$$a_{Top}x + b_{Top}y + c_{Top}z = d_{Top} \tag{A.8}$$

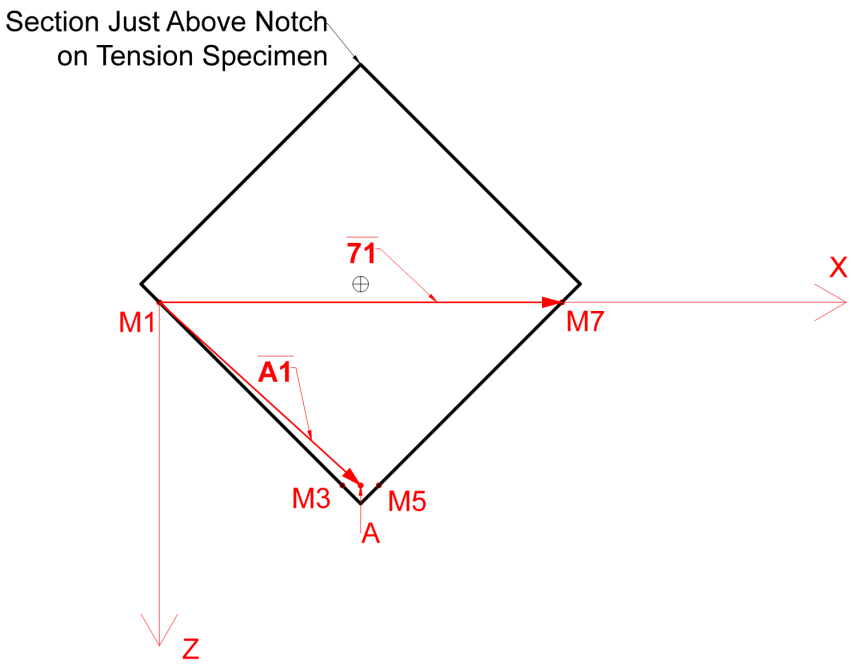

Figure A.4: Vectors To Calculate Crack Opening for Direct Tension Specimens.

Once the planes were defined, the coordinates of the centroid of the block were calculated for each time instant using the data from the markers (see Figure A.5). The X and Z coordinates of the centroid of the prism (X_c and Z_c), assuming no twisting, were calculated as,

$$X_c = \frac{(\sqrt{(X_3 - X_1)^2 + (Z_3 - Z_1)^2} + 0.5in)(X_3 - X_1)}{\sqrt{(X_3 - X_1)^2 + (Z_3 - Z_1)^2}} \tag{A.9}$$

$$Z_c = \frac{-0.5in(Z_3 - Z_1)}{\sqrt{(X_3 - X_1)^2 + (Z_3 - Z_1)^2}} \tag{A.10}$$

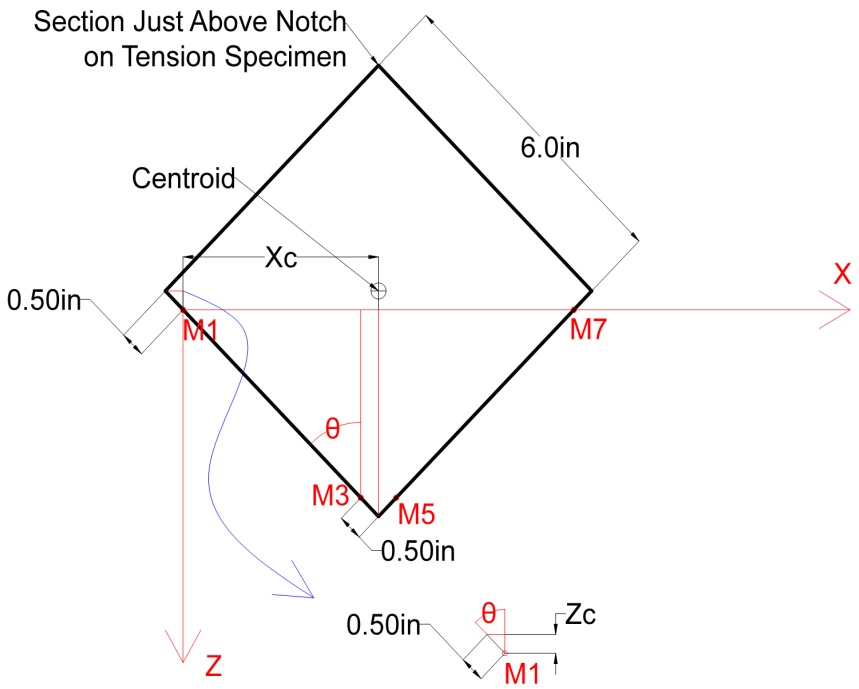

Figure A.5: Centroid Coordinates on Plane XZ for Plane Above Notch.

Once the coordinates of the centroid are calculated they are used with the equations of the planes to obtain the Y-coordinate of the centroid above and below the notch, Y_{Top} and Y_{Bottom}, respectively. The crack opening is then calculated as the difference between Y_{Top} and Y_{Bottom} for each time instant, minus the original difference at initial time, t_0. Although, in general, the Y-axis of the planes rotated different amounts during loading, taking $Y_{Top} - Y_{Bottom}$ was considered accurate enough to calculate the crack width in the direction paralell to the longitudinal axis of the member.

A.4 Calculation of Coupling Beam Shear Distortions

To determine average shear distortions along the length of each coupling beam specimen, the grid of Optotrak markers was divided into several marker strips. Each marker strip consisted of two adjacent rows of optical markers, which were used to determine the average shear distortion per strip. The marker layout and strips used for the coupling beam specimens with l_n/h of 3.0 and 2.0 are presented in Figures A.6 and A.7, respectively.

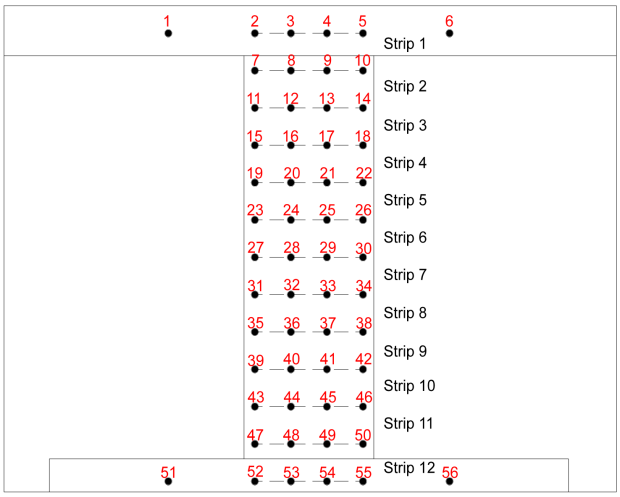

Figure A.6: Marker Strips for Coupling Beams with $l_n/h = 3.0$.

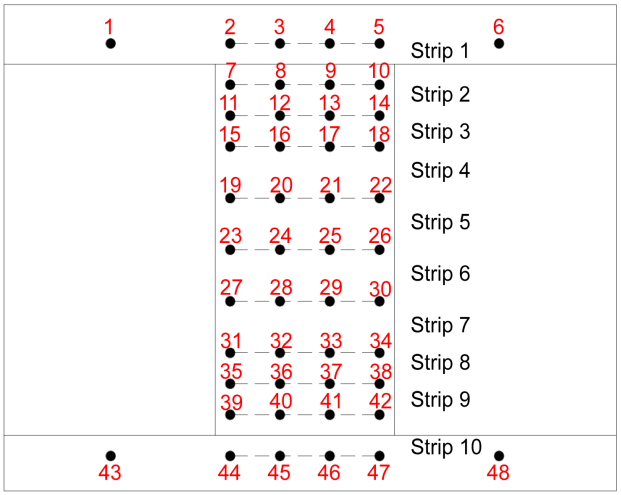

Figure A.7: Marker Strips for Coupling Beams with $l_n/h = 2.0$.

Each marker strip was divided into three rectangular elements with an optical marker at each node. To calculate the average shear distortion for each strip, the average shear distortion γ_n of each individual square element in the strip was calculated. The shear distortion of each element throughout the coupling beam and the average shear distortion per strip were calculated for each time instant. For illustration purposes, consider the element shown in Figure A.8, which is defined by markers 1 through 4 (M1-M4). At any given time t, the coordinates of M1 through M4 define the shape of the n^{th} element on the beam and hence the distortion angle γ_n can be calculated using Equation A.11,

$$\gamma_n = \frac{\alpha_T + \alpha_B}{2} + \frac{\alpha_L + \alpha_R}{2} \tag{A.11}$$

where the angles α_T, α_B, α_L, and α_R are as shown in Figure A.8. The angles α_T and α_B must not be confused with the angles shown in Figure A.1, used for the adjusted drift calculations. These angles are calculated based on the coordinates of each marker as,

$$\alpha_T = \frac{Y_2 - Y_1}{X_2 - X_1};\ \alpha_B = \frac{Y_4 - Y_3}{X_4 - X_3};\ \alpha_L = \frac{X_1 - X_3}{Y_1 - Y_3};\ \alpha_R = \frac{X_2 - X_4}{Y_2 - Y_4} \tag{A.12}$$

The average shear distortion of the i^{th} strip, formed by elements n, $n+1$ and $n+2$, was then calculated as,

$$(\gamma_s)_i = \frac{\gamma_n + \gamma_{n+1} + \gamma_{n+2}}{3} \tag{A.13}$$

In cases where some markers were compromised by concrete crushing and spalling, an average shear distortion was calculated for the strip using the four most reliable strip markers available closest to the beam edges.

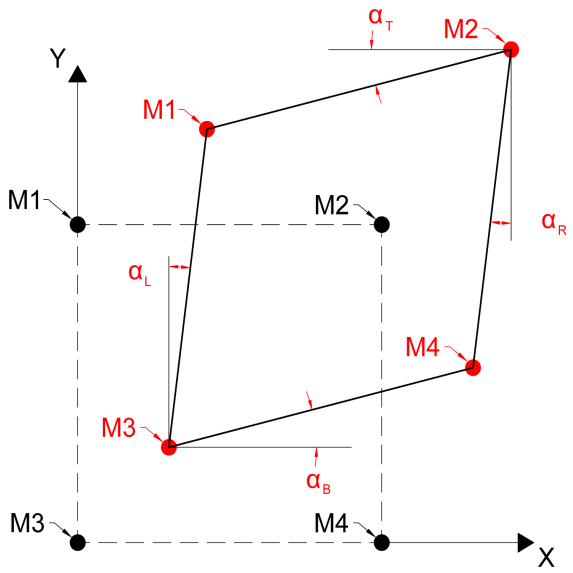

Figure A.8: Shear Distortion of Individual Element.

A.5 Calculation of Coupling Beam Curvatures

The average curvature for each marker strip was calculated based on the coordinates of the markers using various approaches. The first approach considered only the markers located at the corners of each strip while the other two approaches considered all the markers in a given marker strip.

A.5.1 Curvatures Calculated With Outer Markers

The markers identified as TL_i, TR_i, BL_i and BR_i on Figure A.9 define the location of the four corners of the i^{th} strip in the coupling beam.

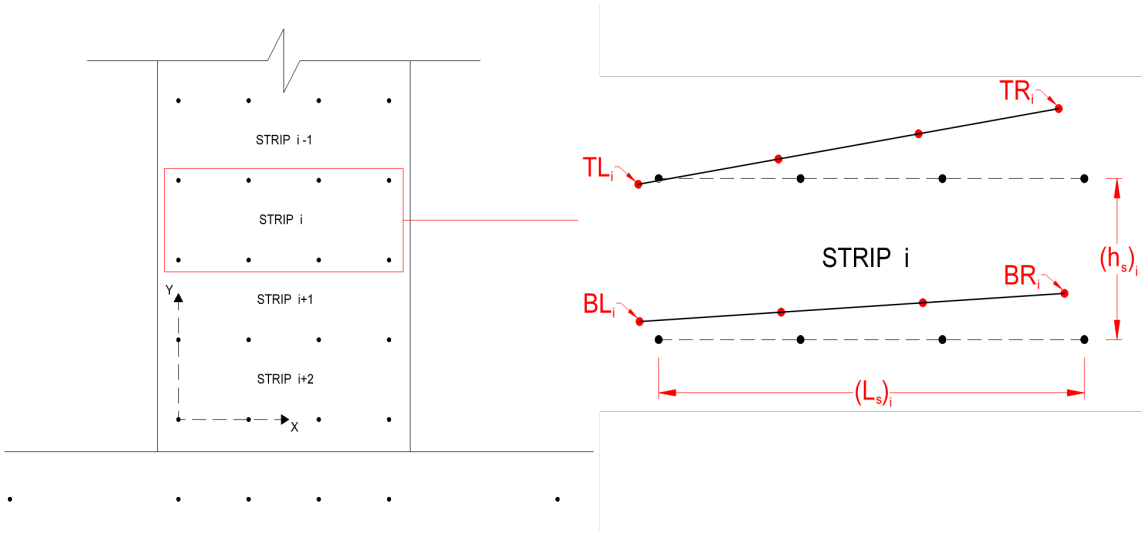

Figure A.9: Curvature Calculation Variables For a Given Strip.

Based on their position data, the average strains at the left and right side of the strip were calculated and used to define the average curvature of the strip as follows,

$$\phi_i = \frac{\epsilon_{R_i} - \epsilon_{L_i}}{L_{s_i}} = \frac{(Y_{TR} - Y_{BR})_i - (Y_{TL} - Y_{BL})_i}{L_{s_i} h_{s_i}} \tag{A.14}$$

where ϵ_{R_i} and ϵ_{L_i} are the strains at the right and left side of strip$_i$ as shown in Figure A.9, L_{s_i} is the average length of the strip, h_{s_i} is the average height of the strip, and ϕ_i is the curvature of the i^{th} strip on the coupling beam at any given time t.

A.5.2 Curvatures and Rotations Calculated Using Linear Fits

The Optotrak™ markers on any given strip were used to calculate the average strains occurring along the depth of the coupling beams. The average curvature of the plastic hinges was calculated as the slope of a least squares linear fit of the strain profile generated using the calculated strains at four different locations along the beam depth. Figure A.10 shows the markers and distances used to calculate strains, rotations, and curvatures.

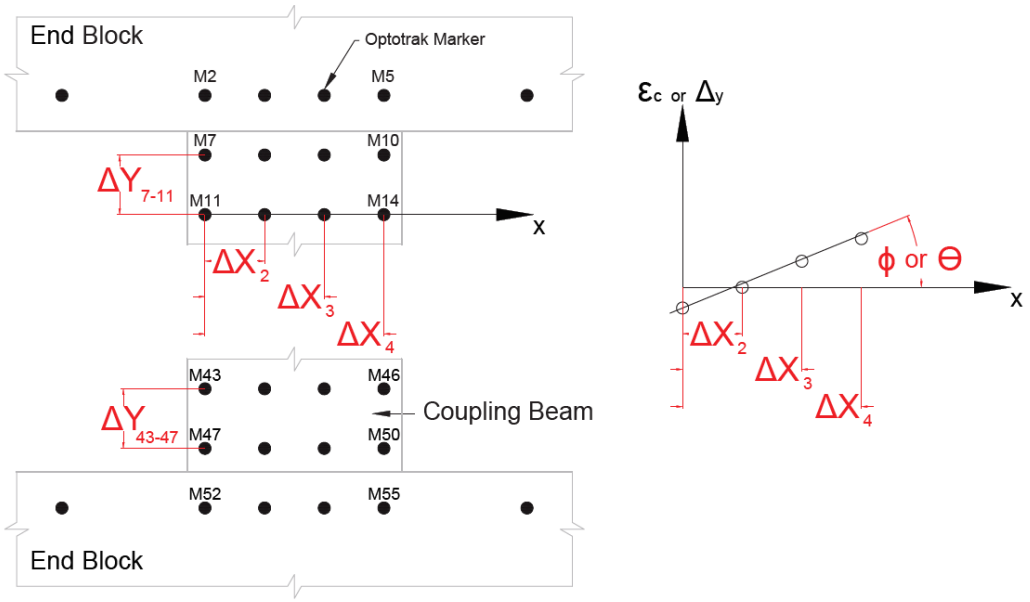

Figure A.10: Optical Markers Near the Coupling Beam Ends.

In some cases, cracking and damage at the plastic hinges compromised the data of one or more markers. For such cases, a fit of the strain profile may not adequately capture the rotations of a marker row at the damaged region. Therefore, a third

approach for calculating curvatures was used. Similar to the linear fits approach for calculating curvatures from strain profiles, linear fits of the marker position data for each marker row were calculated using all available and reliable markers. Once the rotation of each marker row was calculated, the average curvature of the region between two marker rows was calculated as the rotation change between the two marker rows divided over the distance between them. Figure A.11, shows the curvatures calculated for Strip 11 of Specimen CB5 using the different approaches previously discussed, where $\phi_{S11_{OM}}$, $\phi_{S11_{\epsilon Fit}}$, and $\phi_{\theta_{Fit}}$ are the curvatures calculated using the outer markers only, linear fit of the strains, and using a linear fit of data from reduced number of markers, respectively.

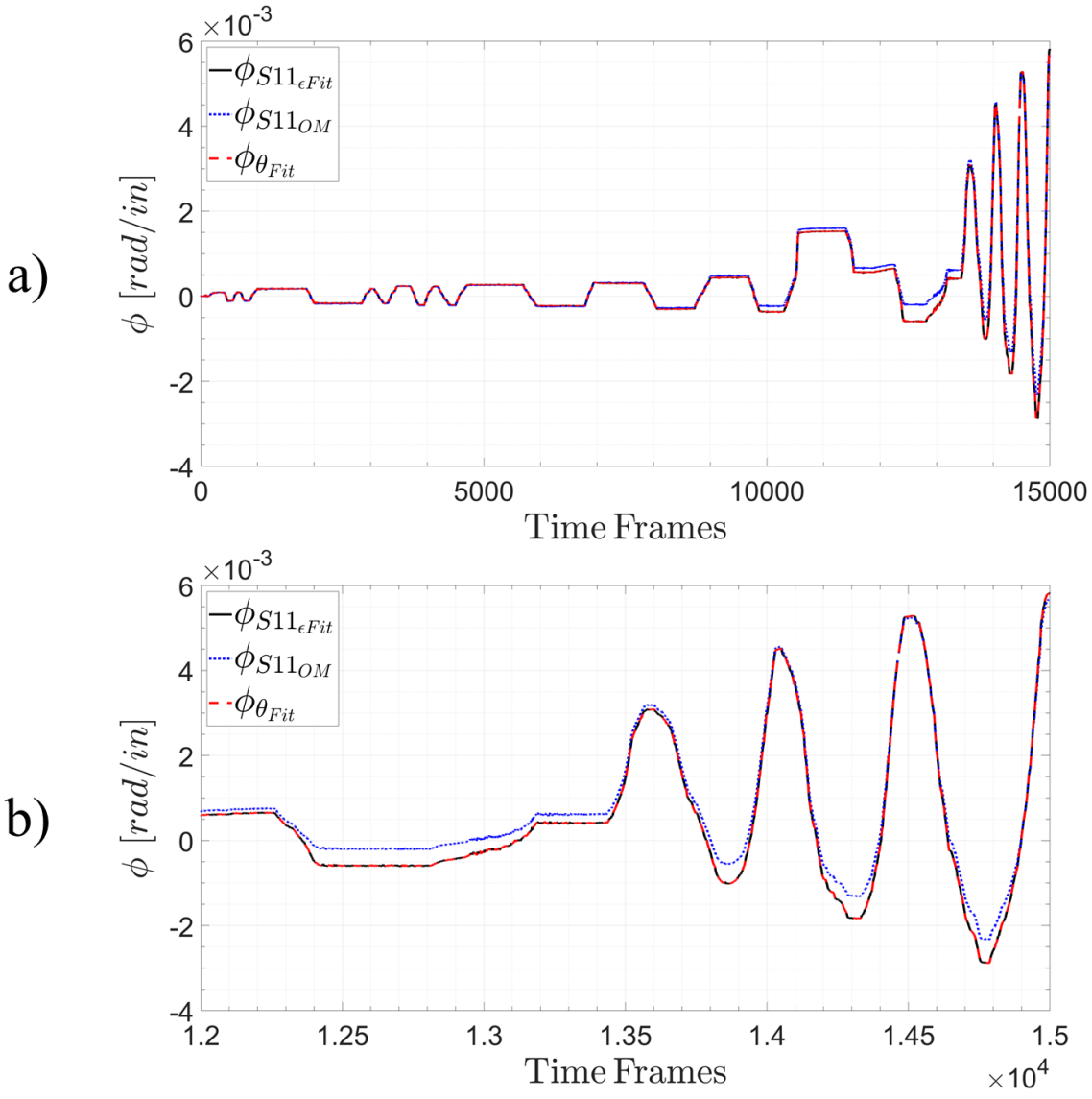

Figure A.11: Curvatures Calculated Using Different Methods for Strip 11 of Specimen CB5. a) Entire Test; b) Last Few Cycles.

B.1 SFRC Notched Beams

The equivalent flexural stress versus mid-span deflection responses of the notched beam specimens are shown in Figures B.1 through B.8. Figures B.9 trough B.16, on the other hand, show the flexural responses of the SFRC notched beams in terms of equivalent flexural stress versus crack opening. The specimens were identified according to the following naming convention: coupling beam number (e.g. CB1, CB2), followed by specimen type, where NB stands for notched beams, and ending with the specimen number. An example of this is CB1NB1, which identifies the first notched beam corresponding to the SFRC used in Coupling Beam CB1.

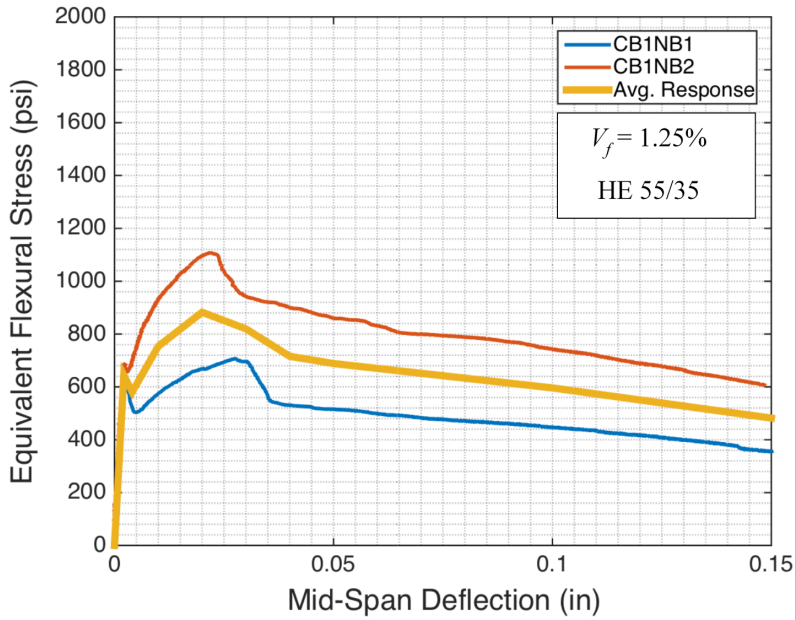

Figure B.1: Stress-Deflection Response (Notched Beams from Specimen CB1).

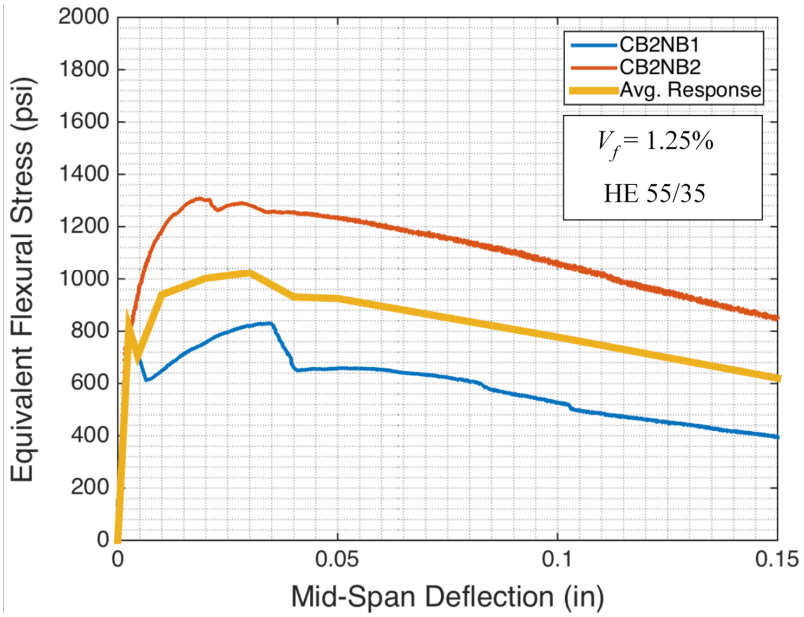

Figure B.2: Stress-Deflection Response (Notched Beams from Specimen CB2).

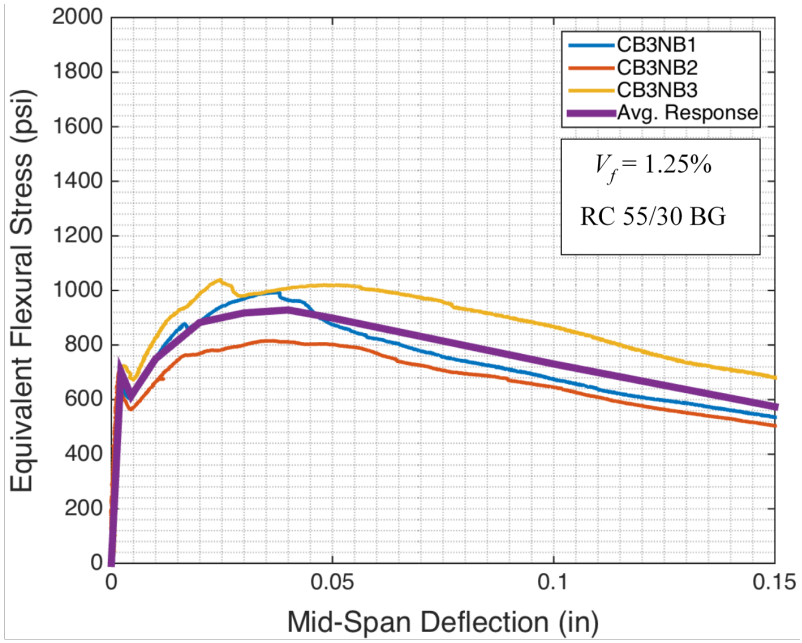

Figure B.3: Stress-Deflection Response (Notched Beams from Specimen CB3).

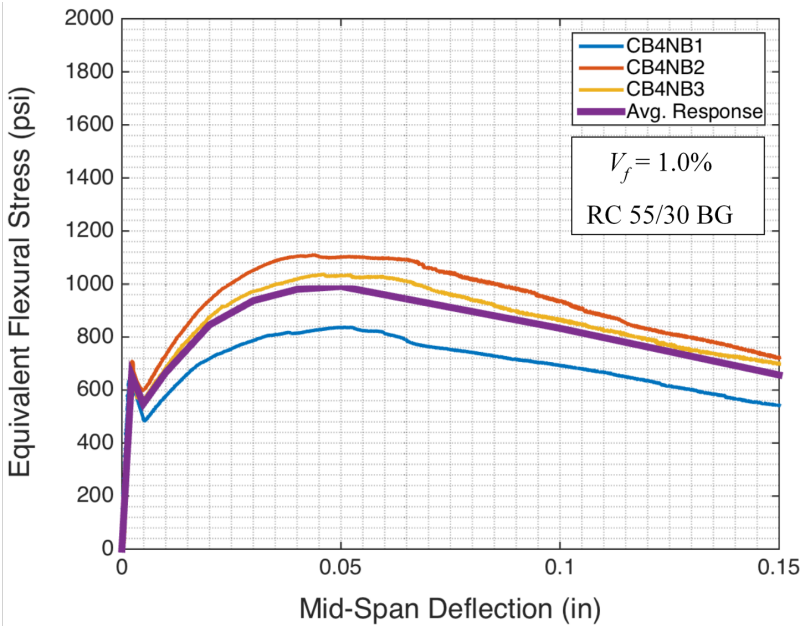

Figure B.4: Stress-Deflection Response (Notched Beams from Specimen CB4).

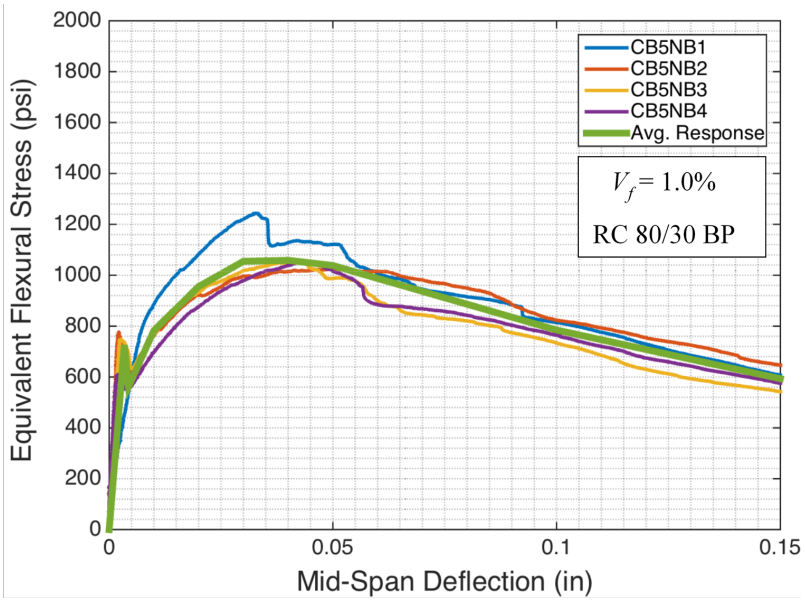

Figure B.5: Stress-Deflection Response (Notched Beams from Specimen CB5).

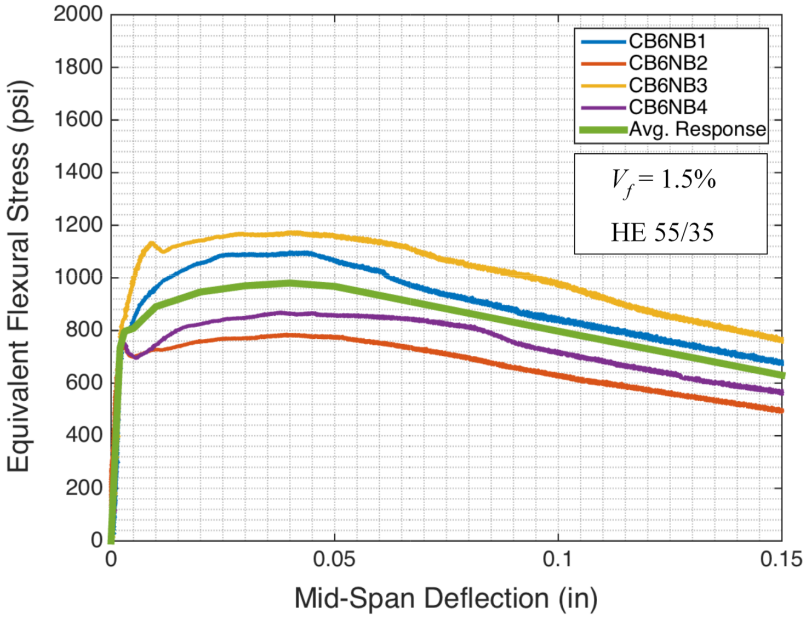

Figure B.6: Stress-Deflection Response (Notched Beams from Specimen CB6).

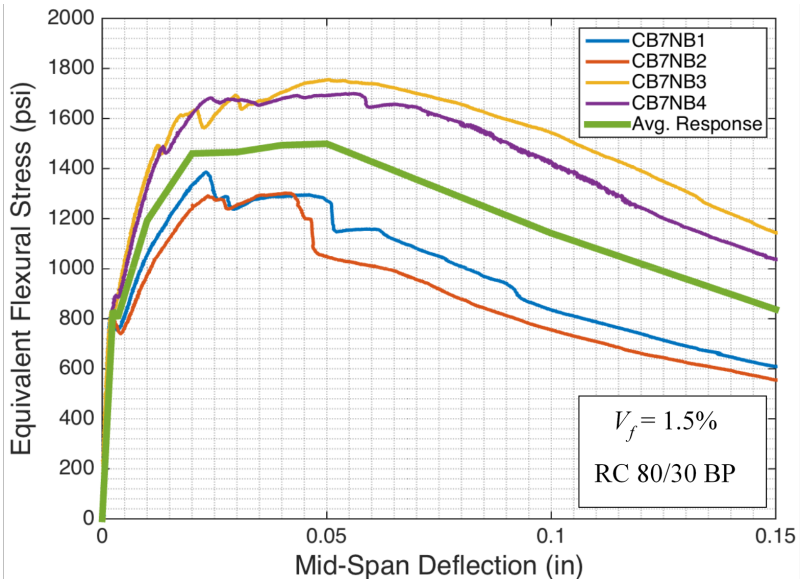

Figure B.7: Stress-Deflection Response (Notched Beams from Specimen CB7).

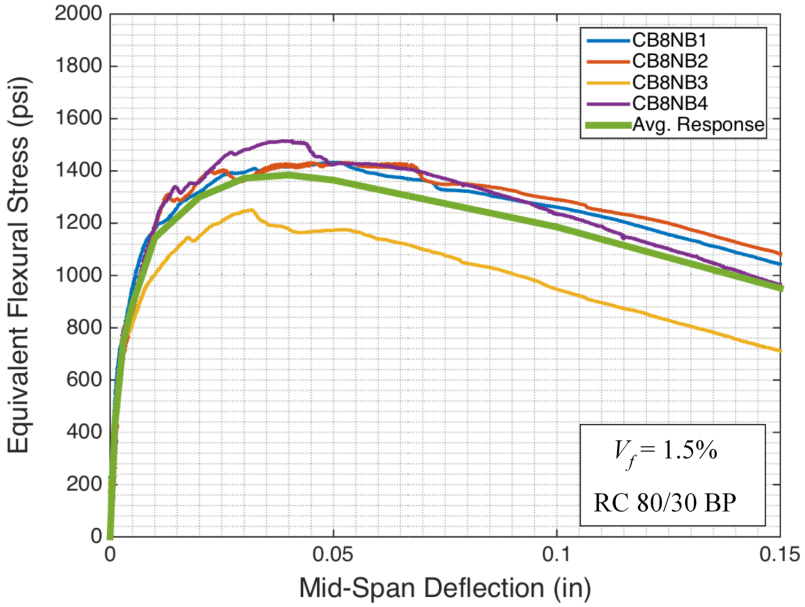

Figure B.8: Stress-Deflection Response (Notched Beams from Specimen CB8).

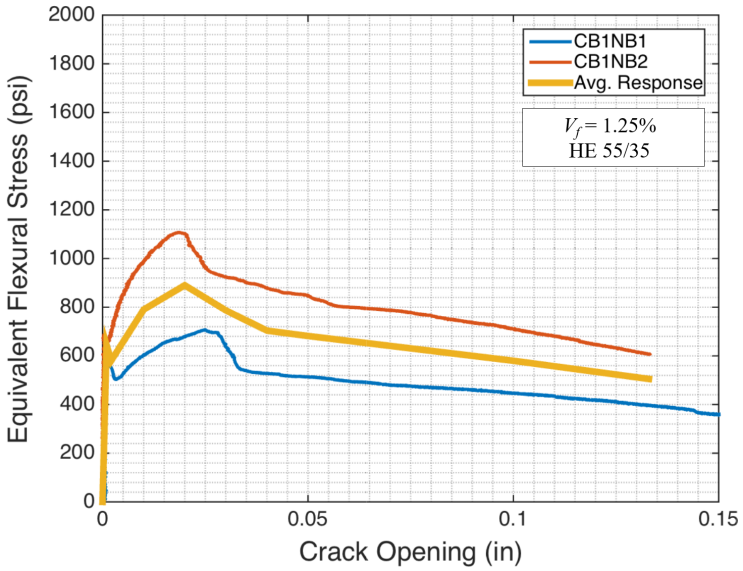

Figure B.9: Stress-Crack Width Response (Notched Beams from Specimen CB1).

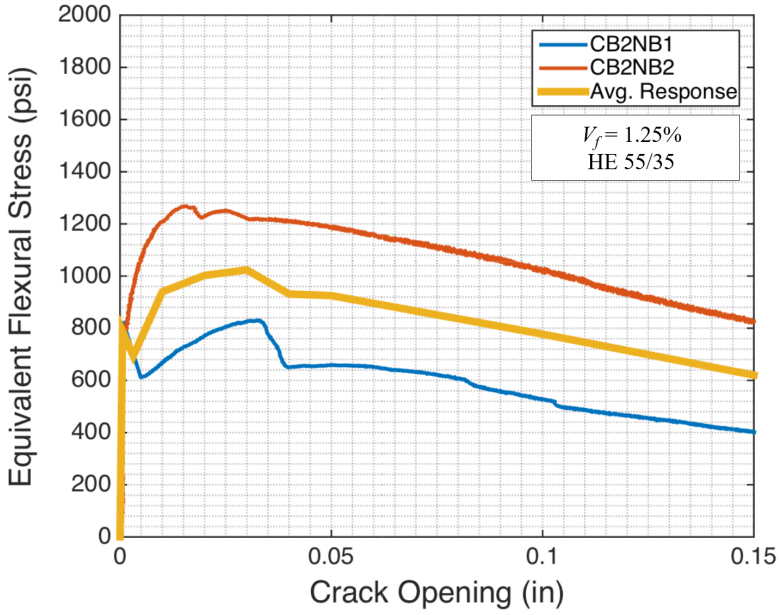

Figure B.10: Stress-Crack Width Response (Notched Beams from Specimen CB2).

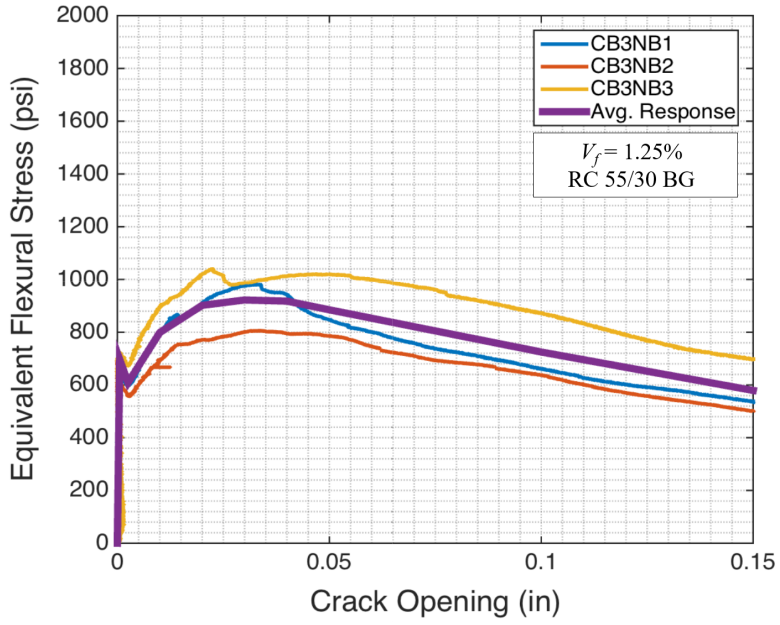

Figure B.11: Stress-Crack Width Response (Notched Beams from Specimen CB3).

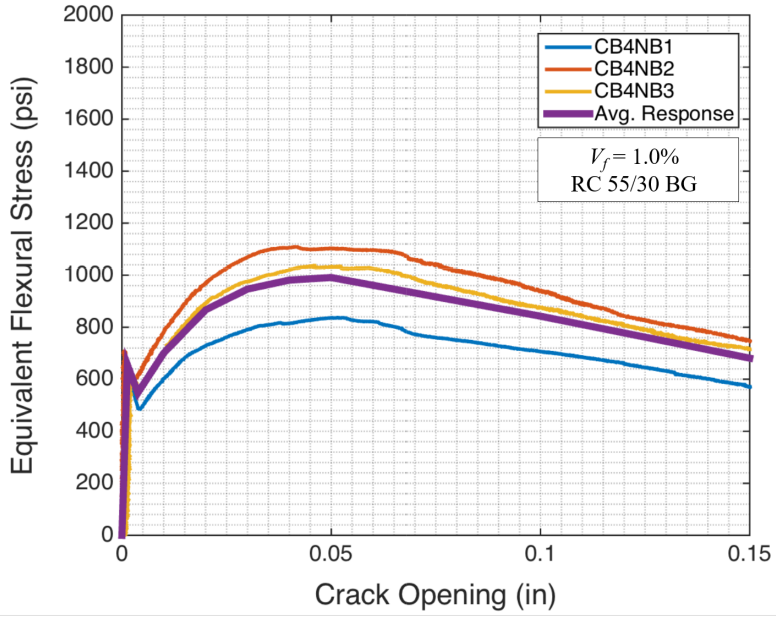

Figure B.12: Stress-Crack Width Response (Notched Beams from Specimen CB4).

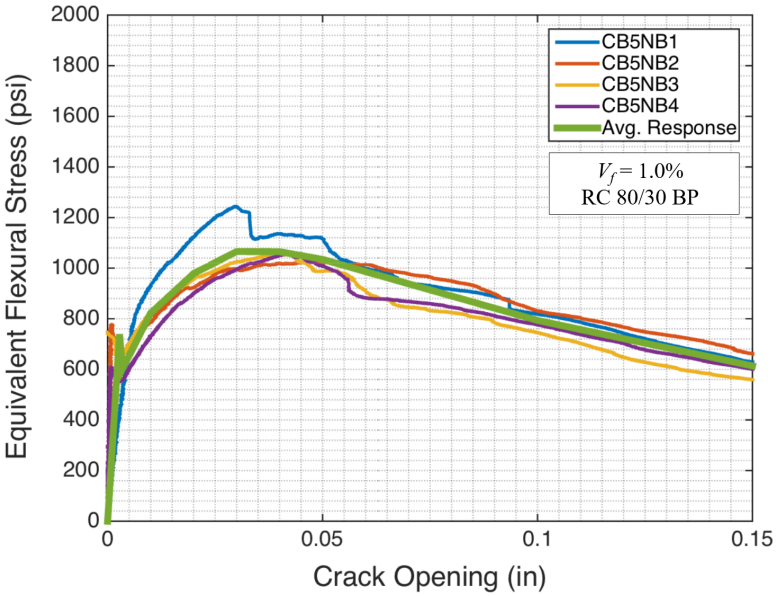

Figure B.13: Stress-Crack Width Response (Notched Beams from Specimen CB5).

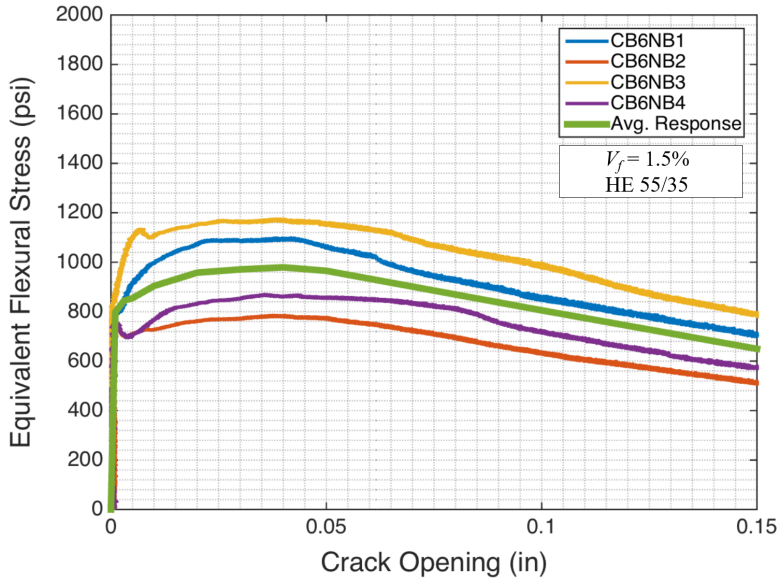

Figure B.14: Stress-Crack Width Response (Notched Beams from Specimen CB6).

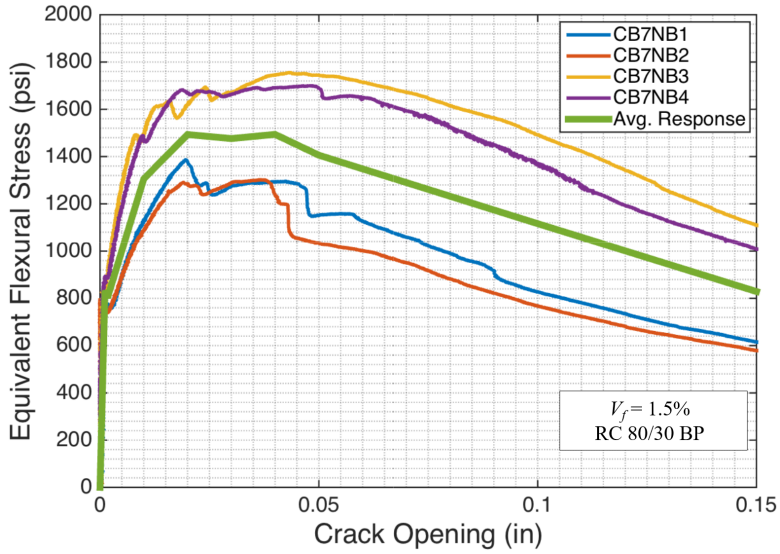

Figure B.15: Stress-Crack Width Response (Notched Beams from Specimen CB7).

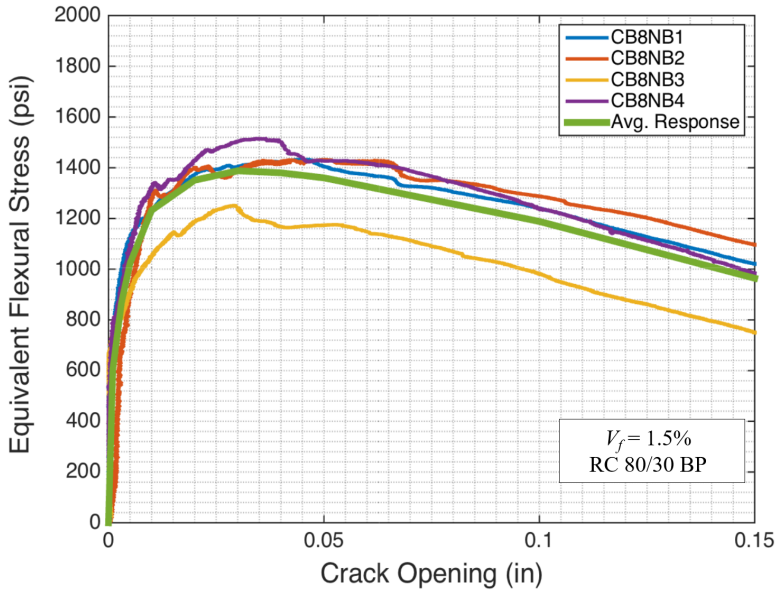

Figure B.16: Stress-Crack Width Response (Notched Beams from Specimen CB8).

B.2 SFRC Un-Notched Beams

The flexural response of the investigated SFRCs as measured by four-point bending tests per ASTM1609-12 are shown in Figures B.17 through B.24. The notation used is the same as for the notched beams (Appendix B.1), but the coupling beam specimen is followed by a "B", rather than "NB". The responses are shown in terms of equivalent flexural stress versus mid-span deflection, along with the calculated average response. It must be noted that the average response presented for the specimens corresponding to Coupling Beams CB1 and CB2 excludes Specimens CB1B2 and CB2B1, respectively. These specimens were eliminated from the average response calculation due to their considerably different behavior, which were considered to be not representative of the overall material behavior (See Figures B.17 and B.18).

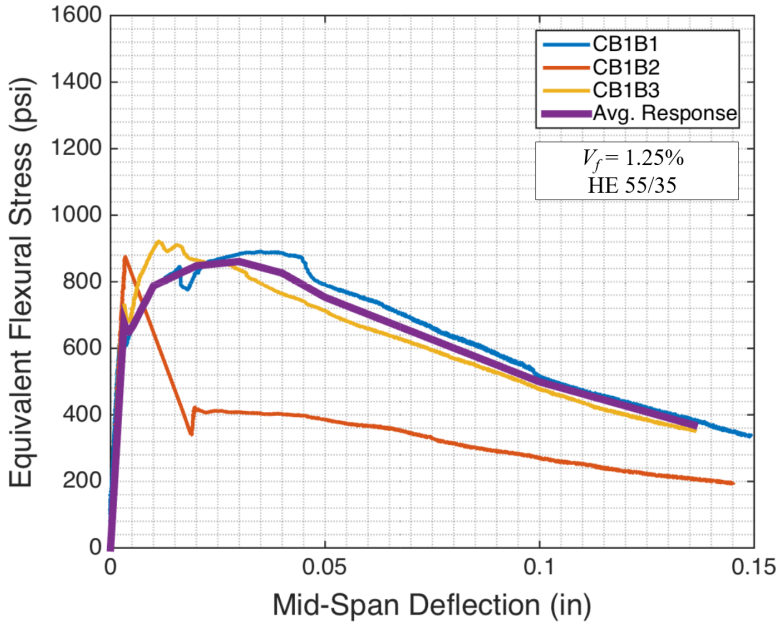

Figure B.17: Stress-Deflection Response (Un-notched Beams from Specimen CB1).

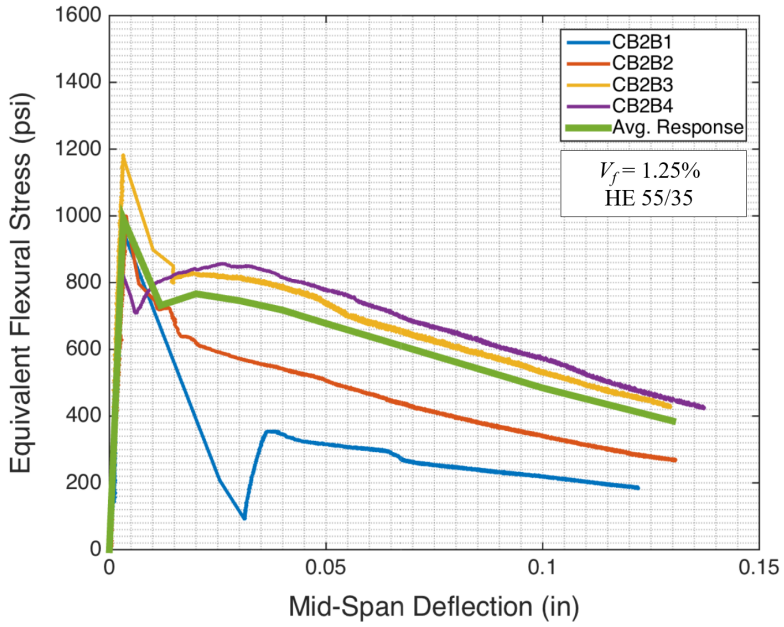

Figure B.18: Stress-Deflection Response (Un-notched Beams from Specimen CB2).

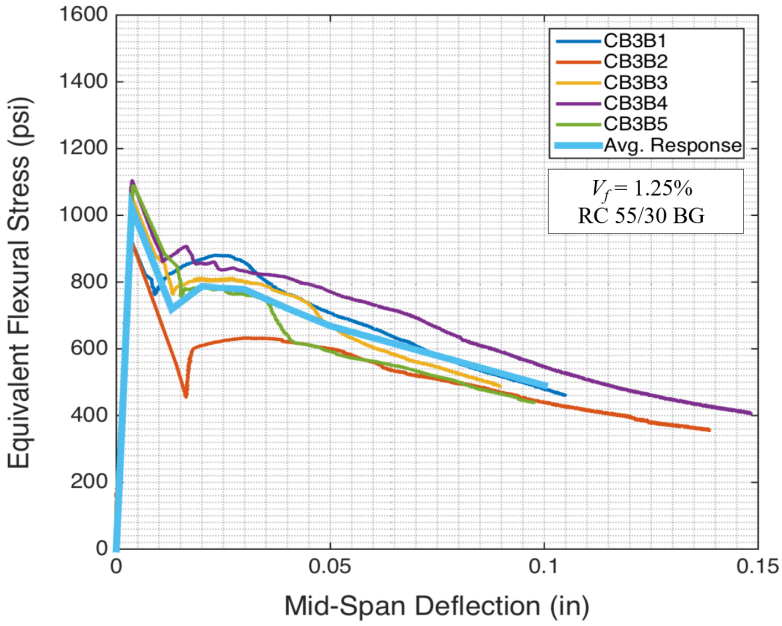

Figure B.19: Stress-Deflection Response (Un-notched Beams from Specimen CB3).

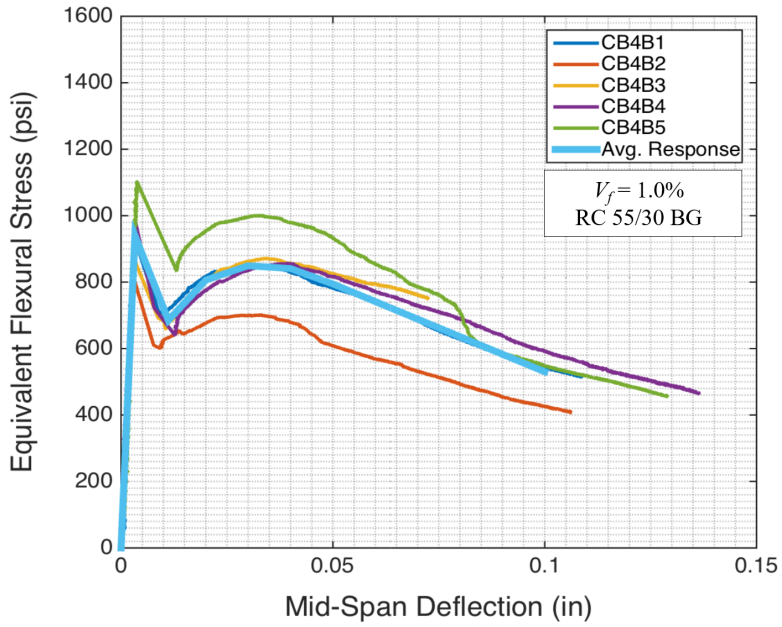

Figure B.20: Stress-Deflection Response (Un-notched Beams from Specimen CB4).

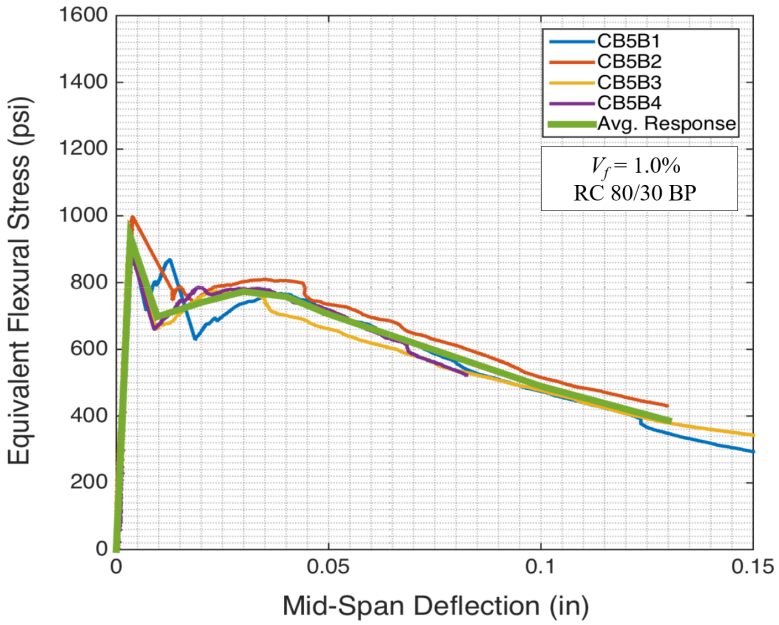

Figure B.21: Stress-Deflection Response (Un-notched Beams from Specimen CB5).

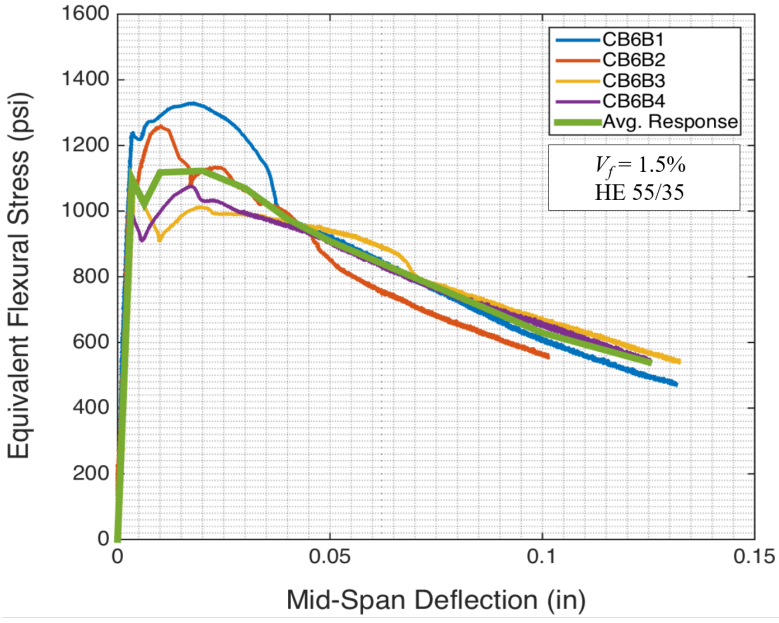

Figure B.22: Stress-Deflection Response (Un-notched Beams from Specimen CB6).

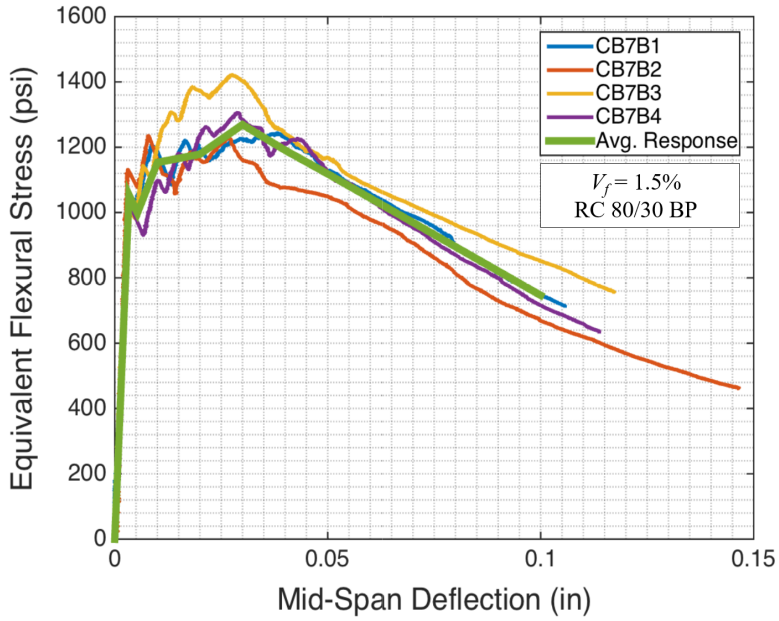

Figure B.23: Stress-Deflection Response (Un-notched Beams from Specimen CB7).

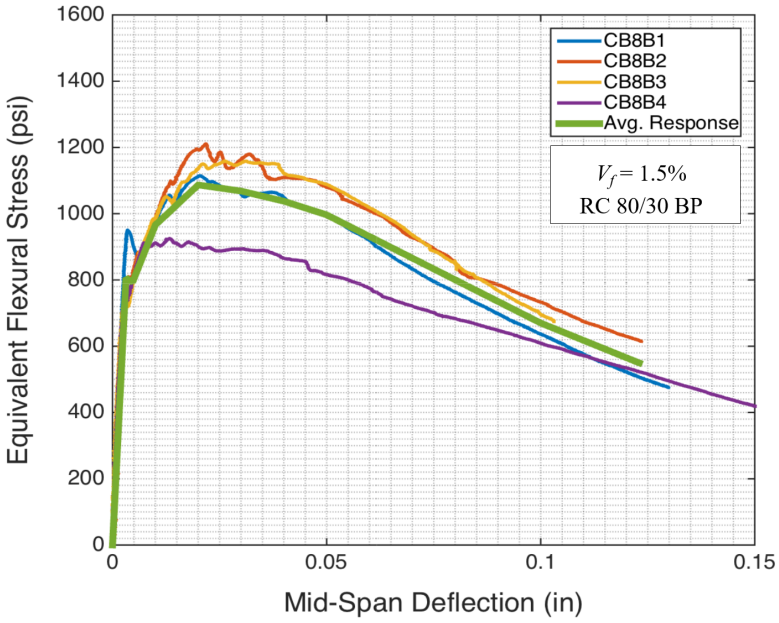

Figure B.24: Stress-Deflection Response (Un-notched Beams from Specimen CB8).

Concrete specimens for bending tests do not generally crack at mid-span. Therefore, the mid-span deflection may not be as robust of a measurement to describe the flexural behavior of the SFRC, as the flexural crack opening (i.e., crack width, w_{cr}). Figure B.25 through B.32 show the flexural response of each of the SFRCs in terms of the equivalent flexural stresses versus the crack opening (see Equation).

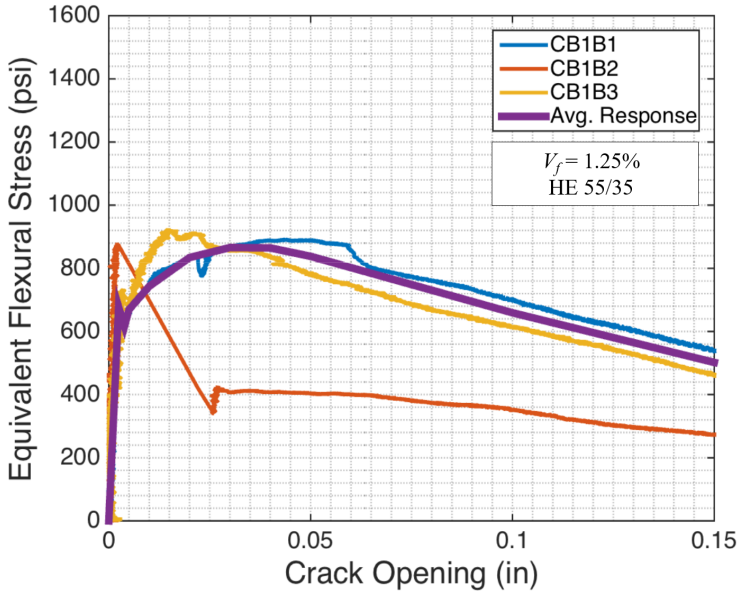

Figure B.25: Flexural Response (Un-notched Beams from Specimen CB1).

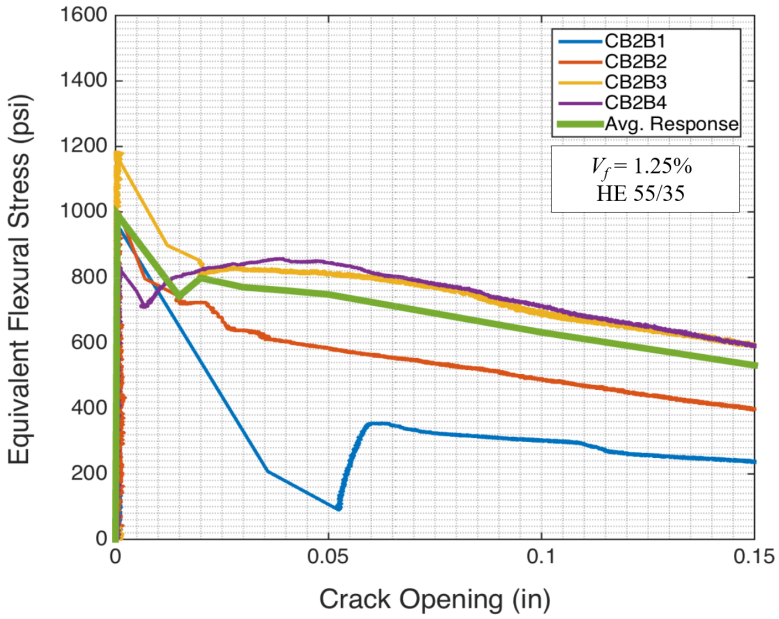

Figure B.26: Flexural Response (Un-notched Beams from Specimen CB2).

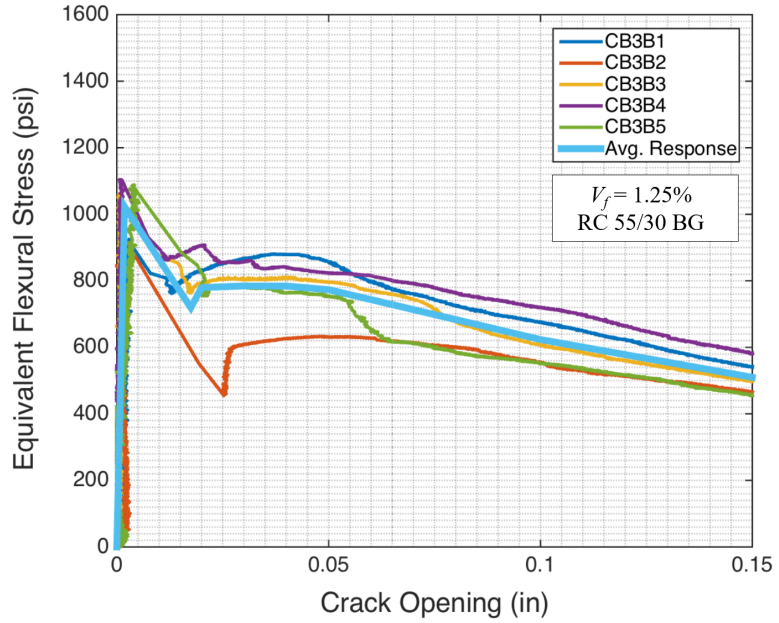

Figure B.27: Flexural Response (Un-notched Beams from Specimen CB3).

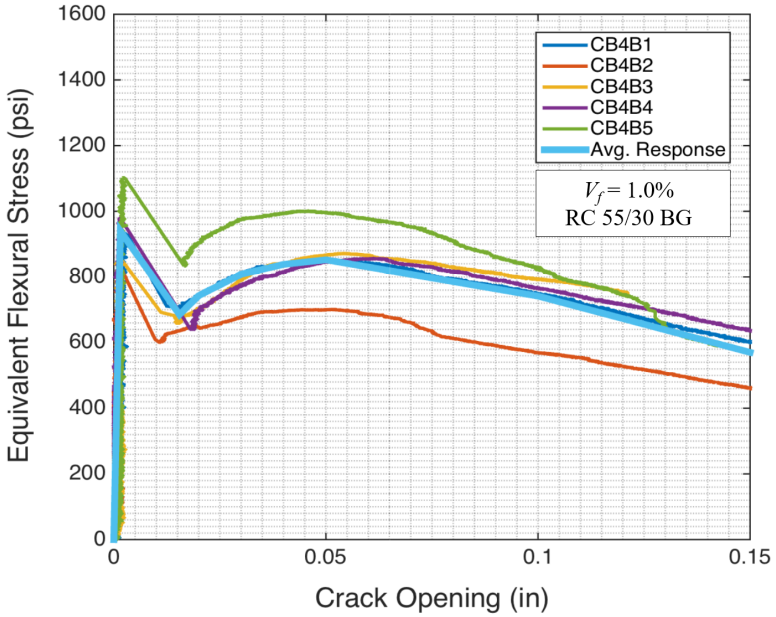

Figure B.28: Flexural Response (Un-notched Beams from Specimen CB4).

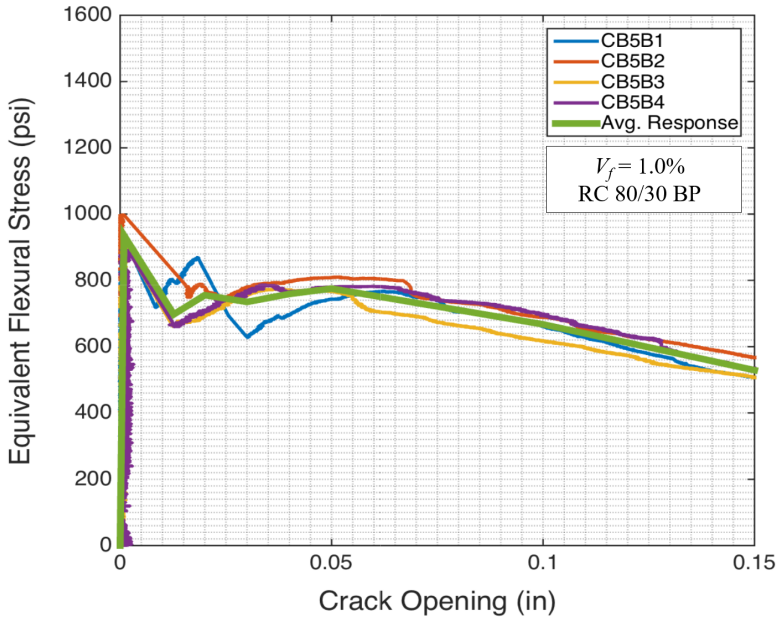

Figure B.29: Flexural Response (Un-notched Beams from Specimen CB5).

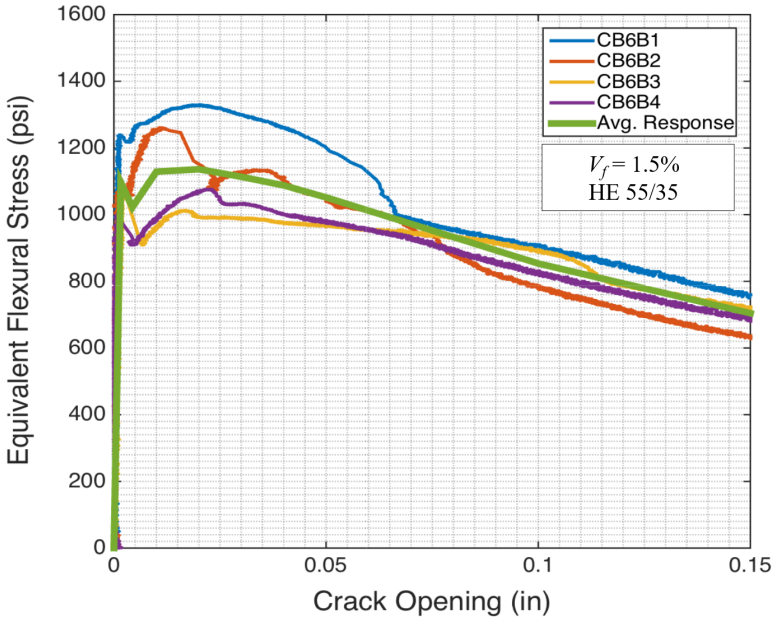

Figure B.30: Flexural Response (Un-notched Beams from Specimen CB6).

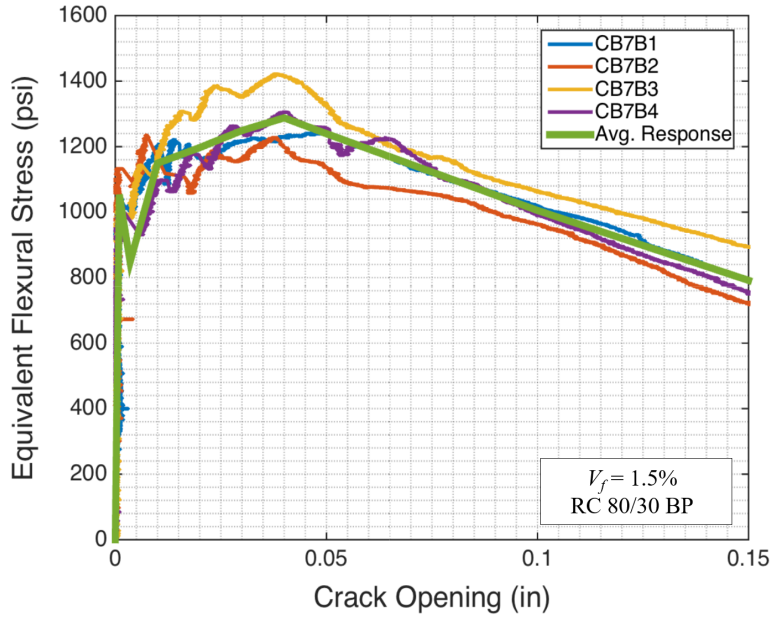

Figure B.31: Flexural Response (Un-notched Beams from Specimen CB7).

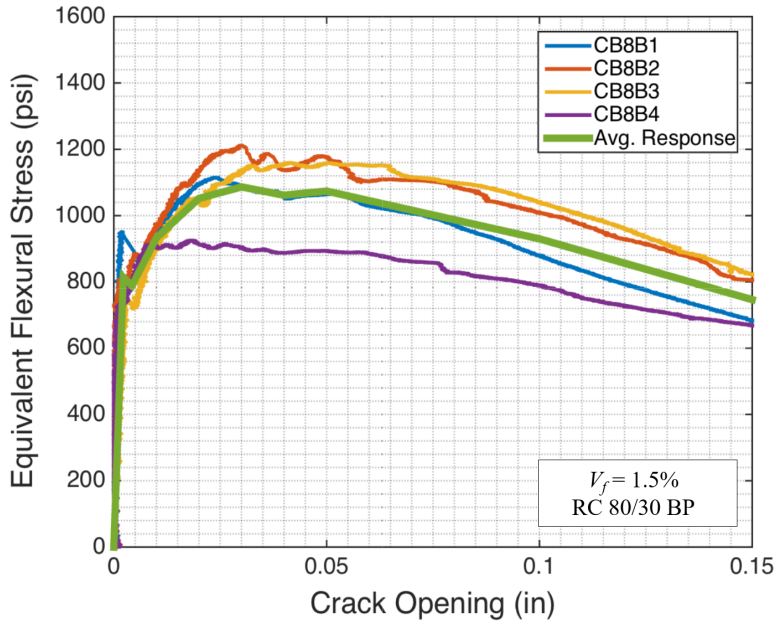

Figure B.32: Flexural Response (Un-notched Beams from Specimen CB8).

B.3 SFRC Tension Specimens

Figure B.33 through B.40 show the tensile response of each of the samples tested Beams from Specimen the SFRC used to cast each of the coupling beam specimens. A detailed discussion of the crack opening calculation is provided in Appendix A.3.

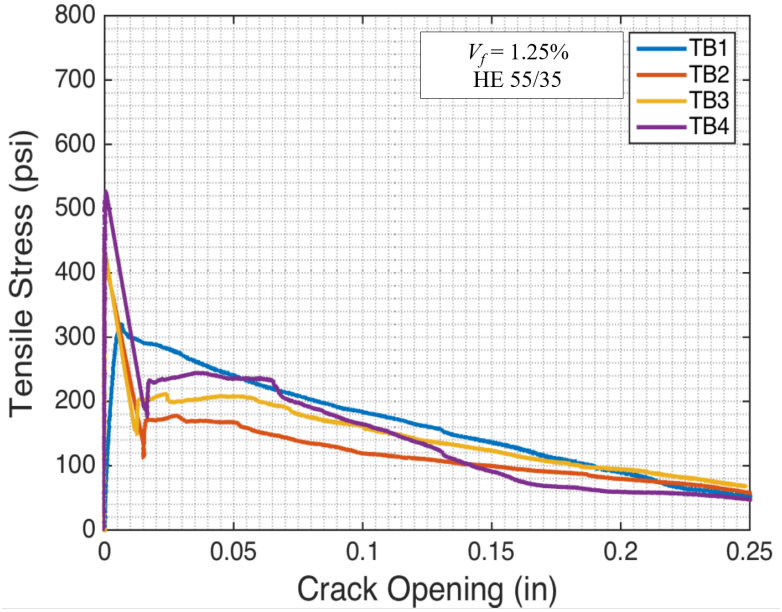

Figure B.33: Tensile Response (Tension Specimens Beams from Specimen CB1).

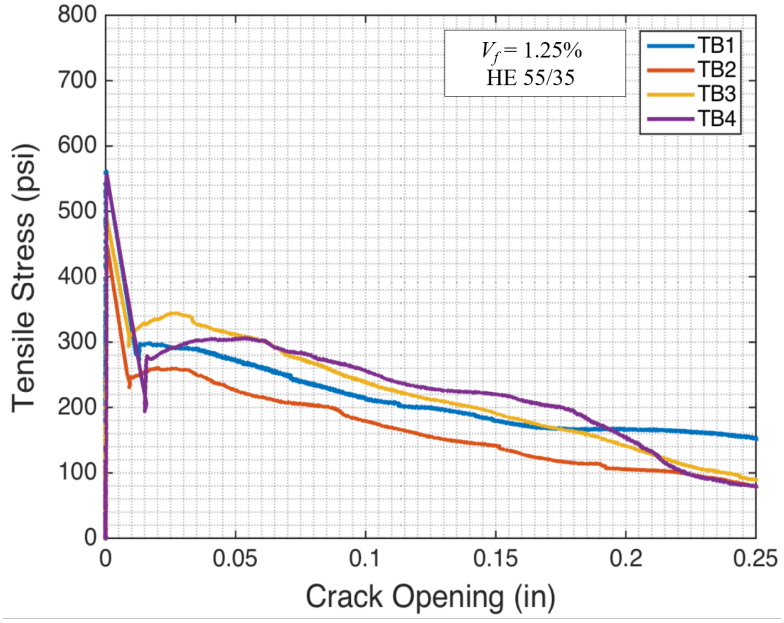

Figure B.34: Tensile Response (Tension Specimens Beams from Specimen CB2).

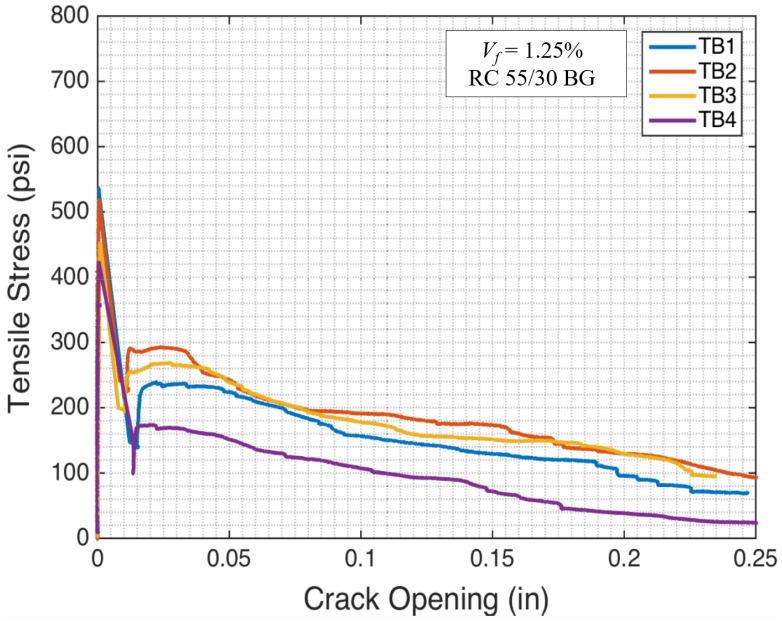

Figure B.35: Tensile Response (Tension Specimens Beams from Specimen CB3).

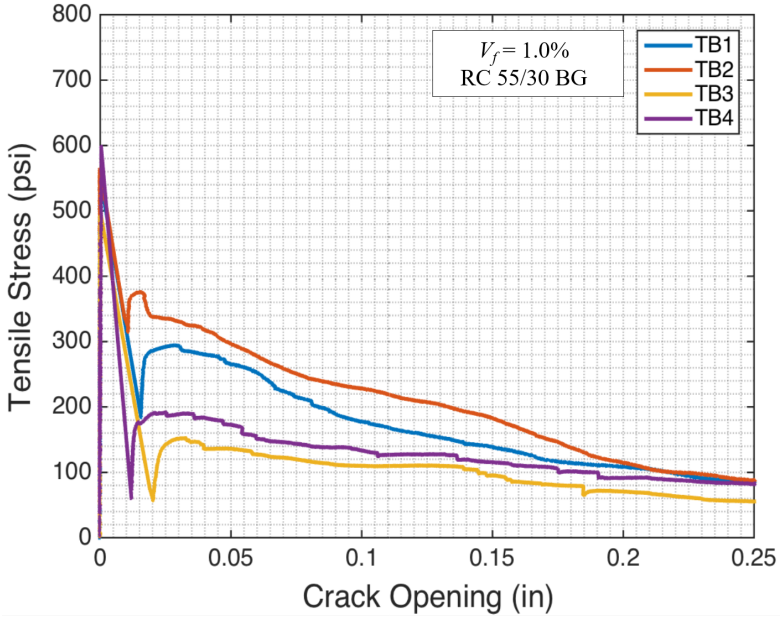

Figure B.36: Tensile Response (Tension Specimens Beams from Specimen CB4).

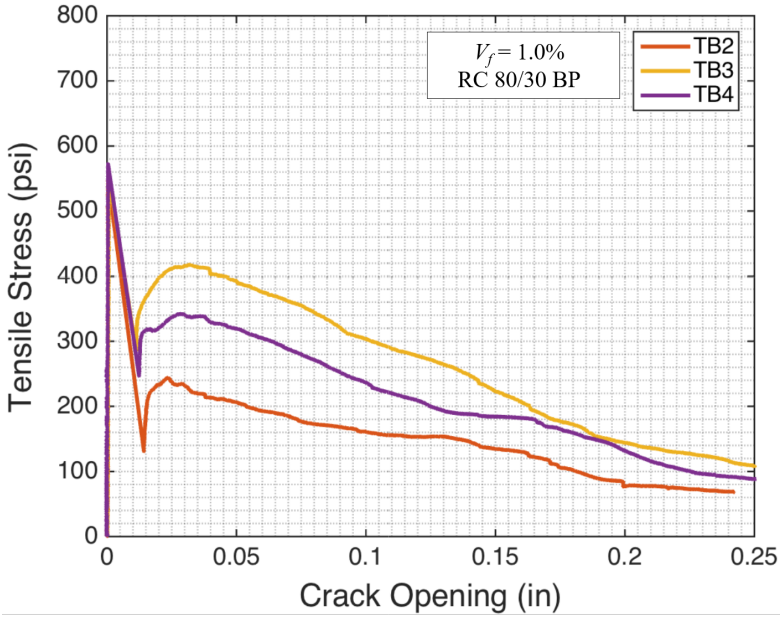

Figure B.37: Tensile Response (Tension Specimens Beams from Specimen CB5).

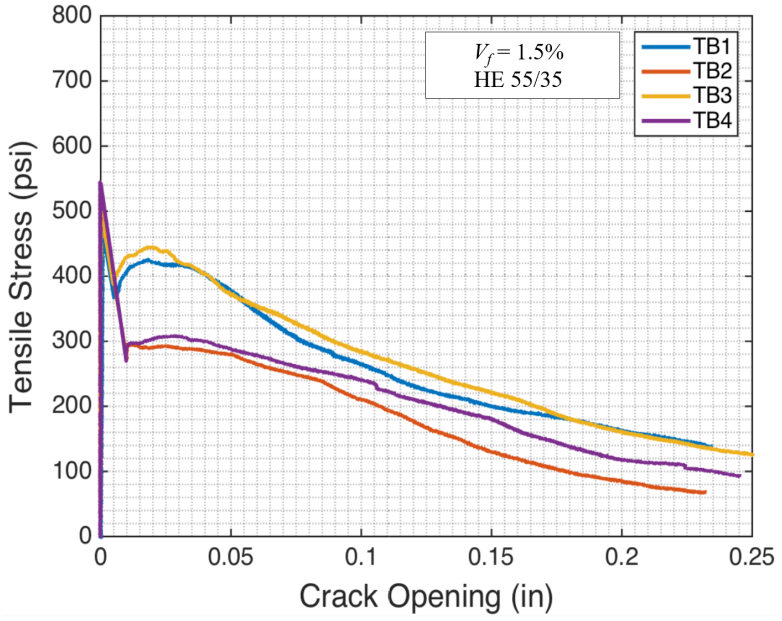

Figure B.38: Tensile Response (Tension Specimens Beams from Specimen CB6).

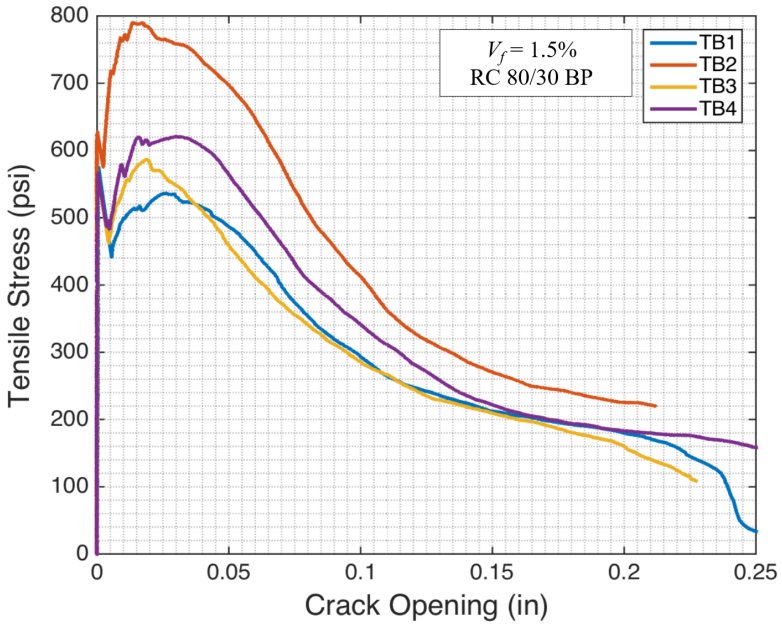

Figure B.39: Tensile Response (Tension Specimens Beams from Specimen CB7).

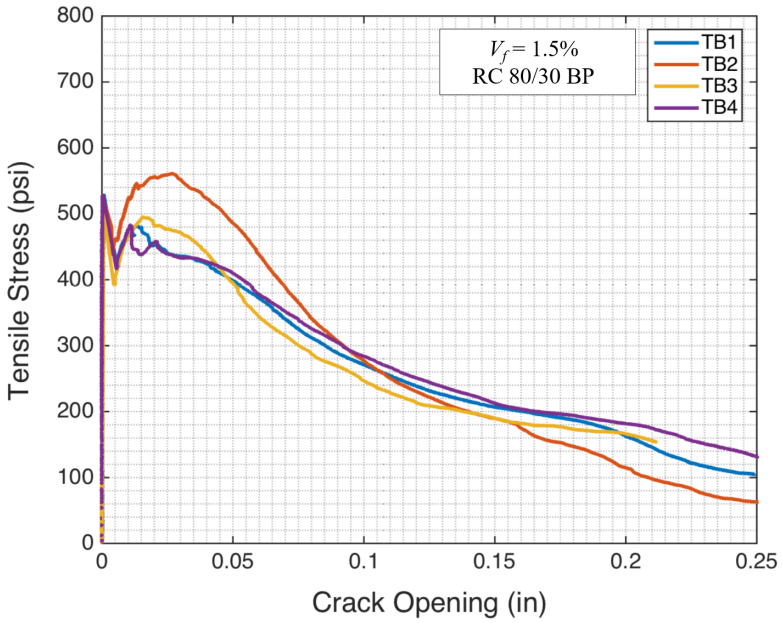

Figure B.40: Tensile Response (Tension Specimens Beams from Specimen CB8).

C SPECIMEN TEST DATES

Table C.1: Tensile and Compressive Test Dates.

CB Test Date	Coupling Beam	Fiber Type	V_f	Tension Blocks			Cylinders		
				ID	Test Date	Age (days)	ID	Test Date	Age (days)
3/31/2015	CB1	HE 55/35	1.25%	CB1T1	4/3/2015	51	CB1CYLN1	3/31/2015	48
		HE 55/35	1.25%	CB1T2	4/3/2015	51	CB1CYLN2	4/8/2015	56
		HE 55/36	1.25%	CB1T3	4/3/2015	51	CB1CYLN3	4/8/2015	56
		HE 55/35	1.25%	CB1T4	4/3/2015	51	CB1CYLN4	4/8/2015	56
5/22/2015	CB2	HE 55/35	1.25%	CB2T1	6/25/2015	62	CB2CYLN1	5/22/2015	28
		HE 55/35	1.25%	CB2T2	6/25/2015	62	CB2CYLN2	5/22/2015	28
		HE 55/36	1.25%	CB2T3	6/25/2015	62	CB2CYLN3	5/29/2015	35
		HE 55/35	1.25%	CB2T4	6/25/2015	62	CB2CYLN4	5/29/2015	35
		HE 55/35	1.25%				CB2CYLN5	5/29/2015	35
7/7/2015	CB3	ZP305 55/30	1.25%	CB3T1	7/14/2015	35	CB3CYLN1	7/7/2015	28
		ZP305 55/30	1.25%	CB3T2	7/14/2015	35	CB3CYLN2	7/7/2015	28
		ZP305 55/30	1.25%	CB3T3	7/14/2015	35	CB3CYLN3	7/7/2015	28
		ZP305 55/30	1.25%	CB3T4	7/14/2015	35	CB3CYLN4	7/7/2015	28
		ZP305 55/30	1.25%				CB3CYLN5	7/7/2015	28
8/7/2015	CB4	ZP305 55/30	1.00%	CB4T1	8/10/2015	31	CB4-CYLN1-B1	8/7/2015	28
		ZP305 55/30	1.00%	CB4T2	8/10/2015	31	CB4-CYLN2-B2	8/7/2015	28
		ZP305 55/30	1.00%	CB4T3	8/10/2015	31	CB4-CYLN1-B1	8/12/2015	33
		ZP305 55/30	1.00%	CB4T4	8/10/2015	31	CB4-CYLN2-B2	8/12/2015	33
		ZP305 55/30	1.00%				CB4-CYLN5-B3	8/12/2015	33
10/5/2015	CB5	80/30BP	1.00%	CB5T1	11/3/2015	60	CB5CYLN1	10/6/2015	32
		80/30BP	1.00%	CB5T2	11/3/2015	60	CB5CYLN2	10/6/2015	32
		80/30BP	1.00%	CB5T3	11/3/2015	60	CB5CYLN3	10/16/2015	42
		80/30BP	1.00%	CB5T4	11/3/2015	60	CB5CYLN4	10/16/2015	42
		80/30BP	1.00%				CB5CYLN5	10/16/2015	42
11/30/2015	CB6	HE 55/35	1.50%	CB6T1	12/16/2015	47	CB6CYLN1	11/30/2015	31
		HE 55/35	1.50%	CB6T2	12/16/2015	47	CB6CYLN2	12/1/2015	32
		HE 55/36	1.50%	CB6T3	12/16/2015	47	CB6CYLN3	12/1/2015	32
		HE 55/35	1.50%	CB6T4	12/16/2015	47	CB6CYLN4	1/22/2016	84
		HE 55/35	1.50%				CB6CYLN5	1/22/2016	84
2/12/2016	CB7	80/30BP	1.50%	CB7T1	2/29/2016	77	CB7CYLN1	2/12/2016	60
		80/30BP	1.50%	CB7T2	2/29/2016	77	CB7CYLN2	2/12/2016	60
		80/30BP	1.50%	CB7T3	2/29/2016	77	CB7CYLN3	6/8/2016	177
		80/30BP	1.50%	CB7T4	2/29/2016	77	CB7CYLN4	6/8/2016	177
		80/30BP	1.50%				CB7CYLN5	6/8/2016	177
6/7/2016	CB8	80/30BP	1.50%	CB8T1	6/10/2016	45	CB8CYLN1	6/7/2016	42
		80/30BP	1.50%	CB8T2	6/10/2016	45	CB8CYLN2	6/7/2016	42
		80/30BP	1.50%	CB8T3	6/10/2016	45	CB8CYLN3	6/10/2016	45
		80/30BP	1.50%	CB8T4	6/10/2016	45	CB8CYLN4	6/10/2016	45
		80/30BP	1.50%				CB8CYLN5	6/10/2016	45

Table C.2: Bending Test Dates.

CB Test Date	Coupling Beam	Fiber Type	V_f	Notched Beams			Un-notched Beams		
				ID	Test Date	Age (days)	ID	Test Date	Age (days)
3/31/2015	CB1	HE 55/35	1.25%	CB1-NB1	4/7/2015	55	CB1B1	4/7/2015	55
		HE 55/35	1.25%	CB1-NB2	4/7/2015	55	CB1B2	4/7/2015	55
		HE 55/36	1.25%				CB1B3	4/7/2015	55
5/22/2015	CB2	HE 55/35	1.25%	CB2-NB1	6/2/2015	39	CB2B1	6/1/2015	38
		HE 55/35	1.25%	CB2-NB2	6/2/2015	39	CB2B2	6/1/2015	38
		HE 55/36	1.25%				CB2B3	6/1/2015	38
		HE 55/35	1.25%				CB2B4	6/2/2015	39
7/7/2015	CB3	ZP305 55/30	1.25%	CB3-NB1-Batch2	7/8/2015	29	CB3-B1-Batch2	7/8/2015	29
		ZP305 55/30	1.25%	CB3-NB2-Batch3	7/8/2015	29	CB3-B2-Batch3	7/8/2015	29
		ZP305 55/30	1.25%	CB3-NB3-Batch3	7/8/2015	29	CB3-B3-Batch3	7/9/2015	30
		ZP305 55/30	1.25%				CB3-B4-Batch3	7/9/2015	30
		ZP305 55/30	1.25%				CB3-B5-Batch1	7/9/2015	30
8/7/2015	CB4	ZP305 55/30	1.00%	CB4-NB1-Batch2	8/11/2015	32	CB4-B1-Batch1	8/11/2015	32
		ZP305 55/30	1.00%	CB4-NB2-Batch3	8/11/2015	32	CB4-B2-Batch2	8/11/2015	32
		ZP305 55/30	1.00%	CB4-NB3-Batch3	8/11/2015	32	CB4-B3-Batch3	8/11/2015	32
		ZP305 55/30	1.00%				CB4-B4-Batch3	8/11/2015	32
		ZP305 55/30	1.00%				CB4-B5-Batch3	8/11/2015	32
10/5/2015	CB5	80/30BP	1.00%	CB5-NB1-Batch2	10/12/2015	38	CB5-B1-Batch1	10/9/2015	35
		80/30BP	1.00%	CB5-NB2-Batch3	10/12/2015	38	CB5-B2-Batch2	10/9/2015	35
		80/30BP	1.00%	CB5-NB3-Batch3	10/12/2015	38	CB5-B3-Batch3	10/9/2015	35
		80/30BP	1.00%	CB5-NB4-Batch3	10/12/2015	38	CB5-B4-Batch3	10/9/2015	35
11/30/2015	CB6	HE 55/35	1.50%	CB6-NB1-Batch1	2/17/2016	110	CB6-B1-Batch1	6/2/2016	216
		HE 55/35	1.50%	CB6-NB2-Batch2	2/17/2016	110	CB6-B2-Batch2	6/2/2016	216
		HE 55/36	1.50%	CB6-NB3-Batch3	2/17/2016	110	CB6-B3-Batch3	6/2/2016	216
		HE 55/35	1.50%	CB6-NB4-Batch3	2/17/2016	110	CB6-B4-Batch3	6/2/2016	216
2/12/2016	CB7	80/30BP	1.50%	CB7-NB1-Batch1	6/3/2016	172	CB7-B1-Batch1	6/2/2016	171
		80/30BP	1.50%	CB7-NB2-Batch2	6/3/2016	172	CB7-B2-Batch2	6/2/2016	171
		80/30BP	1.50%	CB7-NB3-Batch3	6/3/2016	172	CB7-B3-Batch3	6/2/2016	171
		80/30BP	1.50%	CB7-NB4-Batch3	6/3/2016	172	CB7-B4-Batch3	6/2/2016	171
6/7/2016	CB8	80/30BP	1.50%	CB8-NB1-Batch1	6/8/2016	43	CB8-B1-Batch1	6/9/2016	44
		80/30BP	1.50%	CB8-NB2-Batch2	6/8/2016	43	CB8-B2-Batch2	6/9/2016	44
		80/30BP	1.50%	CB8-NB3-Batch3	6/8/2016	43	CB8-B3-Batch3	6/9/2016	44
		80/30BP	1.50%	CB8-NB4-Batch3	6/8/2016	43	CB8-B4-Batch3	6/9/2016	44